Surface Aligned Liquid Crystals on Micropatterned Polyimide Relief Structures

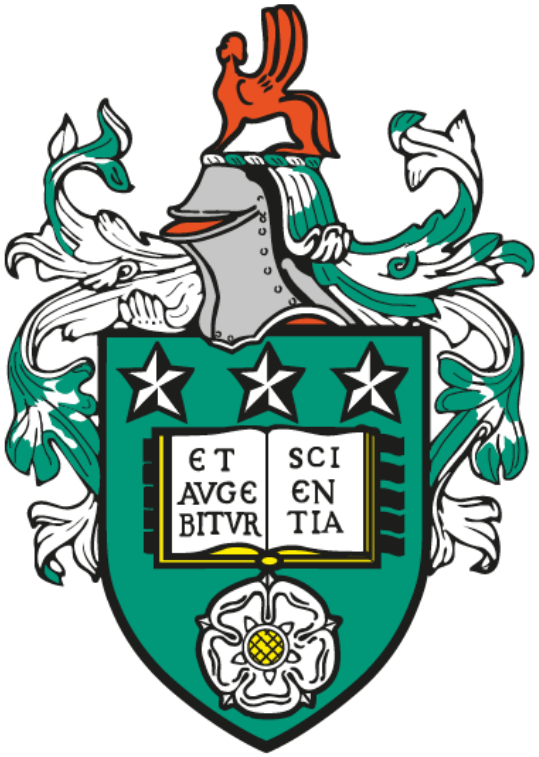

Thomas Andrew Moorhouse

University of Leeds

Department of Physics and Astronomy

Submitted in accordance with the requirements for the degree of

Doctor of Philosophy

November 2024

The candidate confirms that the work submitted is his own, except where work which has formed part of jointly authored publications has been included. The contribution of the candidate and the other authors to this work has been explicitly indicated below. I confirm that appropriate credit has been given within the thesis where reference has been made to the work of others.

Chapter 4 contains work from "Sub-micron Diffractive Optical Elements Facilitated by Intrinsic Deswelling of Auxetic Liquid Crystal Elastomers", which has been published by T. Moorhouse and T. Raistrick in Advanced Optical Materials, 2024, 12, 2400866. Microfabrication, surface metrology (atomic force microscopy (AFM)), construction of diffraction apparatus and diffraction efficiency measurements were carried out by T. Moorhouse; LCE synthesis and compositional changes, diffraction pattern measurements under thermal and mechanical load, phase and thermal behaviour studies (differential scanning calorimetry (DSC), thermogravimetric analysis (TGA)) and device cycle testing (DSC, dynamic mechanical analysis (DMA)) were carried out by T. Raistrick; diffraction efficiency analysis and the writing of the manuscript was carried out collaboratively by T. Moorhouse and T. Raistrick.

Acknowledgements

Firstly, I would like to thank my supervisors Prof. Helen Gleeson and Prof. Edmund Linfield, who have provided me with fantastic supervision and guidance throughout this project, which has had its fair share of disruption that would have been infinitely harder to overcome without their support. Working with Helen has been a pleasure, involving many insightful physics discussions, valuable feedback on conference presentations and job applications and the significant task of overseeing the write-up of this thesis, for which I am incredibly grateful.

From the Soft Matter Physics department at Leeds, I would like thank various current and previous members who have all played their own part in me completing this project and staying motivated throughout the process. These include, Dr. Dan Baker who keeps the department ticking and has helped me with countless experimental endeavours, Dr. Tom Raistrick who I had the pleasure of collaborating with and learning conoscopy from and Dr. Harry Litt for all the valuable discussions and laughs during our time as undergrad and PhD students. I would also like to thank Drs. Pete Wyatt, Devesh Mistry, Matt Reynolds and Rowan Morris for various discussions and assistance throughout this work.

I would also like to acknowledge the technical support I have received during this project. I would like to thank Dr. Mark Rosamond and the Leeds Nanotechnology Cleanroom team for fabricating precision microstructures and assisting in their characterisation. I would also like to thank Stuart Weston and his team in the Physics Mechanical Workshop for constructing and aiding in the design of various bespoke pieces of lab equipment, used frequently throughout the project. Also, I would like to acknowledge Dr. Lekshmi Kailas and Dr. Simon Connell for training and advice on Atomic Force Microscopy.

I would like to give a special thanks to Dr. James Bailey for his support, guidance and mentorship during our time at Dynamic Vision Systems, which allowed me to develop in to the experimentalist I am today. Also, for pushing me to pursue a PhD in the first place, which now this thesis is finally finished, I can say I'm very thankful for. I would also like to thank Prof. Cliff Jones for sparking my interest and passion for liquid crystal research, providing me with great opportunities as a postgraduate and for introducing me to the world of microfabrication, within which I am now grateful to be pursuing a career.

I would like to thank my family for their continual support and encouragement over the years, Mum, Dad, Simon and Claire, thank you all for being there for me. Finally, thank you to Becky, my love, for your endless support and patience throughout this process, I wouldn't be the man I am today if it were not for you.

Abstract

The combination of nematic liquid crystals (LCs) and topographically patterned surfaces has enabled the development of a broad range of functional optoelectronic devices, such as displays, LIDAR (light detection and ranging) systems, dynamic lenses, tunable diffractive optical elements and polarisation converters. The interaction between LCs and patterned surfaces dictates the overall surface alignment and thus the bulk optical properties of a device due to the LC's long-range order. These LC-surface interactions are therefore of great interest and are investigated in this work using planar and homeotropic LC polyimides, patterned with various surface relief structures. The motivation is to demonstrate unique and transferrable surface alignment phenomena, as well as highlight the potential for creating multi-functional LC alignment layers by combining the chemical surface anchoring of polyimides with the presence and physical alignment influence of topography.

Commercially sourced, spontaneously formed and precision engineered microstructures form the three unique starting points for the experimental chapters in this thesis. These structures are transferred in to polyimide alignment layers using a variant of solvent-assisted microcontact moulding (SAMIM); a subcategory of soft lithography. This methodology is discussed in detail to provide LC researchers with an insight in to an accessible and arguably underutilized means of patterning alignment layers, with additional control offered by the inherent surface anchoring properties of conventional LC polyimides.

Micropatterned liquid crystal elastomers (μLCEs) are fabricated using planar polyimide alignment layers imprinted with commercially sourced linear surface relief gratings. Mechanical rubbing overrides the grating alignment effect on these surfaces, allowing for multiple grating orientations on a single monodomain μLCE film. The all-acrylate LCE chosen for this study undergoes anisotropic deswelling upon removal of the non-reactive component (6OCB), enabling controllable miniaturization of surface features, as measured *via* atomic force microscopy (AFM). The original grating pitch of 1040nm, is reduced to 707nm (-32%) or 1010nm (-3%) when the nematic director is aligned parallel ($\hat{\boldsymbol{n}}_{\parallel}$) or perpendicular ($\hat{\boldsymbol{n}}_{\perp}$) to the grating grooves respectively. Varying the composition of the precursor mixture for the μLCE, provides additional control over the deswelling, reducing the original pitch to 770nm (-26%) at 45.7 mol% 6OCB and 643nm (-38%) at 64.4 mol% 6OCB in $\hat{\boldsymbol{n}}_{\parallel}$ samples. The μLCE's thermal response is quantified using optical diffraction measurements, indicating changes in grating pitch of up to 33% over a 215°C temperature range. Pitch expansion and pitch contraction are exhibited by the $\hat{\boldsymbol{n}}_{\parallel}$ and $\hat{\boldsymbol{n}}_{\perp}$ samples respectively upon heating, each with linear variations in pitch spanning ≈50% of their operational temperature range, with respective thermal sensitivities of $+1.2 \pm 0.1$ nm/°C and -2.2 ± 0.1 nm/°C. The mechanical response of the μLCEs is explored by applying uniaxial tensile strains (ε) of up to 157%, where optical diffraction measurements are used to demonstrate a maximum pitch elongation of 1110nm. The μLCE topography, and specifically the height of the grating structures,

is measured as a function of strain using AFM, which exhibits a non-linear relationship attributed to the auxetic response of this class of LCEs. An initial decrease in height is observed at moderate strains ($\varepsilon \leq 40\%$) followed by an increase at large strains ($\varepsilon \geq 80\%$), exceeding the height at rest by as much as 26% (50 ± 2nm at $\varepsilon = 0\%$, 63 ± 3nm at $\varepsilon = 146\%$). The first-order diffraction efficiency (η_1) of the μLCEs is also investigated as a function of temperature and strain. Notably, a distinct transition in the linear behaviour of η_1 is observed with increasing strain, where the gradient shifts from 0.67 for $\varepsilon < 100\%$, to 1.79 for $\varepsilon > 100\%$. This corresponds closely with the emergence of the auxetic response and associated growth in feature height confirmed by AFM, which increases the grating's phase modulation and is therefore suspected to be contributing to the higher gradient of η_1 for $\varepsilon > 100\%$.

Wrinkled surface textures are spontaneously formed on polydimethylsiloxane (PDMS) slabs *via* plasma oxidation under tensile strain. Planar and homeotropic wrinkle-imprinted polyimide (WIP) surfaces are then fabricated using these wrinkle textures, with a wrinkle pitch of 900 ± 20nm and height of 125 ± 10nm. Aperiodic valleys in the PDMS slab formed by surface cracking, are inverted into peaks or 'wall' features on the WIP surfaces during imprinting. Although only artefacts of the wrinkling and imprinting processes, these wall features with a mean spacing of 13 ± 1μm and a mean height of 230 ± 5nm, are found to have a remarkable impact on LC surface alignment. A planar WIP surface in a hybrid aligned nematic (HAN) device results in uniform director alignment parallel to the wrinkles, due to the azimuthal anchoring strength of $\approx 4 \times 10^{-6}$ Jm^{-2} associated with the wrinkles' grating-like structure. The alignment properties of a wrinkled surface with homeotropic anchoring are explored for the first time, contained in a vertically aligned nematic (VAN) device geometry. Conoscopic examination of the VAN device shows a ≈7° degenerate tilt of the optic axis at 20°C ($T/T_{NI} = 0.86$), corresponding to a near-vertical surface pretilt (θ_P) on the wrinkles of $77 \pm 2°$, thought to be caused by director splay over the peaks and troughs of the wrinkles. Heating the VAN device to $T/T_{NI} \approx 0.95$ results in a stark change in optical appearance from near-extinct to transmissive, with a retardation (Γ) of 250 ± 50nm. This is attributed to the director undergoing a surface anchoring transition from near-vertical to significantly tilted ($\theta_P = 35 \pm 9°$) on the wrinkled surface, with the director tilting perpendicular to the wrinkle grooves as confirmed by full-wave plate observations. In this tilted state, the aforementioned wall features are shown to produce elongated alignment domains *via* physical confinement, within which the azimuthal director orientation exhibits an intriguing spatial modulation with periodicities between 10 and 15μm.

Precision engineered linear gratings are fabricated with electron beam lithography and imprinted in to homeotropic polyimides using composite-PDMS replicas as stamps. Scanning electron microscopy identifies the structural limits of the stamps, in terms of grating linewidth (l =150 – 350nm) and mark-to-space ratio (1:1 – 1:2.5), highlighting lateral collapse at $l = 150$nm and structural stability for all mark-to-space ratios at $l \geq 250$nm. Faithful transfer of 500 to 1200nm pitch gratings in to polyimide is

confirmed *via* optical diffraction patterns, with pitch measurements agreeing within ≤2% of the design dimensions. Once assembled in to a VAN device geometry, room temperature polarised microscopy shows that the homeotropic gratings induce a transmissive optical appearance ($\Gamma = 150$ - 250nm), in an otherwise extinct VAN device, where Γ varies as a function of grating dimensions. This is attributed to surface anchoring transitions on the grating surface, driven by topographic distortions of the director field inducing a HAN profile with director tilt perpendicular to the grating grooves, as confirmed by full-wave plate analysis. Conoscopic examination of the induced HAN profiles, shows that lower mark-to-space ratio and shorter pitch gratings result in greater optic axis (OA) tilt (ϕ) and thus lower induced surface pretilt (θ_P) on the gratings. Angular calibration of the microscope back focal plane allows ϕ to be directly measured from the shifted melatope positions in the conoscopy figures, where $\phi = 8.1 - 14.7°$ for grating pitches of 1200 to 500nm, corresponding to $\theta_P \approx 74 - 61°$ at 20°C. Conoscopy also enables the identification of opposing tilt directions on either side of tilt domain walls, demonstrated over length scales of ≤100μm.

In summary, the work presented in this thesis demonstrates that a wealth of LC device functionality can be accessed by tailoring microscale surface topographies and their interactions with LCs. The work on μLCEs demonstrates controllable miniaturization of surface features, thermo- and mechano-responsive diffractive properties and the first evidence of auxetic microscale surface relief structures, with collective applications spanning microfabrication, spectroscopy, diffractive optimization and surface wetting. The work on wrinkled LC alignment layers demonstrates topography-driven modulated director profiles, highlighting an alternative and unique approach to patterning the azimuthal director orientation, with potential applications in LC-based flat optics. Finally, the focused study of frustrated surface anchoring on homeotropic grating structures shows how varying grating dimensions allows for precise control over surface pretilt, which is a notoriously difficult property to fine-tune, with broad applications in all LC devices.

Contents

Acknowledgements ii

Abstract iii

Contents vi

List of Figures xii

List of Tables xxix

Symbols and Abbreviations xxx

Symbols xxx

Abbreviations xxxi

Chapter 1 Motivation and Thesis Outline 1

1.1 Motivation 1

1.2 Thesis Outline 2

Chapter 2 Introduction 4

2.1 Liquid Crystal Fundamentals 4

2.1.1 Nematic Liquid Crystals 4

2.1.2 Elastic Properties 6

2.1.3 Dielectric and Optical Anisotropy 7

2.1.4 Nematic Liquid Crystal Elastomers 9

2.1.4.a Mechanical and Thermal Response 10

2.2 Liquid Crystal Surface Alignment 11

2.2.1 Surface Anchoring 11

2.2.2 Planar Alignment 12

2.2.3 Homeotropic Alignment 14

2.2.4 Bulk Director Configurations 14

2.3 Liquid Crystals and Surface Relief Structures 15

2.3.1 Grating Alignment 15

2.3.2 Grating Alignment Layer Fabrication and Applications 17

2.3.3 Alternative Microstructured Alignment Layers 18

2.4 Summary 20
Chapter 3 Experimental Methods 21
3.1 Liquid Crystal Devices 21
3.1.1 Device Geometry 21
3.1.2 Alignment Layers 22
3.1.2.a Nissan Chemical Polyimides (SUNEVER series) - Film Thicknesses 22
3.1.2.b Mechanical Rubbing 23
3.1.3 Device Characterization 24
3.1.3.a Cell Gap Measurements 24
3.1.3.b Device Filling 25
3.1.3.c Polarized Optical Microscopy 26
3.1.3.c.i Conoscopy 26
3.2 Microfabrication 28
3.2.1 Master Structures 28
3.2.1.a Embossing 28
3.2.2 Soft Lithography 29
3.2.2.a Replica Moulding 29
3.2.2.b Imprinted Polyimides 30
3.2.2.b.i Background 30
3.2.2.b.ii Apparatus and Methodology 31
3.3 Surface Metrology 33
3.3.1 Optical Microscopy 33
3.3.2 Optical Diffraction Patterns 33
3.3.3 Atomic Force Microscopy 35
3.3.3.a Image Analysis 36
3.3.4 Scanning Electron Microscopy 37
3.4 Summary 38

Chapter 4 Micropatterned Liquid Crystal Elastomers *via* Surface-Aligned Relief Structures 39
4.1 Motivation and Overview 39
4.2 Introduction 40
4.3 Methods 43
4.3.1 Fabrication of Imprinted Polyimide Grating Moulds 43
4.3.2 Micropatterned LCE Fabrication 43
4.3.2.a Cell Geometry 43
4.3.2.b LCE Synthesis 44
4.3.3 Actuation of Micropatterned LCEs 45
4.3.3.a Thermal 45
4.3.3.b Mechanical Strain 46
4.4 Results and Discussion 47
4.4.1 Appearance and Alignment of μLCE Films 47
4.4.2 Anisotropic Deswelling and Surface Topography 48
4.4.2.a Original Composition 48
4.4.2.b Repeatability of Anisotropic Deswelling 49
4.4.2.c Composition-driven Tunability 51
4.4.3 Thermal Response of μLCEs 53
4.4.4 Strain Response of μLCEs 54
4.4.5 Diffraction Efficiency of μLCEs 55
4.4.6 Durability Testing 57
4.5 Summary 58
Chapter 5 Liquid Crystals on Spontaneously Wrinkled Surface Topographies 59
5.1 Motivation and Overview 59
5.2 Introduction to Spontaneous Wrinkling 59
5.3 Methods 61
5.3.1 Wrinkle Fabrication 61
5.3.2 Wrinkle-Imprinted Polyimide 62

5.4 Results and Discussion 62
5.4.1 Wrinkled Topography Analysis 62
5.4.2 Planar Wrinkles 63
5.4.2.a Alignment Uniformity 64
5.4.2.b Director Orientation 64
5.4.3 Homeotropic Wrinkles 66
5.4.3.a Topography-Induced Tilt 67
5.4.3.b Surface Anchoring Transition 67
5.4.3.b.i Tilt Direction 69
5.4.3.b.ii Degree of Tilt 69
5.4.3.c Spatial Confinement 70
5.4.3.c.i Origin of Confinement 71
5.4.3.c.ii Temperature Dependence 72
5.4.3.d Modulated Director Profile 72
5.4.3.d.i Alignment Overview 73
5.4.3.d.ii Identifying Modulation 74
5.4.3.d.iii Origin of the Modulation 75
5.5 Summary 76
Chapter 6 Liquid Crystal Surface Alignment and Pretilt on Sub-micron Homeotropic Gratings 77
6.1 Overview 77
6.2 Introduction 77
6.3 Methods 79
6.3.1 Grating Design 79
6.3.2 Master Fabrication 81
6.3.3 Pattern Transfer 82
6.3.3.a Anti-stick Coating 83
6.3.3.b Composite-PDMS Replication 84
6.3.4 LC Device Geometry 85

6.4 Results and Discussion 85
6.4.1 Stability of Composite-PDMS Replica 85
6.4.1.a Feature Collapse – Grating Array (1) 86
6.4.1.b Stable Features – Grating Array (3) 87
6.4.1.c Device Considerations 87
6.4.1.d Imprinted Pitch Confirmation via Diffraction 88
6.4.2 Liquid Crystal Device Characterization 89
6.4.2.a Birefringence Colour Observations 89
6.4.2.b Conoscopy 93
6.4.2.b.i Analysing Conoscopy Figures 94
6.4.2.b.ii Induced Tilt of Optic Axis 96
6.4.2.b.iii Distinguishing Tilt Direction 98
6.4.3 Modelling Bulk Director Profile 100
6.4.3.a Extracting Pretilt from Conoscopy Figures 100
6.5 Summary 102
Chapter 7 Conclusions and Future Work 103
7.1 Conclusions 103
7.1.1 Micropatterned Liquid Crystal Elastomers 103
7.1.2 Spontaneously Wrinkled Polyimide Alignment Layers 105
7.1.3 Liquid Crystal Alignment on Sub-Micron Homeotropic Gratings 107
7.2 Future Work 108
7.2.1 Imprinting Apparatus 108
7.2.2 Micropatterned Liquid Crystal Elastomers 109
7.2.2.a Intermediate Rubbing Directions 109
7.2.2.b Homeotropic μLCEs 109
7.2.2.c Reflective μLCEs and Surface Wettability 110
7.2.3 Spontaneously Wrinkled Alignment Layers 111
7.2.3.a Alternative Wrinkle Geometries 111
7.2.3.a.i Preliminary Work on LC Alignment with Concentric Wrinkles 111

7.2.3.b Exploring Director Modulation with Precision 'Wrinkle-Wall' Structures 113
7.2.4 Sub-Micron Homeotropic Gratings 114
7.2.4.a Electrooptic Response of Current Devices and Inverted Master Structures 114
7.2.4.b Impact of Rubbing on Tilt Degeneracy and Potential Device Applications 114
7.2.4.c Detailed Director Profile Analysis 115
References 116
Appendix A Experimental Methods 140
A.1 Broadband Green Light Spectrum – Conoscopy Experiments 140
A.2 Blue Laser Spectrum (PL205, Thorlabs) – Diffraction Experiments 140
Appendix B Micropatterned LCEs 141
B.1 Rubbed vs Unrubbed Polyimide Gratings in μLCE Cell Geometry 141
B.2 Differential Scanning Calorimetry 142
B.3 Visual Appearance of μLCE Film 143
B.4 Polarised Light Appearance of μLCE Film – No Colour Bands 143
B.5 Atomic Force Microscopy Data 144
B.6 Thermogravimetric Analysis 145
Appendix C Wrinkled LC Alignment Layers 146
C.1 Birefringence Colours of HAN Device with Planar Wrinkles 146
C.2 Identifying Sign of $\boldsymbol{s = 1}$ Point Defect 147
C.3 Conoscopy: Calibrating Back Focal Plane *via* Diffraction 147
C.4 Director Tilt and Effective Birefringence Profiles 148

List of Figures

Figure 1-1: Roadmap highlighting the key components of the thesis. The overarching theme shared by each of the experimental chapters is given, along with the distinct routes taken by each, in terms of the type of surface relief structure being applied. 3

Figure 2-1: (a) Chemical structure and approximated rod-like morphology (blue ellipsoid) of a nematic liquid crystal molecule (4-Cyano-4'-pentylbiphenyl, 5CB). The long molecular axis (blue arrows) is oriented at an angle (β) relative to the average bulk molecular orientation known as the director, defined by the unit vector $\boldsymbol{n}$ (black arrow). (b−d) Illustrations of the temperature dependent phase behaviour and orientational order in a LC medium, with the scalar order parameter (S) defining (b) perfect order (S = 1), (c) nematic order ($0.3 < S < 0.8$) and (d) complete disorder (S = 0). 4

Figure 2-2: Schematics of the three fundamental modes of elastic deformation in a liquid crystal medium, (a) Splay ($K11$), (b) Twist ($K22$) and (c) Bend ($K33$). 6

Figure 2-3: Schematic illustration of how a LC medium alters the polarisation state of incident light and the basic optical arrangement used in polarised microscopy (polariser and analyser with orthogonal/crossed polarisation directions). From left to right, a polariser converts unpolarised light in to linearly polarised light, with an initial linear polarisation state (Pi). The LC's birefringence induces a phase difference ($\Delta\varphi$) between the orthogonal components of Pi, where the e-wave (blue, parallel to ne) propagates slower than the o-wave (green, parallel to no), due to $ne > no$. This induced $\Delta\varphi$ alters Pi, often resulting in some form of elliptical polarisation state (Pe).[32] This results in the LC sample appearing bright due to a sum of components of Pe having non-zero transmission through the analyser, combining to produce a final, observed polarisation state (Pf). If the nematic director was aligned parallel to the polarisation direction of either the polariser or analyser, or if the birefringent sample was removed, Pi would remain unchanged and have zero transmission through the analyser. 8

Figure 2-4: Michel-Lévy colour chart used as a reference point for characterising the optical appearance of LC devices throughout this work, reproduced from reference [49]. The path difference (Γ) in nanometers is on the bottom-horizontal axis, the LC layer thickness (dLC) is on the left-vertical axis and the black lines extending from the origin denote positions on the chart with a given effective birefringence ($\Delta neff(\theta)$), labelled from 0 to 0.20 along the top and right-hand side of the chart. To aid navigating the document, the chart is referred to in sections: 3.1.3.c on polarised microscopy methodology, 4.4.1 on the appearance and alignment of μLCE films, 5.4.3.b.ii on the tilt induced by surface anchoring transitions on homeotropic wrinkles, 6.4.2.a on birefringence colour observations of homeotropic grating devices and Appendix C. 9

Figure 2-5: Schematic representation of the molecular structure of liquid crystal elastomers with (a) main-chain and (b) side-chain mesogenic units (blue) on the polymer backbone (black). Crosslinks between the polymer backbones are not shown in this representation. 10

Figure 2-6: Reference frame and definitions for director ($\boldsymbol{n}$) orientation relative to a surface plane. The easy axis (red) defines an alignment layer's preferred director orientation at equilibrium, with an out-of-plane polar surface pretilt, θP, and an in-plane azimuthal orientation, $\psi 0$. The polar and azimuthal anchoring strengths of an alignment layer, $W\theta$ and $W\psi$ respectively, are given by the elastic energy cost associated with reorienting n from the easy axis, to some arbitrary polar (θ) and azimuthal (ψ) orientation. 12

Figure 2-7: Four fundamental types of surface anchoring on LC alignment layers. (a) Planar degenerate – the director ($\boldsymbol{n}$) lies parallel to the surface plane with a spatially varying azimuthal orientation. (b) Planar homogeneous - $\boldsymbol{n}$ lies parallel to the surface with a uniform azimuthal orientation parallel to the easy axis of the surface, in this case defined by mechanical rubbing with a rubbing direction, RD. (c) Homeotropic - $\boldsymbol{n}$ is oriented near-orthogonal to the surface plane, with a surface pretilt (θP) of ≈90°. (d) Tilted - $\boldsymbol{n}$ is uniformly tilted with a pretilt angle of $0° < \theta P < 90°$ and a uniform azimuthal orientation parallel to the applied RD. Note that n tilts towards the direction of rubbing. 13

Figure 2-8: Bulk director profiles of assembled LC devices. (a) Opposing planar surfaces with anti-parallel rubbing directions (RD), resulting in a uniform polar director orientation throughout the LC layer. (b) Opposing planar surfaces with parallel RDs, resulting in a splayed director profile. (c) Vertically-aligned nematic (VAN) device comprised of opposing surfaces with homeotropic anchoring. (d) Hybrid-aligned nematic (HAN) device comprised of dissimilar surfaces with rubbed planar anchoring opposed by homeotropic anchoring. (e) Twisted nematic (TN) device with an azimuthal director orientation that rotates by 90° throughout the LC layer, imposed by rubbed planar surfaces with orthogonal RDs. 15

Figure 2-9: Schematic illustrations of the interaction between the nematic director ($\boldsymbol{n}$) and a linear grating topography with grooves ($\boldsymbol{g}$) aligned parallel to y. (a) Energetically unfavourable scenario with $\boldsymbol{n}$ aligned orthogonal to $\boldsymbol{g}$, resulting in elastic deformation of the director field in the x-z plane (highlighted in a.ii), as it attempts to conform to the undulating topography. (b) Energetically favourable scenario with $\boldsymbol{n}$ aligned parallel to $\boldsymbol{g}$, resulting in minimal elastic distortion. This highlights the principle of 'grating alignment' on a grooved topography with planar anchoring. .. 16

Figure 2-10: Grating alignment applications. (a) Measurement of the polar and azimuthal anchoring strengths of polymer alignment layers, using linear surface relief gratings of varying pitch (d) as reference points. Rubbing applied perpendicular to the grooves (a.i), competes against the varied anchoring strengths of the gratings, resulting in different twist angles and optical appearances (a.ii)

from which the anchoring strengths are inferred.[83] (b) Sub-micron pitch, indium tin oxide (ITO) grating structures (b.i – b.ii), with a groove direction indicated by the red arrows, applied simultaneously as electrodes and grating alignment layers (b.iii–b.iv).[105]..... 17

Figure 2-11: Applications of microstructured alignment layers for non-uniform or patterned director alignment. (a) LC microlens arrays based on the Pancharatnam-Berry phase. Sub-micron pitch surface relief gratings are precisely patterned with spatially varying groove directions (a.i–a.ii). The patterned grooves result in azimuthal rotation of director across the surface, resulting in a modulated phase profile as shown in the polarised microscopy image in (a.iii), with a corresponding director profile shown in (a.iv).[21] (b) Polarisation converter based on the circular/azimuthal director alignment (b.ii) imposed by physical confinement of a LC in a cylindrical cavity (b.iii). The circular alignment from the cavity combines with a planar-aligned polyimide (PI) surface to produce alternating uniform and twisted bulk director profiles around the cavity, with an optical appearance shown in (b.iv).[27] 18

Figure 2-12: Application of micropatterned surface topographies, combined with homeotropic anchoring, for creating a tunable diffractive optical element. (a) Micropillar structures with a homeotropic coating (CYTOP) results in a frustrated/distorted near-surface director field. Applying electric fields to the LC ($\Delta\epsilon < 0$), parallel to z in (a), results in further director field distortion that forms intricate nematic defect arrays, with optical appearances shown in the left panels of (b) and (c). These images demonstrate how the arrangement of the defect arrays can be altered by varying the voltage and frequency of the applied field, which in turn changes the optical diffraction patterns produced by laser light incident on the device (right panels of (b) and (c)).[22] 19

Figure 3-1: LC device schematics. (a) Exploded view of a LC device highlighting each of the constituent layers, including: indium-tin oxide (ITO) coated glass, polyimide (PI) alignment layers and spacers for defining the thickness of the LC slab. (b) Collapsed view of an assembled LC device, showing the lateral offset of the substrates that provides a ledge for capillary filling the device with LC material. (c) Cross sectional view indicating the typical thicknesses of each of the device layers. Grey circles denote the spherical polystyrene spacer beads that are dispersed in the UV-curable glue seals..... 21

Figure 3-2: Spin coating and post-processing of polyimide alignment layers. (a) Approximately 0.1ml of PI solution is drop dispensed on to a static substrate, whilst secured to the spin coater's vacuum chuck. A pipette tip is used to spread the droplet across the surface to ensure full coverage. (b) Spin coater rotates the substrate at high speed, ejecting material and forming a uniform thin film. (c) Freshly spun film is placed on a 70°C hotplate for 60s to evaporate any remaining solvent and solidify the layer. (d) Finally, the film is cured/imidized on a 200°C hotplate for 30mins. 22

Figure 3-3: (a) Schematics showing the process of measuring PI film thicknesses with a stylus profiler. (a1) Pristine PI thin film (yellow) as found after spin coating. (a2) A region of PI film is removed with a scalpel, exposing the underlying ITO layer (gold). The path of the stylus profiler's tip is indicated by the black arrow, stepping down from the PI film on to the ITO surface. (a3) Example of output data from the stylus profiler, showing the step height/thickness of the PI film (hPI). (b) Film thicknesses of Nissan Chemical Polyimides (SUNEVER series), spin coated at different spin speeds. Orange data points indicate films with planar or tilted (SE-3510) anchoring and blue indicates homeotropic anchoring. 23

Figure 3-4: Surface alignment via mechanical rubbing. (a) Alignment layer with planar anchoring before rubbing. Near-surface polymer chains (black lines) are randomly oriented, resulting in no orientational preference of the near-surface director (blue ellipsoids). (b) Rubbing machine schematic, showing coated substrate on a vacuum stage passing beneath a rotating roller. White arrows denote each component's direction of travel, with the single rotation direction of the roller defining the rubbing direction (RD) applied to the alignment layer. (c) Resulting polymer chain orientation and subsequent director alignment of a unidirectionally rubbed, planar alignment layer. 23

Figure 3-5: (a) Typical reflection spectrum of an empty LC device, with a cell gap (dLC) of ≈8μm. This is used with equation (3-1) to calculate dLC. (b) Approximate illustration of white light incident on an empty LC device, showing the reflected beams from the top and bottom cell surfaces that interfere and produce the intensity minima and maxima in the reflection spectra. (Note: In practice, the light is normally incident on the device but is shown at angles in the diagram to highlight the source of the interference.) 24

Figure 3-6: Schematic overview of conoscopy setup, highlighting key components in the optical path. 27

Figure 3-7: Embossing process. (a) UV-curable resin (orange) is drop dispensed on to a glass substrate treated with an adhesion promoter. (b) Microstructured surface relief grating (SRG) film is embossed in to the resin via translation beneath a pressurized roller. Black arrows denote directions of applied pressure and travel. (c) Glass-resin-film stack is exposed to UV illumination to cure the resin. (d) SRG film is peeled away to reveal a resin replica of the SRG on the glass substrate. 28

Figure 3-8: PDMS replica moulding process. (a) PDMS prepolymer and crosslinker are thoroughly mixed, forming a homogeneous PDMS solution. (b) Mixture is degassed in a vacuum desiccator, removing air bubbles formed during mixing. (c) Master structures are placed in a non-stick casting vessel and the PDMS mixture is cast on top, to a thickness 1-2mm greater than the substrate thickness. (d) Following degassing and curing at 80°C, the PDMS slab is demoulded from the structures and trimmed to form a working stamp for pattern transfer. 30

Figure 3-9: Hotplate press apparatus. (a) Overview showing the hotplate, suspended toggle-clamp assembly and surface thermometer. (b) Support column with millimetre scale, providing a reference point for imprint pressure in the absence of a formal pressure sensor. (c) Foot of the press in its raised position, with glass carrier substrate adhered to the underside for temporary mounting of PDMS working stamps. (d) Foot of the press in its lowered/clamped position during imprinting. (e) Batch of micropatterned polyimide substrates fabricated with the hotplate press. Scale bar = 20mm. 31

Figure 3-10: Schematic of the polyimide imprinting process. (a) A PDMS working stamp is secured to the glass carrier of the hotplate press and a test substrate is used to set the imprint pressure. (b) Polyimide film is spin coated with reduced speed and time, then (c) transferred to a 75°C hotplate and immediately imprinted with the hotplate press. (d) Working stamp is demoulded from the polyimide and the micropatterned polyimide film is cured at 200°C. 32

Figure 3-11: Microscope stage micrometre imaged through (a) 20x and (b) 100x magnification objectives, featuring a 1mm scale divided in to 100 minor increments of 10μm. 33

Figure 3-12: Experimental setup used to display optical diffraction patterns and measure a sample's periodicity/pitch. (a) Photograph of the benchtop diffraction setup showing the arrangement of optical components, each labelled 1 through 9 to indicate their order in the beam path, between the λ=404nm laser diode (1) and the projection screen with millimetre scale (9). (b) Schematic cross-section of the setup between the fixed mirror (5) and the projection screen (9). This defines the measured distance between the 0th (m=0) and 1st order (m=$\pm$1) diffraction maxima on the screen (x) and the sample-screen separation (L), which are used to calculate the diffraction angle (θd) and pitch (d). 34

Figure 3-13: Schematic of the key components in an atomic force microscope (AFM). In tapping mode, the cantilever is oscillated close to its resonant frequency ($f0$). Raster scan is carried out by piezo x-y translation of the scanner head and the z-height is dictated by the feedback loop from the photodetector signal. 36

Figure 3-14: Summary of AFM image analysis used to measure the pitch and height of a microstructure. (a) 5x5μm AFM image of a periodic linear surface relief grating. White dashed boxes indicate the multiple areas from which cross-sectional data is exported from a single scan. (b) Example of height data from one of the box selection regions on the AFM image. (c) Height data imported in to OriginPro software with 'Peak Analyser' applied to locate the peaks (P) and valleys (V). Black dashed lines indicate the vertical (z) and lateral (x) positions of the peaks and valleys, with subscripts P and V to identify each respectively. (d) Equations used to calculate the pitch and height of the structure from the values of x and z, where n is the number of peaks and valleys. 37

Figure 4-1: Chemical structures of constituent chemicals used in the synthesis of nematic LCEs. The non-reactive mesogen, 6OCB, is removed after polymerization by washing the LCE in a solvent, resulting in anisotropic deswelling. 41

Figure 4-2: Illustration highlighting how the nematic director orientation ($\boldsymbol{n}$) is defined arbitrarily with respect to the groove direction ($\boldsymbol{g}$) of an underlying IPI grating. Configurations with (a) the director perpendicular to $\boldsymbol{g}$ and (b) the director parallel to $\boldsymbol{g}$ are shown, indicating the IPI and Polyvinyl alcohol (PVA) alignment layer rubbing directions ($RD_{IPI,}$ RD_{PVA}) on the opposing cell substrates. 42

Figure 4-3: Schematic representation of the key stages in the microfabrication process of IPI grating moulds. (a) A linear surface relief grating (SRG) film is embossed in to a UV-curable resin on a glass backing substrate. (b) A polydimethylsiloxane (PDMS) replica is taken of the embossed SRG, forming a soft working stamp for pattern transfer. (c) A spin coated layer of planar polyimide is imprinted with the PDMS working stamp. (d) The imprinted polyimide (IPI) surface is mechanically rubbed with a cotton roller, with a rubbing direction (RD_{IPI}). 43

Figure 4-4: Summary of the cell geometry used to fabricate nematic µLCE devices and the two resulting µLCE varieties. (a) Schematic of the parallel-plate cell geometry used as a mould for the µLCEs, featuring an IPI surface (yellow) with two mutually-orthogonal grating regions. A global rubbing direction is applied to the IPI surface (RD_{IPI}), to form a single µLCE film with discrete regions where the nematic director ($\boldsymbol{n}$) is aligned parallel ($\boldsymbol{n} \parallel$) or perpendicular ($\boldsymbol{n} \perp$) to the grating grooves ($\boldsymbol{g}$). (b) Filled cell cross-sections of (i) $\boldsymbol{n} \parallel$ and (ii) $\boldsymbol{n} \perp$ regions. (c) Schematic representations of (i) $\boldsymbol{n} \parallel$ and (ii) $\boldsymbol{n} \perp$ µLCE films, emphasizing the relative of orientations of $\boldsymbol{n}$ and $\boldsymbol{g}$ in each variety..... 44

Figure 4-5: Schematic of the experimental setup used to measure the thermal response of the µLCEs and the associated change in diffraction angle ($\Delta\theta d$). Pitch (d) is inferred from the diffraction patterns of λ=404nm laser light, on a screen L = 118 ± 2mm away from the µLCEs. The lateral distance between m=0 and m=1 diffraction orders (x), is measured using the millimetre scale on the screen, allowing the diffraction angle (θd) and grating pitch to be calculated using Equations (4-1) and (4-2)..... 46

Figure 4-6: Schematic representation of uniaxial tensile strain being applied to a µLCE film. (a) Both ends of a rectangular section of µLCE film (≈15 x 5mm), are secured in a bespoke strain rig using clamps. The sample is pulled taut and the initial clamp separation/sample length ($L0$) is measured. (b) Strain (ε) is incrementally applied by moving the clamps in opposite directions via a fine thread adjustment, followed by measuring the strained sample length (LS) to calculate the applied strain. 46

Figure 4-7: Photographs of a full μLCE film fabricated using the IPI cell geometry detailed in section 4.3.2.a. (a) Film placed on a glass microscope slide in ambient white light illumination, highlighting the mutually-orthogonal grating regions ($\boldsymbol{n}$ ∥ and $\boldsymbol{n}$ ⊥) present on the same film (blue arrows indicate grating groove directions, $\boldsymbol{g}$). Vibrant structural colour can be seen in the $\boldsymbol{n}$ ∥ region, due to diffracted light from this grating orientation. (b) Film imaged between crossed polarisers (P, A) with the rubbing direction (RD)/nematic director orientation at (i) 0° and ii) 45° to the polarisers. Dashed white lines indicate a 3mm wide strip of the film without any grating structures, separating the two grating regions. Scale bars = 10mm. 47

Figure 4-8: AFM surface profilometry of nematic μLCE films at 20°C. The plots in (a) and (c) include AFM surface profiles of the IPI grating moulds (yellow) used during fabrication (pitch = 1040 ± 5nm, height = 130 ± 5nm), to highlight the reduced dimensions of the μLCEs (cyan). (a, b) $\boldsymbol{n}$ ∥ μLCE fabricated with the nematic director ($\boldsymbol{n}$) aligned parallel to the grating grooves ($\boldsymbol{g}$) (pitch = 707 ± 10 nm, height = 53 ± 3 nm). (c, d) $\boldsymbol{n}$ ⊥ μLCE fabricated with $\boldsymbol{n}$ aligned perpendicular to $\boldsymbol{g}$ (pitch = 1010 ± 5 nm, height = 68 ± 3 nm). 49

Figure 4-9: Compositional dependence of the dimensions of $\boldsymbol{n}$ ∥ μLCEs on the concentration of 6OCB in the LCE precursor mixture. (a) AFM surface profilometry of the $\boldsymbol{n}$ ∥ μLCEs with (i) 45.7 mol %, (ii) 54.6 mol %, (iii) 64.4 mol % and (iv) 70.7 mol % of 6OCB. (b) Compositional dependence of (i) pitch and (ii) height on concentration of 6OCB in precursor mixture as measured by AFM. The composition used in the previous and subsequent sections of this chapter is marked with an asterisk. (c) Diffraction patterns of the $\boldsymbol{n}$ ∥ μLCEs with increasing 6OCB concentration, from top to bottom. 51

Figure 4-10: Thermal response of $\boldsymbol{n}$ ∥ and $\boldsymbol{n}$ ⊥ μLCEs measured via optical diffraction measurements. (a, b) Diffraction patterns showing the opposing thermal responses of $\boldsymbol{n}$ ∥ and $\boldsymbol{n}$ ⊥ μLCEs, where (a) $\boldsymbol{n}$ ∥ exhibits pitch expansion and (b) $\boldsymbol{n}$ ⊥ exhibits pitch contraction respectively upon heating. (c) The relative thermal change in grating pitch of $\boldsymbol{n}$ ∥ (blue triangles) and $\boldsymbol{n}$ ⊥ (orange diamonds) nematic μLCE films determined from diffraction measurements. The grey circles in (c) are the relative thermal changes in pitch for an isotropic sample of the same composition. 53

Figure 4-11: Tensile strain testing on $\boldsymbol{n}$ ∥ nematic μLCE. (a) Relationship between grating pitch (d) and strain. Pitch measurements are taken using optical diffraction patterns (diamonds) and AFM (triangles). (b) Relative height (h) of the μLCE surface relief grating as a function of applied strain, measured via AFM. Dashed horizontal lines denote the static height ($h0$). (c) Cross-sectional line profiles from AFM scans of the μLCE i) at rest, ii) at 41% strain and iii) at 146% strain. 54

Figure 4-12: First order diffraction efficiency ($\eta 1$) of the μLCEs under various conditions. (a, b) $\boldsymbol{n}$ ∥ and $\boldsymbol{n}$ ⊥ μLCE upon heating, (c) $\boldsymbol{n}$ ∥ μLCE under strain. The grey dotted line is the theoretical predicted efficiency for the given grating depth and laser wavelength. 55

Figure 4-13: AFM surface profilometry of nematic μLCE films. (a) $\boldsymbol{n} \parallel$ μLCE pre- (cyan) and post- (red) heating to 240°C. (b) $\boldsymbol{n} \perp$ μLCE pre- (cyan) and post- (red) heating to 240°C. (c) $\boldsymbol{n} \parallel$ μLCE pre- (cyan) and post- (red) straining to 156%. 57

Figure 5-1: Schematic of PDMS wrinkling. (a) A compliant PDMS slab with initial length (L_0), is (b) elongated by a distance (x) via tensile strain (ε_{pre}). (c) Under static strain, plasma oxidation forms a stiff surface layer on the PDMS slab, with a thickness (h_f). (d) Upon strain release, the bulk compliant PDMS contracts whereas the surface layer buckles/wrinkles to relieve the internal stresses accumulated during its strained formation, resulting in a periodic wrinkle texture with a wrinkle periodicity (d)..... 60

Figure 5-2: PDMS wrinkling via mechanical strain and plasma oxidation. Schematics (top row) and images (bottom row) of a PDMS sample at each stage of the wrinkling process. (a) The PDMS slab is secured in a uniaxial strain rig and pulled taut to measure the initial slab length (L_0). (b) Clamp separation is increased to apply 60% tensile strain (ε) and a plasma treatment is applied, where the PDMS slab is elongated by a distance (x), where $\varepsilon = x/L_0 = 0.6$. (c) Tensile strain is released after plasma treatment, inducing surface wrinkling. Note the change in appearance of the PDMS slab (denoted by the dashed lines) from highly transmissive in (a) and (b), to strongly diffractive in (c), due to interactions between visible light and the microscale, periodic features of the wrinkled surface. 61

Figure 5-3: Schematic of transferring wrinkled PDMS surface textures in to LC devices. (a) PI thin film is spin coated on 1mm thick, indium tin oxide (ITO) coated glass. (b) Wrinkled PDMS slab is placed in conformal contact with the solvent-rich PI film at 70°C, solidifying the imprinted PI layer as the solvent evaporates. (c) Wrinkle-imprinted polyimide (WIP) surfaces, with a wrinkle periodicity and height of the order of 900nm and 100nm respectively, are assembled in a parallel-plate configuration, opposite an ITO substrate coated with a flat, homeotropic PI layer. The cavity between the PI surfaces, with a thickness of the order of 10μm, is capillary filled with LC in the isotropic phase at 70°C (MLC-6204, Merck). 62

Figure 5-4: Surface topography of wrinkle-imprinted polyimide (WIP) alignment layers. (a) Optical microscopy image of a WIP surface captured with a 100x microscope objective. Scale bar = 10μm. (b) AFM scan of a WIP surface highlighting the protruding 'wall' features quasi-parallel to X, and the periodic wrinkles parallel to Y. (c) AFM height profile of the grating-like wrinkles along line 1 – 2 in (b), with a groove direction ($\boldsymbol{g}$), an average pitch (d) of 900 ± 20nm and an average height ($h1$) of 125 ± 10nm. (d) AFM height profile of a 'wall' feature on a WIP surface, along line 3 – 4 in (b), with a mean spacing of 13 ± 1μm and a mean height ($h2$) of 230 ± 5nm. 63

Figure 5-5: HAN LC device comprised of a planar WIP surface opposing a flat, homeotropic PI surface. Filled with MLC-6204 with an LC layer thickness (dLC) of 10±1µm. (a) Schematic of the HAN device geometry, indicating the region of interest (ROI) on the boundary between (i) a wrinkled PI area and (ii) a flat PI area. (b,c) POM images of the ROI indicated by the red box in (a), imaged at 59°C (nematic phase), with the wrinkle grooves ($\boldsymbol{g}$) at 0° and 45° with respect to the crossed polarizers (P,A). The images show homogeneous director alignment in the wrinkled area (i), and planar degenerate alignment in the unpatterned PI area (ii). Scale bars = 100µm. 64

Figure 5-6: POM images of the same region of interest (ROI) shown in Figure 5-5c, with the addition of a full-wave compensation plate (λ-plate) with slow axis orientation, λp. Used to confirm the relative orientation of the director ($\boldsymbol{n}$) and the wrinkle grooves ($\boldsymbol{g}$). (a) Broad view of the ROI on the boundary of (i) wrinkled and (ii) unpatterned PI areas. Yellow circle in region (ii) highlights the $s = -1$ point defect used a reference point. Scale bar = 100µm (b) Enlarged image of $s = -1$ reference defect highlighted in (a). Overlaid green dashes show the known $\boldsymbol{n}$ profile surrounding a $s = -1$ point defect. Imaged at 59°C. Scale bar = 20µm. 65

Figure 5-7: VAN device featuring a homeotropic WIP surface opposite a flat, homeotropic PI surface. Filled with MLC-6204 with an LC layer thickness (dLC) of 12±1µm and imaged at 20°C. (a) POM image of a device region without wrinkles i.e. flat homeotropic PI on both surfaces. P, A = polariser and analyser orientations. (b) POM image of a device region with homeotropic wrinkles. Insets show conoscopy figures captured in each region, using broadband green illumination ($\lambda = 533 \pm 52nm$). Scale bars = 50µm (c) Schematic of VAN device geometry, indicating (1) flat PI and (2) wrinkled PI regions shown imaged in (a) and (b), and the groove direction ($\boldsymbol{g}$). (d) Intensity profiles of the inset conoscopy figures in (a) and (b), measured along the orange dashed lines X-Y, showing isogyre splitting in region (2) as a result of degenerate director tilt induced by the wrinkled surface topography. 66

Figure 5-8: POM images of the homeotropic WIP device on heating through 60°C to 62.7°C, showing the change in optical properties due to a surface anchoring transition. (a) Device at 60°C appearing near-extinct due to bulk HT alignment. (b) Onset of surface anchoring transition at 62.5°C, indicated by small patches of the field of view (FOV) transitioning from extinct to transmissive. (c) Majority of FOV becomes transmissive at 62.7°C, as tilted director profile propagates on heating. Addition of a λ-plate (a2-c2), with slow axis (λp) perpendicular to the wrinkle grooves ($\boldsymbol{g}$), shows an additive colour shift to blue, indicating director tilt parallel to λp and hence perpendicular to $\boldsymbol{g}$. Scale bar = 100µm. 68

Figure 5-9: Director tilt in the homeotropic WIP device. (a) Tilt shown in 3D space on a CAD representation of the wrinkled surface, with wrinkle grooves ($\boldsymbol{g}$) (parallel to Y), slow axis of λ-plate (λp) as oriented in Figure 5-8c.2 (parallel to X) and director tilt in XZ plane. (b) Degree of degenerate pretilt (θp) of the director ($\boldsymbol{n}$) prior to the surface anchoring transition, as covered in section 5.4.3.a. (c) Degree of θp after the surface anchoring transition. 69

Figure 5-10: Comparison of alignment characteristics between VAN devices with (a) a homeotropic WIP surface and (b) a homeotropic PI surface imprinted with a linear surface relief grating (SRG), following a surface anchoring transition. Confirms the origin of the alignment domains observed in the homeotropic WIP device. (a.1) Optical microscopy image of a WIP surface. (a.2,a.3) POM observations of the homeotropic WIP device, exhibiting alignment domain formation. (b.1) Optical microscopy image of an imprinted SRG. (b.2,b.3) POM observations of the SRG device used as a control, exhibiting a near-uniform optical texture, without domains. Groove direction ($\boldsymbol{g}$), full-wave plate slow axis (λp). 71

Figure 5-11: POM images showing the broadening of spatially-confined alignment domains on heating. (a) Homeotropic WIP device at 62.8°C (0.3°C above anchoring transition onset temperature). (b) Homeotropic WIP device at 63.4°C (0.9°C above anchoring transition onset temperature). Wrinkle groove direction ($\boldsymbol{g}$), full-wave plate slow axis (λp) and scale bars = 100μm. 72

Figure 5-12: POM observations of the modulated director profile in the homeotropic WIP device, (a−c) at 63.8°C after cooling through the isotropic-nematic phase transition and (d) at 62.7°C on heating through the nematic phase. (a) Wrinkle grooves ($\boldsymbol{g}$) at 45° to the polarisers (P,A). (b) $\boldsymbol{g}$ aligned parallel to a polariser. (c) Enlarged image of the region indicated by the white box in b.2, with proposed director ($\boldsymbol{n}$) profile denoted by black arrows. Full-wave plate slow axis (λp). 73

Figure 5-13: Schematic representations of, (a) director ($\boldsymbol{n}$) splay in the YZ plane associated with the wall features, (b) director tilt in the XZ plane associated with the periodic wrinkles and (c) the proposed modulated director profile between two adjacent wall features. The 'nail representation' is used in (c) to signify tilt, where the 'T' or nail symbols indicate the projection of $\boldsymbol{n}$ onto the plane of the page. The head of the nail symbols protrude out of the plane of the page. 75

Figure 6-1: Schematic surface relief grating profiles with line/trench width (l), space/ridge width (w), pitch (d) and line-space ratios of a) 1:1, b) 1:1.5, c) 1:2 and d) 1:2.5. The terms 'line' and 'space' are defined in d). 79

Figure 6-2: (a) Wafer, (b) array and (c) LC device arrangements, with grating areas denoted by purple boxes. 81

Figure 6-3: Process flow for patterning grating master structures into a silicon-oxide layer, on a silicon wafer. (a) Oxide layer is grown on the wafer using plasma-enhanced chemical vapour deposition (PECVD), with a layer thickness (t) of 372 ± 3nm. (b) A layer of UV60 (deep-UV photoresist) is spin coated on the oxide layer. (c) Line-space pattern is written into the photoresist using electron-beam lithography and developed to create an etch mask. (d) Anisotropic dry etching, with trifluoromethane (CHF_3) and Argon (Ar) process gases, transfers the mask pattern into the underlying oxide layer. The oxide is cleared in the etched regions (entirely removed to expose the underlying silicon surface)..... 81

Figure 6-4: Process of transferring silicon-oxide grating structures in to a polyimide LC alignment layer via a soft replica. (a) Anti-stick coating of perfluorooctyltrichlorosilane (FOTS) is vapour deposited on the grating master structures, to assist in demoulding. (b) A high-modulus PDMS (hPDMS) prepolymer is spin coated on the FOTS-treated wafer and partially cured. (c) The wafer is then cast in a conventional 'soft' PDMS (sPDMS) prepolymer, followed by thermal curing. (d) The PDMS is demoulded from the wafer, forming a composite-PDMS working stamp with a stiff hPDMS surface layer supported by a compliant sPDMS backing. (e) A spin coated layer of homeotropic polyimide (SE-4811) is imprinted with the composite stamp and (f) assembled in to a parallel-plate LC device, opposite a flat layer of SE-4811..... 82

Figure 6-5: Imaged contact angles of 10μL droplets of de-ionized water on (a) untreated (θU) and (b) FOTS-treated (θT) sections of PECVD silicon-oxide. This shows the increased hydrophobicity/reduced surface energy of the master wafer, as a result of the FOTS anti-stick coating..... 83

Figure 6-6: (a) Photograph of the original wafer, with square regions of linear surface relief gratings patterned via electron-beam lithography. Arrow denotes one of four sacrificial grating areas on the wafer perimeter, used for cross-sectional imaging via SEM. (b) Photograph of the composite-PDMS replica of the wafer. 84

Figure 6-7: (a) Photograph of (1) composite-PDMS working stamps and (2) assembled LC devices. (b) Schematic cross-section of LC devices featuring homeotropic grating structures with a height (h), and an LC layer thickness (dLC) of the order of 7μm. Vertical black dashed lines indicate the boundaries of grating and non-grating regions in the devices, highlighting the expected hybrid-aligned nematic (HAN) and vertically-aligned nematic (VAN) director profiles in each area. 85

Figure 6-8: SEM cross sections of grating array 1 (linewidth = 150nm), with line-space ratios of (1) 1:2.5, (2) 1:2, (3) 1:1.5 and (4) 1:1. (a) Original, etched silicon-oxide grating structures and (b) composite-PDMS replicas. (b.2, b.3) Examples of paired ridges (two ridges coalescing in to one) due to lateral collapse. (b.4) Left and middle coalesced ridges show a three-ridge collapse. Scale bars = 200nm. 86

Figure 6-9: SEM cross sections of grating array 3 (linewidth = 250nm), with line-space ratios of (1) 1:2.5, (2) 1:2, (3) 1:1.5 and (4) 1:1. (a) Original, etched silicon-oxide grating structures and (b) composite-PDMS replicas. At this linewidth, the PDMS structures remain stable at all line-space ratios. 87

Figure 6-10: Pitch measurements of imprinted polyimide gratings via optical diffraction. (a) Plot of grating pitch for a given line-space ratio in grating arrays 3 and 5, as specified in the initial design (diamonds) and as measured via optical diffraction (triangles). (b) Transmission diffraction grating schematic showing the grating groove direction ($\boldsymbol{g}$) and zeroth (m=0) and first order (m=±1) diffraction modes. (c) Combined image of the diffraction patterns produced by 404nm laser light incident on each of the four imprinted gratings within array 3. Line-space ratios from top to bottom of the image are: 1:2.5, 1:2, 1:1.5 and 1:1. The patterns are projected on a screen at 91±1mm from the sample. 88

Figure 6-11: Polarised microscopy images of an LC device featuring a homeotropic polyimide surface imprinted with grating array 3 (filled with MLC-6204, LC layer thickness = 6 ± 1μm, imaged at 20°C). The images show different grating areas within the device, with line-space ratios of (a) 1:2.5, (b) 1:1.5 and (c) 1:1. The grating groove direction ($\boldsymbol{g}$) is varied between (1) 0° and (2, 3) 45° to the crossed polarisers (P, A), with full-wave plate slow axis orientation (λp) indicated in (3). Schematic cross sections of the grating profiles are shown in (4), indicating linewidth (l), spacewidth (w) and pitch (d). Surface pretilt on the grating surface (θP) is also shown, as a reference point and approximate guide as to how the gratings are influencing surface director orientation. Scale bar = 100μm. 90

Figure 6-12: Polarised microscopy images of the 1:1 line-space ratio grating area of the array 3 device, with the grating grooves ($\boldsymbol{g}$) aligned parallel to one of the polarisers, highlighting the azimuthal deviation of the tilted HAN director profile. Images captured (a, c) with and (b) without a full-wave plate with slow axis orientation (λp). (b) Extinct and (a, c) first-order magenta regions at the bottom of the images correspond to areas without a grating, with a VAN director profile. Scale bar = 100μm. 92

Figure 6-13: Conoscopic examination of LC devices featuring homeotropic grating structures. (a) Schematic cross-sections of the homeotropic polyimide surface topographies where the conoscopic figures in (b) and (c) were captured, indicating grating linewidth (l), spacewidth (w) and pitch (d). Numbering denotes (1) an area of flat unpatterned polyimide, (2) a grating area with a 1:2.5 line-space ratio and (3) a grating area with a 1:1 line-space ratio. (b, c) Conoscopic figures produced by the devices containing grating array 3 and array 5 respectively, with grating groove ($\boldsymbol{g}$) and polariser

orientations (P, A). The grating pitch associated with each figure is indicated in the top-right of the images. Horizontal white lines denote the vertical position of the melatope in each figure, highlighting the change in position and thus optic axis orientation between different device areas. 93

Figure 6-14: Method of measuring the shift in melatope position from conoscopy figures with varying degrees of optic axis tilt. (a) Grayscale versions of the conoscopy figures shown in Figure 6-13.c, from device regions with (1) unpatterned polyimide, (2) a 1225nm pitch grating and (3) a 700nm pitch grating. (b) Plot of grayscale intensity profiles taken along the horizontal, yellow dashed lines on each figure in (a). The blue, green and orange vertical dashed lines indicate the positions of the intensity minima/melatopes in the images of device areas (1), (2) and (3) respectively. The same colour-coding and vertical dashed lines are shown in the corresponding images in (a) for reference. 95

Figure 6-15: Calibration of the back focal plane of the objective via diffraction patterns, to convert distances on conoscopy figures to angular deviation. (a) Conoscopic figure with central melatope, defining the radial distance (R) from the centre of the figure. (b) Schematic of the transmission diffraction grating arrangement used to image the diffraction patterns. (c) Diffraction patterns of (1) 1225nm pitch, (2) 875nm pitch and (3) 700nm pitch gratings imaged on the back focal plane, using the same optical setup as used in (a). The vertical orange dashed lines show how the positions of the first-order ($m = 1$) diffraction maxima, with well-defined diffraction angles (θd), relate to different values of R in the conoscopy figures. (d) Plot of $m = 1$ diffraction peak positions on the imaged diffraction patterns (green diamonds), against $m\lambda d = sin\theta d$. The good linear fit to the diffraction peaks (blue dashed line) indicates minimal optical distortions in back focal plane for values of $R <$ 300px. 96

Figure 6-16: Analysis of conoscopy figures produced by devices containing grating arrays 3 and 5, with respective grating linewidths (l) of 250nm and 350nm. The calculated tilt of the optic axis away from the surface normal (ϕ) and measured shift in melatope position are plotted against (a) grating pitch and (b) mark-space ratio (w/l), where (a.1) and (b.1) show the equations of the linear fits in each the plot. (c) Schematic of the HAN director profile in the devices, approximating how the director orientation (blue rods) varies throughout the layer. An average optic axis (OA) is indicated to approximate the tilt represented by the conoscopy figures, which is some average of the different director orientations in the device. Pretilt at the grating interface (θP) and the dimensions of ridges/marks (w), lines/spaces (l) and pitch (d) are also included for reference. 97

Figure 6-17: Differentiating between adjacent HAN domains with opposing tilt directions. (a) Polarised microscopy image of the 500nm pitch grating area in the array 3 device, showing an overview of the tilt domain structure. Green dashed line denotes the boundary between grating (HAN) and non-grating areas (VAN). Scale bar = 100μm. (b.1) Enlarged view of the area marked with the orange box in (a), spanning a reverse-tilt disclination line. (b.2) Schematic highlighting the HAN director profile on either side of the disclination line (marked by the orange dashed line). (c) Conoscopy figures imaged in the left (L, c.1) and right (R, c.2) regions shown in (b.1). (d) Enlarged view of the area marked by the blue box in (a), showing the alternating appearance of consecutive tilt disclination lines. Scale bar = 20μm. 99

Figure 6-18: (a) HAN director profiles with a linearly varying director orientation (θ) with distance (z) in to the thickness (dLC) of an LC slab, for various surface pretilts (θP). (b) Schematic of HAN director profile defining key device parameters such as, the pretilt on the grating surface (θP) and the unpatterned polyimide surface ($\theta 1$), the average director orientation (θavg) for the HAN profile with a given θP and the average tilt of the optic axis from the surface normal (ϕ) obtained via conoscopy. 100

Figure 6-19: (a) Plot of the optic axis tilt (ϕ) obtained from conoscopy, and the inferred grating pretilt (θP) for each value, as a function of grating mark-space ratio (wl). (b) Schematic grating profiles with mark-space ratios of 1.0 and 2.5 and their associated surface pretilts. 101

Figure 7-1: Fabrication and alignment properties of concentric wrinkle textures. (a,b) Circular PDMS slab mounted in the radial-strain apparatus at low and high tensile strains. (c) Visual appearance of wrinkled PDMS slab after oxygen plasma etching and strain release. Scale bar = 10mm. (d) Image of a CD as a reference point, with similar diffractive optical appearance to the wrinkled slab. (e) Schematic geometry of the LC device containing the concentric wrinkle texture. Upper, unpatterned planar polyimide surface is rubbed with a rubbing direction (RD) and the lower, wrinkle-imprinted polyimide surface is left unrubbed. Filled with 5CB, with an LC layer thickness (dLC) of 10 ± 1μm. (f−h) Polarised microscopy images of the filled wrinkle device at different analyser (A) orientations. (i−l) Device geometry and polarised microscopy images of the reference device made by Wang et al., with the same bulk director configurations and comparable optical appearance to the wrinkle device. 112

Figure A-1: Spectrum of broadband green light referred to in the conoscopy methods section (3.1.3.c.i) and used during conoscopy experiments on devices with homeotropic wrinkles (section 5.4.3) and homeotropic gratings (section 6.4.2.b). This light is produced by placing a green filter over the white light source of a Leica DM2700P optical microscope. The light's bandwidth of 52nm is taken from a Gaussian fit of the spectrum (red), as the full width at half of the maximum/peak intensity. 140

Figure A-2: Spectrum of Thorlabs PL205 blue laser diode, used during diffraction experiments on micropatterned liquid crystal elastomers (section 4.4) and imprinted polyimide grating structures (section 6.4.1.d). 140

Figure B-1: Polarised microscopy observations of the same cell geometry used to fabricate nematic μLCE films in Chapter 4, comparing (a) rubbed and (b) unrubbed imprinted polyimide (IPI) grating surfaces. This comparison is referred to in the sections on μLCE fabrication (section 4.3.2.a) and resulting appearance and alignment (section 4.4.1). Devices are imaged at 20°C, filled with E7 and the confining surfaces are separated by 100μm thick spacer film. (a) Homogeneously rubbed IPI cell shows uniform extinction in both mutually-orthogonal grating regions, indicating that the surface alignment is dominated by the applied rubbing direction ($RDPI$) and not the grating topography. If this wasn't the case it would be most visible in the left-hand region where the grating grooves and $RDPI$ are perpendicular, which would have increased transmittance if any induced twist was present. (b) Unrubbed IPI cell showing significant transmission in the left-hand region, where $RDPVA$ is perpendicular to the IPI grating grooves. This indicates that a twisted nematic (TN) director profile is present, due to the director aligning parallel to the grating grooves on the IPI surface, in the absence of an applied rubbing direction. 141

Figure B-2: DSC traces of the (a) 54.6 mol% 6OCB precursor mixture. (b) 45.7 mol% 6OCB precursor mixture and (c) 70.7% 6OCB precursor mixture. The nematic-to-isotropic transition temperature, Tni, for each sample is shown. The 70.7 mol% 6OCB precursor mixture displays a cold crystallization (Tcc) and melting (Tm) peak on heating. 142

Figure B-3: Photograph of a fabricated μLCE film in ambient white light, highlighting the structural colour in the $\boldsymbol{n} \perp$ region of the film, caused by the diffractive nature of the periodic grating structure. The variation in colour is due to the sample being at an angle relative to direction of observation, which shows the wavelength dispersion of white light associated with the 1st order diffraction mode. This is referred to in section 4.4.1 on the appearance and alignment of the μLCE films. 143

Figure B-4: Confirmation that the birefringence colour bands shown in Figure 4-7b.ii in section 4.4.1 are an artefact of the screen backlight used to illuminate the sample. (a, b) Monodomain μLCE film illuminated with an alternative white light source, imaged between crossed polarisers (P, A), with the rubbing direction (RD)/director orientation at (i) 0° and (ii) 45° to the polarisers. The images in (a.ii) and (b.ii) show the expected saturated white appearance of the μLCE film, compared to the banded appearance when imaged in the same orientation using the screen backlight shown in (c). Scale bar = 10mm. 143

Figure B-5: (Left) AFM scan of an imprinted polyimide (IPI) grating, with a pitch of 1040 ± 5nm and a height of 130 ± 5nm, used as a mould in Chapter 4 for fabricating μLCEs and as a reference surface for the homeotropic wrinkle device in section 5.4.3.c.i. (Middle, Right) AFM scans of μLCEs

fabricated with the nematic director parallel ($\boldsymbol{n} \parallel$) and perpendicular ($\boldsymbol{n} \perp$) to the grating orientation. 144

Figure B-6: AFM scans of $\boldsymbol{n} \parallel$ µLCEs with varying concentrations of 4'-hexyloxy-4-cyanobiphenyl (6OCB). 144

Figure B-7: AFM scans of $\boldsymbol{n} \parallel$ µLCEs under strain, at various fractional lengths ($L/L0$), where applied strain (ε) $= (L/L0) - 1$ 144

Figure B-8: Photographs showing the manual strain approach used to perform AFM measurements on µLCE films under strain, referred to in section 4.4.4 on the strain response of the µLCEs. The images show a µLCE film with both ends secured to a glass slide using adhesive tape, at (a) 0% and (b) 110% tensile strain. The strain is adjusted by moving one end of the film and re-adhering it in a different location. Strain is calculated from measurements of the sample length/tape separation at each strain increment. Scale bars = 5mm. 144

Figure B-9: TGA results on the 54.6 mol% 6OCB µLCE with thermal degradation (defined as the temperature at 5% mass loss) occurring at $Tdeg = 382$°C. 145

Figure C-1: Polarised optical microscopy (POM) observations of the hybrid aligned nematic (HAN) device discussed in section 5.4.2.a, featuring a planar wrinkle-imprinted polyimide surface. The device has an LC layer thickness of 10 ± 1µm and is imaged upon cooling from 60 to 30°C, on the boundary between wrinkled (uniform) and flat (Schlieren) polyimide regions. Temperatures and approximate retardations (Γ) associated with the observed colours are indicated on the POM images. A section of the Michel-Lévy colour chart, adapted from reference [49], is shown at the bottom of the figure, with a rectangular highlighted region indicating a range of 2nd (II) order birefringence colours that correspond closely to those shown in the POM images above. The sequence of colours observed in the POM images upon cooling therefore confirms that the observed orange colour at 59°C is 2nd order orange ($\Gamma \approx$ 950nm), rather than 1st order orange ($\Gamma \approx$ 450nm). 146

Figure C-2: POM observations of the HAN device with planar wrinkles, discussed in section 5.4.2. These images confirm the sign ($\pm$) of the $s = 1$ point defect, which is used as a reference point in section 5.4.2.b to confirm the azimuthal director orientation. (a) Broad view of the device with the reference defect highlighted by the orange box. Scale bar = 200µm. (b – d) Enlarged views of the 4-brush $s = 1$ point defect at successive stages during clockwise (CW) sample rotation, with scale bars = 5µm. The dark brush marked with the pink ⊗ symbol in (b) is used as a reference point. This brush can be seen to rotate CW as the sample is rotated CW, indicated by the orange and turquoise ⊗ symbols in (c) and (d) respectively. This matching sense of rotation between the sample and the brushes confirms that this is a $s = -1$ defect, as the brushes of a $s = +1$ defect would rotate in the opposite sense relative to the sample rotation.[218] 147

Figure C-3: Conoscopy figure calibration using the diffraction pattern of a linear surface relief grating, as referred to in section 3.1.3.c.i on the conoscopy methodology and section 5.4.3.a on the tilt of homeotropic wrinkles. (a) 3D topographic data from a 5x5μm atomic force microscopy scan of the calibration grating. (b) Cross-sectional height profile of the grating, with pitch (d=1040nm), taken along line A-B in (a). (c) Conoscopic figures with identical fields of view, produced by (c.1) the calibration grating, imaged without an analyser, and (c.2) a vertically aligned nematic LC device with homeotropic wrinkles, imaged between crossed polarisers. The diffraction pattern in (c.1) shows the grating's zeroth ($m = 0$) and first ($m = \pm 1$) order diffraction modes, with xc denoting the separation of $m = 0$ and $m = \pm 1$ in pixels. This is measured from the centre of each maxima ($\oplus$), located using the 'Analyze Particles' tool in ImageJ analysis software (NIH, USA). (d) The 'degrees per pixel' calibration factor for the conoscopy figures is calculated by relating the diffraction angle (θd) of light with a given wavelength (λ), from a grating with pitch (d), to the zeroth and first order maxima separation (xc) shown in (c.1). 147

Figure C-4: Supporting data used to approximate wrinkled surface pretilt (θp) in the homeotropic wrinkle device discussed in section 5.4.3.b.ii, following the surface anchoring transition. (a) Theoretical linear director tilt profiles ($\theta zdLC$) as a function of normalized slab thickness ($zdLC$), for a hybrid-aligned nematic (HAN) device geometry with different θp on one surface, generated from equation (5-3). (b) Corresponding variation in $(neff(zdLC)) - no)$ for each tilt profile, calculated using equation (5-4) for the effective refractive index ($neff$), and the refractive indices of MLC-6204 at $TTNI$ = 0.99 (ne=1.595 and no=1.507). (c) Resulting birefringence of the LC slab ($\Delta neff$) as a function of θp, calculated by integrating the functions in (b) from $zdLC$ = 0 to $zdLC$ = 1. The two blue cross (×) symbols on the y-axis denote the top and bottom of the range of $\Delta neff$ values obtained from comparing the observed birefringence colours of the device with the Michel-Lévy chart (Figure 2-4). The orange shaded areas indicate how these measured values are cross-referenced with the calculated $\Delta neff$ data to obtain a range of θp for the wrinkled surface. 148

List of Tables

Table 3-1: Physical properties of LC the mixture MLC-6204 (Merck, Germany) measured at 589nm. Room temperature data (T=20°C) was sourced from the manufacturer's data sheet and high temperature data (T=40, 63°C) was sourced from reference [119]. The properties at 63°C or $TTNI = 0.99$ are given specifically in relation to the temperature study in section 5.4.3. 25

Table 4-1: Chemical compositions of LCEs used in this work. Composition LCE-2, marked with an asterisk (*), is the primary composition used in the majority of the work presented. The far right-hand column shows the composition of a final LCE film (post-wash), which started with the LCE-2 composition initially (pre-wash). Compositions 1, 3 and 4 are solely used in section 4.4.2.c, for investigating how the chemical composition of the LCE impacts deswelling. 45

Table 4-2: Results of AFM topography analysis carried out on three individually fabricated μLCE samples, with identical chemical compositions (LCE-2, see Table 4-1). The mean grating pitch (d) and height (h) in the $\boldsymbol{n} \parallel$ and $\boldsymbol{n} \perp$ regions of each sample is shown, along with the range of these mean values in nanometres and as a percentage of the values themselves. The pitch and height changes are relative to the dimensions of the IPI grating mould (pitch = 1040 ± 5nm, height = 130 ± 5nm). The number of scans/scan locations refers to the number of 5 x 5μm AFM scans, and associated height profile data, used to calculate each sample mean. Each scan of a given sample is acquired in a unique location within the ≈3cm^2 area occupied by both $\boldsymbol{n} \parallel$ and $\boldsymbol{n} \perp$ grating regions. 50

Table 6-1: Summary of grating dimensions selected for study, showing the grating pitch (d) for a given line-space ratio and linewidth (l). Gratings with the same linewidth are grouped into 'arrays' numbered 1 through 5. Highlighted columns denote the structures used in the final LC devices, chosen based on the observed structural stability of the PDMS working stamps discussed in section 6.4.1. 80

Symbols and Abbreviations

Symbols

Γ	Optical Path Difference/Retardation
d	Grating Pitch/Period
d_{LC}	Cell Gap
ε	Tensile Strain
$\epsilon_{\parallel}$	Dielectric Permittivity Parallel to the Director
$\epsilon_{\perp}$	Dielectric Permittivity Perpendicular to the Director
$\Delta\epsilon$	Dielectric Anisotropy
η_1	First Order Diffraction Efficiency
$\boldsymbol{g}$	Grating Groove Direction
h	Grating Height/Depth
θ	Polar Director Orientation
θ_d	Diffraction Angle
θ_P	Surface Pretilt Angle/Polar Easy Axis Orientation
λ	Wavelength of Light
λ_p	Slow Axis of Full-Wave Compensation Plate (λ-plate)
m	Diffraction Order
$\widehat{\boldsymbol{n}}$	Nematic Director
$\widehat{\boldsymbol{n}}_{\parallel}$	Director Parallel to Grating Grooves
$\widehat{\boldsymbol{n}}_{\perp}$	Director Perpendicular to Grating Grooves
n_{avg}	Average Refractive Index
n_e	Extraordinary Refractive Index

n_{eff}	Effecive Refractive Index
n_o	Ordinary Refractive Index
Δn	Birefringence
Δn_{eff}	Effective Birefringence
T	Temperature
T_{NI}	Nematic-Isotropic Transition Temperature
ϕ	Tilt of Optic Axis from Vertical
$\Delta\varphi$	Phase Difference
ψ	Azimuthal Director Orientation
ψ_0	Azimuthal Easy Axis Orientation
W_θ	Polar Anchoring Strength
W_ψ	Azimuthal Anchoring Strength

Abbreviations

A	Analyser
AFM	Atomic Force Microscopy
EBL	Electron-Beam Lithography
$FOTS$	1H,1H,2H,2H-Perfluorooctyltrichlorosilane
FOV	Field of View
HAN	Hybrid-Aligned Nematic
HT	Homeotropic
IPI	Imprinted Polyimide
ITO	Indium Tin Oxide
LC	Liquid Crystal

LCE	Liquid Crystal Elastomer
NIL	Nanoimprint Lithography
OA	Optic Axis
P	Polariser
$PDMS$	Polydimethylsiloxane
PI	Polyimide
POM	Polarised Optical Microscopy
ROI	Region of Interest
RD	Rubbing Direction
$SAMIM$	Solvent-assisted Microcontact Moulding
SEM	Scanning Electron Microscopy
SRG	Surface Relief Grating
UV	Ultraviolet
UVO	Ultraviolet-Ozone
μLCE	Micropatterned Liquid Crystal Elastomer
VAN	Vertically-Aligned Nematic
WIP	Wrinkle-Imprinted Polyimide
ZBD	Zenithal Bistable Display

Chapter 1 Motivation and Thesis Outline

1.1 Motivation

Liquid crystal (LC) surface alignment is a critical aspect of all LC devices as it enables significant control over their bulk optical properties, and is consequently a cornerstone of the display and LC device industry. It is most commonly achieved by tailoring the chemistry and topography of the solid surfaces in contact with the LC medium. Well established processes associated with polymer alignment layers and microfabrication, enable LC-surface interactions to be adjusted and thus the bulk LC properties and final device characteristics to be readily controlled. Although spatially uniform alignment layers contributed heavily towards the rise of flat-panel liquid crystal displays (LCDs),[1,2] alignment layers with spatially varying or patterned properties have since enabled improvements in LCD performance,[3,4] the study of fundamental physics such as topological defects,[5–7] and the development of various functional optoelectronic devices.[8–14]

The work in this thesis explores the LC alignment properties of topographically patterned alignment layers, comprised of sub-micron scale surface relief structures created using a selection of microfabrication processes.[15] The combination of LCs and surface relief structures has led to a variety of technological developments such as the Zenithal Bistable Display (ZBD),[16,17] vehicular LIDAR (light detection and ranging) systems with optical beam steering capabilities [18,19] and static [20] and dynamic [21] metalenses for low form factor optics. The LC alignment capability of surface relief structures has also been used to realize electrically tunable 2D diffraction gratings,[22–24] optical filters [25,26] and polarisation converters.[27]

The aim of this work is to create surface relief structures comprised of conventional LC polyimides, to investigate how LC surface alignment is affected by the physical influence of the relief structures and the chemical influence of the polyimides combined. Polyimides are selected due to their relevance and widespread use as alignment layers in both research and industrial LC device fabrication, stemming from their high anchoring strengths and range of available pretilts,[28] as well as thermal, chemical and mechanical resistance.[29] The accessibility and versatility of using micropatterned polyimide alignment layers is also emphasized throughout this work, highlighting the control offered by applying polyimide surface anchoring conditions to structures with different dimensions and arrangements, and the ability to template or mould other mediums with structures that possess inherent functionality e.g. diffractive properties.

1.2 Thesis Outline

An outline of the thesis is shown in the roadmap in Figure 1-1, highlighting each of the constituent chapters, the overarching theme and the primary distinctions between each of the experimental chapters. Chapter 2 introduces the key concepts and background physics explored throughout the experimental work. This covers the physical properties of nematic liquid crystals and discusses LC surface alignment on flat and topographically patterned surfaces.

Chapter 3 describes the experimental methods used to fabricate and analyse the surface relief structures and resulting LC devices, including a detailed discussion on the overarching method of polyimide imprinting.

Chapter 4 investigates the fabrication of micropatterned liquid crystal elastomers (μLCEs) using planar polyimides imprinted with commercially-sourced linear surface relief gratings. The inherent anisotropic deswelling of the μLCEs is explored, demonstrating miniaturization of surface features, and the μLCE topography and diffraction efficiency are both characterized under thermal and mechanical actuation. This work has been published in T. Moorhouse and T. Raistrick "Sub-micron Diffractive Optical Elements Facilitated by Intrinsic Deswelling of Auxetic Liquid Crystal Elastomers", *Advanced Optical Materials*, 2024, 12, 2400866.[30]

Chapter 5 focuses on the LC alignment properties of spontaneously formed periodic wrinkle textures, transferred in to planar and homeotropic polyimides. The wrinkled topography is measured with atomic force microscopy, allowing connections to be drawn between key surface features and the resulting LC alignment observed *via* polarised microscopy. The temperature dependence of the alignment is studied within the nematic phase and the source of complex modulated surface alignments is discussed.

Chapter 6 covers the transfer of precision grating structures, fabricated with electron-beam lithography, in to layers of homeotropic polyimide. Arrays of sub-micron scale gratings are used to determine the limits of pattern transfer with PDMS working stamps, using scanning electron microscopy and optical diffraction patterns. LC surface alignment on the resulting structures is analysed *via* birefringence colour observations, indicating the occurrence of surface anchoring transitions, and also *via* conoscopy, showing how device parameters such as surface pretilt can be tuned by altering the grating geometry.

Chapter 7 summarizes the key findings and conclusions of Chapters 4 to 6 and potential directions for future work are proposed.

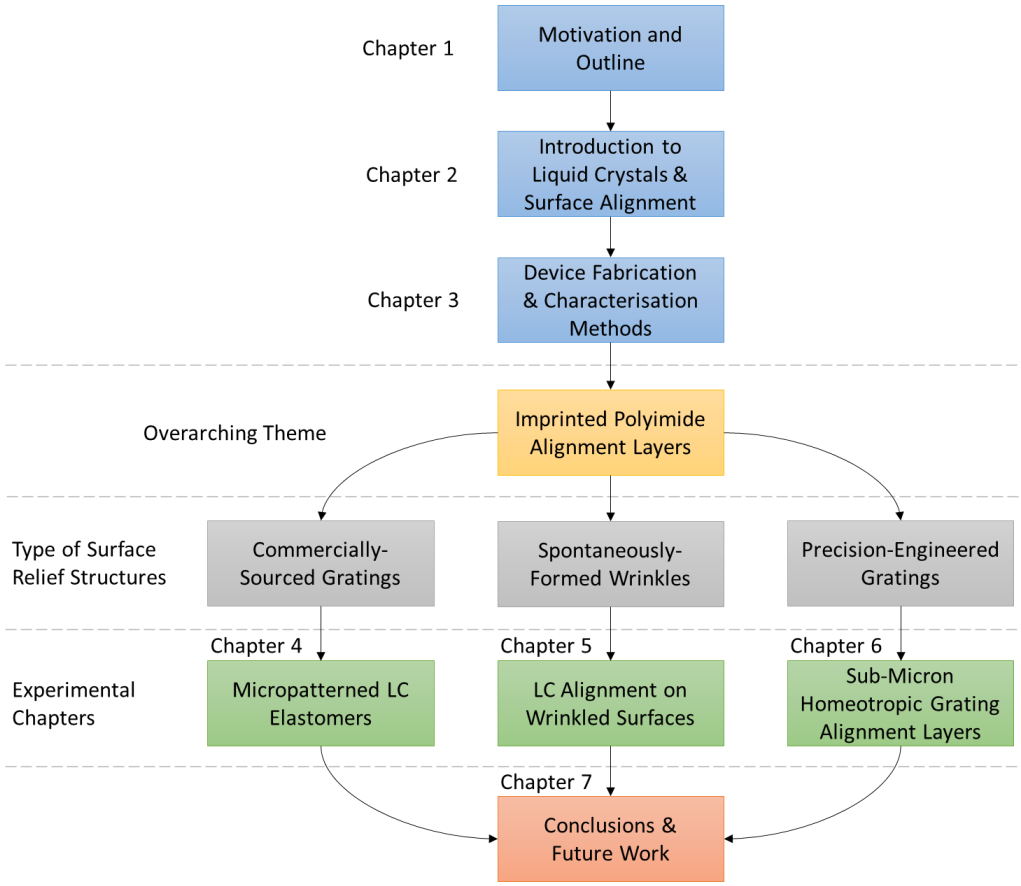

Figure 1-1: Roadmap highlighting the key components of the thesis. The overarching theme shared by each of the experimental chapters is given, along with the distinct routes taken by each, in terms of the type of surface relief structure being applied.

Chapter 2 Introduction

This chapter provides an introduction to the key concepts and background physics that underpin the experimental work presented in this thesis. An overview of nematic liquid crystals (LC) is given, highlighting the physical properties of these materials that lead to the rich variety of phenomena observed in this work. As surface alignment is the focal point of the project, this topic is then covered in some detail, first describing the more conventional alignment interactions between LCs and flat surfaces, followed by the diverse LC alignment behaviour imposed by topographically patterned surfaces. Relevant literature surrounding the area of LCs on surface relief structures will then be presented, to give the reader a broad overview of this area of LC research and the potential device applications associated with this work.

2.1 Liquid Crystal Fundamentals

2.1.1 Nematic Liquid Crystals

As the name suggests, liquid crystals are a phase of soft condensed matter possessing properties of both disordered liquids and crystalline solids. This equilibrium phase of matter is best described in terms of its molecular order, which is an intermediary between the long-range positional and orientational order of a crystal, and the complete disorder of an isotropic liquid.[31] Molecules within a liquid can freely diffuse throughout the bulk material, which is also true for the molecules within a LC phase. However, the distinguishing feature of LCs is the positional and/or orientational order exhibited by the constituent molecules.[32]

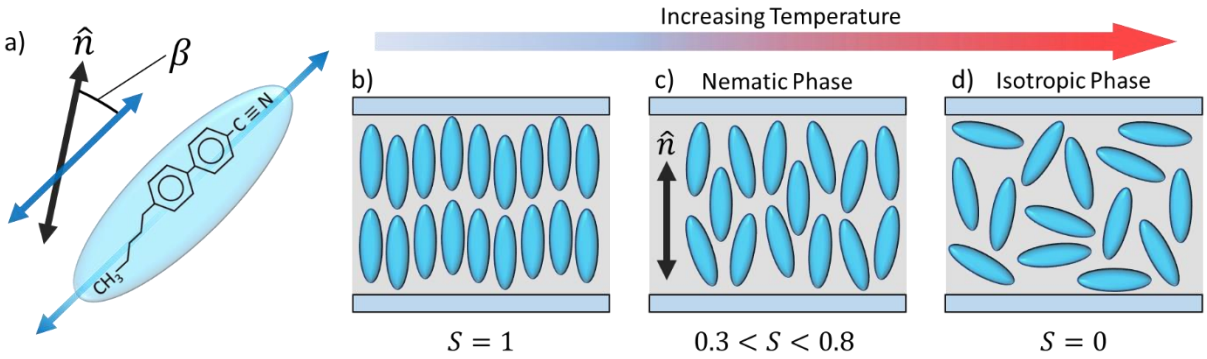

Figure 2-1: (a) Chemical structure and approximated rod-like morphology (blue ellipsoid) of a nematic liquid crystal molecule (4-Cyano-4'-pentylbiphenyl, 5CB). The long molecular axis (blue arrows) is oriented at an angle (β) relative to the average bulk molecular orientation known as the director, defined by the unit vector $\hat{\boldsymbol{n}}$ (black arrow). (b−d) Illustrations of the temperature dependent phase behaviour and orientational order in a LC medium, with the scalar order parameter (S) defining (b) perfect order ($S = 1$), (c) nematic order ($0.3 < S < 0.8$) and (d) complete disorder ($S = 0$).

The formation of LC phases broadly relies upon the presence of mesogenic units that are geometrically anisotropic. This anisotropy is most commonly provided by elongated rod-like molecules, represented schematically in Figure 2-1a. These are typically comprised of two or more rigid-linked ring structures, terminated with hydrocarbons or a chemical unit with a strong dipole, such as a CN group. Materials that are comprised of rod-like mesogens and exhibit LC phases are known as calamitic liquid crystals.[32] The most disordered phase of this class of LCs is the nematic phase, which does not possess any positional order, as the molecular centres of mass are randomly distributed within the bulk, but does possess orientational order where the long axes of the molecules tend to align parallel to one another, oriented in an average direction known as the director (defined by a unit vector, $\hat{\boldsymbol{n}}$).[33]

Amongst the variety of LC mesophases, conventional nematic phase LCs are the only materials considered in this work. However, variants of the nematic phase exist, such as chiral nematics,[34,35] twist-bend nematics [36] and ferroelectric nematics (N_F),[37–39] which exhibit more complex molecular arrangements like the symmetry breaking in N_F materials, imposed by the polar nature of the constituent molecules. There is also a diverse range of liquid crystal phases that combine orientational order with some degree of positional order, as described in many standard texts.[31–33] These are not, however, the topic of this thesis and so are not considered further.

The degree of orientational order or alignment of the molecular long axes relative to the director, is quantified by the scalar order parameter (S),

$$S = \frac{1}{2}\langle 3cos^2\beta - 1\rangle, \tag{2-1}$$

where β is the angle between the molecular long axes and the director (Figure 2-1a), and the angled brackets represent a statistical average taken over a large number of molecules. This quantity can take values between S = 0 and S = 1, corresponding to complete disorder and perfect order respectively. Typical nematic liquid crystal systems have order parameters between 0.3 and 0.8, the value of which is dependent on the temperature of the system.[32] An increase in temperature reduces order and eventually results in a weakly first-order phase transition from the nematic phase to the isotropic phase, as depicted in Figure 2-1c,d. Upon cooling an isotropic mixture of suitable calamitic molecules, the nematic phase forms at a temperature defined as the nematic-to-isotropic phase transition temperature (T_{NI}).[31] The temperature-dependent phase stability of nematic phase calamitic LCs, classifies them as thermotropic materials.

2.1.2 Elastic Properties

An important property of LC systems is their elasticity, which arises from the preservation of long-range orientational order between the constituent molecules. The presence of this elasticity means that there is an elastic energy cost associated with perturbing a uniform director field, by means of external stimuli such as electric or magnetic fields, or by alignment interactions with containing surfaces.

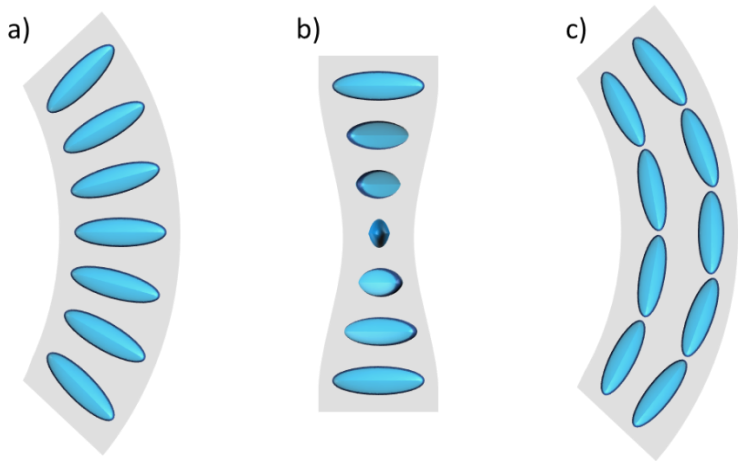

Figure 2-2: Schematics of the three fundamental modes of elastic deformation in a liquid crystal medium, (a) Splay (K_{11}), (b) Twist (K_{22}) and (c) Bend (K_{33}).

In scenarios where the director field is distorted by any of these means, the spatial variation in director orientation is assumed to be smooth and gradual, occurring over distances much greater than the molecular length scale.[33] As such, the LC medium can be treated as a continuum with a constant order parameter, where the associated elasticity is sufficiently described using theory taken from the elastic behaviour of solids. This forms the basis of the Oseen-Frank continuum theory, used to describe the elastic deformation of uniaxial LCs.[40,41] The commonly used result of this theoretical description for nematic liquid crystals is,

$$F_{ela} = \frac{1}{2}K_{11}(\nabla \cdot \hat{n})^2 + \frac{1}{2}K_{22}(\hat{n} \cdot \nabla \times \hat{n})^2 + \frac{1}{2}K_{33}(\hat{n} \times \nabla \times \hat{n})^2, \qquad (2\text{-}2)$$

which is the free energy cost per unit volume associated with the three basic modes of elastic distortion in an LC continuum. The values of K_{11}, K_{22} and K_{33} are the elastic constants associated with splay, twist and bend deformations of the director field, which are shown schematically in Figure 2-2. These elastic constants are analogous to the spring constant in Hooke's law, describing how resistant a LC material is to each of the three types of elastic distortion. With values of the order of pico-newtons, the bend elastic constant (K_{33}) is typically the largest of the three, and therefore in most LC materials it is more difficult/energetically costly to induce bend deformation in the director field than it is splay and twist.[32]

An important aspect of the elastic constants is that they are theoretically proportional to the square of the order parameter, and since order is reduced upon heating through the nematic phase, so too are the elastic constants.[42–45] This plays a crucial role in the experimental work in Chapter 5, where elevated temperatures and reduced elastic constants allow for a deeper study of the alignment influence of surface topography; the effects of which are not observed at room temperature as the higher elastic constants dominate over the topographic influence.

2.1.3 Dielectric and Optical Anisotropy

A nematic LC possesses anisotropic bulk physical properties such as dielectric permittivity and refractive index, due to the anisotropic shape of the calamitic LC molecules and the associated orientational order. This anisotropic molecular shape results in two distinct polarizabilities of mobile charge within the molecules, and thus permittivities (ϵ) within the bulk LC material, parallel ($\epsilon_{\parallel}$) and perpendicular ($\epsilon_{\perp}$) to the nematic director. This dielectric anisotropy ($\Delta\epsilon$) leads to molecular reorientation in the presence of electric fields above a material dependent threshold voltage. The charge separation in the molecules results in induced dipole moments that align the molecular long axes parallel to the field direction (for $\Delta\epsilon > 0$) provided the elastic energy, which tends to promote uniform nematic alignment, is overcome.[31]

At optical frequencies (10^{14}Hz) this same dielectric anisotropy gives rise to anisotropic optical properties, in the form of dissimilar refractive indices parallel (n_e) and perpendicular (n_o) to the director, where $n_e > n_o$. This optical anisotropy or birefringence (Δn, equation (2-3) is a key property of LCs that allows them to be used for optical modulation, by changing the polarisation state of incident light.

$$\Delta n = n_e - n_o \tag{2-3}$$

Uniaxial nematic LCs have an axis of cylindrical symmetry parallel to the molecular long axes, known as the optic axis, perpendicular to which the refractive index is n_o. Therefore, when the propagation direction of plane-polarized light coincides with the optic axis, the LC medium appears optically isotropic ($\Delta n = 0$), as the light only experiences a single refractive index (n_o). However, if the plane-polarized light propagates perpendicular or at some angle to the optic axis, the birefringence emerges as the polarised component parallel to n_e travels slower than the component parallel to n_o, since $n_e > n_o$. When the optic axis is at some intermediate angle (θ) relative to the light's propagation direction, n_o remains unchanged but n_e is reduced to an effective refractive index (n_{eff}) using,[46,47]

$$n_{eff}(\theta) = \frac{n_o n_e}{\left(n_e{}^2\, sin^2(\theta) + n_o{}^2\, cos^2(\theta)\right)^{1/2}}. \tag{2-4}$$

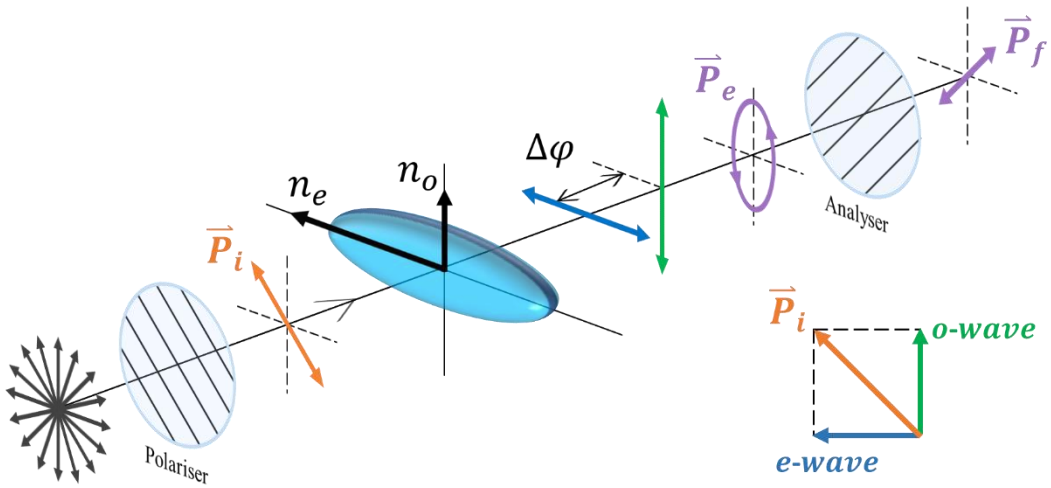

Figure 2-3: Schematic illustration of how a LC medium alters the polarisation state of incident light and the basic optical arrangement used in polarised microscopy (polariser and analyser with orthogonal/crossed polarisation directions). From left to right, a polariser converts unpolarised light in to linearly polarised light, with an initial linear polarisation state ($\vec{P}_i$). The LC's birefringence induces a phase difference ($\Delta\varphi$) between the orthogonal components of $\vec{P}_i$, where the e-wave (blue, parallel to n_e) propagates slower than the o-wave (green, parallel to n_o), due to $n_e > n_o$. This induced $\Delta\varphi$ alters $\vec{P}_i$, often resulting in some form of elliptical polarisation state ($\vec{P}_e$).[32] *This results in the LC sample appearing bright due to a sum of components of $\vec{P}_e$ having non-zero transmission through the analyser, combining to produce a final, observed polarisation state ($\vec{P}_f$). If the nematic director was aligned parallel to the polarisation direction of either the polariser or analyser, or if the birefringent sample was removed, $\vec{P}_i$ would remain unchanged and have zero transmission through the analyser.*

When linearly polarised light is incident on a LC medium, the polarisation state is broken down into two orthogonal components, one oscillating parallel to the projection of n_e on the polarisation plane (extraordinary wave) and one oscillating parallel to n_o (ordinary wave). As these orthogonal components propagate at different speeds, a phase difference ($\Delta\varphi$) is induced between them,[47] as illustrated in Figure 2-3,

$$\Delta\varphi = 2\pi\frac{(n_{eff}(\theta) - n_o)d_{LC}}{\lambda}, \tag{2-5}$$

which changes the polarisation state of the incident light where,

$$\Gamma = (n_{eff}(\theta) - n_o)d_{LC} = \Delta n_{eff}(\theta)d_{LC}, \tag{2-6}$$

represents the optical path difference or retardance (Γ) induced between the two components due to a LC layer with an effective birefringence ($\Delta n_{eff}(\theta)$) and thickness (d_{LC}). When a LC (or any other birefringent) layer is observed between crossed polarisers, with the projection of the optic axis on the polarisation plane at 45° to the extinction directions of the polarisers, transmission of light through the final polariser (T) is given by,[48]

$$T = sin^2\left(\pi\frac{\Gamma}{\lambda}\right). \tag{2-7}$$

For an LC layer with a given path difference (Γ), the observed transmission therefore varies for different optical wavelengths (λ). This results in LC samples exhibiting birefringence colours under white light illumination between crossed polarisers, where minimal transmission of a given wavelength results in the observed colour of a sample being dominated by the associated complementary colour. This forms the basis of the Michel-Lévy colour chart that relates the observed colour of a birefringent slab to the optical path difference and thus its thickness and birefringence.[49] Sørensen's revised version of the Michel-Lévy colour chart (Figure 2-4), is used throughout the experimental work in this thesis, for optically characterising LC devices from their birefringence colours.

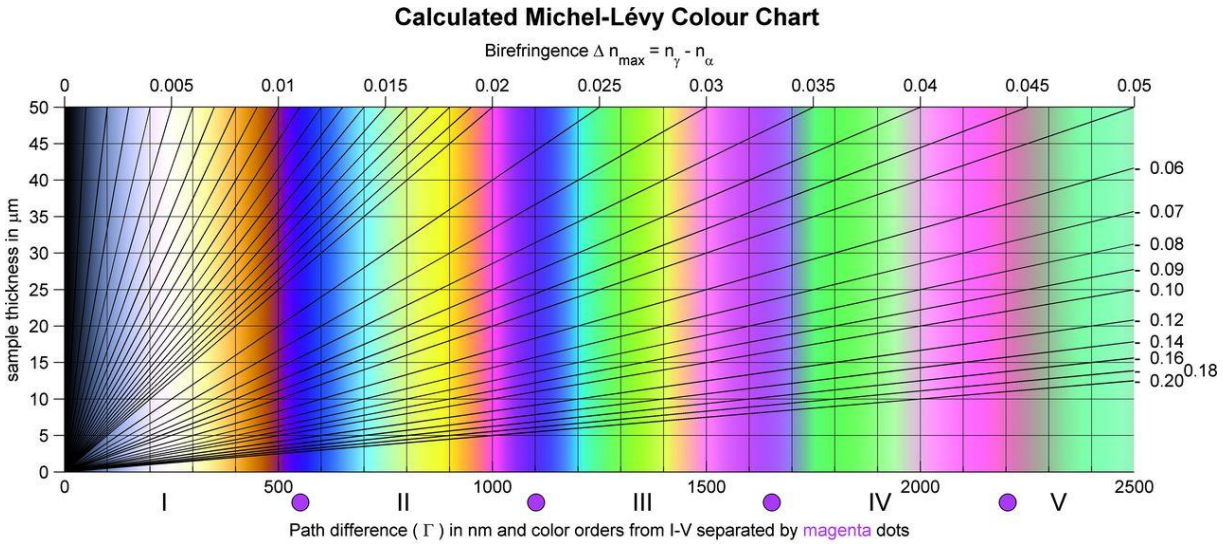

Figure 2-4: Michel-Lévy colour chart used as a reference point for characterising the optical appearance of LC devices throughout this work, reproduced from reference [49]. *The path difference (Γ) in nanometers is on the bottom-horizontal axis, the LC layer thickness (d_{LC}) is on the left-vertical axis and the black lines extending from the origin denote positions on the chart with a given effective birefringence ($\Delta n_{eff}(\theta)$), labelled from 0 to 0.20 along the top and right-hand side of the chart. To aid navigating the document, the chart is referred to in sections: 3.1.3.c on polarised microscopy methodology, 4.4.1 on the appearance and alignment of μLCE films, 5.4.3.b.ii on the tilt induced by surface anchoring transitions on homeotropic wrinkles, 6.4.2.a on birefringence colour observations of homeotropic grating devices and Appendix C.*

2.1.4 Nematic Liquid Crystal Elastomers

Although the majority of the work in this thesis is concerned with conventional low molecular mass (LMM) LCs, the experimental work in Chapter 4 utilizes a high molecular mass LC material in the form of liquid crystal elastomers (LCEs), the key features of which will now be introduced.

Liquid crystal elastomers are polymeric materials comprised of a network of linear polymer chains, featuring mesogenic molecules attached either in-line or as side-groups to the polymer backbones. The anisotropic orientation of these attached LC molecules, gives rise to nematic ordering and thus liquid crystalline properties in the resulting elastomers.[50] The type of attachment used for the mesogenic component defines the two types of LCE, main-chain LCEs and side-chain LCEs (Figure 2-5), with this

work using a side-chain variant.[51] LCEs are similar to conventional elastomers in that they can withstand large deformations that result in the reorientation and extension of the constituent polymer network, but differ in that the mesogenic components can be aligned to form a nematic phase, which can produce unique bulk responses to external stimuli.[52]

It is desirable to uniformly align the nematic director within a LCE, such that uniform, macroscopic optical and mechanical properties are exhibited, making them more suitable for device applications and material characterisation. These are referred to as monodomain LCEs, which can be obtained by applying uniaxial strain to reorient the mesogenic units in a partially cross-linked state,[53] applying magnetic [54] or electric [55] fields to an LCE prepolymer or by applying anisotropic surfaces such as mechanically rubbed polymer alignment layers during fabrication.[56,57]

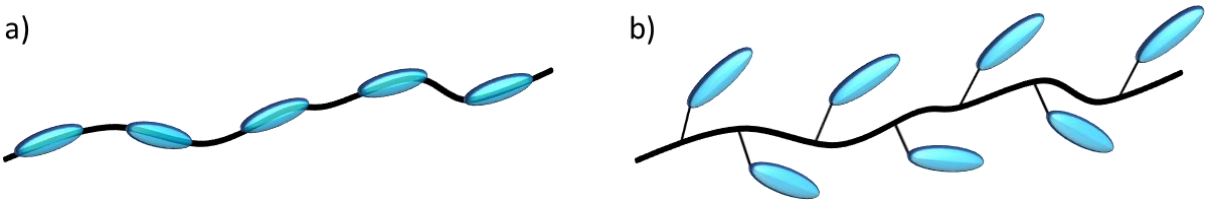

Figure 2-5: Schematic representation of the molecular structure of liquid crystal elastomers with (a) main-chain and (b) side-chain mesogenic units (blue) on the polymer backbone (black). Crosslinks between the polymer backbones are not shown in this representation.

2.1.4.a Mechanical and Thermal Response

Upon application of a uniaxial tensile strain, the polymer backbones of a LCE's weakly cross-linked polymer network adopt an increasingly anisotropic conformation. If starting from a poorly aligned or polydomain sample, this strain-induced anisotropy results in uniform director alignment, due to the coupling between the main chain orientation and the long range orientational order of the mesogenic side groups.[58] If strain is applied to an aligned nematic LCE, the mesogenic units will tend to orient in the direction of the strain. In fact, the direction of applied strain, relative to the initial director orientation ($\hat{\boldsymbol{n}}_{\boldsymbol{0}}$), strongly affects the rate at which the director rotates as a function of strain. When strain is applied perpendicular to $\hat{\boldsymbol{n}}_{\boldsymbol{0}}$, the most common deformation is termed 'semi-soft elastic' in which the director rotates continuously to align with the direction of strain. In some monodomain LCEs, the deformation occurs differently and apparently an abrupt 90° director reorientation occurs at a critical strain, which has been termed the mechanical Fréedericksz transition (MFT).[57]

Recently, it has been established that the LCE system used in this work deforms biaxially and the apparent discontinuity is a consequence of the biaxial axis changing sign, seen in one plane as a sudden rotation of the preferred orientation.[55] Strains applied at oblique angles to $\hat{n}_0$ result in a more continuous director reorientation, as determined by theoretical modelling [52,59] and experimental studies of this behaviour.[60] Mistry *et al.* established that the all-acrylate LCEs used in this work, seemed to exhibit a MFT under strain and it has since been shown that the biaxial deformation mode is

related to the unique auxetic strain response of these materials.[57,61] Monodomain LCEs also exhibit striking responses to changes in temperature, in the form of spontaneous shape change. This macroscopic thermal response follows microscopic changes in anisotropy in the nematic polymer network. The shape change doesn't manifest as a distinct transition, but as more of a continuous effect as the nematic order increases with increasingly anisotropic chain conformations and vice versa.[62] This continuous shape change is particularly prominent in the all-acrylate LCEs used in this work, which display a near-linear change in birefringence and order, and thus a similarly linear change in macroscopic dimensions.[57]

2.2 Liquid Crystal Surface Alignment

The interaction between LCs and their containing surfaces is a critical aspect of all LC devices, as the director orientation imposed by a surface has a profound influence on the bulk director profile, due to the elasticity of the LC medium. Surface alignment focuses on controlling this interaction, where appropriately defining the surface director orientation ensures that a device exhibits macroscopic anisotropy in the absence of external stimuli, which is crucial in display applications for maximizing contrast ratios.[63] There are various approaches to defining surface alignment including, mechanical rubbing of polymer films,[64,65] UV irradiation of photosensitive polymers,[66–68] chemical adsorption of monolayers,[69–71], oblique evaporation of inorganic materials.[72,73] and the fabrication of surface relief gratings,[74,75] as will be discussed in detail in section 2.3.1. The following sections will cover the key aspects of surface alignment associated with the experimental work in thesis, where basic alignment parameters and anchoring conditions will be defined, select polymer alignment layers will be discussed and relevant bulk director configurations imposed by two parallel alignment surfaces will be summarized.

2.2.1 Surface Anchoring

Surface anchoring is a term used to describe the orientation in which a surface preferentially aligns the director. If a surface results in the director lying parallel to the substrate plane, it is said to have planar anchoring, and if the director aligns perpendicular to the substrate plane, it is said to have homeotropic anchoring. The alignment ability of a given alignment layer is quantified by the anchoring strength, which is contained in the surface anchoring energy term (F_{surf}) of the total free energy of a static LC system (F_T, equation (2-8)),[76,77] along with the bulk thermal (F_{th}) and elastic deformation (F_{ela}) free energies. A surface's contribution to the total free energy is then determined by integrating F_{surf} over the area of interest, which could be a flat plane or an undulating surface topography.

$$F_T = \int_V F_{th} + F_{ela}\, dV + \int_A F_{surf}\, dA. \tag{2-8}$$

If the surface director orientation is anisotropic, either by the nature of the alignment layer or a treatment applied to the alignment layer, the preferential orientation is defined as the easy axis of the surface. The

anchoring strength of an alignment layer describes how difficult it is to rotate the director away from the easy axis, in both polar (θ) and azimuthal (ψ) directions (Figure 2-6). These anchoring strengths (W) are contained within the Rapini-Papoular approximation of the surface anchoring energy,[46]

$$F_{surf} = W_0 + W_\theta sin^2(\theta - \theta_P) + W_\psi sin^2(\psi - \psi_0), \quad (2\text{-}9)$$

where θ_P is the polar angle or pretilt of the easy axis from the surface, ψ_0 is the azimuthal angle of the easy axis, W_θ is the polar anchoring strength, W_ψ is the azimuthal anchoring strength and W_0 is an isotropic term representing the surface tension of the substrate experienced by the LC when $\hat{\boldsymbol{n}}$ coincides with the easy axis (at equilibrium).[78] A variety of techniques have been demonstrated for measuring these anchoring strengths experimentally, through the application of electric fields,[79,80] wedged cell geometries [81] and surface relief gratings.[82,83]

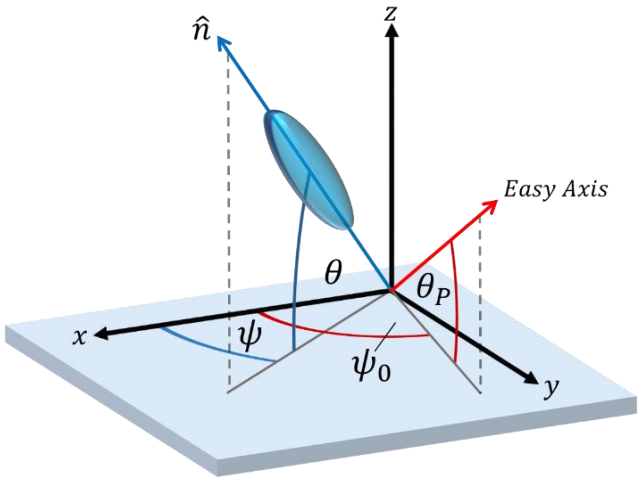

Figure 2-6: Reference frame and definitions for director ($\hat{\boldsymbol{n}}$) orientation relative to a surface plane. The easy axis (red) defines an alignment layer's preferred director orientation at equilibrium, with an out-of-plane polar surface pretilt, θ_P, and an in-plane azimuthal orientation, ψ_0. The polar and azimuthal anchoring strengths of an alignment layer, W_θ and W_ψ respectively, are given by the elastic energy cost associated with reorienting $\hat{n}$ from the easy axis, to some arbitrary polar (θ) and azimuthal (ψ) orientation.

Surface anchoring on a single substrate can be split into four basic types as shown in Figure 2-7, which form the building blocks for standard parallel-plate LC devices and more sophisticated optical components relying on complex surface alignments.

2.2.2 Planar Alignment

An alignment layer is classed as 'planar' when the director preferentially lies parallel to the plane of the surface. If an easy axis is not defined, the azimuthal director orientation will vary randomly across the surface, resulting in planar degenerate alignment (Figure 2-7a). The most accessible and widely adopted method for defining the easy axis of an alignment layer with planar anchoring, is mechanical rubbing. Originally demonstrated as a means of alignment on glass surfaces by Mauguin,[84] this simple technique involves passing a substrate beneath a cotton/nylon coated roller and allowing the fabric

fibres to make gentle contact with the surface. This treatment is typically applied to thin films of polyvinyl alcohol (PVA), polystyrene or polyimide, where polyimide is often the alignment layer of choice due to its strong anchoring properties and high chemical and thermal stability.[64,85–87]

Applying uniaxial rubbing to a planar alignment layer results in the azimuthal director orientation aligning parallel to the direction of rubbing (Figure 2-7b), a phenomenon that was initially attributed to the mechanical contact of the rubbing cloth forming microgrooves on the polymer layers. However, through UV and IR dichroic measurements [64] and grazing incidence X-ray scattering,[65] it was found that the alignment mechanism is dominated by the rubbing-induced realignment of the near-surface (<5nm) polyimide polymer backbones, which have strong intermolecular interactions with LC molecules. A critical aspect of rubbed alignment is that it defines a spatially uniform pretilt direction, where the director tilts, usually at small angles of a few degrees, towards the rubbing direction (Figure 2-7d). This is important in device construction, as having (usually) anti-parallel rubbing directions on opposite substrates is essential for avoiding reverse tilt domains and achieving desired bulk director profiles in final devices.[46]

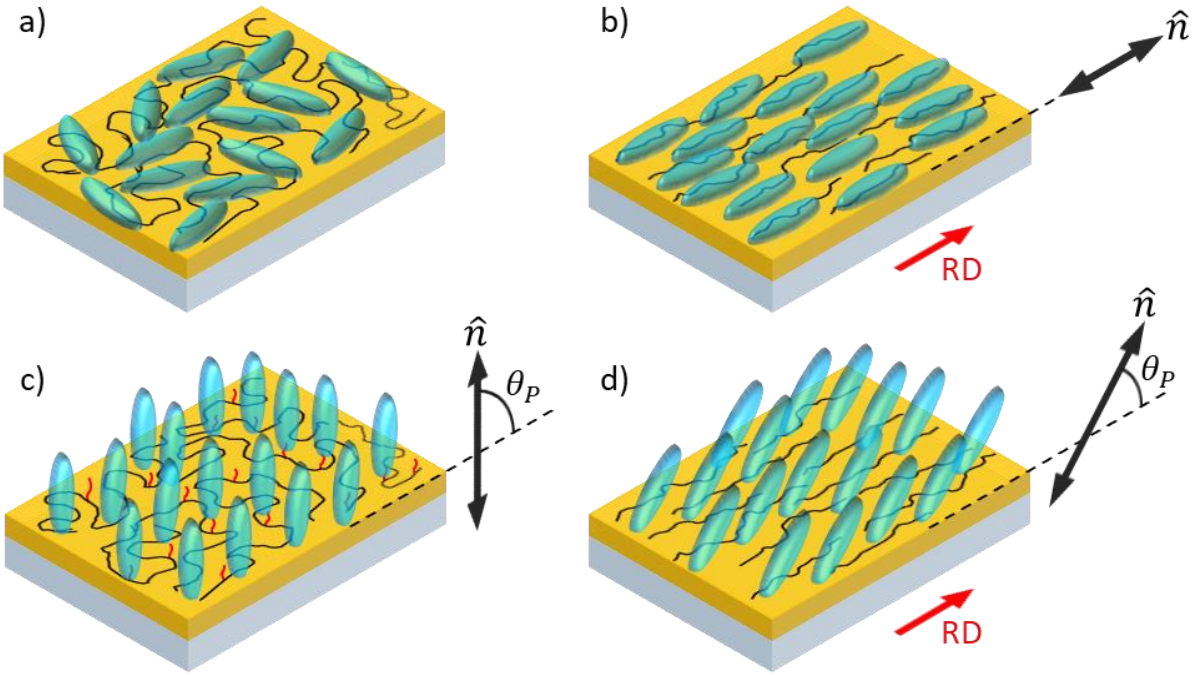

Figure 2-7: Four fundamental types of surface anchoring on LC alignment layers. (a) Planar degenerate – the director ($\hat{\boldsymbol{n}}$) lies parallel to the surface plane with a spatially varying azimuthal orientation. (b) Planar homogeneous - $\hat{\boldsymbol{n}}$ lies parallel to the surface with a uniform azimuthal orientation parallel to the easy axis of the surface, in this case defined by mechanical rubbing with a rubbing direction, RD. (c) Homeotropic - $\hat{\boldsymbol{n}}$ is oriented near-orthogonal to the surface plane, with a surface pretilt (θ_P) of ≈90°. (d) Tilted - $\hat{\boldsymbol{n}}$ is uniformly tilted with a pretilt angle of $0° < \theta_P < 90°$ and a uniform azimuthal orientation parallel to the applied RD. Note that $\hat{n}$ tilts towards the direction of rubbing.

2.2.3 Homeotropic Alignment

Aligning the director perpendicular to a surface can be achieved through a variety of homeotropic surface treatments. These include, oblique evaporation of silicon oxide,[88] UV-induced out-of-plane reorientation of hydrophobic units in photopolymers,[89] deposition of side chain polymers with mesogenic side groups [90] and self-assembly of amphiphilic monolayer coatings.[46,69]

Modified polyimides such as Nissan Chemical's SE1211 and SE4811, are also commonly used to promote homeotropic alignment, where the polyimide main chains feature long alkyl side chains. These side chains orient perpendicular to the plane of the film and through strong interactions with the alkyl tails of LC molecules, align the director perpendicular to the surface, as illustrated in Figure 2-7c.[91] Similarly, polyimides with rigid biphenyl side groups terminated with alkoxy end groups result in homeotropic anchoring, given the end groups are sufficiently long.[92] The use of these rigid units in polyimide side chains has been shown to stabilize the terminating alkyl chains during the mechanical rubbing process.[93] In the absence of rubbing, homeotropic polyimides impose a near-vertical polar director orientation, where the slight tilt away from vertical has a random azimuthal orientation. Applying rubbing causes the protruding chain units and thus slight tilt of the director to align parallel to the applied rubbing direction, with a spatially uniform azimuthal orientation.[91,94]

In the previous two sections, introductions have been given to the basic mechanisms behind planar and homeotropic anchoring of LCs at a solid interface. Focus has been placed on the chemical interactions between the LC medium and the containing alignment layers, specifically flat layers with no topography, where any imposed alignment behaviour is solely due to the chemical nature of the surface. This provides valuable context for the experimental work in Chapters $4-6$, where the chemical alignment properties of planar and homeotropic polyimide layers combine with the physical alignment properties of imprinted surface relief structures, the latter of which will be introduced in section 2.3.

2.2.4 Bulk Director Configurations

So far, the alignment properties of single surfaces with planar or homeotropic anchoring have been considered, where the near-surface director orientation has been the focus. As the ultimate aim of surface alignment is to establish a desired bulk director profile between two parallel plates, some of the more relevant bulk director configurations related to the work in this thesis are presented in Figure 2-8. This aims to provide the reader with a summary of alignment layer combinations and the associated bulk director profiles that arise from the LC elasticity and constrained surface director orientations.

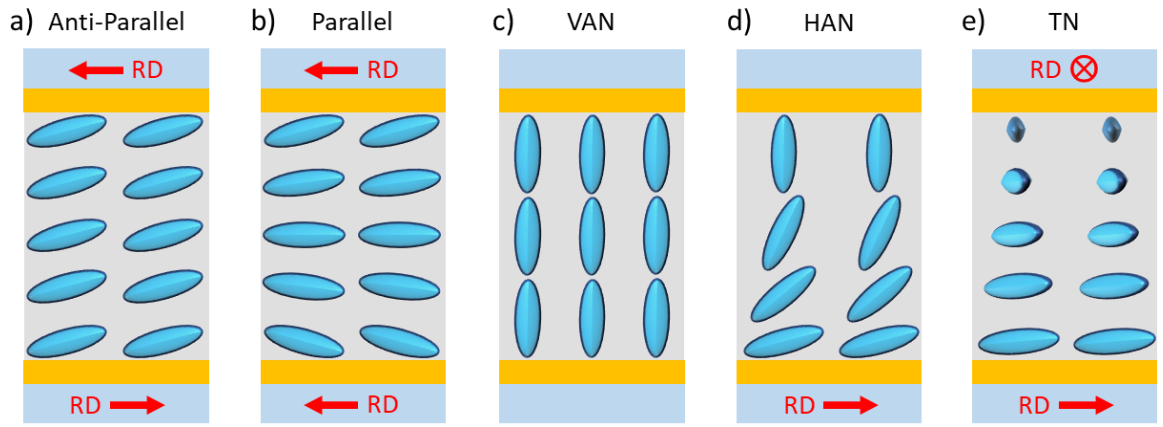

Figure 2-8: Bulk director profiles of assembled LC devices. (a) Opposing planar surfaces with anti-parallel rubbing directions (RD), resulting in a uniform polar director orientation throughout the LC layer. (b) Opposing planar surfaces with parallel RDs, resulting in a splayed director profile. (c) Vertically-aligned nematic (VAN) device comprised of opposing surfaces with homeotropic anchoring. (d) Hybrid-aligned nematic (HAN) device comprised of dissimilar surfaces with rubbed planar anchoring opposed by homeotropic anchoring. (e) Twisted nematic (TN) device with an azimuthal director orientation that rotates by 90° throughout the LC layer, imposed by rubbed planar surfaces with orthogonal RDs.

2.3 Liquid Crystals and Surface Relief Structures

With the more general aspects of LC surface alignment covered in section 2.2, this section introduces the area of LC alignment on topographically patterned surfaces, which is the focal point of the experimental work in this thesis. Formative works in the area and associated theory will be covered, along with some of the notable research and applications that followed. Broadly speaking, a topographically patterned surface is one that possesses a naturally occurring or fabricated arrangement of protruding features. Throughout this work a variety of terms are used synonymously when referring to these surfaces and their features, such as textures, topographies, relief structures and microstructures.

2.3.1 Grating Alignment

The study of LC alignment on microstructures stems from the works of Berreman,[74,95] where abrasive rubbing compounds were used to form microscale grooves on glass surfaces, which were shown to uniformly align the nematic director parallel to the groove direction. This alignment capability can be explained in terms of the elastic free energy of the system, in that there is an unfavourable elastic energy cost associated with the director aligning perpendicular to the grooves, due to the corrugated texture distorting the near-surface director (Figure 2-9a). This distortion and thus the free energy of the system is therefore minimized when the director is aligned parallel to the grooves (Figure 2-9b).[74]

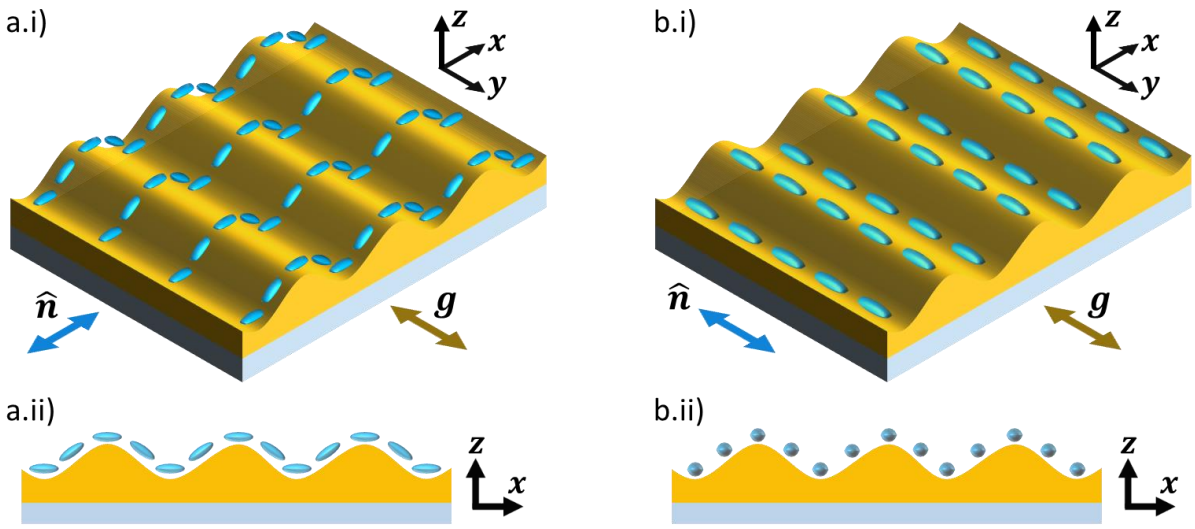

Figure 2-9: Schematic illustrations of the interaction between the nematic director ($\hat{\boldsymbol{n}}$) and a linear grating topography with grooves ($\boldsymbol{g}$) aligned parallel to y. (a) Energetically unfavourable scenario with $\hat{\boldsymbol{n}}$ aligned orthogonal to $\boldsymbol{g}$, resulting in elastic deformation of the director field in the x-z plane (highlighted in a.ii), as it attempts to conform to the undulating topography. (b) Energetically favourable scenario with $\hat{\boldsymbol{n}}$ aligned parallel to $\boldsymbol{g}$, resulting in minimal elastic distortion. This highlights the principle of 'grating alignment' on a grooved topography with planar anchoring.

This method of homogeneously aligning the azimuthal director orientation with a parallel groove structure, is broadly referred to as 'grating alignment' and is arguably the most common LC-microstructure combination. A clear demonstration of the effectiveness of grating alignment is given by Kim *et al.*, where a photoalignment polymer is patterned with a region of linear surface relief grating and the director is shown to preferentially align parallel to the grating grooves, rather than the photoaligned easy axis of the underlying azo-polymer.[75]

Berreman proposed a theoretical model to describe this interaction between a LC and a sinusoidal groove profile, which results in a relationship between the azimuthal anchoring strength (W_ψ) of a grating, and the pitch (d) and amplitude of its grooves ((2-10). It is worth clarifying that the amplitude (A) is half of the peak-to-peak value ($2A$) of a sinusoidal profile, and that throughout this work the height (h) of surface relief structures will be quoted rather than the amplitude, where $h = 2A$.

$$W_\psi = \frac{2\pi^3 K A^2}{d^3} \tag{2-10}$$

Various assumptions were used in formulating this equation, including a mean elastic constant ($K = \sqrt{K_{11}K_{33}}$), infinitely strong polar anchoring and negligible azimuthal distortion. Although it is beyond the scope of this work, it is worth acknowledging that Berreman's theory has since been re-examined by Faetti,[96] to account for finite polar anchoring strengths and obtain a more general W_ψ for practical cases, and by Fukuda et al.,[97] highlighting the importance of considering azimuthal distortions when calculating W_ψ.

Multiple researchers have experimentally investigated the relationship between W_ψ and grating dimensions, with Kawata *et al.* showing that longer pitch gratings ($d \gtrsim 10\mu m$) struggle to uniformly align the director, due to grating sidewall interactions causing the azimuthal director orientation to drift between adjacent features, whereas shorter pitch gratings ($d \lesssim 2\mu m$) avoid the sidewall effect and promote uniform alignment due to stronger anchoring.[98] Sub-wavelength pitch gratings ($d \ll 400nm$) were applied by Gear *et al.* to demonstrate the tunability of W_ψ enabled by varying the grating geometry, with measured values of W_ψ in good agreement with theoretical predictions.[99]

2.3.2 Grating Alignment Layer Fabrication and Applications

Grating-based and other forms of microstructured alignment layers can be fabricated using a variety of patterning approaches, such as photolithography,[98,100] imprint lithography,[101–103] dry etching [104] and deposition [105] of inorganic materials and laser inscription of azopolymer alignment films.[75,106] Aside from engineered relief structures, grating alignment properties can also be possessed by naturally corrugated surfaces, such as spontaneously-formed wrinkle textures,[107] which will be covered in detail later as the focal point of Chapter 5.

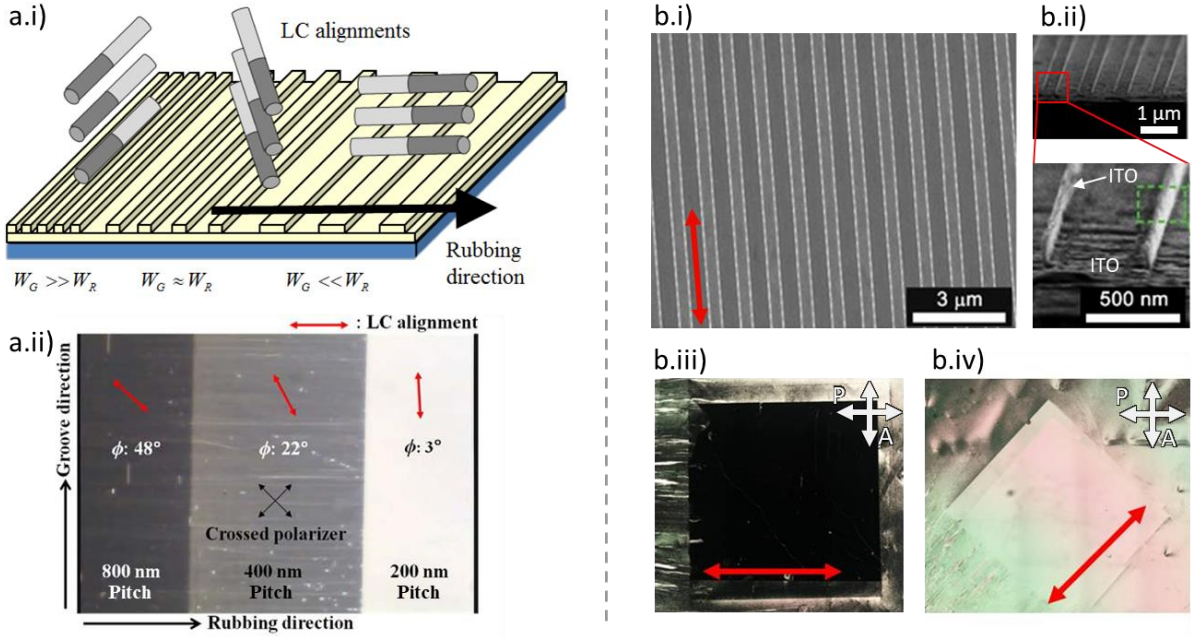

Figure 2-10: Grating alignment applications. (a) Measurement of the polar and azimuthal anchoring strengths of polymer alignment layers, using linear surface relief gratings of varying pitch (d) as reference points. Rubbing applied perpendicular to the grooves (a.i), competes against the varied anchoring strengths of the gratings, resulting in different twist angles and optical appearances (a.ii) from which the anchoring strengths are inferred.[83] *(b) Sub-micron pitch, indium tin oxide (ITO) grating structures (b.i – b.ii), with a groove direction indicated by the red arrows, applied simultaneously as electrodes and grating alignment layers (b.iii–b.iv).*[105]

Grating alignment has been successfully applied in various LC devices, enabling the characterization of alignment layer materials and the development of a range of functional optoelectronic devices. Polyimide gratings with varying pitch (d), and thus W_ψ (equation (2-10)), have been applied by Choi *et al.* as reference points for measuring the polar and azimuthal anchoring strengths of polymer alignment layers (Figure 2-10a),[83] using all-optical twist angle measurements.[108]

Alongside their LC alignment ability, grating structures can be engineered with inherent functionality by tailoring the materials from which they are made; forming multipurpose grating alignment layers. Flanders *et al.* applied gold surface relief gratings as the alignment layers on both surfaces of a twisted nematic (TN) device, serving as in-built crossed polarisers, with their orthogonal arrangement, and as electrodes for controlling director orientation.[104] Similarly, Jeong *et al.* demonstrated the use of indium-tin oxide (ITO) gratings, formed *via* secondary sputter deposition, as both alignment layers and electrodes (Figure 2-10b), whilst retaining the superior conductivity of a pristine ITO surface.[105] Recently it has also been shown that gold metasurfaces comprised of grating-like nanorod arrays can promote uniform LC alignment, enabling dynamic control over the plasmonic resonance of the surfaces *via* the LC's electric field response.[109] Grating structures can also be superimposed on existing functional surface topography to provide uniform director alignment in cases where rubbing is unsuitable, as demonstrated by Chang *et al.* in their electrically tunable LC-based infrared filter.[25]

2.3.3 Alternative Microstructured Alignment Layers

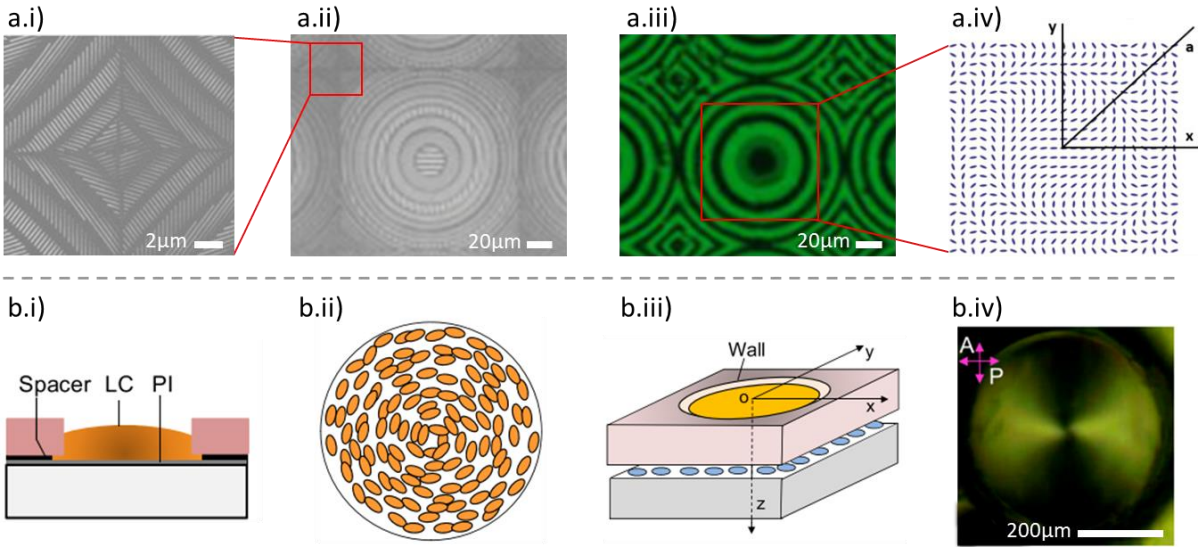

Figure 2-11: Applications of microstructured alignment layers for non-uniform or patterned director alignment. (a) LC microlens arrays based on the Pancharatnam-Berry phase. Sub-micron pitch surface relief gratings are precisely patterned with spatially varying groove directions (a.i—a.ii). The patterned grooves result in azimuthal rotation of director across the surface, resulting in a modulated phase profile as shown in the polarised microscopy image in (a.iii), with a corresponding director profile shown in (a.iv).[21] *(b) Polarisation converter based on the circular/azimuthal director alignment (b.ii) imposed by physical confinement of a LC in a cylindrical cavity (b.iii). The circular alignment from the cavity combines with a planar-aligned polyimide (PI) surface to produce alternating uniform and twisted bulk director profiles around the cavity, with an optical appearance shown in (b.iv).*[27]

The grating alignment examples presented in the previous section 2.3.2, solely focused on linear surface relief gratings, which result in spatially uniform planar alignment of the director. However, there are various examples of modified-grating and non-grating surface topographies that have enabled fascinating alignment states and device functionalities to be realized, further highlighting the wealth of potential offered by exploring LC-microstructure interactions.

A notable application of grating alignment in a non-standard arrangement is presented by He *et al.*, where spatially varying groove directions are used to modulate the azimuthal director orientation in a device (Figure 2-11a), resulting in a switchable mircolens array based on the wavefront-shaping capability of the Pancharatnam-Berry phase.[21] Spatial control over director orientation has also been achieved *via* a confinement approach, using polymer microchannels with sub-wavelength pitch grating structures on the sidewalls, as a physical guide for the azimuthal director orientation.[110] Wang *et al.* demonstrated that topographic confinement of LCs in cylindrical cavities can produce non-trivial, radial and azimuthal surface alignments that can be used to create polarisation converter devices (Figure 2-11b).[27,111] Topography can also have a profound effect on out-of-plane (polar) director orientation, as shown by Kumar *et al*. who applied self-assembled nanoparticle arrays as unconventional homeotropic alignment layers, relying on the elastic distortion of the nanoparticles' topography to promote homeotropic surface anchoring.[112]

Although elastic deformation of the director field is energetically costly and actively avoided in a traditional grating alignment scenario, there are ways in which topography can distort the near-surface director and produce a favourable bulk alignment effect. Kim and Serra demonstrate this strikingly in their work on topological defect arrays, which are established and patterned *via* the topographic director distortion of micropillar structures with homeotropic surface anchoring, resulting in electrically tunable diffractive optical elements with variable pitch and arrangement (Figure 2-12).[22–24]

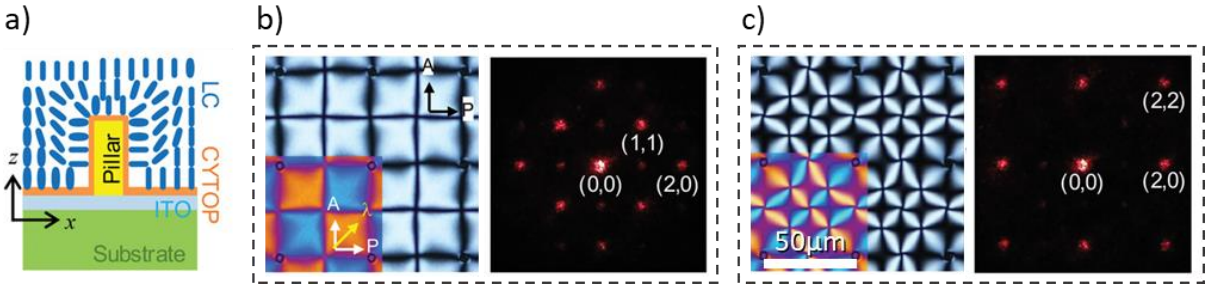

Figure 2-12: Application of micropatterned surface topographies, combined with homeotropic anchoring, for creating a tunable diffractive optical element. (a) Micropillar structures with a homeotropic coating (CYTOP) results in a frustrated/distorted near-surface director field. Applying electric fields to the LC ($\Delta\epsilon < 0$), parallel to z in (a), results in further director field distortion that forms intricate nematic defect arrays, with optical appearances shown in the left panels of (b) and (c). These images demonstrate how the arrangement of the defect arrays can be altered by varying the voltage and frequency of the applied field, which in turn changes the optical diffraction patterns produced by laser light incident on the device (right panels of (b) and (c)).[22]

Crucially, this relies on competing alignment contributions between the physical influence of a micropillar topography and the chemical influence of a surface coating with homeotropic anchoring. This competition between topography and surface anchoring has also facilitated the development of the commercially successful Zenithal Bistable Display (ZBD).[16,17] This employs a deep, sub-micron pitch grating structure with homeotropic anchoring to distort the director field, allowing two unique surface pretilts and thus bulk director profiles to be stabilized and reversibly switched between. Cattaneo *et al.* carried out a targeted investigation of similar frustrated director profiles to those found in the ZBD system, characterizing how the onset of distortion-induced surface anchoring transitions and the resulting director orientation is affected by the height of a homeotropic grating topography.[113] Further discussion and background of LCs on homeotropic surface topographies will be covered in the introduction to Chapter 6, which aims to build upon the work of Cattaneo *et al.* by focusing on how the lateral dimensions of homeotropic gratings affect the properties of frustrated surface alignments.

2.4 Summary

This chapter has introduced the fundamental physical properties of nematic LCs, covering their temperature dependent phase behaviour, orientational order, elasticity and optical anisotropy. A brief introduction to nematic liquid crystal elastomers was also given, highlighting their defining features and distinct responses to mechanical and thermal stimuli. The concept of LC surface alignment was then described in some detail, outlining how these materials interact with their containing surfaces, the various types of surface anchoring and how bulk material properties are affected by different alignment layer combinations.

With the focus of this work being surface alignment on topographically patterned surfaces, the physical alignment properties of topography was discussed by introducing the concept of grating alignment as well as other notable LC-microstructure combinations. Finally, a short review was presented on the previous applications of microstructured alignment layers in functional LC devices, highlighting the wide variety of alignment phenomena afforded by tailoring surface topography and the active area of research that will be explored throughout the experimental chapters of this thesis, using the general methods described in the following chapter.

Chapter 3 Experimental Methods

This chapter details the key experimental methods used in the preparation and characterisation of LC devices featuring topographically patterned alignment layers. The previous chapter introduced the physical properties of these systems, which will be explored using these methods in the subsequent experimental chapters. Focused methods sections are included in each of the experimental chapters, covering more specialized techniques, whereas this chapter details the more general methods used throughout the thesis. The structure and preparation of the LC devices will be covered first, followed by the characterisation techniques used to quantify their properties. General microfabrication processes used to form surface relief structures will then be discussed, highlighting how the master structures, replicas and final patterned alignment layers are fabricated. Finally, contact and non-contact surface metrology approaches will be covered, used to measure the dimensions of any surface relief structures.

3.1 Liquid Crystal Devices

3.1.1 Device Geometry

The LC devices used in this work have a parallel-plate geometry, where two parallel substrates are separated by spacers to create a cavity that will be filled with LC material (Figure 3-1). The substrates are 1.1mm thick glass, coated with ≈70nm of indium tin oxide (ITO) from the supplier. Prior to use, the ITO glass substrates undergo a three-stage cleaning process in an ultrasonic bath, comprised of a degreasing step in dilute Decon-90 and two solvent washes in acetone followed by isopropanol. Spacing is provided by spherical polystyrene beads with a diameter of the order of 10µm, dispersed in the UV-curable adhesive (NOA 91, Norland Products Inc.) used to laminate the two substrates together.

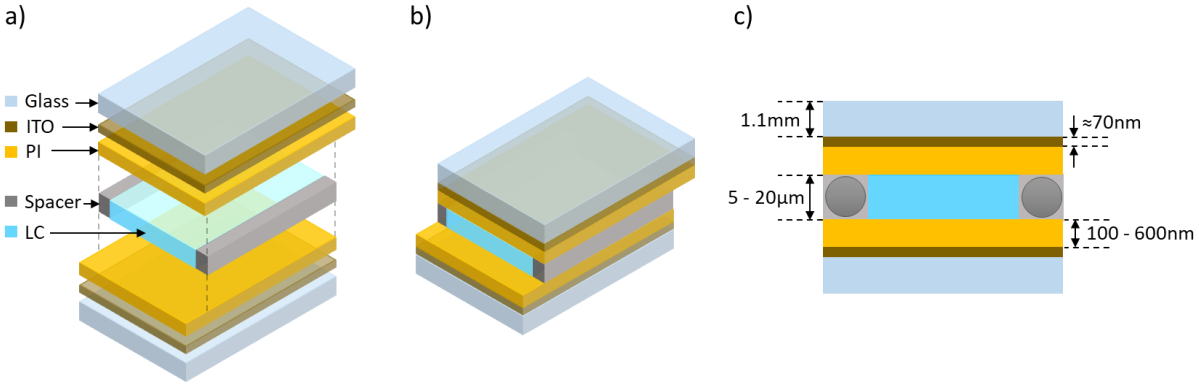

Figure 3-1: LC device schematics. (a) Exploded view of a LC device highlighting each of the constituent layers, including: indium-tin oxide (ITO) coated glass, polyimide (PI) alignment layers and spacers for defining the thickness of the LC slab. (b) Collapsed view of an assembled LC device, showing the lateral offset of the substrates that provides a ledge for capillary filling the device with LC material. (c) Cross sectional view indicating the typical thicknesses of each of the device layers. Grey circles denote the spherical polystyrene spacer beads that are dispersed in the UV-curable glue seals.

3.1.2 Alignment Layers

This work focuses on the use of polyimide (PI) thin films as alignment layers, which are applied to the ITO surfaces of the glass substrates using spin coating (Figure 3-2). Prior to spin coating, the ITO surfaces are exposed to an ultraviolet-ozone treatment for 10 minutes to remove any organic contaminants that would disrupt thin film uniformity, and increase the surface wettability (more hydrophilic) to maximize adhesion between the substrate and the dispensed PI solution.[114]

The spin coating process involves securing the substrate (≈2.0 x 2.5cm) to the centre of the spin coater's vacuum chuck, drop dispensing the PI solution on to the static substrate and rapidly accelerating the substrate up to rotational speeds of 2000 – 5000rpm. Once reached, these spin speeds are sustained for 40 - 60s, during which time the deposited solution flows radially across the substrate as a result of shearing, induced by adhesion at the liquid-substrate interface and the centrifugal forces experienced by the liquid. The majority of the dispensed solution is ejected from the substrate due to the radial flow, but as the solvent evaporates and the polymer concentration increases in the remaining solution, a uniform polymer thin film is formed on the surface.[115]

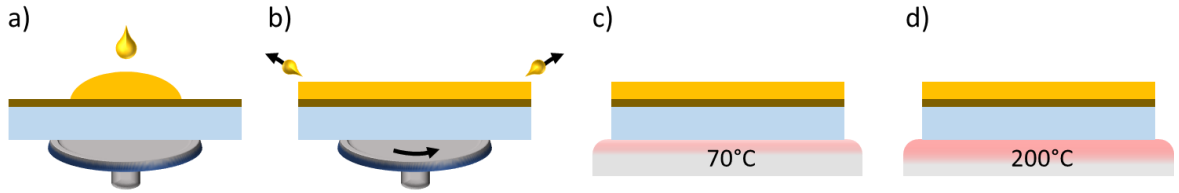

Figure 3-2: Spin coating and post-processing of polyimide alignment layers. (a) Approximately 0.1ml of PI solution is drop dispensed on to a static substrate, whilst secured to the spin coater's vacuum chuck. A pipette tip is used to spread the droplet across the surface to ensure full coverage. (b) Spin coater rotates the substrate at high speed, ejecting material and forming a uniform thin film. (c) Freshly spun film is placed on a 70°C hotplate for 60s to evaporate any remaining solvent and solidify the layer. (d) Finally, the film is cured/imidized on a 200°C hotplate for 30mins.

3.1.2.a Nissan Chemical Polyimides (SUNEVER series) - Film Thicknesses

A selection of polyimide alignment layers from Nissan Chemical Industries Ltd. are used in this work, with planar (SE-130, SE-2170) and homeotropic (SE-4811) anchoring. As the PI layers are intended to be imprinted with surface relief structures, it is beneficial to select an appropriate PI film thickness to suit the depth of the structures, to maximize the fidelity of the imprinted features by avoiding partial filling of the valleys in the stamps.[116] The film thicknesses of each PI variety are measured by stripping select regions of the films with a scalpel and measuring the film-ITO step heights using a stylus profiler (DektakXT®, Bruker) with a 2µm tip radius (Figure 3-3a). A summary of the PI film thicknesses as a function of spin speed is shown in Figure 3-3b, including the tilted SE-3510 variety, which isn't used as an alignment layer in this work but was measured to provide a complete summary of all available PI varieties.

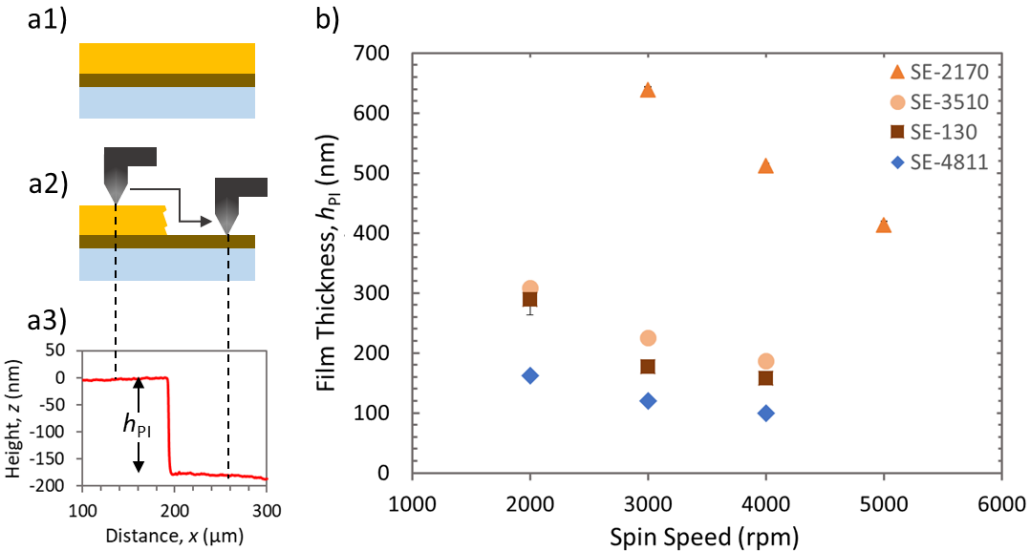

Figure 3-3: (a) Schematics showing the process of measuring PI film thicknesses with a stylus profiler. (a1) Pristine PI thin film (yellow) as found after spin coating. (a2) A region of PI film is removed with a scalpel, exposing the underlying ITO layer (gold). The path of the stylus profiler's tip is indicated by the black arrow, stepping down from the PI film on to the ITO surface. (a3) Example of output data from the stylus profiler, showing the step height/thickness of the PI film (h_{PI}). (b) Film thicknesses of Nissan Chemical Polyimides (SUNEVER series), spin coated at different spin speeds. Orange data points indicate films with planar or tilted (SE-3510) anchoring and blue indicates homeotropic anchoring.

3.1.2.b Mechanical Rubbing

Alignment layers with planar anchoring undergo a mechanical rubbing process before final device assembly. This rubbing treatment causes the initially randomly oriented polymer backbones (Figure 3-4a) of the alignment layer to align parallel to the direction of rubbing (Figure 3-4c), resulting in a uniform azimuthal director orientation once the device is filled with liquid crystal.[64,65]

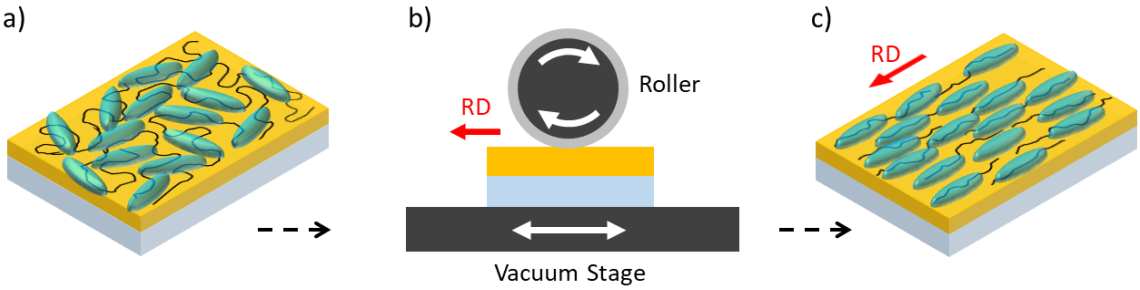

Figure 3-4: Surface alignment via mechanical rubbing. (a) Alignment layer with planar anchoring before rubbing. Near-surface polymer chains (black lines) are randomly oriented, resulting in no orientational preference of the near-surface director (blue ellipsoids). (b) Rubbing machine schematic, showing coated substrate on a vacuum stage passing beneath a rotating roller. White arrows denote each component's direction of travel, with the single rotation direction of the roller defining the rubbing direction (RD) applied to the alignment layer. (c) Resulting polymer chain orientation and subsequent director alignment of a unidirectionally rubbed, planar alignment layer.

The rubbing process is performed with a custom rubbing machine, comprised of a drum roller coated in a cotton velvet fabric and a vacuum translation stage that secures the substrates and passes them beneath the roller (Figure 3-4b). The height of the roller is set such that the cotton fabric makes gentle contact with the substrate, as aggressive contact can physically damage the alignment layer. An appropriate roller height is selected by placing an un-coated substrate of the same thickness on the translation stage without the vacuum applied, allowing the substrate to move freely. From a raised position, the roller is then gradually lowered until the substrate starts being pushed back by the roller during translation; this defines the point of gentle contact and is an appropriate roller height for rubbing. Coated substrates are then secured on the vacuum stage and pass back and forth beneath the roller twice (4 passes total) at a speed of 10mm/s. The roller rotates in a single direction with a rotational speed of 100rpm, defining the rubbing direction (RD) of the alignment layer.

3.1.3 Device Characterization

3.1.3.a Cell Gap Measurements

Once a device has been assembled as shown in Figure 3-1b and prior to filling with liquid crystal, the distance between the two parallel substrates or the 'cell gap' (d_{LC}) is measured using white light interferometry. This allows the thickness of the LC slab to be confidently inferred once the device is filled. This measurement is carried out using a microscope in reflection mode, where an empty device is illuminated with white light and the reflected light is analysed *via* a UV-Vis (450-700nm) spectrometer (Flame-S-UV-VIS, Ocean Optics).

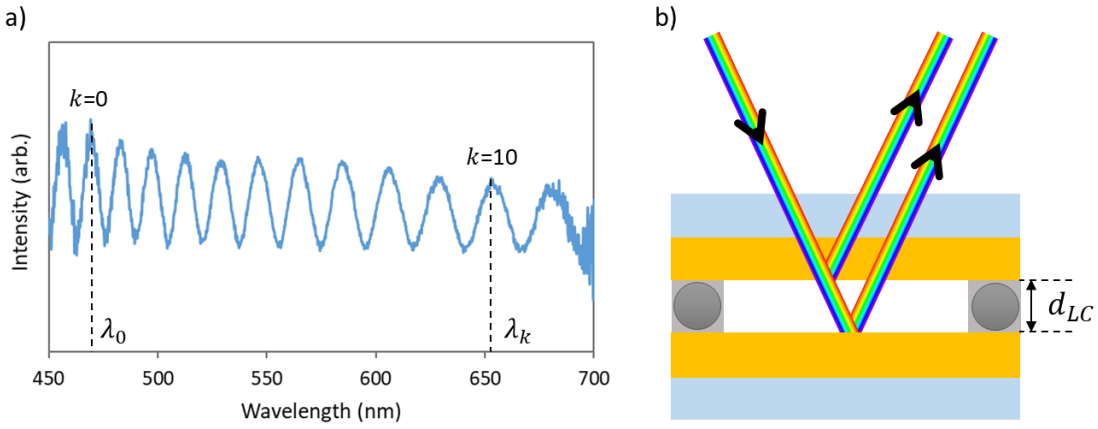

Figure 3-5: (a) Typical reflection spectrum of an empty LC device, with a cell gap (d_{LC}) of ≈8μm. This is used with equation (3-1) to calculate d_{LC}. (b) Approximate illustration of white light incident on an empty LC device, showing the reflected beams from the top and bottom cell surfaces that interfere and produce the intensity minima and maxima in the reflection spectra. (Note: In practice, the light is normally incident on the device but is shown at angles in the diagram to highlight the source of the interference.)

The empty device is placed on a glass microscope slide and the sample height is adjusted until the spacer beads in the glue seal are in focus, ensuring the focal point of the objective lens coincides with the cell cavity. With the microscope in this position, the sample is removed from the beam path and replaced with a reflective slide followed by a black-coated slide to capture bright and dark reference spectra respectively. Returning the device to the beam path results in an output spectrum with oscillating intensity as a function of wavelength, as shown in Figure 3-5a. This oscillation occurs as a result of constructive and destructive interference between the visible light reflecting off the top and bottom surfaces of the cell cavity (Figure 3-5b). The thickness of the cavity dictates the path difference between the two reflected beams, where for a given wavelength (λ), constructive or destructive interference occurs if d_{LC} is a multiple of $\lambda/2$ or $\lambda/4$ respectively. The cell gap is then calculated using the reflection spectra and Equation (3-1),[117,118] where λ_0 is the wavelength of first selected peak, λ_k is the wavelength of the last selected peak and k is the number peaks between the first and last (last inclusive). These measurements are performed in the centre and at the four corners of a device to get an average cell gap, typically with standard errors of ±0.5μm.

$$d_{LC} = \frac{k\lambda_0\lambda_k}{2(\lambda_k - \lambda_0)} \tag{3-1}$$

3.1.3.b Device Filling

Once the cell gap has been measured, the devices are capillary filled with liquid crystal. Besides the work in Chapter 4, where devices are filled with a liquid crystal elastomer precursor, all studied cells are filled with the LC mixture MLC-6204 (Merck, Germany) with physical properties summarized in Table 3-1. This mixture was chosen as its properties have been well characterised [119] and it has previously been applied in homeotropic grating-based devices, similar to those studied throughout this work.[120] Device filling is carried out at 70°C where MLC-6204 is in the isotropic phase, which helps avoid unwanted flow alignment effects that can dominate the alignment if filled in the nematic phase.

Table 3-1: Physical properties of LC the mixture MLC-6204 (Merck, Germany) measured at 589nm. Room temperature data (T=20°C) was sourced from the manufacturer's data sheet and high temperature data (T=40, 63°C) was sourced from reference [119]. *The properties at 63°C or $T/T_{NI} = 0.99$ are given specifically in relation to the temperature study in section 5.4.3.*

Temperature, T (°C)	T/T_{NI}	MLC-6204 ($T_{NI} = 66$°C)				
		n_e	n_o	Δn	k_{11} (pN)	k_{33} (pN)
20	0.87	1.652	1.504	0.148	8	15
40	0.94	1.630	1.503	0.127	6	9
63	0.99	1.595	1.507	0.088	≲3	≲4

3.1.3.c Polarized Optical Microscopy

The optical appearance and alignment properties of filled LC devices are analysed using a polarising optical microscope (Leica DM2700P). The devices are observed in transmission under white light illumination, positioned on a rotating sample stage located between two polarisers with orthogonal polarisation directions. The devices are observed through microscope objective lenses with 10x, 20x and 50x magnification and 10x eyepieces. A Mettler FP92HT hotstage ($\pm$0.1°C) and FP90 controller are used when studying device behaviour above room temperature.

In the absence of a birefringent sample, this crossed polariser arrangement results in no light transmission through the final polariser (analyser). When a birefringent sample such as a LC device is added, with the projection of its optic axis at some angle relative to the crossed polariser orientations, the orthogonal components of the incident linearly polarised light acquire a relative phase difference as they propagate through the sample. This alters the polarisation state exiting the sample, resulting in non-zero transmission through the analyser (Figure 2-3). The transmitted light that is then observed in the microscope eyepieces, has a characteristic colour determined by the thickness of the LC slab (d_{LC}) and the birefringence (Δn) of the LC material. These colours are presented in the Michel-Lévy colour chart shown in Figure 2-4, which is used a semi-quantitative tool for understanding the alignment characteristics within a LC device.

3.1.3.c.i Conoscopy

The standard polarised microscopy approach described above, refers to the use of orthoscopic illumination, where the incident light is perpendicular to the sample plane. Conoscopy is a type of polarised microscopy that utilizes highly convergent light to view birefringent samples, known as conoscopic illumination. It is a longstanding characterisation technique that has been used to classify the optical properties of minerals and crystals,[121] identify three dimensional wavelength-scale periodicities in LC blue phases,[122] observe biaxial order in auxetic LCEs [55] and generally provide detail on the orientation and degree of optical anisotropy in birefringent media.[123]

This optical arrangement is achieved through the addition of a condenser lens between the first polariser and the sample, shown schematically in Figure 3-6. The result is a cone of linearly polarised light incident on the sample, within which the light rays have a range of incident angles on the birefringent medium. The ordinary and extraordinary components of these rays are refracted by different amounts and therefore take different paths through the medium, depending on the refractive index they experience. As these components recombine upon exiting the sample, a variation in polarisation state may be found as a function of cone angle in the now diverging light cone, which is brought in to focus by the microscope objective. This results in an incident-angle-dependent variation in transmission through the analyser, which with the addition of a Bertrand lens between the eyepieces and the objective, images the conoscopic figure which is at the back focal plane of the objective.[123,124]

Conoscopy observations have the benefit of extracting a lot of information about a sample's optical properties in multiple directions, from a single conoscopic figure with high spatial resolution.[125]

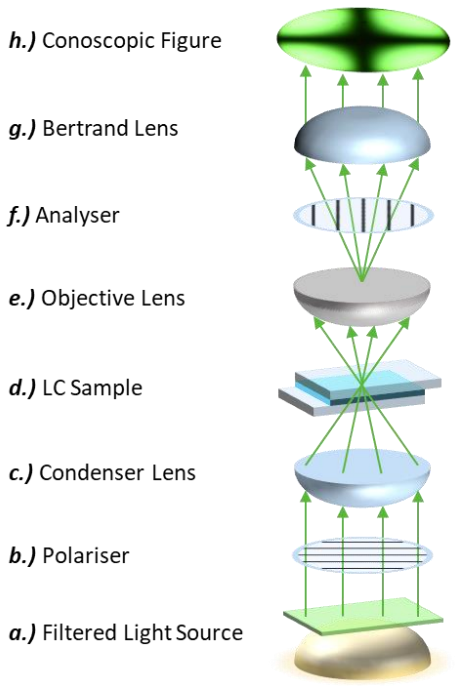

Figure 3-6: Schematic overview of conoscopy setup, highlighting key components in the optical path.

The experimental conoscopy setup utilizes the Leica DM2700P polarizing microscope with a green filter on the white light source, producing broadband green light with a central wavelength λ=533nm and a bandwidth $\Delta\lambda$=52nm (appendix Figure A-1). Samples are placed at the focal point of a condenser lens, with a numerical aperture (NA) of 0.9. Two different microscope objectives are used; a 0.40 NA 20x Leica objective, with a smaller cone angle that gives an enlarged view of the central melatope for identifying marginal isogyre splitting, and a 0.75 NA ULWD 80x Olympus objective, with a wider cone angle for capturing off-centre melatope positions. Conoscopic figures are viewed by inserting a Bertrand lens in the optical path, between the object and the eyepieces. Where angular measurements are taken from the captured conoscopy figures, the back focal plane is calibrated using the diffraction patterns of linear diffraction gratings with well-defined pitch and diffraction angles, using the same conoscopic arrangement used to image the LC devices. This calibration approach is covered in detail in section 6.4.2.b.i and appendix C.3, and has previously been described by Miller and Gleeson.[122]

3.2 Microfabrication

Microfabrication forms the backbone of the experimental work in this thesis. Called upon throughout the following chapters, a select few techniques from its vast toolbox are combined in three distinct workflows, all with the aim of creating textured polyimide LC alignment layers. The three workflows are best distinguished by how the first micropatterned surface or master structure in each is made, and their different levels of precision and complexity. In this section, the shared/more general microfabrication methods used in these workflows are described. The unique aspects of each will be covered in the focused methods sections of the experimental chapters 4−6, to provide a clear origin of the structures in question before exploring their influence on LC alignment.

3.2.1 Master Structures

3.2.1.a Embossing

Commercially available microstructures can often be supplied on a flexible plastic backing, as a result of them being manufactured with roll-to-roll nanoimprint lithography (NIL).[126,127] The aim of this work is to transfer microstructures in to polyimide thin films, which involves contact with strong solvents that would damage a flexible plastic substrate and a copying step that requires structures to be on a rigid backing. As such, commercially-sourced structures on a film backing are transferred in to a UV-curable resin on a glass substrate *via* embossing.[17,128] This approach has been used and documented by multiple researchers [77,129,130] and is represented schematically in Figure 3-7.

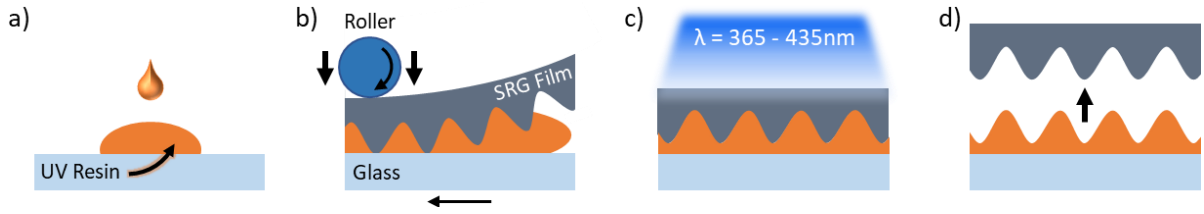

Figure 3-7: Embossing process. (a) UV-curable resin (orange) is drop dispensed on to a glass substrate treated with an adhesion promoter. (b) Microstructured surface relief grating (SRG) film is embossed in to the resin via translation beneath a pressurized roller. Black arrows denote directions of applied pressure and travel. (c) Glass-resin-film stack is exposed to UV illumination to cure the resin. (d) SRG film is peeled away to reveal a resin replica of the SRG on the glass substrate.

The glass backing substrates are first treated with an adhesion promoter solution, comprised of 5 parts dilute acetic acid (1:10, acid:de-ionized water) and 3 parts adhesion promoter (1:200, 3-(Trimethoxysilyl)propyl methacrylate:methanol). Approximately 0.3mL of the solution is dispensed on to the glass, spin coated at 3000rpm for 45s and then dried at 130°C for 60s. 20µL of UV-curable resin (MINS-311RM, Minuta Technology Co.) is then dispensed along the length of the glass substrate and a surface relief gating (SRG) film (1000 lines/mm, Edmund Optics Ltd.) is placed grating-side down on top of the resin and allowed to capillary fill between the glass and the film. This stack is then transferred to a custom embossing machine, where it travels at ≈1mm/s beneath a roller applying a

pressure of 3.5MPa. Once embossed, the resin is then cured for 60s under UV illumination (365 - 435nm) at an intensity of ≈10μW/cm^2. The SRG film is then peeled away from the cured resin, leaving behind a resin copy of the film's grating structure on the glass substrate. The embossed structures are rinsed in acetone to remove any uncured resin and then re-exposed to UV for a further 120s to ensure complete curing.

3.2.2 Soft Lithography

Despite a variety of techniques being used to fabricate the master structures in this thesis, soft lithography is consistently used as the final patterning step for fabricating the micropatterned polyimide alignment layers, forming the basis of the three experimental chapters. Soft lithography is a microfabrication approach pioneered by Whitesides *et al.*,[131,132] revolving around the use of soft elastomeric substrates with micropatterned surfaces, which are used as stamps for pattern transfer *via* deposition or moulding of materials. A range of techniques exist within the area of soft lithography, including: microcontact printing (μCP),[133,134] replica moulding in elastomeric materials,[135,136] UV-assisted imprinting [137] and thermal-assisted imprinting.[138,139]

3.2.2.a Replica Moulding

The first soft lithography process that is used in this work is replica moulding with polydimethylsiloxane (PDMS, Sylgard-184, Dow Corning Inc.), which is a simple and convenient method of creating a soft elastomeric copy of a micropatterned surface (Figure 3-8). PDMS is a silicone-based elastomer that has solidified its place in micro and nanofabrication,[133,140–143] owing to desirable properties such as: low surface energy, high UV transparency, nanoscale moulding capability and biocompatibility.

A PDMS solution is prepared by mixing the prepolymer and cross-linker at a ratio of 10:1, with total volumes ranging from 15 – 50mL depending on the size of the casting vessel. Once thoroughly mixed for around 2 minutes, the PDMS solution is degassed in a vacuum desiccator for 1 hour. This is critical to ensure that all of the air bubbles are removed, as any remaining bubbles will result in defects in the final replica. The micropatterned substrates that are to be copied, are placed at the bottom of a non-stick coated (see section 6.3.3.a) glass petri dish, which forms the casting vessel. The PDMS solution is then slowly cast on top of the substrate until it is completely covered with a PDMS layer ≈1-2mm thicker than the master substrate (Figure 3-8c). Keeping the PDMS thickness in the 1-2mm range results in working stamps that provide more control and better contact during the subsequent imprinting step. The filled vessel is then degassed to remove any bubbles formed during casting and then placed in an 80°C oven overnight (≈16 hours) to thermally cure the PDMS. Once cured, the PDMS slab is carefully demoulded from the master structures and trimmed to form the final PDMS working stamp, removing any raised sections that would prevent uniform contact during imprinting (Figure 3-8d).

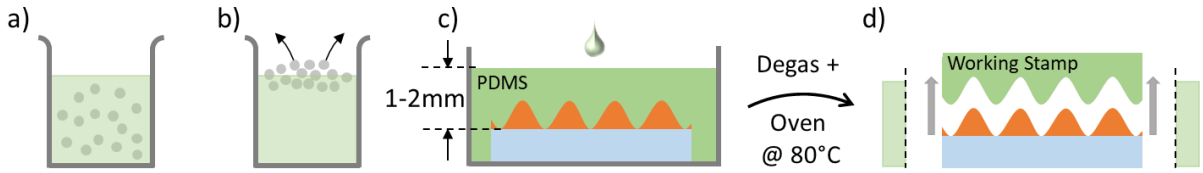

Figure 3-8: PDMS replica moulding process. (a) PDMS prepolymer and crosslinker are thoroughly mixed, forming a homogeneous PDMS solution. (b) Mixture is degassed in a vacuum desiccator, removing air bubbles formed during mixing. (c) Master structures are placed in a non-stick casting vessel and the PDMS mixture is cast on top, to a thickness 1-2mm greater than the substrate thickness. (d) Following degassing and curing at 80°C, the PDMS slab is demoulded from the structures and trimmed to form a working stamp for pattern transfer.

3.2.2.b Imprinted Polyimides

The final soft lithography step involves using PDMS working stamps to transfer micropatterns in to polyimide LC alignment layers. The polyimide imprinting process described in this section, using commercial LC polyimides, offers an accessible and versatile means of creating topographically patterned alignment layers, with the benefit of inherent surface anchoring properties and the ability to process the resulting surfaces with conventional alignment techniques, such as mechanical rubbing. An introduction to this area of soft lithography will first be given, covering the more general microfabrication works that lead to polyimide imprinting being attempted, followed by a summary of polyimide-specific examples to highlight different process variations. Details will also be given on the bespoke imprinting apparatus that was made, along with the adopted methodology.

3.2.2.b.i Background

Relative to the standard polyimide thin film processing described in section 3.1.2, polyimide imprinting is performed as an intermediate step between spin coating (Figure 3-2b) and drying (Figure 3-2c) a polyimide film. The imprinting process begins whilst the film is solvent-rich, directly after spin coating, and is completed as the film dries/solvent evaporates. As such, this approach can be classed as a form of solvent-assisted microcontact moulding (SAMIM); a subcategory of soft lithography developed by Kim *et al.*[144]

The original SAMIM methodology involves wetting a PDMS stamp with a solvent (i.e. using the solvent as an ink) and placing it in conformal contact with an initially solid polymer layer. This partially dissolves the polymer and allows it to flow in to the channels/relief structures on the PDMS stamp, transferring the pattern in to the polymer as it re-solidifies. Photoresists are commonly used as the polymer layer in SAMIM, which has enabled maskless sub-optical photolithography using imprinted structures [145] and the fabrication of thermo-responsive plasmonic surfaces.[146] Rather than wetting the stamp with a solvent, SAMIM has also been demonstrated with dry stamps on freshly spin coated photoresist films, where the high solvent concentration present immediately after spin coating provides a sufficiently fluid layer for pattern transfer.[147] This ‘dry stamp-wet film’ approach was the primary inspiration behind attempting to imprint spin coated layers of polyimide in this work.

Polyimide alignment layers have been patterned *via* imprinting in a variety of ways. Thermal-assisted imprinting has been demonstrated on uncured dry films [148] and custom hybrid polyimide films,[149] both requiring the use of high temperatures (180-200°C) and pressures for pattern transfer. Although these methods avoid the high temperatures needed to overcome the glass transition of cured polyimide (>350°C), the high pressures required would likely cause a soft PDMS stamp to deform, making them unsuitable for this work. Polyimide films have also been imprinted with rigid silicon stamps,[150] which isn't an ideal stamp material for repeated imprinting, easy demoulding and conformal contact; as is offered by an elastomeric working stamp. With a close resemblance to SAMIM, polyimide solutions have been used to as an ink with PDMS stamps, to transfer a pattern *via* imprinting at room temperature.[151] This approach offers greater control by being able to specify the quantity of solution used for each imprint, rather than relying on an unknown amount of residual solvent in a freshly spin coated film.[152] However, this only allows the areas covered by the working stamp to be coated in polyimide, whereas imprinting a spin coated film results in a fully coated substrate with select patterned regions, which can be beneficial for achieving full-substrate alignment, as will be used in Chapter 4.

3.2.2.b.ii Apparatus and Methodology

The imprinting procedure used to fabricate the micropatterned polyimide alignment layers throughout this work, is carried out with the custom imprinting apparatus presented in Figure 3-9 using the workflow illustrated in Figure 3-10.

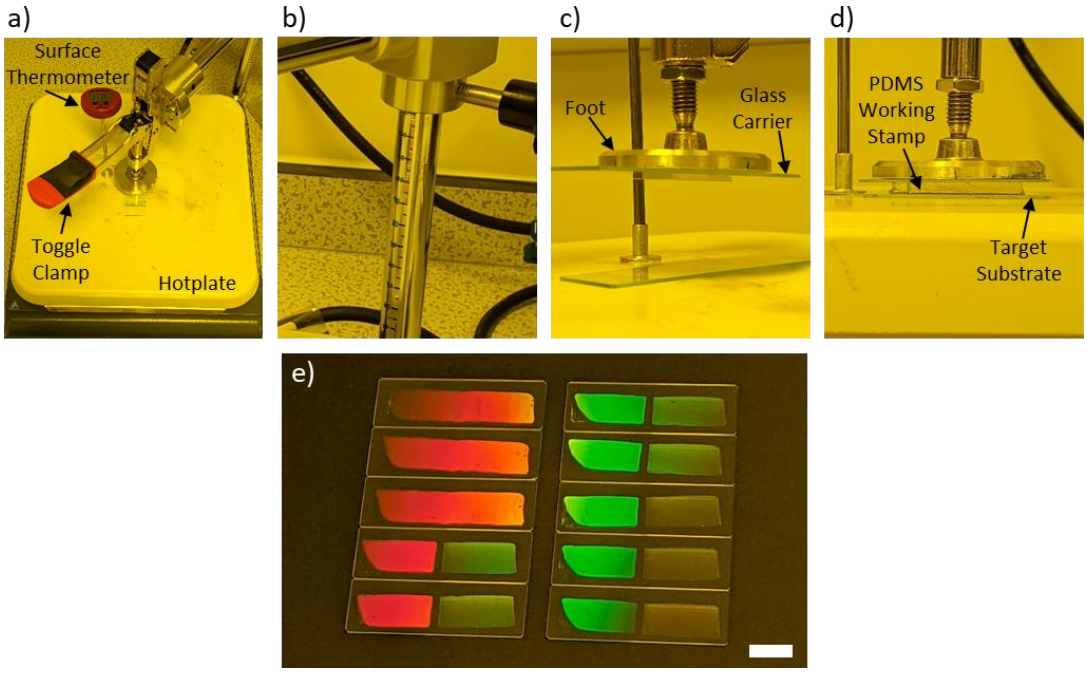

Figure 3-9*: Hotplate press apparatus. (a) Overview showing the hotplate, suspended toggle-clamp assembly and surface thermometer. (b) Support column with millimetre scale, providing a reference point for imprint pressure in the absence of a formal pressure sensor. (c) Foot of the press in its raised position, with glass carrier substrate adhered to the underside for temporary mounting of PDMS working stamps. (d) Foot of the press in its lowered/clamped position during imprinting. (e) Batch of micropatterned polyimide substrates fabricated with the hotplate press. Scale bar = 20mm.*

The imprinting apparatus is a purpose-built attachment for a laboratory hotplate (C-MAG HP 10, IKA®), with the basic function of applying light, sustained pressure to a target substrate at an elevated temperature. Herein referred to as the 'hotplate press', the setup is comprised of a toggle clamp (STC-IHH25, Bessey Tools) suspended above the hotplate, on a vertical support column mounted to the standard M10 accessory thread at the rear of the hotplate (Figure 3-9a). The applied pressure is adjusted by altering the height of the clamp on the support column, using the scribed millimetre scale as a reference point (Figure 3-9b). A glass carrier substrate is adhered to the foot of the hotplate press, allowing PDMS stamps to be temporarily secured during imprinting and easily removed afterwards (Figure 3-9c). A surface thermometer (TPP2-C1, Amprobe®) is placed adjacent to the imprinting location, to ensure the local hotplate temperature is stable and at the desired level prior to imprinting.

The over-center operation of the toggle clamp allows a stamp to be brought in to conformal contact with a target substrate, and a constant pressure to be maintained so as not to disturb the polyimide layer as it dries (Figure 3-9d). Preliminary imprinting attempts carried out by hand, resulted in low quality pattern transfer as a result of the stamp being unstable as the polyimide dried; an issue that was avoided by using the hotplate press. Repeatable, large-area imprints of microscale structures have been successfully achieved using this simple hotplate press, as shown by the small batch of imprinted polyimide substrates in Figure 3-9e.

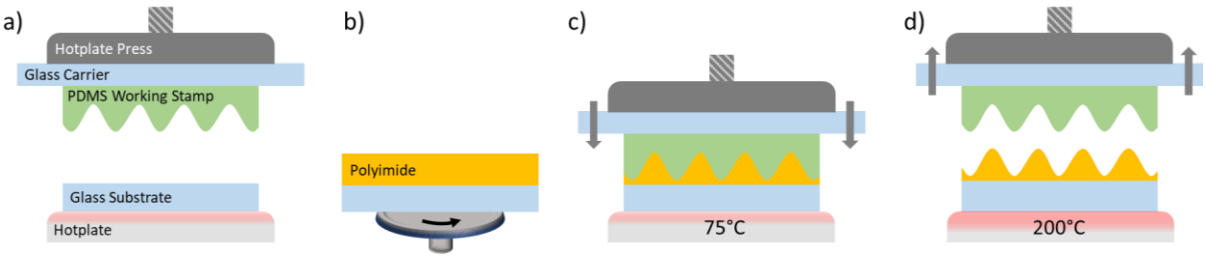

Figure 3-10*: Schematic of the polyimide imprinting process. (a) A PDMS working stamp is secured to the glass carrier of the hotplate press and a test substrate is used to set the imprint pressure. (b) Polyimide film is spin coated with reduced speed and time, then (c) transferred to a 75°C hotplate and immediately imprinted with the hotplate press. (d) Working stamp is demoulded from the polyimide and the micropatterned polyimide film is cured at 200°C.*

The imprinting process starts by attaching the working stamp to the glass carrier of the hotplate press. A substrate with the same thickness as the one to be coated in polyimide, is placed beneath the press to set the height/imprint pressure for the thickness of stamp being used. This is adjusted until the toggle clamp can be latched easily with one finger, and the working stamp is clamped without bulging or deforming (Figure 3-9d). The hotplate is heated up until the surface thermometer reads 75°C, which was found to be the optimal imprinting temperature, where the polyimide didn't dry too quickly and cause poor pattern transfer, or dry too slowly and damage the PDMS stamp due to prolonged solvent exposure.

The target substrate is spin coated with polyimide at 2000rpm for 40s, which is slower and shorter than typical processing to ensure a wet solvent-rich film is produced.[147] Immediately after spinning, the coated substrate is transferred to the pre-heated hotplate and the working stamp is swiftly brought in to conformal contact using the hotplate press. The applied pressure is maintained for 2 minutes and then the press is raised, followed by demoulding of the stamp from the polyimide. The imprinted polyimide substrate is then cured at 200°C for 30 minutes.

3.3 Surface Metrology

3.3.1 Optical Microscopy

Distances are measured from microscope images using a stage micrometre as a reference point (Figure 3-11). The 1mm scale is divided in to 10µm increments, with a tolerance of ±1µm. These scale images are analysed using Image J software (NIH, USA), allowing values of distance per pixel to be obtained for each of the different magnification objective lenses used, and thus scales to be assigned to any captured images. This approach is primarily used to measure larger features (≥5µm) on patterned surfaces or in the optical textures of liquid crystals.

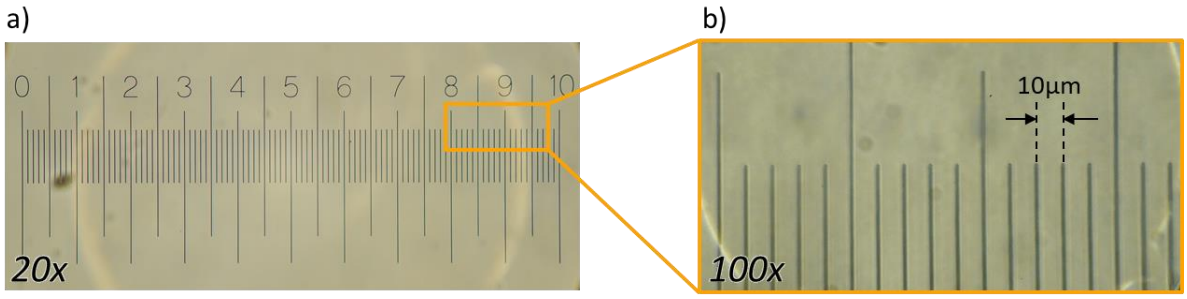

Figure 3-11: Microscope stage micrometre imaged through (a) 20x and (b) 100x magnification objectives, featuring a 1mm scale divided in to 100 minor increments of 10µm.

3.3.2 Optical Diffraction Patterns

A custom optics setup was designed and constructed to observe and measure the optical diffraction patterns created by the transmission of laser light through samples with periodic structures. This non-contact measurement approach enables the periodicity/pitch (d) of a transmissive sample to be inferred from the diffraction pattern created by the incident laser light. Similar transmission diffraction setups have been described and applied in the same manner elsewhere.[9,153,154] An overview of the experimental setup is shown in Figure 3-12a, and is constructed as follows.

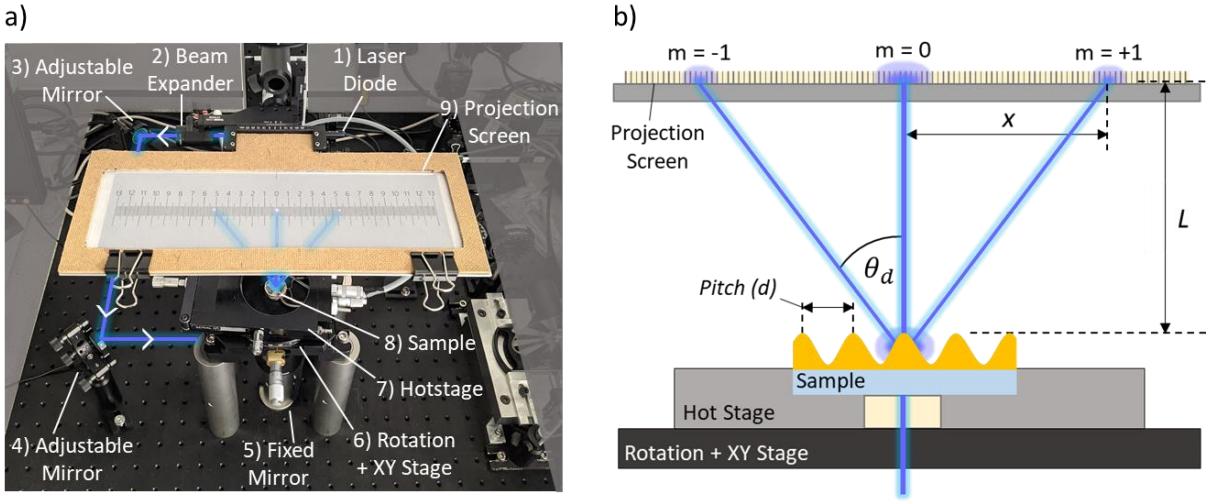

Figure 3-12: Experimental setup used to display optical diffraction patterns and measure a sample's periodicity/pitch. (a) Photograph of the benchtop diffraction setup showing the arrangement of optical components, each labelled 1 through 9 to indicate their order in the beam path, between the λ=404nm laser diode (1) and the projection screen with millimetre scale (9). (b) Schematic cross-section of the setup between the fixed mirror (5) and the projection screen (9). This defines the measured distance between the 0th (m=0) and 1st order (m=$\pm$1) diffraction maxima on the screen (x) and the sample-screen separation (L), which are used to calculate the diffraction angle (θ_d) and pitch (d).

A 0.5mW laser diode with a wavelength (λ) of 404nm (PL205, Thorlabs) is directed parallel to the bench towards a beam expander, reducing the spot size from 3mm to 1.5mm, to make reading the maxima positions off the screen easier (laser spectrum shown in appendix A.2). The beam is then folded by two adjustable mirrors, which are aligned so that the beam hits the following fixed mirror and reflects perpendicular to the bench and therefore at normal incidence to a sample on the rotation stage. This vertical alignment is confirmed by mounting two concentric pinholes, at the top and bottom of the vertical mounting rail, and adjusting the two mirrors until maximum transmission is obtained through the final pinhole.

Samples are placed either directly on the rotation stage or on a Linkam THMS 600 hotstage with a TMS 94 controller when performing temperature studies. The projection screen, featuring a millimetre scale, is suspended above the sample on the vertical rail and is aligned parallel to the bench using a spirit level. A translation mount is used to adjust the scale's lateral position on the rail, such that the central 0th order (m = 0) beam is aligned with the '0' increment on the scale, allowing for simple measurement of the distance between the 0th and 1st order beams (x).The pitch of a structure is extracted by first using the screen scale to measure the distance x ($\pm$0.5mm), between the 0th and 1st order maxima, where an average value is calculated from the m = +1 and m = -1 values.

An average sample-screen separation (L, $\pm$1mm) is obtained from measurements in the center and at the four corners of the screen holder. The diffraction angle (θ_d) is then calculated using these measured values in equation (3-2), which is then substituted in to equation (3-3) with m=1 and λ=404nm to obtain the pitch of the structure (d).

$$\theta_d = \tan^{-1}\left(\frac{x}{L}\right) \tag{3-2}$$

$$m\lambda = d\sin(\theta_d) \tag{3-3}$$

3.3.3 Atomic Force Microscopy

Atomic Force Microscopy (AFM) is a form of scanning probe microscopy, in which the topography of a surface is measured by scanning a nanoscale probe across a surface.[155] AFM measures the forces between a tip and a surface, rather than a tunnelling current as with scanning tunnelling microscopy (STM), which makes it ideal for investigating insulating surfaces, such as the polymer structures in this work. The probe of an AFM is a sharp tip with a radius of the order of 10nm, at the end of a cantilever, which bends in close proximity to a surface due to the intermolecular forces between the surface and the tip. A laser beam is reflected from the top of the cantilever and directed towards a photodetector, which is used to monitor the cantilever's deflection as the tip scans over the surface (Figure 3-13). This measured deflection is used in a feedback loop to maintain a constant force between the tip and the surface, by adjusting the applied potential across the piezo-element that controls the z-height of the scanner and tip. The resulting AFM image is built from the spatial variation of this applied potential as the tip is raster scanned across a sample. This description covers what is known as contact mode AFM, where the tip remains in contact with the surface at all times and the cantilever's deflection is used to create an image.

There are also scanning modes where the tip makes intermittent contact with the surface, such as tapping mode AFM. In tapping mode, whilst the tip remains in close proximity to the surface, the cantilever is oscillated close to its resonant frequency during the scan. The frequency of oscillation varies as a function of the sample's surface topography, which is used as the feedback loop in this mode. The variation in phase and amplitude of this oscillation is measured and then used to construct the final image using this approach. Tapping mode is chosen for the AFM measurements in this work, as it is best suited for soft polymer samples, where contact mode can exert high compressive and lateral forces that can disrupt the sample surface.[156] AFM was performed using TESPA-V2 probes (Bruker, USA) on a Bruker MultiMode® 8-HR, and for larger samples a Veeco Dimension 3100 system.

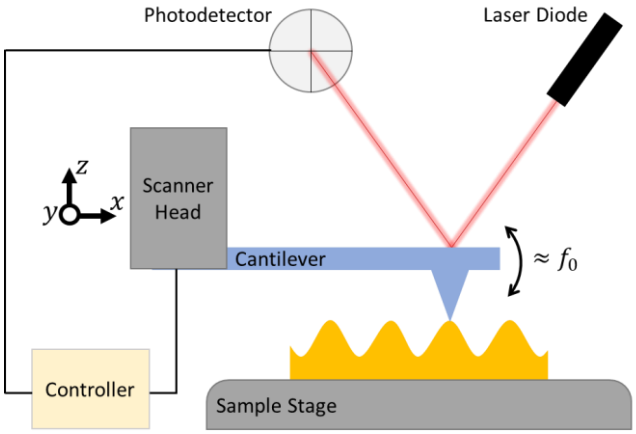

Figure 3-13: Schematic of the key components in an atomic force microscope (AFM). In tapping mode, the cantilever is oscillated close to its resonant frequency (f_0). Raster scan is carried out by piezo x-y translation of the scanner head and the z-height is dictated by the feedback loop from the photodetector signal.

3.3.3.a Image Analysis

AFM images are analysed using Nanoscope Analysis software (v 1.9) and the extracted data are used to measure the pitch (d) and height (h) of micropatterned surfaces. The workflow used to obtain these pitch and height values is summarized in Figure 3-14. First, the cross-section tool in Nanoscope Analysis is used to gather height data in at least five different locations of a given scan. This is done using 'box select' mode, which means the resulting cross-section data is the average of the single line scans within the box selection area, indicated by the white dashed boxes in Figure 3-14a. These have a width of ≈200nm and a length spanning the full image and are used to reduce noise relative to a single line scan, whilst remaining representative of the local topography. The resulting height data (Figure 3-14b) for each selected area is then exported. The data is then imported in to OriginPro graphing software (v 10) and the 'Peak Analyser' tool is used as a consistent method of locating the peaks (P) and valleys (V) of the periodic structure, marked by the vertical red lines on the data in Figure 3-14c. This provides the vertical and lateral positons of each of the peaks and valleys, which are then used in the basic equations shown in Figure 3-14d to calculate the pitch a height of the structure. This process is carried out on each set of exported cross sectional data, across at least 3 AFM scans taken in unique locations of a given sample. The final quoted values of pitch and height are taken as the mean values across all scans of a given sample.

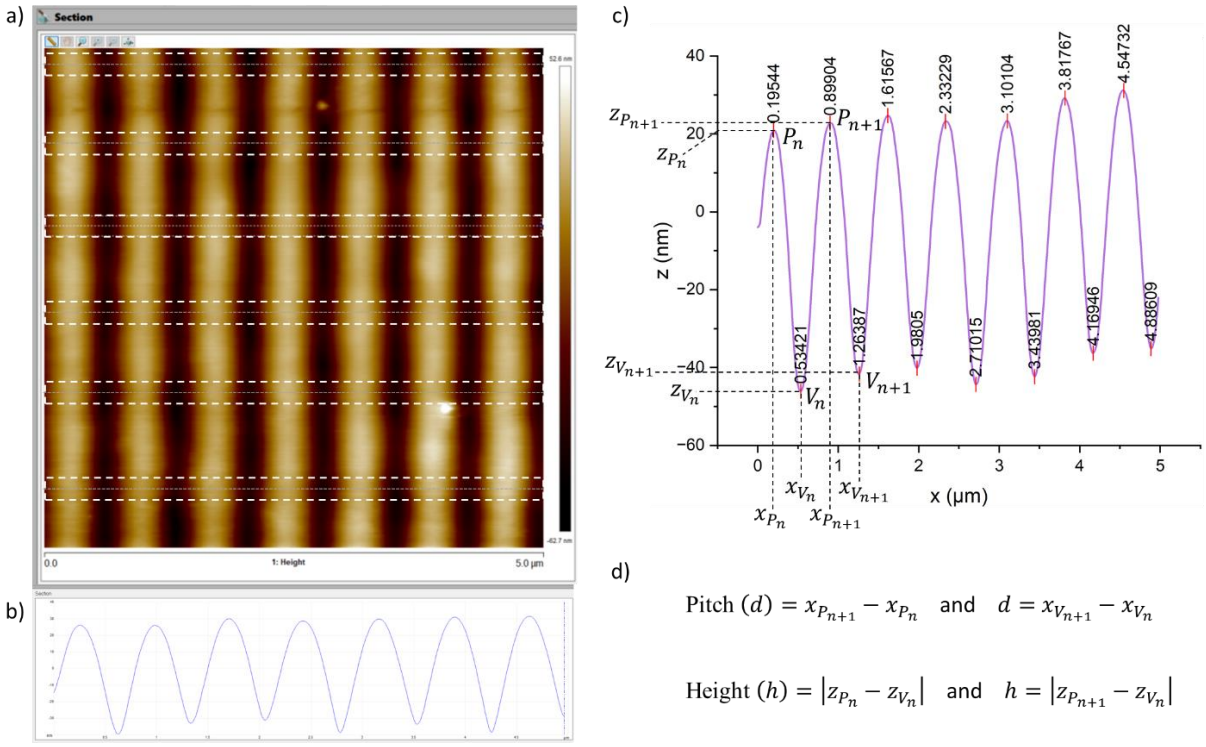

Figure 3-14: Summary of AFM image analysis used to measure the pitch and height of a microstructure. (a) 5x5µm AFM image of a periodic linear surface relief grating. White dashed boxes indicate the multiple areas from which cross-sectional data is exported from a single scan. (b) Example of height data from one of the box selection regions on the AFM image. (c) Height data imported in to OriginPro software with 'Peak Analyser' applied to locate the peaks (P) and valleys (V). Black dashed lines indicate the vertical (z) and lateral (x) positions of the peaks and valleys, with subscripts P and V to identify each respectively. (d) Equations used to calculate the pitch and height of the structure from the values of x and z, where n is the number of peaks and valleys.

3.3.4 Scanning Electron Microscopy

Scanning electron microscopy (SEM) is used to image some of the microscale surface topographies found in this work, in particular the cross sections of surface relief gratings. A Zeiss Leo 1530 SEM is used for imaging, with a field emission gun electron source at an accelerating voltage of 4kV. The sample chamber is kept under vacuum at $\approx 10^{-5}$ Pa, to prevent the incident electron beam being disturbed by gas molecules. The electron beam is raster scanned across the sample area and the resulting secondary and back scattered electrons are detected and used to create an image. Given the deep sub-micron scale features used in this work, images are captured at 105,000x magnification with a field of view of the order of 5µm^2. This imaging approach is chosen over AFM in cases where deep, densely packed structures are encountered, which are notoriously difficult for the tip of an AFM probe to faithfully capture due to unwanted collisions between the structures and the tapered body of the tip, resulting in tip convolution artefacts.[157,158]

3.4 Summary

This chapter has introduced the general experimental methods that are used throughout the subsequent experimental chapters of this thesis. LC device fabrication and characterisation was covered, detailing cell construction, polyimide alignment layer processing, cell gap measurements and polarised microscopy techniques. A summary of the key microfabrication processes used to create micropatterned polyimide alignment layers was also given, covering embossing (UV-NIL), replica moulding (soft lithography) and polyimide imprinting (SAMIM). The polyimide imprinting approach was described in detail, as this is a lesser adopted methodology in LC device fabrication and is relied upon heavily throughout this work. Surface metrology techniques including optical microscopy, diffraction pattern analysis, AFM and SEM were also discussed. Any specialized experimental methods will be introduced in the focused methods sections of the experimental chapters.

Chapter 4 Micropatterned Liquid Crystal Elastomers *via* Surface-Aligned Relief Structures

4.1 Motivation and Overview

As detailed in the previous chapter, soft-lithography enables the transfer of microstructures into polyimide (PI) alignment layers *via* a simple imprinting process. In most liquid crystal device applications, PI layers with planar or homeotropic anchoring are used, both of which can be patterned using the imprinted-polyimide (IPI) methodology detailed in section 3.2.2.b. This chapter focuses on imprinting the planar PI variety, demonstrating how micropatterned planar PI surfaces can be treated with a conventional rubbed alignment process (section 3.1.2.b), to provide uniform alignment of the nematic director, independent of underlying surface topography. This approach is applied as a novel means of fabricating monodomain liquid crystal elastomers (LCEs, section 2.1.4) featuring embedded surface relief gratings. The resulting micropatterned-LCEs (μLCE) are multi-faceted devices applied as diffractive optical elements (DOEs), exhibiting: feature size reduction *via* anisotropic deswelling, thermo-responsive grating pitch and diffraction angle, auxetic growth in feature height under strain and dimensional stability under repeat actuation.

This chapter begins with a general introduction to tunable DOEs and the miniaturization of surface features, followed by an overview of LCEs and their applicability in both areas. The fabrication of topographically patterned LCEs is then presented, where planar IPI grating surfaces serve as both moulds for pattern transfer and alignment layers for uniformly aligning the nematic director. Atomic force microscopy (AFM) and optical diffraction patterns provide an insight in to the μLCE surface topography in both static and dynamic scenarios. The response of these diffractive μLCEs to thermal and mechanical stimuli is explored, shedding light on their broad tunability ranges and the associated impact on diffraction efficiency.

The majority of the work presented in this chapter has been published in T. Moorhouse and T. Raistrick "Sub-micron Diffractive Optical Elements Facilitated by Intrinsic Deswelling of Auxetic Liquid Crystal Elastomers", *Adv. Optical. Mater, 2024, 12, 2400866*. The content of the chapter is therefore a modified reproduction of this publication, where the associated experimental and analytical work was performed collaboratively by the co-authors. Microfabrication of grating structures, surface metrology (AFM), construction of diffraction apparatus and diffraction efficiency measurements were carried out by T. Moorhouse; LCE synthesis and compositional changes, measurement of diffraction patterns under

thermal and mechanical load, phase and thermal behaviour studies (differential scanning calorimetry (DSC), thermogravimetric analysis (TGA)) and device cycle testing (DSC, dynamic mechanical analysis (DMA)) were carried out by T. Raistrick; diffraction efficiency analysis and manuscript preparation was carried out in collaboration with T. Raistrick.

4.2 Introduction

The recent growing interest in elastomeric optical elements, over their solid counterparts, has been driven by an increased demand for device tunability and biocompatibility, and the continued development of flexible electronics and photonics.[159–163] Many optical devices rely on the production of soft DOEs with sub-micrometre features, such as soft grating couplers [164,165] and grating-enhanced solar cells.[166] The phenomenon of responsive 'structural colour', which has far-reaching implications in display devices,[167] chemical-free textile production,[168] and biomedical technology,[169] similarly requires the production of structures with sub-micron periodicity. Here we present an approach which uses the intrinsic deswelling of LCEs to produce sub-micron DOEs with a high degree of tunability and stimuli responsiveness.

Soft lithography offers a lower cost and more accessible means of surface patterning relative to traditional techniques such as photo- and electron beam- lithography, which rely on expensive systems and complex multistep processes.[131,170,171] Miniaturization of surface features with shape-memory polymers has been demonstrated as a feasible approach to sub-micron scale patterning *via* soft lithography.[146,147] Subtractive patterning of shape-memory polymers with dry-etch processes introduces an inherent surface roughness that results in a loss of structural fidelity in a little as one miniaturization cycle.[147] Achieving high-fidelity sub-micron embedded relief structures using this technique is therefore limited without additional steps in the process. Solvent-assisted nanoscale embossing instead uses additive patterning of shape-memory polymers and solvent swelling,[146] providing an alternative miniaturization framework for producing variable nanostructured surfaces.

The use of LCEs provides another layer of tunability to existing miniaturization frameworks, due to their inherent anisotropic deswelling properties [172,173] and stimuli responsiveness (thermal, mechanical, photo and chemical). LCEs are lightly cross-linked polymeric materials containing, typically rod-like, mesogenic units within their network (Figure 4-1). The coupling between liquid crystal order and the macroscopic shape of an LCE leads to stimuli-induced shape actuation.[174] Furthermore, the formation of the LCE network in the presence of a solvent and its subsequent removal results in a controllable anisotropic deswelling of the network.

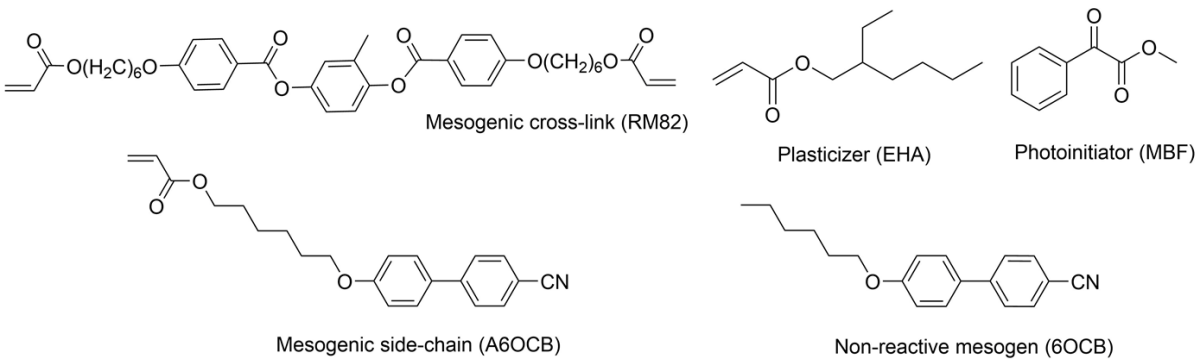

Figure 4-1: Chemical structures of constituent chemicals used in the synthesis of nematic LCEs. The non-reactive mesogen, 6OCB, is removed after polymerization by washing the LCE in a solvent, resulting in anisotropic deswelling.

Intrinsic anisotropic deswelling has been leveraged to produce chiral nematic LCEs with structural colour, by physically restraining the sample whilst deswelling;[173] the simplicity of which allows for easy scalability to industry relevant sizes. In this work, the facile anisotropic deswelling of LCEs is leveraged to produce sub-micron scale DOEs using alignment techniques common and relevant to the liquid crystal display industry. As the alignment of the LCE can be tailored with respect to the grating orientation, the use of nematic LCEs and a nematic solvent allows for responsiveness to be optimized for the desired response, i.e. pitch reduction upon increasing temperature and vice-versa.

Due to their stimuli-responsive nature, LCEs are ideal candidates for sensor applications enabled by their highly-tunable optical and mechanical properties.[163,174–177] LCEs have previously been used to form stimuli-responsive diffraction gratings,[178,179] however these previous reports did not explore the production of gratings on the sub-micron length scale. In these earlier reports, the diffractive effect is induced *via* refractive index modulation across a sample, by exploiting cis-trans isomerization of azo-benzene mesogenic units.[178,179] These refractive index modulated diffractive LCEs show high sensitivity to changes in temperature, but given the micron-scale grating dimensions, the achieved diffraction angles were small, limiting the applicability of these materials. Similarly, Zhang *et al.* recently reported a soft lithographic approach to incorporating a periodic surface topography on an LCE, by imprinting a partially cross-linked LCE gel with a 6.7 micron pitch surface relief grating (SRG).[180] A second cross-linking step was performed under strain to produce a macroscopically aligned, and therefore stimuli shape-responsive, LCE with a 11.7 micron pitch grating. Upon heating to 84°C, the imprinted grating pitch contracted to 7.8 micron (-33%). Whilst Zhang *et al*. demonstrates the stimuli-responsiveness of imprinted LCE gratings, a pitch smaller than the initial SRG was not reported and miniaturization of surface features was not achieved.

In this work, a novel method for realizing LCE DOEs with sub-micron scale features is reported, *via* solvent mediated miniaturization. The use of an IPI grating alignment layer as a mould, allows for conventional rubbed alignment to be applied to the grating structures, overriding their inherent topographic influence on the director orientation.[83] This rubbed grating technique, used previously

for characterizing polyimide anchoring strengths in low molar mass liquid crystal devices, is applied to LCE device fabrication for the first time, allowing the swollen LCEs to be formed with an arbitrary director alignment relative to the grating orientation (outlined in Figure 4-2).

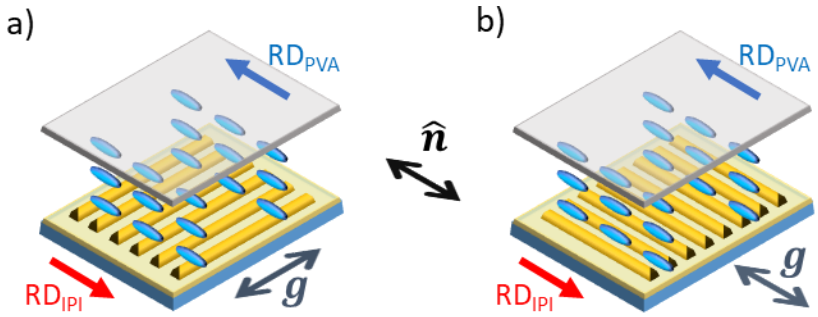

Figure 4-2: Illustration highlighting how the nematic director orientation ($\hat{\boldsymbol{n}}$) is defined arbitrarily with respect to the groove direction ($\boldsymbol{g}$) of an underlying IPI grating. Configurations with (a) the director perpendicular to $\boldsymbol{g}$ and (b) the director parallel to $\boldsymbol{g}$ are shown, indicating the IPI and Polyvinyl alcohol (PVA) alignment layer rubbing directions (RD_{IPI}, RD_{PVA}) on the opposing cell substrates.

By using a class of all-acrylate LCEs, synthesized in the presence of non-reactive liquid crystalline components, an inherently swollen network is produced upon polymerization [57,181] (chemical components shown in Figure 4-1). Removal of the non-reactive liquid crystalline component causes a controllable anisotropic deswelling of the network, enabling the miniaturization of surface features. The LCEs used here are unique as they deform *via* a "mechanical Fréedericksz transition" and display a negative Poisson ratio (or "auxetic") response under mechanical deformation.[55,61,181] Using atomic force microscopy (AFM), an auxetic response was measured in the height of the grating structures on the LCE i.e. the grating height increases as the films are subjected to tensile strains. Thus, these LCEs may overcome the diffraction efficiency losses associated with surface feature height reduction under strain, which is a fundamental issue with elastomeric DOEs.[170,182] Other more conventional LCEs deform *via* a different mechanism, known as semi-soft elasticity, characterized by the appearance of 'stripe domains'. This involves counter-rotating domains that strongly scatter light [58,183] and thus limits their applications as stretchable DOEs. By comparison, the all-acrylate LCEs in this work, which deform *via* the so-called mechanical Fréedericksz transition, remain optically clear under strain and with affine deformations.[57] Here it is demonstrated that the imprinted LCEs have a pitch tunability of 1110nm over a strain range of 157%, making them ideal candidates for mechanical beam steering applications.

In addition to their response under strain, the all-acrylate LCEs display a highly super-critical response to temperature, displaying near-linear changes in birefringence upon heating when compared to the highly non-linear response of conventional semi-soft elastic LCEs.[57,184] The temperature-responsiveness of the LCEs is demonstrated through a +211 or -322nm change in grating pitch (depending on director orientation with respect to grating grooves), over a temperature range of 215°C.

This report is therefore the first demonstration of sub-micron DOEs produced using LCEs with a high degree of chemical, thermal, and mechanical tunability.

4.3 Methods

4.3.1 Fabrication of Imprinted Polyimide Grating Moulds

A commercially sourced, linear SRG film (1000 lines/mm, Edmund Optics Ltd.) serves as the master structure for fabricating the μLCEs, which is transferred on to a glass backing substrate *via* embossing (covered in section 3.2.1.a). The methodology of transferring from film to imprinted polyimide is outlined in Figure 4-3**.** Polydimethylsiloxane (Sylgard-184, Dow Corning Inc.) with a 10:1 prepolymer-crosslinker ratio is cast and thermally cured upon the embossed SRG, forming a soft working stamp after demoulding. A planar polyimide (SE-130, Nissan Chemical) is spin coated at 2000rpm for 45s, imprinted with the working stamp at 75°C for 2 minutes and baked at 200°C for 30 minutes, forming an IPI grating alignment layer. Mechanical rubbing with a cotton rubbing cloth, defines the preferential azimuthal director orientation of the IPI layers (RD_{IPI}) coated on glass, and the PVA layers (RD_{PVA} - Polyvinyl alcohol, MW=13,000, Sigma Aldrich) coated on Melinex® 401 films (DuPont Teijin).

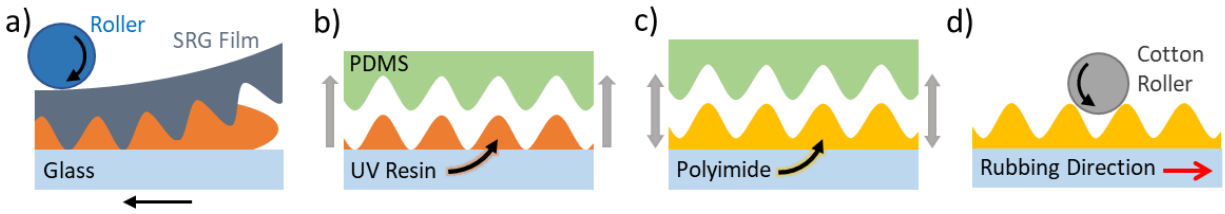

Figure 4-3: Schematic representation of the key stages in the microfabrication process of IPI grating moulds. (a) A linear surface relief grating (SRG) film is embossed in to a UV-curable resin on a glass backing substrate. (b) A polydimethylsiloxane (PDMS) replica is taken of the embossed SRG, forming a soft working stamp for pattern transfer. (c) A spin coated layer of planar polyimide is imprinted with the PDMS working stamp. (d) The imprinted polyimide (IPI) surface is mechanically rubbed with a cotton roller, with a rubbing direction (RD_{IPI}).

4.3.2 Micropatterned LCE Fabrication

4.3.2.a Cell Geometry

The cell geometry used to fabricate the μLCEs is shown in Figure 4-4. To ensure that samples are chemically identical when comparing how grating orientation affects the final devices, the cell is constructed from a single IPI surface with two mutually-orthogonal grating regions (Figure 4-4a). This surface is homogeneously rubbed to define a global, uniform director orientation across the whole surface (RD_{IPI}). A comparison between the resulting director alignment due to rubbed and unrubbed versions of these IPI grating surfaces is presented in appendix section B.1, confirming that the rubbed alignment dominates [83] over any potential alignment influence from the IPI grating topography.[74]

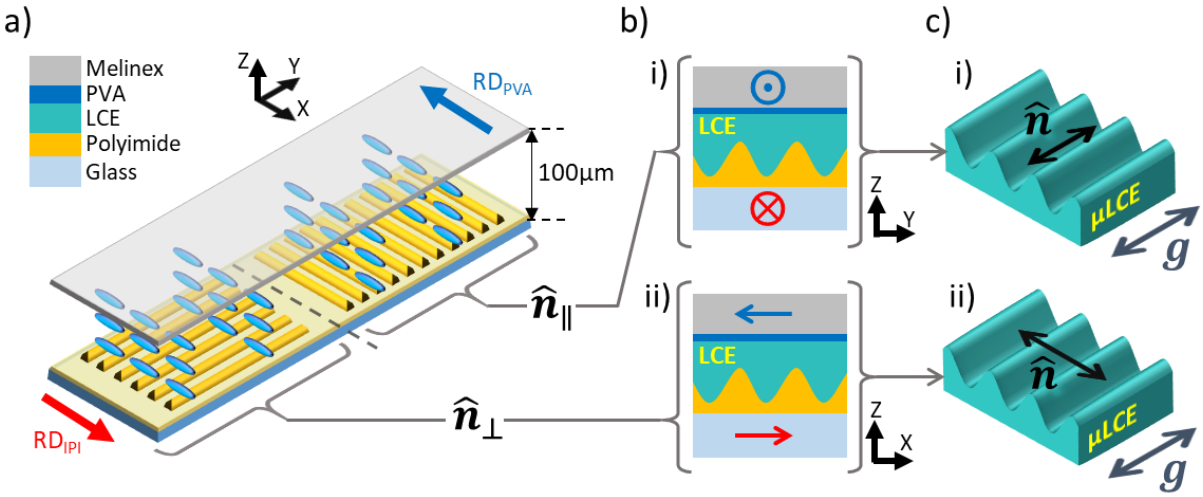

Figure 4-4: Summary of the cell geometry used to fabricate nematic µLCE devices and the two resulting µLCE varieties. (a) Schematic of the parallel-plate cell geometry used as a mould for the µLCEs, featuring an IPI surface (yellow) with two mutually-orthogonal grating regions. A global rubbing direction is applied to the IPI surface (RD_{IPI}), to form a single µLCE film with discrete regions where the nematic director ($\hat{\boldsymbol{n}}$) is aligned parallel ($\hat{\boldsymbol{n}}_{\parallel}$) or perpendicular ($\hat{\boldsymbol{n}}_{\perp}$) to the grating grooves ($\boldsymbol{g}$). (b) Filled cell cross-sections of (i) $\hat{\boldsymbol{n}}_{\parallel}$ and (ii) $\hat{\boldsymbol{n}}_{\perp}$ regions. (c) Schematic representations of (i) $\hat{\boldsymbol{n}}_{\parallel}$ and (ii) $\hat{\boldsymbol{n}}_{\perp}$ µLCE films, emphasizing the relative of orientations of $\hat{\boldsymbol{n}}$ and $\boldsymbol{g}$ in each variety.

4.3.2.b LCE Synthesis

Using the cells detailed in the previous section, LCEs are synthesized using the method described previously.[55,61] The constituent chemicals of the LCEs are shown in Figure 4-1 and the mol % of the chemicals are shown in Table 4-1. 6-(4-cyano-biphenyl-4'-yloxy)hexyl acrylate (A6OCB) is a monofunctional reactive mesogenic, 1,4-bis-[4-(6-acryloyloxyhexyloxy)benzoyloxy]-2methylbenzene (RM82) is a mesogenic crosslinker, 2-ethylhexyl acrylate (EHA) is a monofunctional plasticizer, methyl benzoylformate (MBF) is a UV-photoinitiator, and 4'-hexyloxy-4-cyanobiphenyl (6OCB) is a nonreactive mesogen which is added to broaden the nematic phase of the precursor mixture and produces a swollen LCE network. The 100µm thick cell cavity (Figure 4-4a) is capillary filled with the LCE precursor mixture and left to align for 20 minutes. The filled cell is irradiated with 370nm UV light at 15mW/cm^2 for 2 hours to ensure complete polymerization. To form LCEs in the nematic phase, the UV polymerization step is performed at room temperature. A chemically identical isotropic LCE is synthesized using the 'LCE-2' composition in Table 4-1**,** by performing the polymerization step at 60°C, which is above the nematic-to-isotropic transition of the monomer mixture (37.1°C *via* DSC, appendix Figure B-2a), as described previously.[175,185]

After curing, the cells are deconstructed by carefully peeling the flexible Melinex substrate away using a scalpel. The spacers are then removed from the cell and the swollen LCE is removed from the glass slide using flat-tipped tweezers. In its swollen state, the LCE is washed with a 70:30 methanol:dichloromethane solution. First the swollen film is submerged in a petri dish filled with methanol. Dichloromethane is slowly added step-wise until a 30% concentration is reached. The LCE

is left in the methanol:dichloromethane solution for 24 hours to remove the 6OCB. After 24 hours the LCE films are removed from the solution and dried for 4 hours at 40°C in a fume hood, to remove the excess methanol:dichloromethane solution.[175]

Table 4-1: Chemical compositions of LCEs used in this work. Composition LCE-2, marked with an asterisk (*), is the primary composition used in the majority of the work presented. The far right-hand column shows the composition of a final LCE film (post-wash), which started with the LCE-2 composition initially (pre-wash). Compositions 1, 3 and 4 are solely used in section 4.4.2.c, for investigating how the chemical composition of the LCE impacts deswelling.

Chemical name	LCE-1 (mol%)	LCE-2 (*) (mol%)	LCE-3 (mol%)	LCE-4 (mol%)	LCE-2(*) Final film (post wash) (mol%)
RM82	4.2	3.5	2.8	2.3	8.0
A6OCB	29.2	24.4	19.2	15.8	55.6
6OCB	45.7	54.6	64.4	70.7	-
EHA	19.1	16.0	12.5	10.3	36.4
MBF	1.8	1.5	1.1	0.9	-

4.3.3 Actuation of Micropatterned LCEs

4.3.3.a Thermal

The thermal response of the μLCEs is investigated through their application as transmission diffraction gratings, and using the resulting diffraction patterns as a means of optically tracking the microscopic changes in surface topography. A Linkam hot stage (THMS 600, ±0.1°C) and controller (TMS 94) are used to adjust the temperature of the samples, where small sections of each μLCE variety (≈15 x 5mm, L x W) are placed grating-side up on a glass coverslip, on top of the hot stage heating element. The experimental setup, as shown in Figure 4-5, is comprised of a 404nm wavelength (λ), 0.5mW laser shone upon the μLCEs at normal incidence, with a spot size of 1.5 mm. The diffraction patterns are projected on to a screen with a millimetre scale. Direct measurement of the distance (x), between zeroth ($m = 0$) and first ($m = \pm 1$) order diffraction modes, along with the sample-screen separation (L), allows the diffraction angle (θ_d) and thus the grating pitch/period (d) to be calculated using equations (4-1) and (4-2).[186]

$$m\lambda = d\sin(\theta_d) \tag{4-1}$$

$$\theta_d = \tan^{-1}\left(\frac{x}{L}\right) \tag{4-2}$$

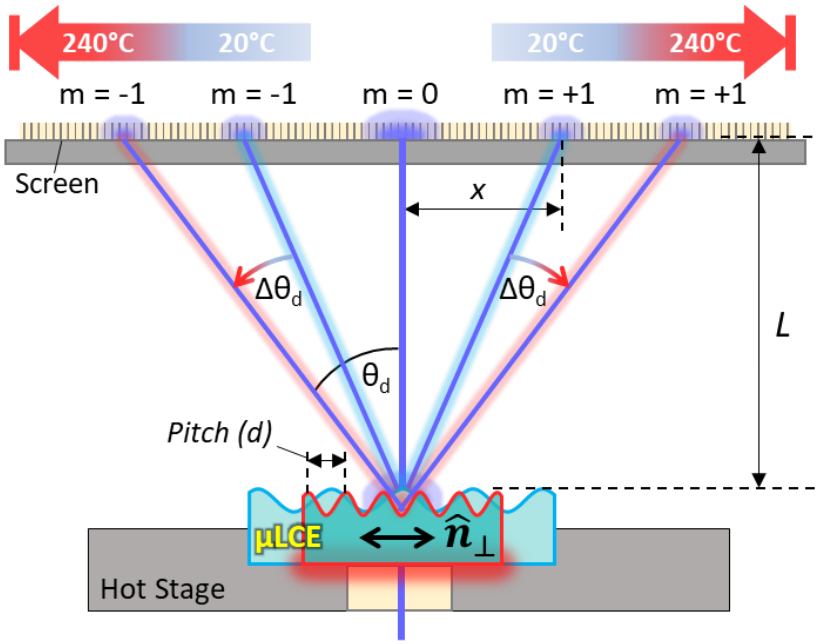

Figure 4-5: Schematic of the experimental setup used to measure the thermal response of the μLCEs and the associated change in diffraction angle ($\Delta\theta_d$). Pitch (d) is inferred from the diffraction patterns of λ=404nm laser light, on a screen L = 118 ± 2mm away from the μLCEs. The lateral distance between m=0 and m=1 diffraction orders (x), is measured using the millimetre scale on the screen, allowing the diffraction angle (θ_d) and grating pitch to be calculated using Equations (4-1) and (4-2).

4.3.3.b Mechanical Strain

The μLCEs are subjected to uniaxial tensile strain to probe how the grating dimensions respond to mechanical deformation. This is measured optically using the same diffraction setup shown in Figure 4-5, with the hot stage removed and the μLCE mounted in a bespoke strain rig (Figure 4-6). The change in diffraction angle (θ_d) is measured as a function of applied strain (ε) and the grating pitch (d) is calculated as described in 4.3.3.a. The initial length of the sample (L_0) and the strained length (L_S) are measured with digital callipers (±0.02mm), from which the applied strain is then calculated ($\varepsilon = (L_S - L_0)/L_0$).

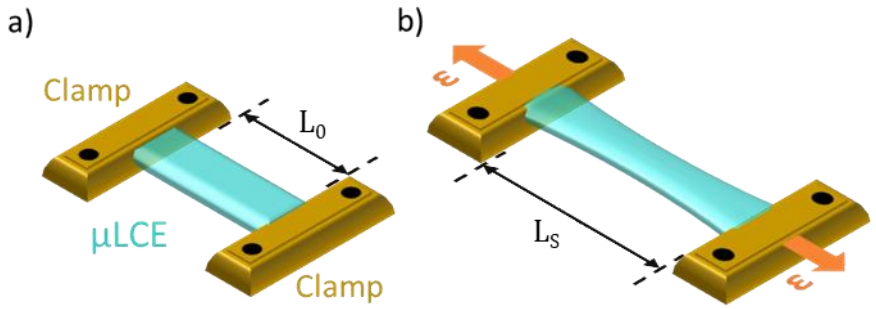

Figure 4-6: Schematic representation of uniaxial tensile strain being applied to a μLCE film. (a) Both ends of a rectangular section of μLCE film (≈15 x 5mm), are secured in a bespoke strain rig using clamps. The sample is pulled taut and the initial clamp separation/sample length (L_0) is measured. (b) Strain (ε) is incrementally applied by moving the clamps in opposite directions via a fine thread adjustment, followed by measuring the strained sample length (L_S) to calculate the applied strain.

4.4 Results and Discussion

4.4.1 Appearance and Alignment of µLCE Films

A macroscopic perspective of the final µLCE films is now presented. These visual observations help communicate the length-scale on which the fabrication method has been applied, and provides insight into the quality and uniformity of the resulting microstructures and alignment. The photographs in Figure 4-7 show the appearance of a µLCE film fabricated as described in sections 4.3.1 and 4.3.2, in ambient white light (Figure 4-7a) and between crossed polarisers (Figure 4-7b).

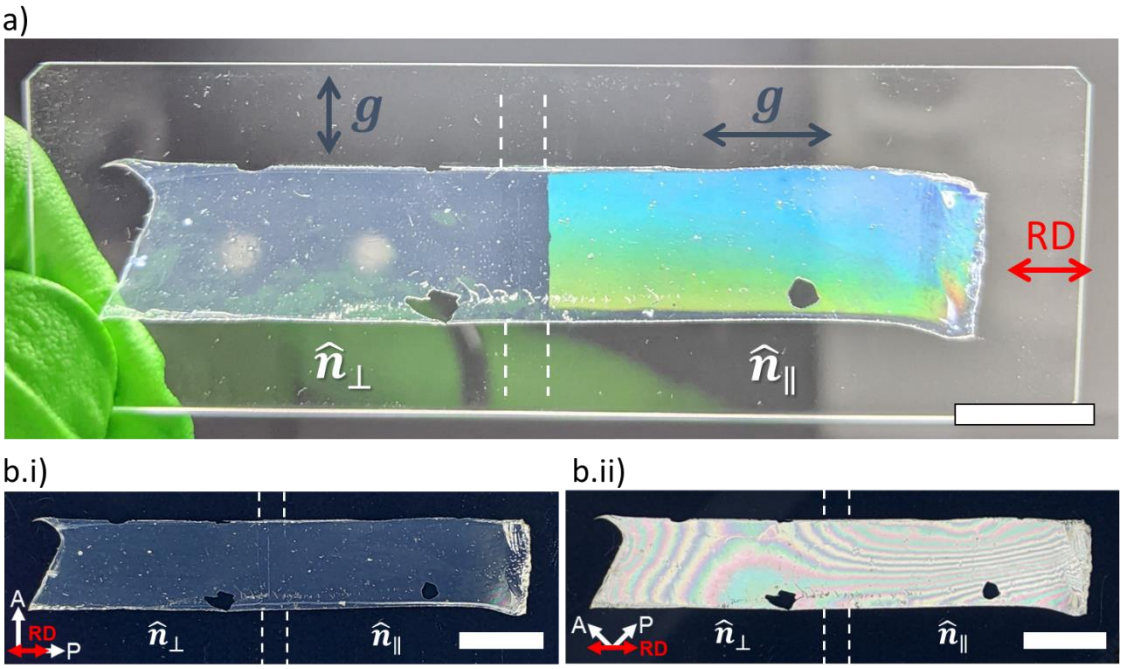

Figure 4-7: Photographs of a full µLCE film fabricated using the IPI cell geometry detailed in section 4.3.2.a. (a) Film placed on a glass microscope slide in ambient white light illumination, highlighting the mutually-orthogonal grating regions ($\hat{\boldsymbol{n}}_\parallel$ and $\hat{\boldsymbol{n}}_\perp$) present on the same film (blue arrows indicate grating groove directions, $\boldsymbol{g}$). Vibrant structural colour can be seen in the $\hat{\boldsymbol{n}}_\parallel$ region, due to diffracted light from this grating orientation. (b) Film imaged between crossed polarisers (P, A) with the rubbing direction (RD)/nematic director orientation at (i) 0° and ii) 45° to the polarisers. Dashed white lines indicate a 3mm wide strip of the film without any grating structures, separating the two grating regions. Scale bars = 10mm.

The unpolarised image in Figure 4-7a, gives an indication of the film's optical transparency in the $\hat{\boldsymbol{n}}_\perp$ region and intrinsic structural colour in the $\hat{\boldsymbol{n}}_\parallel$ region. This colour is observed due to the wavelength dispersion of white light in the non-zeroth order diffraction modes, caused by the periodic grating structure on the surface of the µLCE.[187] At this angle of observation, the uniformity of this colour along the ≈25mm length of this region, is a good indication of a spatially uniform grating pitch, since the pitch of the grating determines the angle at which a given wavelength is diffracted, as per equation (4-1). The colour change from blue to green over the sample width, is attributed to the film being slightly tilted towards the camera upon imaging. These diffraction-induced colours are strongly dependent on

the light's angle of incidence, the angle of observation and the structure's direction of periodicity.[182] Hence, given that each linear grating region is mutually-orthogonal, simultaneously imaging the colour displayed by each region is non-trivial. Rotating the sample by 90° shows the structural colour of the $\hat{\boldsymbol{n}}_{\perp}$ region (see appendix Figure B-3), confirming the presence of a grating in both areas of the film.

Imaging the film between crossed polarisers shows that the nematic director is homogenously aligned throughout the sample, as indicated by the uniformly extinct appearance in Figure 4-7b.i, where the rubbing direction (RD) is parallel to one of the polarisers (P, A). It is worth noting that uniform extinction is observed for the anti-parallel rubbed cells, regardless of the alignment being defined in the presence of two mutually-orthogonal IPI grating regions, with their own topographic alignment contribution.[74] This implies that the anchoring strength associated with mechanically rubbing the polyimide layer, is sufficient to overcome the anchoring strength of the IPI grating structures. If however, the grating alignment contribution was significant, this would be noticeable in the $\hat{\boldsymbol{n}}_{\perp}$ region of the sample in Figure 4-7b.i, where the grating orientation ($\boldsymbol{g}$) is orthogonal to the antiparallel rubbing directions (RD) of the PI and PVA surfaces. In this case, the azimuthal director orientation would lie at an intermediate angle between $\boldsymbol{g}$ and RD on the PI surface, leading to increased transmission in this region due to induced director twist between the PI and PVA surfaces (as demonstrated in appendix Figure B-1b).[83] Upon rotation, the sample appears bright when the rubbing direction is at 45° to the polarisers, due to the birefringence of the LCE (Figure 4-7b.ii). The observed bands of birefringence colours are an artefact of the screen backlight used to illuminate the samples, which likely features a retardation/compensation film, and are not representative of the μLCE's actual birefringence of approximately 0.15. With this birefringence and a thickness of the order 100μm, the μLCE's associated retardance corresponds to a saturated white colour on the Michel-Lévy chart (Figure 2-4). This is confirmed in appendix Figure B-4, which shows the same μLCE sample imaged between crossed polarisers with an alternative light source, showing a saturated white colour without any colour banding.

4.4.2 Anisotropic Deswelling and Surface Topography

4.4.2.a Original Composition

Fabricating μLCEs using an IPI grating alignment layer, allows for the nematic director orientation ($\hat{\boldsymbol{n}}$) to be aligned at an arbitrary angle with respect to the gratings, *via* a simple rubbing step. Here, the effect of director orientation on the topographic features of the μLCE is demonstrated, by synthesizing two chemically identical (composition LCE-2, Table 4-1) LCE varieties with $\hat{\boldsymbol{n}}$ either parallel ($\hat{\boldsymbol{n}}_{\parallel}$) or perpendicular ($\hat{\boldsymbol{n}}_{\perp}$) to the grooves of the IPI gratings ($\boldsymbol{g}$). Figure 4-8 summarizes the resulting surface topography of the μLCEs after fabrication, measured *via* AFM using a Veeco Dimension 3100 in tapping mode. Accompanying AFM data for the results presented in Figure 4-8**,** can be found in appendix Figure B-5.

The anisotropic nature of the deswelling process causes contrasting reductions in pitch in the $\hat{\boldsymbol{n}}_{\parallel}$ or $\hat{\boldsymbol{n}}_{\perp}$ regions of the µLCEs. In the $\hat{\boldsymbol{n}}_{\parallel}$ case the pitch is reduced by 32% relative to the mould, from 1040nm to 707nm. This significant pitch reduction of 333nm, investigated in detail in the following section, demonstrates the ability for sub-micron pitch surface features to be produced from a micron-scale mould, using the intrinsic anisotropic deswelling of the LCEs (Figure 4-8b,c). In contrast, minimal pitch reduction is observed in the $\hat{\boldsymbol{n}}_{\perp}$case, contracting by only 3% (Figure 4-8c,d). This demonstrates the simplest facet of µLCE tunability, which is controlling the pitch of surface features using the rubbing-defined orientation of $\hat{\boldsymbol{n}}$ relative to $\boldsymbol{g}$; capable of varying the resulting pitch by up to 30%. Rubbing at intermediate angles between parallel and perpendicular to $\boldsymbol{g}$, may offer incremental control over the deswelling, if calibrated and proven robust. In the vertical (height) dimension, a 59% and 48% reduction in grating height (h) is observed in $\hat{\boldsymbol{n}}_{\parallel}$ and $\hat{\boldsymbol{n}}_{\perp}$cases respectively. Both varieties result in surface profiles bearing a close resemblance to that of the IPI moulds used during fabrication, but with an altered grating pitch and height.

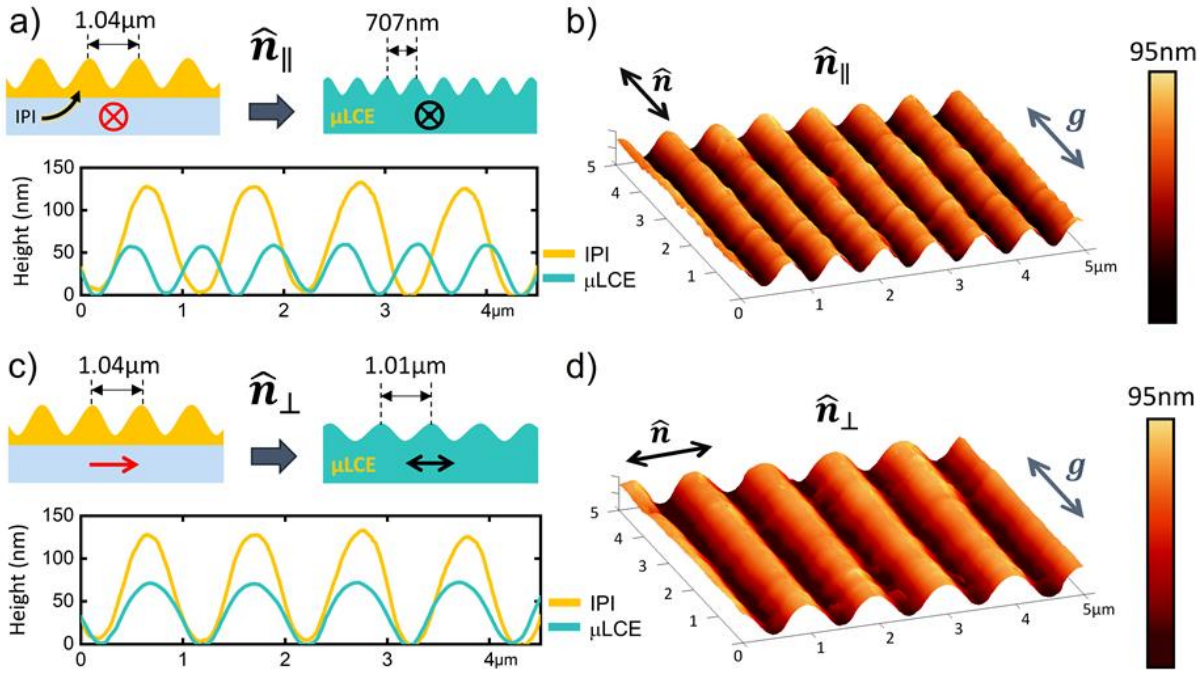

Figure 4-8: AFM surface profilometry of nematic µLCE films at 20°C. The plots in (a) and (c) include AFM surface profiles of the IPI grating moulds (yellow) used during fabrication (pitch = 1040 ± 5nm, height = 130 ± 5nm), to highlight the reduced dimensions of the µLCEs (cyan). (a, b) $\hat{\boldsymbol{n}}_{\parallel}$ µLCE fabricated with the nematic director ($\hat{\boldsymbol{n}}$) aligned parallel to the grating grooves ($\boldsymbol{g}$) (pitch = 707 ± 10 nm, height = 53 ± 3 nm). (c, d) $\hat{\boldsymbol{n}}_{\perp}$ µLCE fabricated with $\hat{\boldsymbol{n}}$ aligned perpendicular to $\boldsymbol{g}$ (pitch = 1010 ± 5 nm, height = 68 ± 3 nm).

4.4.2.b Repeatability of Anisotropic Deswelling

As the µLCEs demonstrate a miniaturization capability *via* deswelling, the repeatability of this deswelling behaviour is an important aspect to investigate; particularly so for further direct application as devices, or intermediate application as substrates for dimensional reduction. To explore the

repeatability, three μLCE films were individually fabricated using the same method detailed in section 4.3.2 and with identical chemical compositions ('LCE-2', see Table 4-1). For each sample, the pitch and height of the resulting $\hat{\boldsymbol{n}}_{\parallel}$ and $\hat{\boldsymbol{n}}_{\perp}$ gratings are measured *via* AFM, and the mean values are extracted *via* the peak analysis workflow detailed in section 3.3.3.a. The results of this repeatability study are presented in Table 4-2.

Table 4-2: Results of AFM topography analysis carried out on three individually fabricated μLCE samples, with identical chemical compositions (LCE-2, see Table 4-1). The mean grating pitch (d) and height (h) in the $\hat{\boldsymbol{n}}_{\parallel}$ and $\hat{\boldsymbol{n}}_{\perp}$ regions of each sample is shown, along with the range of these mean values in nanometres and as a percentage of the values themselves. The pitch and height changes are relative to the dimensions of the IPI grating mould (pitch = 1040 ± 5nm, height = 130 ± 5nm). The number of scans/scan locations refers to the number of 5 x 5μm AFM scans, and associated height profile data, used to calculate each sample mean. Each scan of a given sample is acquired in a unique location within the ≈3cm² area occupied by both $\hat{\boldsymbol{n}}_{\parallel}$ and $\hat{\boldsymbol{n}}_{\perp}$ grating regions.

	Sample No.	Mean pitch, ***d*** (nm)	Pitch reduction (%)	Mean height, ***h*** (nm)	Height reduction (%)	No. scans/ locations
$\hat{\boldsymbol{n}}_{\parallel}$	1	706 ± 10	32	54 ± 2	58	9
	2	716 ± 12	31	62 ± 4	52	3
	3	723 ± 10	30	61 ± 3	53	4
	Range	17nm (2%)	-	8nm (14%)	-	-
$\hat{\boldsymbol{n}}_{\perp}$	1	1007 ± 10	3	67 ± 2	48	3
	2	998 ± 13	4	68 ± 2	48	3
	3	1011 ± 8	3	71 ± 3	45	5
	Range	13nm (1%)	-	4nm (6%)	-	-

The errors in the mean pitch for each sample are 1.3% on average, with a maximum of 2% in the $\hat{\boldsymbol{n}}_{\parallel}$ region of sample 2. This indicates that for a given sample, the grating pitch has good spatial uniformity after deswelling. Between the three individually fabricated samples, the range of mean pitch values in $\hat{\boldsymbol{n}}_{\parallel}$ and $\hat{\boldsymbol{n}}_{\perp}$ grating regions is 17nm and 13nm respectively, which as a percentage of the mean pitch, equates to 2% and 1% respectively. This shows that the deswelling process can reliably reduce the pitch of topographic surface features in the plane of the film, relative to pitch of the IPI moulds, both parallel and perpendicular to the nematic director. This is also reflected in the narrow range of relative pitch reduction observed in each grating region, which serves as a crucial reference point for targeting specific lateral feature sizes after deswelling. The surface feature height shows a significant reduction of ≈50% relative to the moulds upon deswelling. The errors in the mean height are higher on average than the pitch at 4%, with a maximum of 6% in the $\hat{\boldsymbol{n}}_{\parallel}$ region of sample 2, but remain low enough to indicate good spatial uniformity within a given sample. Broader ranges of 14% and 6% are observed between the mean heights of $\hat{\boldsymbol{n}}_{\parallel}$ and $\hat{\boldsymbol{n}}_{\perp}$ grating regions in individual samples.

4.4.2.c Composition-driven Tunability

Alongside director orientation, the concentration of the non-reactive mesogen 6OCB, provides further dimensional tunability by varying the amount of deswelling that occurs upon its removal after polymerization. Four µLCE compositions (outlined in Table 4-1) are produced with varying concentrations of 6OCB content and used to fabricate µLCEs in the $\hat{\boldsymbol{n}}_{\parallel}$ configuration (Figure 4-4c.i). The LCE marked with an asterisk (*) in Table 4-1, is the composition used in section 4.4.2.a and the remainder of this chapter. Figure 4-9 summarizes the surface topography of the resulting µLCEs with varying 6OCB concentrations, measured *via* AFM.

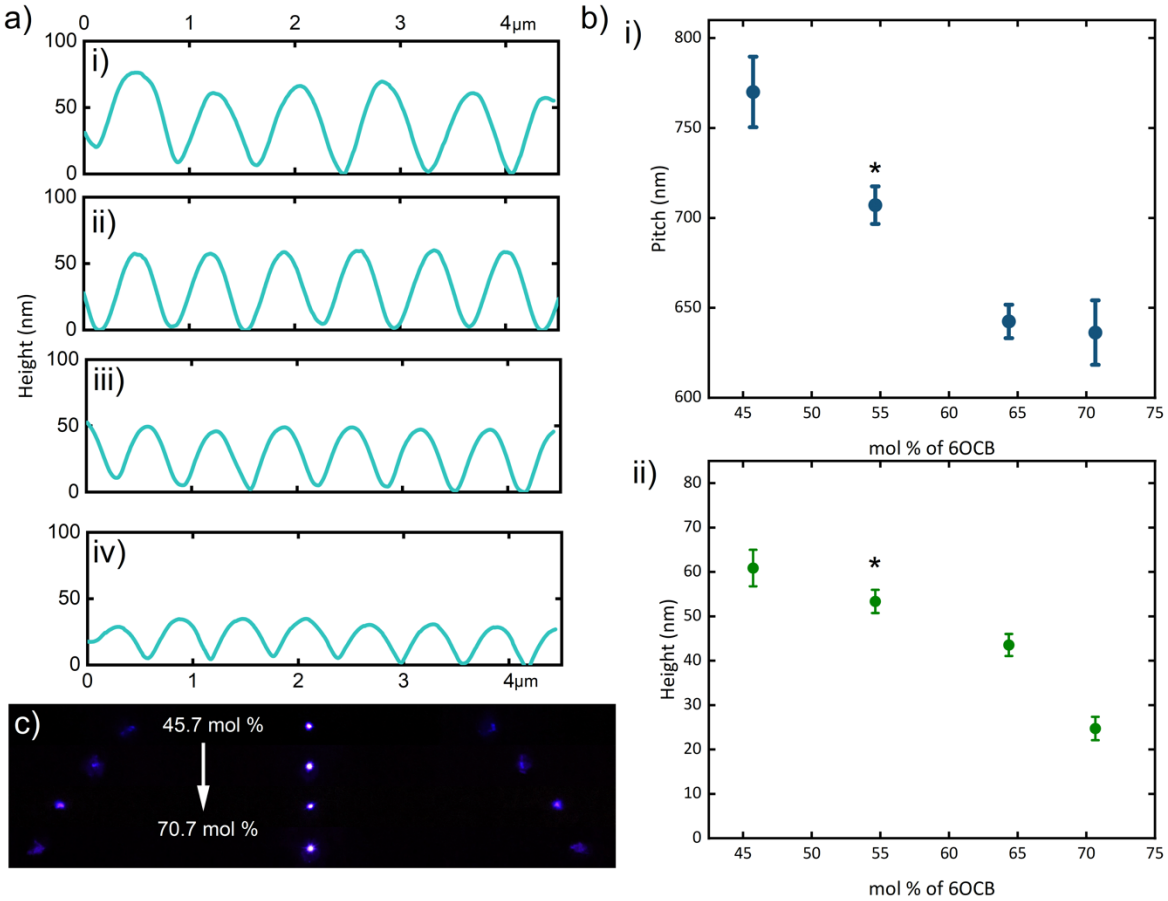

Figure 4-9: Compositional dependence of the dimensions of $\hat{\boldsymbol{n}}_{\parallel}$ µLCEs on the concentration of 6OCB in the LCE precursor mixture. (a) AFM surface profilometry of the $\hat{\boldsymbol{n}}_{\parallel}$ µLCEs with (i) 45.7 mol %, (ii) 54.6 mol %, (iii) 64.4 mol % and (iv) 70.7 mol % of 6OCB. (b) Compositional dependence of (i) pitch and (ii) height on concentration of 6OCB in precursor mixture as measured by AFM. The composition used in the previous and subsequent sections of this chapter is marked with an asterisk. (c) Diffraction patterns of the $\hat{\boldsymbol{n}}_{\parallel}$ µLCEs with increasing 6OCB concentration, from top to bottom.

AFM height profiles of the µLCEs, with varying concentrations of 6OCB are shown in Figure 4-9a. Both the pitch and height of the resulting µLCE gratings display an inverse non-linear relationship with 6OCB concentration (Figure 4-9b), showing that compositional changes impact both lateral and vertical feature dimensions simultaneously.

For example, the 64.4 mol% 6OCB sample has a 38% and 52% *decrease* in pitch and height respectively, whereas the 45.7% 6OCB sample displays a 32% and 65% *decrease* in pitch and height respectively, when compared to the IPI grating mould. The diffraction patterns of the μLCEs for the different compositions are shown in Figure 4-9c.

Previously, anisotropic deswelling has been used to form chiral nematic and smectic LCEs, where a partially cross-linked isotropic gel was synthesized in toluene and mechanical fields are then applied.[172,173,188] During evaporation of the toluene, alignment is achieved by deswelling combined with the final cross-linking step. Here instead, a non-polymerizable nematic component, 6OCB, is used in the LCE precursor mixture. The presence of 6OCB allows for the monomer mixture to be a nematic liquid at room temperature, which means surface alignment can be established prior to polymerization. The aligned LCE precursor produces a monodomain nematic LCE film upon UV irradiation. As such, there is a requirement for the LCE precursor mixture to be sufficiently deep within the nematic phase, to allow for high quality monodomain alignment, and sufficiently far away from the point at which crystallization/solid formation occurs. These two requirements set the range for the amount of 6OCB that can be included in the LCE precursor mixture and the extent of anisotropic deswelling that can be currently achieved.

The nematic-to-isotropic transition temperatures, T_{NI}, of the precursor mixtures were determined *via* differential scanning calorimetry (DSC) on cooling at a rate of 10°C/min. The 45.7 mol% 6OCB precursor mixture has a T_{NI} of 30.4°C whilst the 70.7 mol% 6OCB precursor mixture has a T_{NI} of 49.5°C (appendix Figure B-2b,c). UV polymerization is performed at room temperature (25°C) which is 5.4°C and 24.5°C below T_{NI} for the 45.7 mol% and 70.7 mol% 6OCB precursor mixtures respectively. For the 45.7 mol% 6OCB precursor mixture, the polymerization temperature may not be sufficiently below T_{NI} to allow for the high quality monodomain alignment required for surface features with uniform pitch and amplitude (Figure 4-9a,b) to be achieved. During μLCE production, the LCE precursor mixture is left to surface align for 20 minutes prior to polymerization. The 70.7 mol% 6OCB sample was also found to be spatially inhomogeneous (Figure 4-9b plots the average of the measured pitch values, 664 ± 15 nm and 597 ± 13 nm, for different areas of the 70.7 mol% 6OCB sample). Whilst the 70.7 mol% 6OCB precursor mixture is polymerized deep within the nematic phase, the precursor mixture is prone to phase separation and partial crystallization, as evidenced by a cold-crystallization and melting peak on DSC traces (appendix Figure B-2c). The spatially inhomogeneous pitch observed in the sample with 70.7 mol% 6OCB (Figure 4-9a,b) is therefore attributed to partial crystallization during polymerization. Thus, the nematic-to-isotropic transition temperature and the stability of the precursor mixture limits the range of pitches which are practically attainable *via* anisotropic deswelling.

4.4.3 Thermal Response of µLCEs

The thermal response of the µLCEs is investigated with diffraction angle measurements over a temperature range of 20 - 235°C, using a 404nm laser with a 1.5mm spot size. The $\hat{\boldsymbol{n}}_{\parallel}$ µLCE exhibits pitch expansion upon heating (Figure 4-10a), indicated by a decrease in diffraction angle ($\Delta\theta_d < 0$) of up to 10° over the full temperature range, corresponding to a 212nm increase (+31%) in pitch relative the sample at 20°C. Conversely, the $\hat{\boldsymbol{n}}_{\perp}$ µLCE exhibits pitch contraction upon heating (Figure 4-10b), indicated by an increase in diffraction angle ($\Delta\theta_d > 0$) of up to 14° over the full temperature range, which corresponds to a 322nm reduction (-33%) in pitch relative to the sample at 20°C.

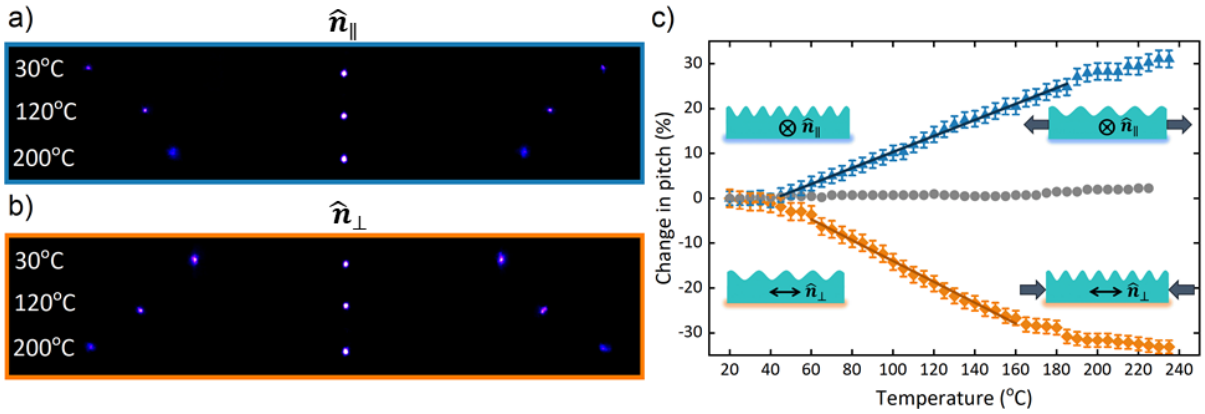

Figure 4-10: Thermal response of $\hat{\boldsymbol{n}}_{\parallel}$ and $\hat{\boldsymbol{n}}_{\perp}$ µLCEs measured via optical diffraction measurements. (a, b) Diffraction patterns showing the opposing thermal responses of $\hat{\boldsymbol{n}}_{\parallel}$ and $\hat{\boldsymbol{n}}_{\perp}$ µLCEs, where (a) $\hat{\boldsymbol{n}}_{\parallel}$ exhibits pitch expansion and (b) $\hat{\boldsymbol{n}}_{\perp}$ exhibits pitch contraction respectively upon heating. (c) The relative thermal change in grating pitch of $\hat{\boldsymbol{n}}_{\parallel}$ (blue triangles) and $\hat{\boldsymbol{n}}_{\perp}$ (orange diamonds) nematic µLCE films determined from diffraction measurements. The grey circles in (c) are the relative thermal changes in pitch for an isotropic sample of the same composition.

The $\hat{\boldsymbol{n}}_{\parallel}$ and $\hat{\boldsymbol{n}}_{\perp}$ µLCEs both exhibit broad, near-linear regimes in their thermal response due to the supercritical nature of this class of LCEs.[57] Figure 4-10c includes linear fits over selected temperature ranges where the response of the µLCEs is most linear; the slopes of which indicate thermal sensitivity. The pitch of the $\hat{\boldsymbol{n}}_{\parallel}$ sample has a thermal sensitivity of 1.2 ± 0.1 nm/°C (taken from a linear fit over 40 – 185°C) whereas the pitch of the $\hat{\boldsymbol{n}}_{\perp}$ sample exhibits a higher thermal sensitivity of -2.2 ± 0.1 nm/°C (taken from a linear fit over 60 – 160 °C). Figure 4-10c also shows data for an isotropic µLCE, which has as an identical chemical composition to its nematic counterpart, but is instead polymerized in the isotropic phase, as described previously.[175] The isotropic µLCE does not shape actuate and has a thermal sensitivity of 0.21 nm/°C, which can be attributed to the general thermal expansion of isotropic materials. This demonstrates the importance of, and uniqueness offered by, anisotropy in the thermal actuation response of the nematic µLCE diffraction gratings.

4.4.4 Strain Response of µLCEs

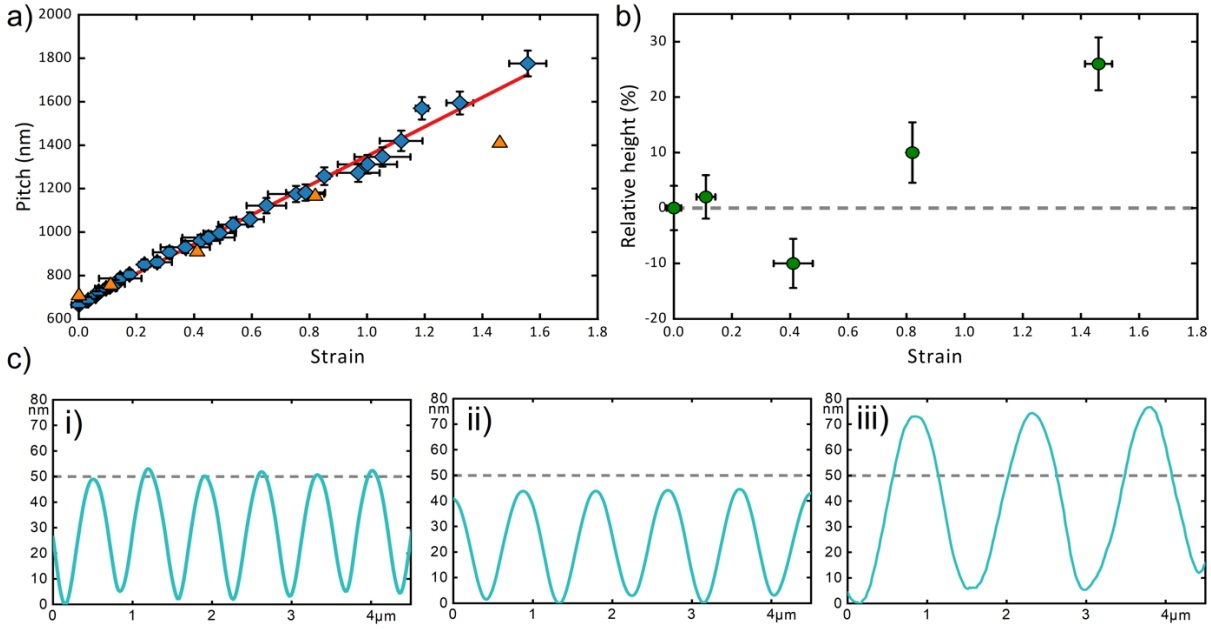

Figure 4-11: Tensile strain testing on $\hat{\boldsymbol{n}}_{\parallel}$ nematic µLCE. (a) Relationship between grating pitch (d) and strain. Pitch measurements are taken using optical diffraction patterns (diamonds) and AFM (triangles). (b) Relative height (h) of the µLCE surface relief grating as a function of applied strain, measured via AFM. Dashed horizontal lines denote the static height (h_0). (c) Cross-sectional line profiles from AFM scans of the µLCE i) at rest, ii) at 41% strain and iii) at 146% strain.

Application of tensile strain changes the macroscopic dimensions of the µLCE and thus the dimensions of the grating structure embedded in the surface. Mechanical tests are performed on the $\hat{\boldsymbol{n}}_{\parallel}$ µLCE with strains applied perpendicular to $\hat{\boldsymbol{n}}$ and $\boldsymbol{g}$. A linear increase in pitch of up to 1110nm (167% as measured by diffraction) is observed as the LCE is stretched by a factor of 156%. The surface topography of the strained µLCE is also characterized *via* AFM, imaged at multiple strain levels over the range tested during diffraction measurements. Figure 4-11a shows good agreement between the pitch values obtained *via* diffraction and AFM.

In contrast to diffraction measurements, AFM enables the grating depth/height (h) to be directly measured. Carrying out AFM measurements under strain, does not allow the typical strain rig (Figure 5-2) to be used, due to restricted space under the AFM scanner head. As such, a manual approach is taken (outlined in appendix Figure B-8) by adhering each end of the µLCE sample to a glass slide using tape, and re-adhering one end of the sample at varying distances from the other to apply tensile strain. This approach also has the added benefit of a solid backing for the film, which helps prevent unwanted movement of the sample during scanning.

The AFM results reveal the consequences of the selected LCE's auxetic nature on the grating dimensions, in the form of nanoscale growth in feature height at large strains. At a moderate 41% strain, h is reduced by 10% relative to the initial unstrained height (h_0) (Figure 4-11c.ii). This reduction in grating height is consistent with the initially positive Poisson's ratio (i.e. non- auxetic) tensile response

of this LCE.[61,181] However, upon further straining to 82% and 146% strain, the feature height increases and exceeds its initial, unstrained height by 10% and 26% respectively (Figure 4-11c.iii). This behaviour is attributed to the onset of the auxetic response (Figure 4-11b). Worth noting is that the measured auxetic growth of 13 nm between 0% and 146% strain, is significantly larger than the ±3 nm error in the average height of the unstrained µLCE, thus the measured effect is not due to spatial variation in feature height but a real phenomenon and manifestation of the bulk material's auxetic response. Curiously, the auxetic response in grating height, measured *via* AFM, exceeds the height of the original grating. This is a distinctly different response to that seen in the bulk dimensions of auxetic LCEs, where the samples never exceed their original thickness.[55,61,181] Therefore this suggests that the auxetic response of the LCE is enhanced at the surface, on the nanometre scale, when compared to the bulk response. The AFM surface profiles plotted in Figure 4-11c emphasize this unique topographic response, showing the linear increase in pitch and non-linear variation in height as the applied strain is increased.

4.4.5 Diffraction Efficiency of µLCEs

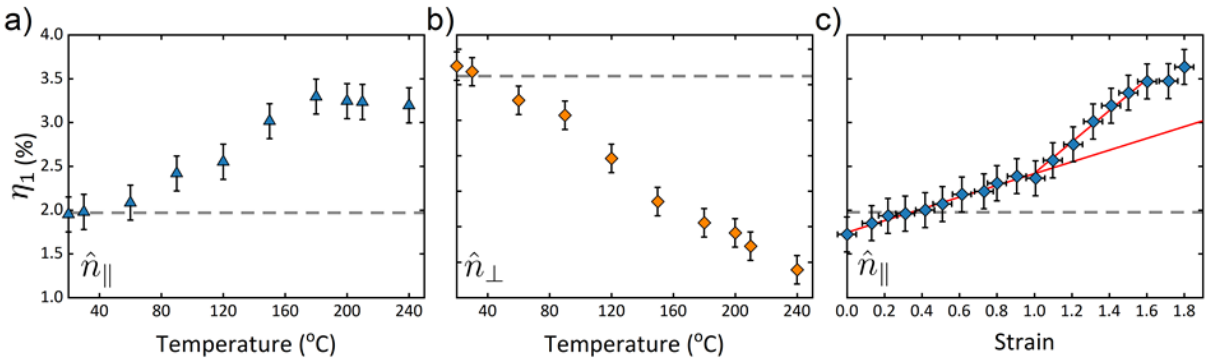

Figure 4-12: First order diffraction efficiency (η_1) of the µLCEs under various conditions. (a, b) $\boldsymbol{n}_{\parallel}$ and $\boldsymbol{n}_{\perp}$ µLCE upon heating, (c) $\boldsymbol{n}_{\parallel}$ µLCE under strain. The grey dotted line is the theoretical predicted efficiency for the given grating depth and laser wavelength.

The first order diffraction efficiency of the µLCEs is investigated under heating and applied strain. To do this, the associated powers of the zeroth (P_{0th}) and first order (P_{1st}) diffraction modes are measured at various temperatures and strains, using a Thorlabs PM100D power meter with a S120VC sensor. The experimental first order diffraction efficiency (η_1) is then calculated using Equation (4-3).

$$\eta_1(\%) = \frac{P_{1st}}{P_{0th} + P_{1st}} * 100 \tag{4-3}$$

The measured thermal and strain response of η_1 is shown in Figure 4-12. The grey dashed line on each subfigure is the theoretically predicted first order efficiency (η_1) for a sinusoidal grating profile, described by Meshalkin *et al.*[189] and provided in Equation (4-4**)** and (4-5), where $\Delta\varphi$ is the phase difference, h is the grating depth and n_{avg} is the average refractive index of the material.

$$\Delta\varphi = \frac{2\pi}{\lambda}\left(h\left(n_{avg} - 1\right)\right) \tag{4-4}$$

$$\eta_1 = \frac{4}{\pi^2}\sin^2\left(\frac{\pi}{2}\right)\sin^2(\Delta\varphi) \tag{4-5}$$

Given that the nematic µLCEs are birefringent materials, circularly polarized light was used during these experiments to allow the refractive index of the µLCEs to be approximated as a single, average refractive index (n_{avg}), with a value of 1.57 [190] in the theoretical prediction. The agreement between theoretical predictions and measured values of η_1 for the un-actuated samples, as indicated by the grey dashed lines in Figure 4-12, validates this approach. The measured diffraction efficiency is comparable to the previously reported diffraction efficiency of refractive index modulated diffraction gratings on LCEs (0.7% at room temperature, 1.2% peak efficiency).[178]

The diffraction efficiency upon heating of the $\boldsymbol{n}_{\parallel}$ and $\boldsymbol{n}_{\perp}$ µLCE is shown in Figure 4-12a and Figure 4-12b respectively, where either an increase ($\boldsymbol{n}_{\parallel}$) or decrease ($\boldsymbol{n}_{\perp}$) in diffraction efficiency is observed. The result can be understood due to the changes in pitch observed in Figure 4-10**.** Very low modulation gratings have a peak efficiency at a wavelength $\lambda_\Delta = 3.4 \times \alpha d$ where $\alpha = h/d$ is the modulation, h is the grating depth and d is the groove spacing.[186] Substituting values into this, λ_Δ is 180 nm and 231 nm for the $\boldsymbol{n}_{\parallel}$ and $\boldsymbol{n}_{\perp}$ µLCE respectively at room temperature. The diffraction efficiency measurements are performed using a 404 nm laser. Upon heating, the pitch increases for $\boldsymbol{n}_{\parallel}$, and therefore λ_Δ shifts closer towards 404 nm and an *increase* in efficiency is observed. Conversely, the pitch *decreases* for $\boldsymbol{n}_{\perp}$, and λ_Δ shifts away from 404 nm and a *decrease* in efficiency is observed. It is noteworthy that this is an optically anisotropic system and that the diffraction efficiency also depends on refractive index, which in this case would be accessed by the two constituent linear modes of the circularly polarised light.[191]

The diffraction efficiency of the $\boldsymbol{n}_{\parallel}$ µLCE was also investigated under strain and the results are shown in Figure 4-12c**.** The application of strain perpendicular to the grating grooves, increases the pitch and an increase in diffraction efficiency is observed due to the shift of λ_Δ towards 404 nm. The change in pitch is linear with respect to the applied strain (ε), as shown in Figure 4-11a. By applying a linear fit to the efficiency data, a cross-over in behaviour becomes apparent at strains close to 100%, where a change in gradient is observed (gradient = 0.67 for ε < 100% and 1.79 for ε > 100%). The change in gradient may be explained by the onset of the auxetic response in these materials causing an increase in feature height upon strain and thus an increase in $\Delta\varphi$ and η_1. Any possible effect of auxeticity is hard to deconvolute from changes in measured efficiency, due to strain induced changes in λ_Δ, however it is interesting to note that the change in gradient occurs near the onset of the auxetic response.

4.4.6 Durability Testing

In section 4.4.3 and 4.4.4, the µLCEs are subjected to temperatures of up to 240°C and strains of up to 157%. The upper thermal limit of stability of the samples was investigated *via* Thermogravimetric analysis by performing a temperature ramp at a rate of 10°C/min. The onset of thermal decomposition of the samples was found to be 382°C (appendix Figure B-9). The effect of high temperature and high strains on the surface topography of the grating was assessed *via* AFM. Figure 4-13 shows AFM profile scans of the µLCEs pre- (cyan) and post- (red) test conditions.

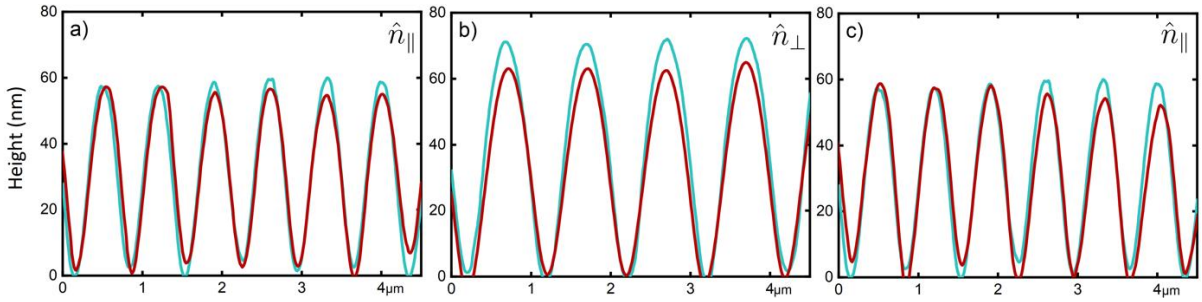

Figure 4-13: AFM surface profilometry of nematic µLCE films. (a) $\boldsymbol{n}_{\parallel}$ µLCE pre- (cyan) and post- (red) heating to 240°C. (b) $\boldsymbol{n}_{\perp}$ µLCE pre- (cyan) and post- (red) heating to 240°C. (c) $\boldsymbol{n}_{\parallel}$ µLCE pre- (cyan) and post- (red) straining to 156%.

Figure 4-13 shows the grating profiles of $\boldsymbol{n}_{\parallel}$ (Figure 4-13a**)** and $\boldsymbol{n}_{\perp}$(Figure 4-13b) samples that have been heated to 240°C and allowed to cool back to room temperature (referred to as 'post-heating'). The post-heating pitch and amplitude were 702 ± 10 nm and 53 ± 2 nm for the $\boldsymbol{n}_{\parallel}$ µLCE, in agreement with the pre-heating pitch and amplitude (707 ± 10nm, 53 ± 3nm). The post-heating first order diffraction efficiency (η_1) of the device was 1.97 ± 0.2% which is agreement with the pre-heating η_1 (1.95 ± 0.2%) and theoretical predictions for the pristine sample (1.97%). The post-heating pitch and amplitude were 989 ± 10 nm and 61 ± 2 nm respectively for the $\boldsymbol{n}_{\perp}$ µLCE, with a reduction in both pitch and amplitude relative to the original sample (1010 ± 5 nm, 68 ± 3 nm). The post-heating η_1 of the device was 2.5 ± 0.2%, which is lower than the pre-heating η_1 (3.76 ± 0.2%) and may be an indication of thermal damage to the µLCEs at temperatures of 240°C.[57] Figure 4-13c shows the grating profile of the $\boldsymbol{n}_{\parallel}$ pre- (cyan) and post- (red) straining to 156%. The pitch and amplitude of the sample post-strain (i.e. strained to 156% and then allowed to relax back to unstrained state) was 696 ± 10 nm and 50 ± 2, which is in agreement with the pre-strain values (707 ± 10 nm, 53 ± 3 nm).

The dimensional stability of the µLCE gratings is assessed under repeated thermal and mechanical actuation by measuring the pitch of the $\hat{\boldsymbol{n}}_{\parallel}$ µLCE over 50 cycles. The post-cycled pitch (d) is compared with the pre-cycled pitch (d_0 = 707 ± 10 nm) of the $\hat{\boldsymbol{n}}_{\parallel}$ µLCE, as measured directly after fabrication and prior to any actuation. After 50 cycles between 20°C to 100°C the thermally actuated µLCE was found to have a pitch of 711 ± 15 nm, with a <1% change relative to d_0. Similarly, after 50 cycles between 0 and 30% strain, the mechanically actuated µLCE had a pitch of 713 ± 17 nm (<1% change).

4.5 Summary

In this work, tunable LCEs with sub-micron features have been obtained *via* intrinsic anisotropic deswelling. These µLCEs are well suited as optical diffraction gratings with a high sensitivity to external thermal and mechanical stimuli. By utilizing the intrinsic anisotropic deswelling of these LCEs, a pitch anisotropy of 303nm was found (1010nm vs. 707nm) in a chemically identical sample. A pitch tunability range of 130nm was achieved by altering the amount of the non-polymerizable mesogenic component of the LCE during synthesis; the lower and upper bounds being limited by the nematic-to-isotropic transition temperature, and phase separation and crystallization respectively. With further investigation this range could likely be extended by introducing other non-polymerizable mesogenic components/mixtures, to suppress crystallization and retain a wide temperature range in the nematic phase.

The sensitivity of the µLCEs to thermal stimuli was investigated, showing a -322nm and +212nm change in initial pitch for the $\hat{\boldsymbol{n}}_{\perp}$ and $\hat{\boldsymbol{n}}_{\parallel}$ respectively over a temperature range of 215°C. The sensitivity of the µLCEs to mechanical stimuli was investigated with the $\hat{\boldsymbol{n}}_{\parallel}$ µLCE variety, showing a 167% (1110nm) increase in pitch over its operational strain range. Diffraction efficiency measurements revealed an increase in first order diffraction efficiency for the $\boldsymbol{n}_{\parallel}$ µLCE and a decrease for the $\boldsymbol{n}_{\perp}$ µLCE upon heating. This change is related to the relative shift in peak efficiency wavelength of the gratings, due to temperature driven changes in pitch.

The auxetic response, a known behaviour in these systems, is also observed in the µLCE gratings as confirmed by AFM, where a growth in grating height of +26% relative to the initial height, is observed at a strain of 146%. An increase in first order diffraction efficiency is observed with applied strain, related to the change in the gratings' peak efficiency wavelength due to strain-driven changes in pitch. A cross-over in diffraction efficiency behaviour is observed at a strain of 100%, which may be related to the auxetic response increasing the depth of the surface features. For deformable diffraction gratings, a reduction in peak diffraction efficiency is observed under strain due to a reduction in surface feature height.[170,182] Thus, the observed auxetic response in the all-acrylate µLCEs may provide a fundamental benefit to their use as mechano-optical diffractive devices. Additionally, it is expected that this response will provide additional functionality to strain-tunable micro-textures in general, for example, controlling surface hydrophobicity.[192]

Preliminary durability tests confirm that the fidelity of the grating profiles is retained under thermal and mechanical actuation of up to 50 cycles. Evidence of a reduction in surface feature height is present in samples taken to 240°C, in agreement with previous thermal studies of these materials,[57] helping guide the operational range of µLCEs for device applications.

Chapter 5 Liquid Crystals on Spontaneously Wrinkled Surface Topographies

5.1 Motivation and Overview

The following chapter focuses on the use of spontaneous wrinkling as a means of adding texture to polyimide (PI) LC alignment layers. This simple, non-lithographic patterning technique provides access to a wealth of topographic length scales and geometries, capable of profoundly influencing nematic director orientation. In this work, a variety of interesting alignment outcomes have been demonstrated through the interactions between LCs and wrinkled surfaces, such as: uniform director alignment, tilted homeotropic alignment, surface anchoring transitions and complex in-plane director modulation driven by spatial confinement.

The chapter begins by first introducing the spontaneous wrinkling phenomena and how it can be used in micro and nanoscale fabrication and LC devices. The remainder of the chapter covers the fabrication and subsequent transfer of a linear wrinkled texture into planar and homeotropic PI alignment layers, using the imprinted polyimide (IPI) methodology detailed in section 3.2.2.b. These wrinkle-imprinted polyimide (WIP) surfaces are used to investigate the wrinkles' topographic influence on director profile, under different surface anchoring conditions.

5.2 Introduction to Spontaneous Wrinkling

Spontaneous wrinkling was first demonstrated as a viable, non-lithographic approach to micro-fabrication by Bowden et al., using metal deposition and thermal actuation of polydimethylsiloxane (PDMS).[193] Deposition induced wrinkling offers excellent control over surface composition and enables the resulting wrinkled surface to be used as its own standalone device without further processing e.g. pliable surface-enhanced Raman spectroscopy (SERS) surfaces [194] and stretchable MOSFETs and p-n diodes.[195] However, the specialist equipment involved in deposition processes limits its general accessibility, driving the development of more facile methods of wrinkle generation.

Since initially reported,[196] surface oxidation has been widely adopted for creating polydimethylsiloxane (PDMS) wrinkles, owing to its simplicity and broad range of attainable periodicities from hundreds of microns to hundreds of nanometers, *via* ultraviolet ozone (UVO) and plasma oxidation treatments.[197–199] These oxidative processes convert PDMS to a bilayer system comprised of a glassy surface layer, 10 to a few 100nm thick,[200,201] bound to the bulk PDMS below. Initiating wrinkling requires the oxidized PDMS to be perturbed in some way, such as: release of a mechanical pre-strain,[198,202,203] thermal actuation [199,204] or swelling via solvent immersion.[205,206] A schematic of the strain-route from a flat PDMS slab to a wrinkled PDMS slab

is shown in Figure 5-1. Wrinkle periodicity (d) scales proportionally with oxidized layer thickness (h_f) and inversely with mechanical pre-strain (ε_{pre}) as given by equation (5-1),

$$d = 2\pi h_f \frac{(\overline{E}_f/3\overline{E}_s)^{1/3}}{(1+\varepsilon_{pre})(1+\xi)^{1/3}} \quad (5\text{-}1)$$

where $\overline{E}_f$ and $\overline{E}_s$ are the plain strain moduli of the oxide film and PDMS slab respectively and $\xi = 5\varepsilon_{pre}(1+\varepsilon_{pre})/32$.[207] As UVO treatments form relatively thick surface layers, they typically result in longer-periods (d > 1µm), whereas air and oxygen plasma treatments, which create thinner surface layers, more readily form shorter-periods (d < 1µm) as low as 100s of nanometres.[202,203]

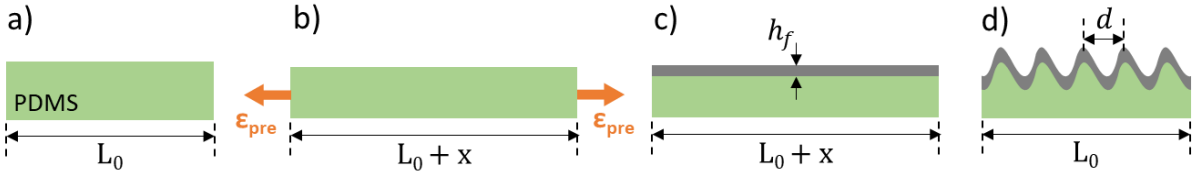

Figure 5-1: Schematic of PDMS wrinkling. (a) A compliant PDMS slab with initial length (L_0), is (b) elongated by a distance (x) via tensile strain (ε_{pre}). (c) Under static strain, plasma oxidation forms a stiff surface layer on the PDMS slab, with a thickness (h_f). (d) Upon strain release, the bulk compliant PDMS contracts whereas the surface layer buckles/wrinkles to relieve the internal stresses accumulated during its strained formation, resulting in a periodic wrinkle texture with a wrinkle periodicity (d).

Wrinkled PDMS surfaces have found inter-disciplinary application in areas such as, biological cell contact guidance,[208] dynamic diffractive optics,[209] microfluidic particle trapping,[197] soft polymer metrology [210] and security substrate fabrication.[211] The shape-memory properties of wrinkled PDMS has enabled reversible tunability of both surface adhesion [212] and optical transmittance [213] *via* mechanical actuation. These applications broadly rely on a periodic surface topography, an inherent property of spontaneously wrinkled surfaces that makes them well-suited for exploring alignment interactions between LCs and surface relief structures, as introduced in section 2.3.

Integrating wrinkled surfaces in to LC systems has demonstrated spatial confinement of nematic defect lines [214] and enhanced viewing angles of selective reflection in cholesteric LC films.[215] The anisotropic, grating-like morphology of periodic wrinkles lends itself to surface alignment applications, as shown by Ohzono *et al*. in both static [107] and dynamic [216] LC devices. Micro [148] and nanoscale [217] wrinkled textures have previously been transferred into planar LC alignment layers *via* soft lithography,[131,132] providing uniform director alignment intended for display-oriented applications. The work described in this chapter explores LC alignment on wrinkled surfaces with planar and homeotropic anchoring. Planar wrinkles are used to demonstrate a simple experimental approach, using birefringence colour observations, to confirm that the nematic director aligns parallel to the wrinkle grooves. Homeotropic wrinkles are investigated for the first time as an LC alignment layer, shedding light on topography-induced director tilt, surface anchoring transitions and modulated director profiles.

5.3 Methods

5.3.1 Wrinkle Fabrication

A wrinkled texture is fabricated using a cured slab of PDMS (Sylgard-184, Dow Corning Inc.). A PDMS precursor mixture is prepared as detailed in section 3.2.2.a and thermally cured in a non-stick casting vessel at 80°C overnight. Rectangular sections are cut from the as-cast PDMS slab, with dimensions of 30 x 6 x 1mm (L x W x H). Extensive works by Cabral and Nania *et al*. on PDMS wrinkling *via* mechanical strain, are used as a guide for selecting appropriate process variables to form wrinkles on the micron and sub-micron length scale.[198,203]

Uniaxial tensile strain (ε) is applied parallel to the long axis of the PDMS slab, using a custom strain rig, and the elongation is measured with a micrometer to apply 60% strain. This strain level was selected to target a sub-micron wrinkle periodicity, based on preliminary tests at 40% strain producing a periodicity of ≈1μm. The strained slab is oxidized for 5 minutes in a PE-25 plasma etcher (Plasma Etch Inc.) with a 13.56MHz radio-frequency (RF) power source, using an RF power of 40W, a chamber pressure of 700mtorr and an oxygen flow rate of 35cc/min. The applied strain is gradually released after etching, resulting in the spontaneous formation of a wrinkled texture. This process is shown schematically with accompanying images in Figure 5-2.

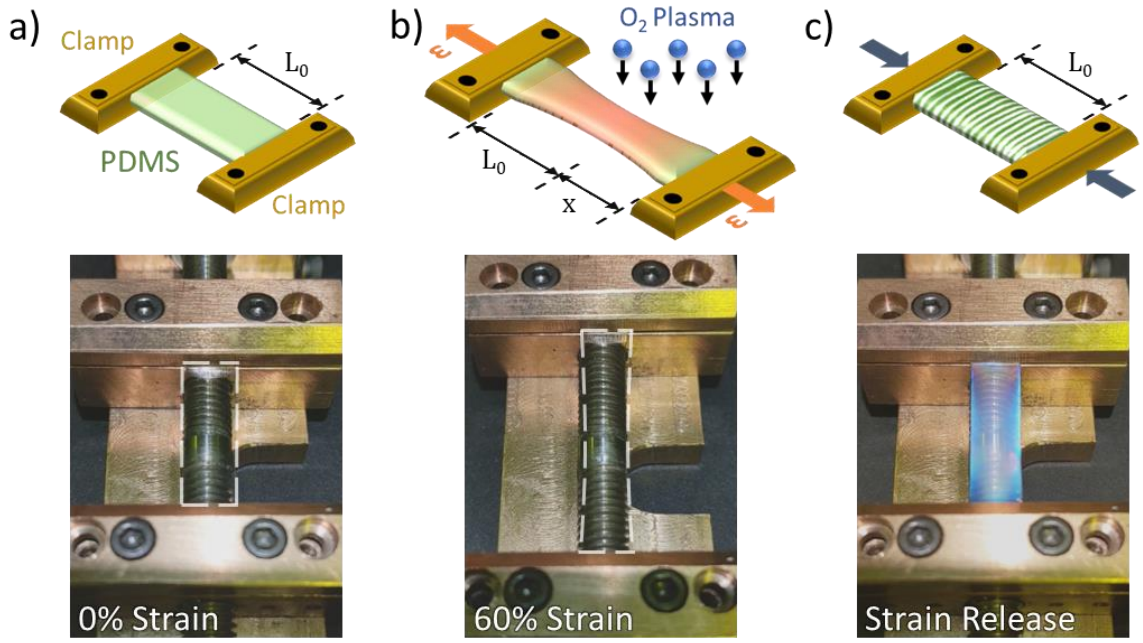

Figure 5-2: PDMS wrinkling via mechanical strain and plasma oxidation. Schematics (top row) and images (bottom row) of a PDMS sample at each stage of the wrinkling process. (a) The PDMS slab is secured in a uniaxial strain rig and pulled taut to measure the initial slab length (L_0). (b) Clamp separation is increased to apply 60% tensile strain (ε) and a plasma treatment is applied, where the PDMS slab is elongated by a distance (x), where $\varepsilon = x/L_0 = 0.6$. (c) Tensile strain is released after plasma treatment, inducing surface wrinkling. Note the change in appearance of the PDMS slab (denoted by the dashed lines) from highly transmissive in (a) and (b), to strongly diffractive in (c), due to interactions between visible light and the microscale, periodic features of the wrinkled surface.

5.3.2 Wrinkle-Imprinted Polyimide

The wrinkled PDMS slab is used as a working stamp to imprint spin-coated layers of planar (SE-2170) and homeotropic (SE-4811) PI on indium tin oxide (ITO) coated glass (Figure 5-3). The solvent-rich PI films are imprinted at 70°C for 2 minutes, evaporating the solvent and transferring the wrinkled texture in to the PI, followed by baking at 200°C for 30 minutes to complete imidization. LC devices are fabricated with planar and homeotropic wrinkle-imprinted polyimide (WIP) surfaces, both of which are assembled opposite flat, unpatterned layers of homeotropic PI. This results in a hybrid aligned nematic (HAN) device geometry when using a planar WIP surface and a vertically aligned nematic (VAN) device geometry when using a homeotropic WIP surface. Both device variants do not feature any mechanically rubbed surfaces and are capillary filled with MLC-6204 (Merck) in the isotropic phase at 70°C (T_{NI} = 66.0°C). MLC-6204 is selected because it has well characterised physical properties, as summarized in Table 3-1 in section 3.1.3.b.

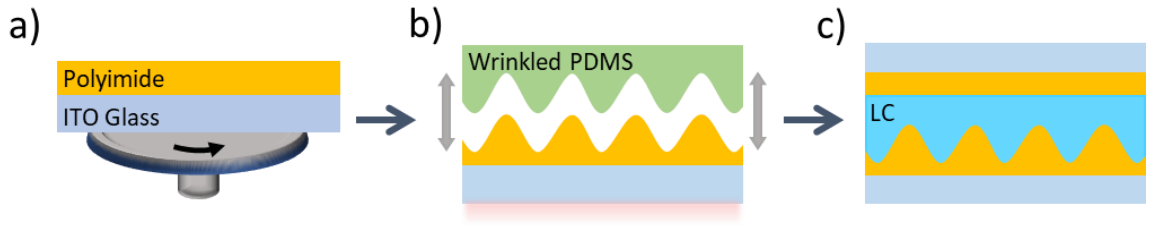

Figure 5-3: Schematic of transferring wrinkled PDMS surface textures in to LC devices. (a) PI thin film is spin coated on 1mm thick, indium tin oxide (ITO) coated glass. (b) Wrinkled PDMS slab is placed in conformal contact with the solvent-rich PI film at 70°C, solidifying the imprinted PI layer as the solvent evaporates. (c) Wrinkle-imprinted polyimide (WIP) surfaces, with a wrinkle periodicity and height of the order of 900nm and 100nm respectively, are assembled in a parallel-plate configuration, opposite an ITO substrate coated with a flat, homeotropic PI layer. The cavity between the PI surfaces, with a thickness of the order of 10μm, is capillary filled with LC in the isotropic phase at 70°C (MLC-6204, Merck).

5.4 Results and Discussion

5.4.1 Wrinkled Topography Analysis

As the WIP surface topography and resulting LC alignment are the focus of this study, it is important identify the key features of the WIP surfaces and their associated dimensions. To do this, a combination of optical microscopy and AFM, with a Bruker MultiMode® 8-HR in tapping mode, is used. Topographic analysis of the WIP surface texture is presented in Figure 5-4. The WIP surfaces are comprised of periodic wrinkles with grooves ($\boldsymbol{g}$) aligned parallel to Y, and aperiodic protrusions (referred to as 'walls') aligned quasi-parallel to X (Figure 5-4a,b). The wrinkles have a sub-micrometre periodicity (d) of 900 $\pm$ 20nm, as expected from the larger applied strain of 60% relative to the micrometre periodicity obtained during initial tests at 40% strain, and a height (h) of 125 $\pm$ 10nm. Pitch and height values are both taken as the average of 30 measurements, across 6 line profiles from distinct locations on a 40 x 40μm AFM scan of the WIP surface (Figure 5-4c).

During device fabrication, the wrinkled PDMS is used as a stamp (Figure 5-3b), which results in the features on the WIP surface being inverted relative to those on the original PDMS slab. This inversion is most prominent in the aperiodic features, which begin as valleys in the wrinkled PDMS surface. These valleys are fissures or cracks in the stiff oxide surface layer, formed as a result of strain-induced necking and subsequent relaxation of the PDMS slab upon strain release.[201,211,213] The schematic in Figure 5-2b shows an exaggerated representation of this strain-induced necking, where the width of the PDMS slab narrows under strain, relative to the width at rest. Aligned quasiparallel to the applied strain (parallel to X in Figure 5-4a,b), these inverted cracks or walls (Figure 5-4d), have a mean spacing of $13 \pm 1\mu m$ and a mean height of $230 \pm 2nm$; protruding above the peaks of the wrinkles by 50 - 100nm.

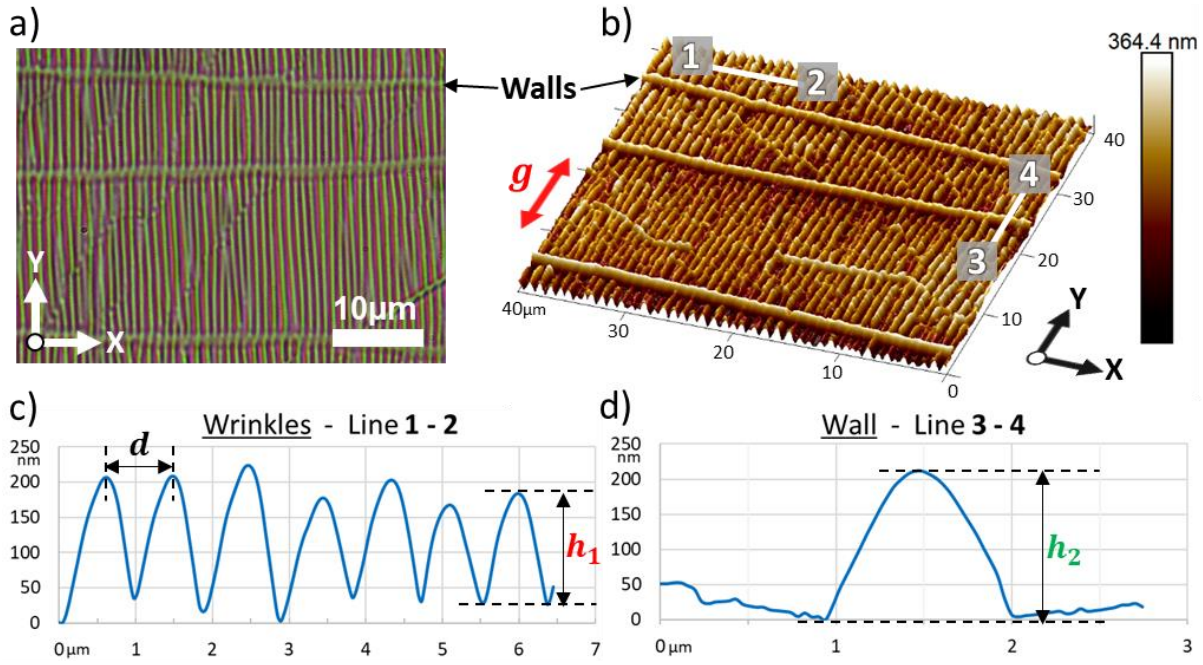

Figure 5-4: Surface topography of wrinkle-imprinted polyimide (WIP) alignment layers. (a) Optical microscopy image of a WIP surface captured with a 100x microscope objective. Scale bar = 10µm. (b) AFM scan of a WIP surface highlighting the protruding 'wall' features quasi-parallel to X, and the periodic wrinkles parallel to Y. (c) AFM height profile of the grating-like wrinkles along line 1 – 2 in (b), with a groove direction ($\boldsymbol{g}$), an average pitch (d) of 900 ± 20nm and an average height (h_1) of 125 ± 10nm. (d) AFM height profile of a 'wall' feature on a WIP surface, along line 3 – 4 in (b), with a mean spacing of 13 ± 1µm and a mean height (h_2) of 230 ± 5nm.

5.4.2 Planar Wrinkles

Identifying the key topographic features of the WIP surfaces and their associated dimensions *via* surface metrology, enables more definitive links to be made between observed LC alignment properties and specific surface features. The first and arguably simplest LC-wrinkle system studied, is one where the wrinkled topography is transferred in to a PI layer with planar anchoring. This planar WIP surface is used to investigate how the azimuthal orientation of the director ($\hat{\boldsymbol{n}}$) is affected by the wrinkled topography.

5.4.2.a Alignment Uniformity

To emphasize the influence of the topography and minimize the influence of the opposing substrate, the WIP surface is left un-rubbed and assembled opposite a flat, un-rubbed homeotropic PI surface in a HAN device geometry with a thickness of 10 ± 1µm, as shown in Figure 5-5a. POM observations of the HAN device (Figure 5-5b,c), highlight the contrasting alignment properties of (i) wrinkled areas and (ii) flat, unpatterned PI areas. This shows how the wrinkles promote uniform alignment of $\hat{\boldsymbol{n}}$ in region (i), signified by a uniformly extinct and second-order orange birefringence colour on rotation, on an otherwise planar-degenerate PI layer, indicated by the typical Schlieren texture observed in region (ii). The second-order orange is distinguished from first-order orange using the sequence of birefringence colours observed upon cooling through the nematic phase (see appendix C.1). These POM observations of the wrinkle-flat boundary strongly resemble POM images from previous reports on nematic LC alignment at a grating-flat boundary, where azopolymer alignment films are selectively patterned with conventional linear surface relief gratings.[106]

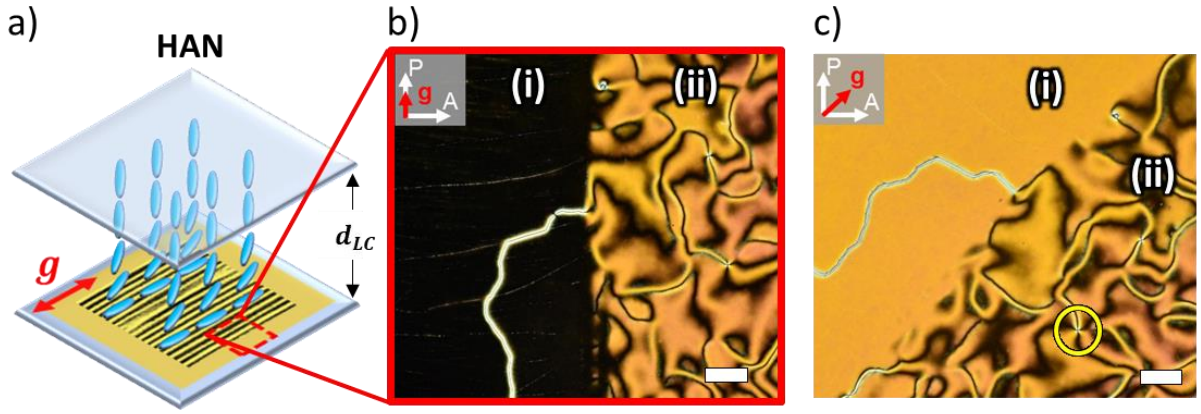

Figure 5-5: HAN LC device comprised of a planar WIP surface opposing a flat, homeotropic PI surface. Filled with MLC-6204 with an LC layer thickness (d_{LC}) of 10±1µm. (a) Schematic of the HAN device geometry, indicating the region of interest (ROI) on the boundary between (i) a wrinkled PI area and (ii) a flat PI area. (b,c) POM images of the ROI indicated by the red box in (a), imaged at 59°C (nematic phase), with the wrinkle grooves ($\boldsymbol{g}$) at 0° and 45° with respect to the crossed polarizers (P,A). The images show homogeneous director alignment in the wrinkled area (i), and planar degenerate alignment in the unpatterned PI area (ii). Scale bars = 100µm.

5.4.2.b Director Orientation

Identifying uniform alignment of $\hat{\boldsymbol{n}}$ is a trivial task using POM, by observing whether a spatially uniform bright and dark state is present upon rotation, as shown in region (i) of Figure 5-5b,c. However, confirming the azimuthal orientation of $\hat{\boldsymbol{n}}$ is less trivial and requires additional optics such as compensation plates. Given that the wrinkled topography closely resembles a linear surface relief grating, it is expected that $\hat{\boldsymbol{n}}$ would align parallel to the micro-scale grooves ($\boldsymbol{g}$) due to their associated azimuthal anchoring strength (W_ψ) of approximately 4×10^{-6} Jm^{-2}, calculated using equation (2-10) from Berreman's theory, as covered in section 2.3.1.[74] For completeness, this is confirmed optically for this system.

The inherent layout of the WIP substrates, with adjacent (i) wrinkled and (ii) unpatterned areas of the same PI material, provides a built-in reference point for confirming azimuthal director orientation; in the form of nematic point defects within the Schlieren texture of region (ii). These 4-brush, $|s| = 1$ point defects have well-known director profiles associated with the $s = +1$ and $s = -1$ variants, distinguishable by how their dark brushes rotate under sample or polarizer rotation.[218] Using this approach (detailed in appendix C.2), an $s = -1$ defect is identified in region (ii) to be used as a reference point. This is shown highlighted with a yellow circle in Figure 5-5c and Figure 5-6a, which are POM images of the same region of interest (ROI), at the same temperature, without and with a full-wave compensation plate respectively.

With the addition of the full-wave plate (λ-plate), the colour of the four bright brushes surrounding the $s = -1$ defect change from second-order orange (Figure 5-5c), to alternating colours depending on the director orientation with respect to the slow axis (λ_p) of the λ-plate (Figure 5-6a,b). The orientation of $\hat{\boldsymbol{n}}$ in the uniformly-aligned region (i), can now be inferred using the known $\hat{\boldsymbol{n}}$ profile around the identified $s = -1$ defect in region (ii), shown overlaid on the magnified POM image in Figure 5-6b. Given that the observed pink birefringence colour of the homogeneously-aligned region (i), matches the colour of the $s = -1$ defect brush where $\hat{\boldsymbol{n}}$ is parallel to $\boldsymbol{g}$ in region (ii), this confirms that $\hat{\boldsymbol{n}}$ is also parallel to $\boldsymbol{g}$ in region (i).

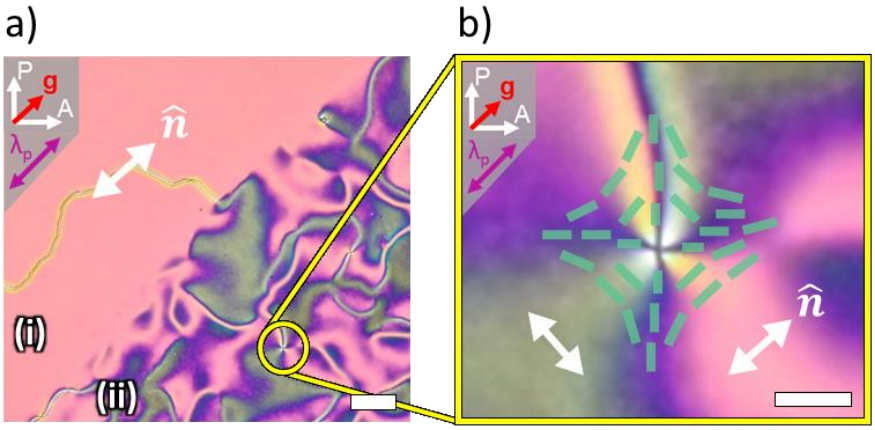

Figure 5-6*: POM images of the same region of interest (ROI) shown in Figure 5-5c, with the addition of a full-wave compensation plate (λ-plate) with slow axis orientation, λ_p. Used to confirm the relative orientation of the director ($\hat{\boldsymbol{n}}$) and the wrinkle grooves ($\boldsymbol{g}$). (a) Broad view of the ROI on the boundary of (i) wrinkled and (ii) unpatterned PI areas. Yellow circle in region (ii) highlights the $s = -1$ point defect used a reference point. Scale bar = 100μm (b) Enlarged image of $s = -1$ reference defect highlighted in (a). Overlaid green dashes show the known $\hat{\boldsymbol{n}}$ profile surrounding a $s = -1$ point defect. Imaged at 59°C. Scale bar = 20μm.*

5.4.3 Homeotropic Wrinkles

The previous section addressed how the azimuthal director orientation is influenced by a wrinkled topography with planar anchoring; a device geometry previously studied in other works.[107,217] Yet to be explored is how a wrinkled topography with homeotropic (HT) anchoring impacts director orientation, investigated here using a homeotropic WIP surface in a VAN device geometry with a thickness of $12 \pm 1\mu m$ (Figure 5-7c). The general layout of the homeotropic WIP substrate is the same as the planar version in the previous section, with a flat area of unpatterned PI (1) surrounding a textured area of wrinkled PI (2). This once again allows for the direct comparison of alignment characteristics in each area within the same device, using POM with orthoscopic and conoscopic illumination.

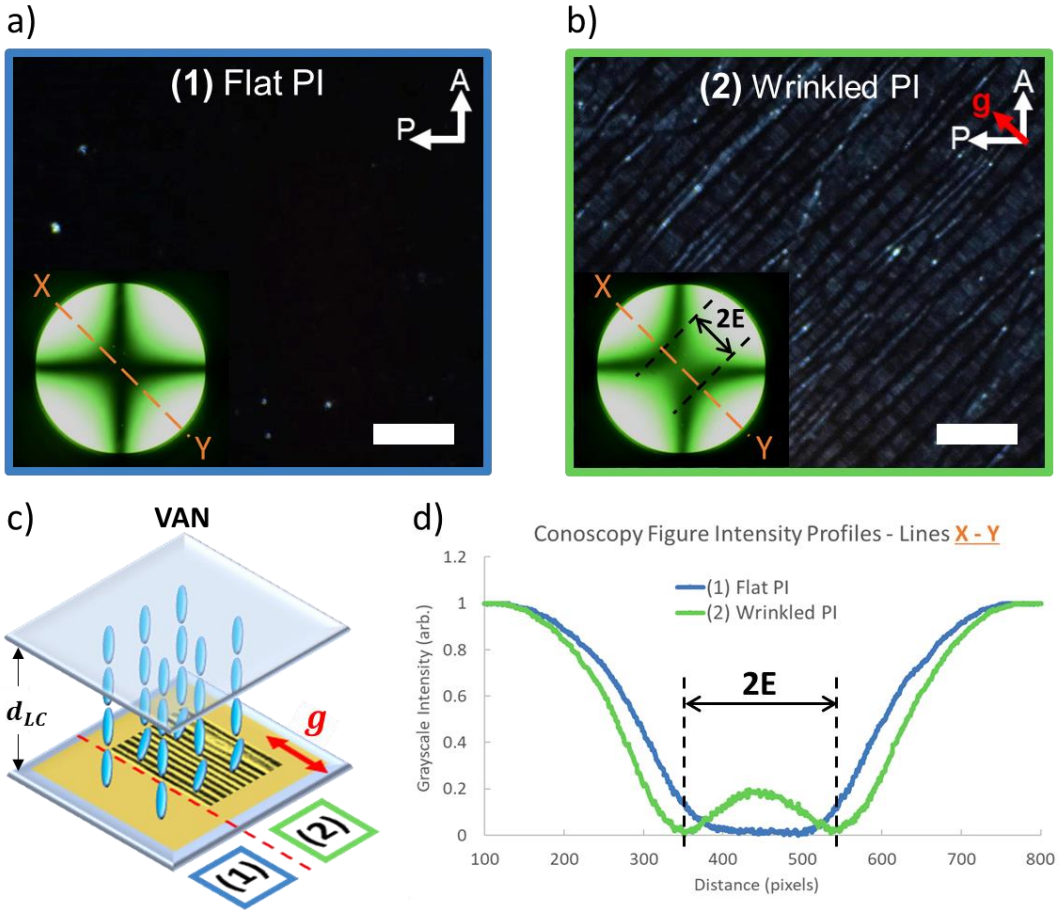

Figure 5-7: VAN device featuring a homeotropic WIP surface opposite a flat, homeotropic PI surface. Filled with MLC-6204 with an LC layer thickness (d_{LC}) of 12±1µm and imaged at 20°C. (a) POM image of a device region without wrinkles i.e. flat homeotropic PI on both surfaces. P, A = polariser and analyser orientations. (b) POM image of a device region with homeotropic wrinkles. Insets show conoscopy figures captured in each region, using broadband green illumination ($\lambda = 533 \pm 52nm$). Scale bars = 50µm (c) Schematic of VAN device geometry, indicating (1) flat PI and (2) wrinkled PI regions shown imaged in (a) and (b), and the groove direction ($\boldsymbol{g}$). (d) Intensity profiles of the inset conoscopy figures in (a) and (b), measured along the orange dashed lines X-Y, showing isogyre splitting in region (2) as a result of degenerate director tilt induced by the wrinkled surface topography.

5.4.3.a Topography-Induced Tilt

The alignment influence of the homeotropic wrinkles is first investigated at room temperature (20°C). Flat areas of polyimide remain extinct under rotation between crossed polarisers, as the director is aligned orthogonal to the substrate plane (Figure 5-7a). This is confirmed by conoscopic examination of the flat areas producing a Maltese cross (inset Figure 5-7a), indicating a vertically aligned optic axis or homeotropic director alignment.[124,219] The wrinkled polyimide areas exhibit slightly modulated transmission upon rotation, maximised when the wrinkle grooves ($\boldsymbol{g}$) are at 45° to the polariser orientations, as shown in Figure 5-7b. Split isogyres are observed in the associated conoscopy figure (inset Figure 5-7b), splitting along the line X-Y or parallel to $\boldsymbol{g}$, indicating tilt of the optic axis away from vertical.[220] From the figure, it can be inferred that the tilt is degenerate, since the splitting is centrosymmetric, and that it is occurring in a plane perpendicular to $\boldsymbol{g}$ i.e. the director is orthogonal to the wrinkled surface and splaying over the peaks and troughs of the periodic wrinkles.

This topography-induced director tilt is quantified by measuring the splitting or angular separation of the isogyres (dark bands in the conoscopy figures). The splitting is measured by taking grayscale intensity profiles of the conoscopy figures along the lines X-Y, and plotting the intensity as a function of pixel position to locate the intensity minima (Figure 5-7d). The separation of the intensity minima ($2E$) in pixels, is converted to an angular value by calibrating the conoscopy figures using the diffraction pattern of a 1.04μm pitch linear diffraction grating (details in appendix C.3).[122] The measured, apparent double-angle made by the optic axes ($2E$) is 21.0 $\pm$ 2.0°, which converts to an axial double-angle ($2V$) of 13.4 $\pm$ 1.0°.[121] Since the tilt is degenerate, V represents the average tilt of the optic axis from vertical (ϕ) induced by the wrinkled topography, where $\phi = 6.8 \pm 0.7°$. The director pretilt (θ_P) on the wrinkled surface can be approximated from the measured value of ϕ, using the method described later in section 6.4.3.a. This assumes a linearly varying director tilt profile ($\theta(z/d_{LC})$) between θ_P on the wrinkles, and θ_1 (≈ 90°) on the opposing flat PI surface. θ_P is approximated by varying its value until the average director orientation (θ_{avg}) of $\theta(z/d_{LC})$ satisfies $\theta_{avg} = 90 - \phi$. For the homeotropic WIP device in question, this results in $\theta_P = 77 \pm 2°$ at 20°C.

5.4.3.b Surface Anchoring Transition

The previous section covered the LC alignment properties of the homeotropic WIP device in its equilibrium state at room temperature (20°C). From here onwards, discussions will be focused on this device's behaviour at elevated temperatures with $T/T_{NI} > 0.95$ (T_{NI} = 66.0°C). As summarised in Table 3-1, MLC-6204 has significantly reduced splay and bend elastic constants at these high temperatures ($k_{11} \leq$ 4pN, $k_{33} \leq$ 5pN) relative to those at room temperature (k_{11} = 7pN, k_{33} = 11pN).[119] This results in the director having greater orientational freedom, which allows the topography of the wrinkled surface to play a more dominant role in the overall alignment of the device.

The homeotropic WIP device exhibits a stark change in optical properties around 4°C below T_{NI} , where its appearance changes from near-extinct at 60°C (T/T_{NI} = 0.98) to markedly transmissive at T ≥ 62.5°C ($T/T_{NI} \geq 0.99$) (Figure 5-8). This contrast in optical properties is attributed to a surface anchoring transition from a slightly tilted to a more significantly tilted director profile, caused by the competing influence of the topography of the wrinkled texture, and the homeotropic anchoring of the PI. The notable features of this tilted/frustrated director profile will be explored in the following sections.

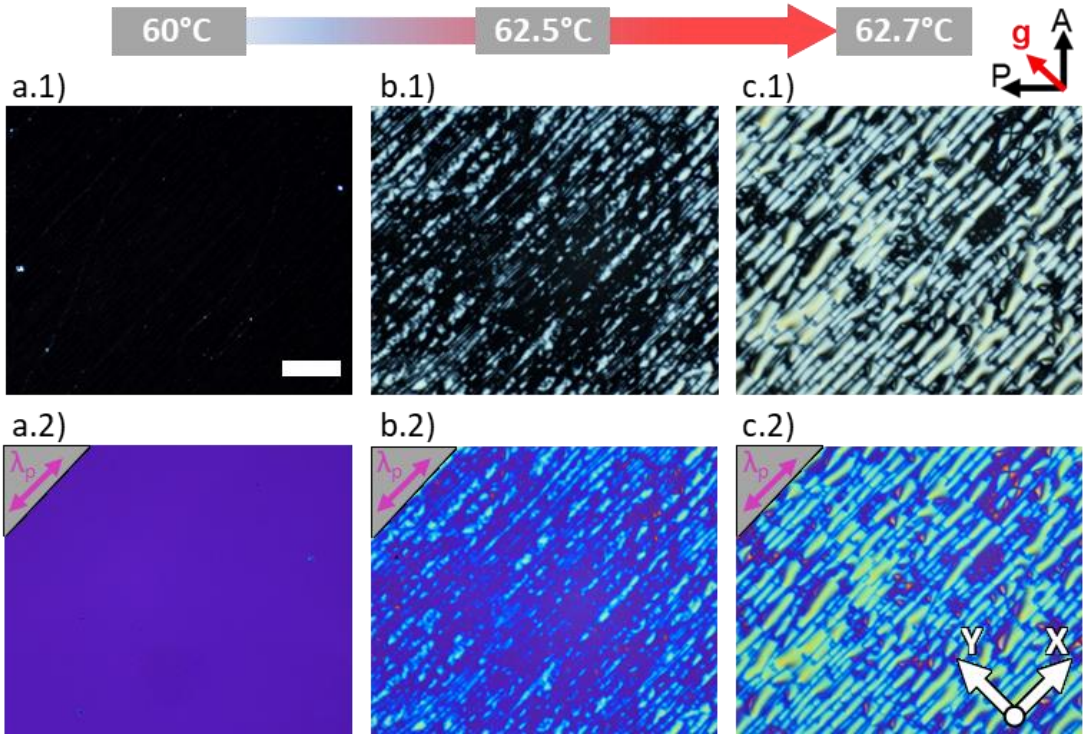

*Figure 5-8: POM images of the homeotropic WIP device on heating through 60°C to 62.7°C, showing the change in optical properties due to a surface anchoring transition. (a) Device at 60°C appearing near-extinct due to bulk HT alignment. (b) Onset of surface anchoring transition at 62.5°C, indicated by small patches of the field of view (FOV) transitioning from extinct to transmissive. (c) Majority of FOV becomes transmissive at 62.7°C, as tilted director profile propagates on heating. Addition of a λ-plate (a2-c2), with slow axis (λ_p) perpendicular to the wrinkle grooves (**g**), shows an additive colour shift to blue, indicating director tilt parallel to λ_p and hence perpendicular to **g**. Scale bar = 100μm.*

From the POM observations shown in Figure 5-8, analysis of this frustrated director profile is performed using the observed birefringence colours and how they change with the addition of a full-wave plate. The most striking feature of this frustrated alignment state is the increased transmission through crossed polarisers (Figure 5-8c), compared to the initially slightly tilted homeotropic configuration (Figure 5-8a). This induced birefringence is associated with the presence of a larger component of n_e in the propagation direction of the incident linearly polarised light, as a result of the anchoring transition. Given the initial VAN geometry of this device (Figure 5-7c), this induced birefringence suggests that the anchoring transition results in a tilted director configuration on the wrinkled surface, which leads to a HAN director profile overall.

5.4.3.b.i Tilt Direction

The tilt direction is determined through the addition of a full-wave plate between the polariser and the sample, with its slow axis (λ_p) at 45° to the polariser orientations (P, A). When λ_p is aligned parallel the slow axis of the LC (n_e), this gives an additive condition where a blue-cyan birefringence colour is observed.[221,222] As shown in Figure 5-8c.2, the tilted alignment state exhibits a blue-cyan birefringence colour when λ_p is aligned perpendicular to the wrinkle grooves ($\boldsymbol{g}$), confirming that the induced director tilt is occurring in a plane perpendicular to $\boldsymbol{g}$. This is illustrated in Figure 5-9a, which shows the tilt occurring in the XZ plane of the defined coordinate system, where $\boldsymbol{g}$ is parallel to the Y axis. For reference, the XY axes in Figure 5-9a are consistent with XY labels used previously in Figure 5-4 and Figure 5-8 and from here onwards. Director tilt occurring perpendicular to the grooves of a grating-like surface with homeotropic anchoring, has previously been reported by Cattaneo *et al*. in their frustrated-alignment LC devices; the optical textures of which closely resemble those of the homeotropic WIP device after the surface anchoring transition.[113]

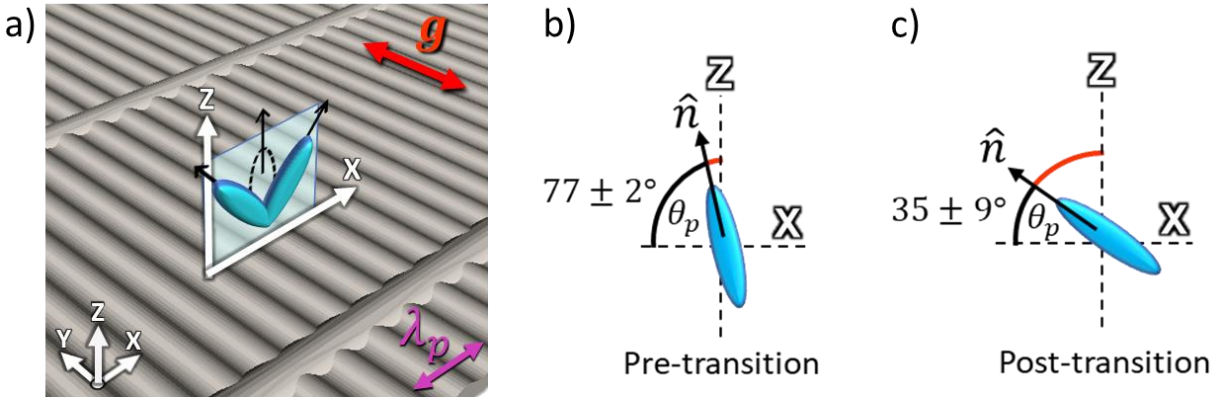

Figure 5-9: Director tilt in the homeotropic WIP device. (a) Tilt shown in 3D space on a CAD representation of the wrinkled surface, with wrinkle grooves ($\boldsymbol{g}$) (parallel to Y), slow axis of λ-plate (λ_p) as oriented in Figure 5-8c.2 (parallel to X) and director tilt in XZ plane. (b) Degree of degenerate pretilt (θ_p) of the director ($\hat{\boldsymbol{n}}$) prior to the surface anchoring transition, as covered in section 5.4.3.a. (c) Degree of θ_p after the surface anchoring transition.

5.4.3.b.ii Degree of Tilt

With the tilt direction confirmed, further characterisation of this alignment state is carried out by quantifying the amount of tilt induced by the surface anchoring transition. Ideally, the induced tilt of this now HAN director profile would be measured using the crystal rotation method.[113,223] Given that this alignment state only exists at high temperatures and is not spatially uniform, this makes using the crystal rotation method experimentally complex and ultimately unfeasible in the case of the homeotropic WIP device. Instead, a semi-quantitative approach is used to approximate the pretilt on the wrinkled surface (θ_P), by comparing the observed retardation (Γ) and corresponding birefringence of the device (Δn_{eff}) in the tilted alignment state, with theoretical values of Δn_{eff} calculated for HAN director profiles with linearly varying director orientations.

The observed, first-order pale-yellow birefringence colour of the HT WIP device (Figure 5-8c.1) corresponds to an approximate retardation of $\Gamma = 250 \pm 50$nm when compared with the Michel-Lévy chart (Figure 2-4).[49] Δn_{eff} can then be calculated using the measured LC layer thickness (d_{LC}) of 12 ± 1μm and the relation,

$$\Gamma = \Delta n_{eff} d_{LC}. \tag{5-2}$$

To account for the uncertainty associated with visually determining Γ, the upper and lower values of Γ ($\pm$50nm) and d_{LC} ($\pm$1μm) are used to calculate a range of possible Δn_{eff} values, resulting in $\Delta n_{eff} = 0.015 - 0.027$. Theoretical HAN director profiles are then generated by defining linear director tilt profiles ($\theta(z/d_{LC})$) for $0° \leq \theta_P < 90°$ using,

$$\theta(z/d_{LC}) = (\theta_1 - \theta_P)(z/d_{LC}) + \theta_P, \tag{5-3}$$

where z/d_{LC} is the normalised distance in to the LC slab and θ_1 is the assumed pretilt of the opposing flat homeotropic PI surface ($\approx 90°$). These tilt profiles (appendix C.4.a) are then used along with the refractive indices of MLC-6204 at T/T_{NI} = 0.99 (n_e=1.595 and n_o=1.507) in Equation (5-4), to calculate how the effective refractive index varies with distance through the slab ($n_{eff}(z/d_{LC})$).

$$n_{eff}(z/d_{LC}) = \frac{n_e n_o}{\sqrt{{n_e}^2 sin^2(\theta\,(z/d_{LC})) + {n_o}^2 cos^2(\theta\,(z/d_{LC}))}} \tag{5-4}$$

$n_{eff}(z/d_{LC})) - n_o$ is then plotted as a function z/d_{LC} (appendix C.4.b), and each function is integrated for z/d_{LC} between 0 and 1 to obtain the total birefringence of the slab (Δn_{eff}) for each value of θ_P. The range of measured Δn_{eff} values determined from polarised microscopy observations are then cross-referenced with these calculated values, using a plot of Δn_{eff} as a function θ_P (appendix C.4.c), to extract an approximate director pretilt on the wrinkled surface of $\theta_P = 35 \pm 9°$.

5.4.3.c Spatial Confinement

Another prominent feature of the LC alignment following the surface anchoring transition, is the tendency for the newly formed alignment state to self-organize in to elongated domains, aligned quasi-parallel to X (Figure 5-10a). As discussed in section 5.4.1, the aperiodic wall features of the WIP surfaces, formed by the inversion of cracks in the PDMS slab, are also aligned quasi-parallel to X. This elongated domain structure is therefore attributed to spatial confinement of the near-surface director, imposed by the presence of the protruding wall structures on the WIP surface. The measured mean wall spacing of 13$\pm$1μm, is in good agreement with the width of the elongated domains shown in Figure 5-10a.2,a.3, which are of the order 10−20μm wide (parallel to Y).

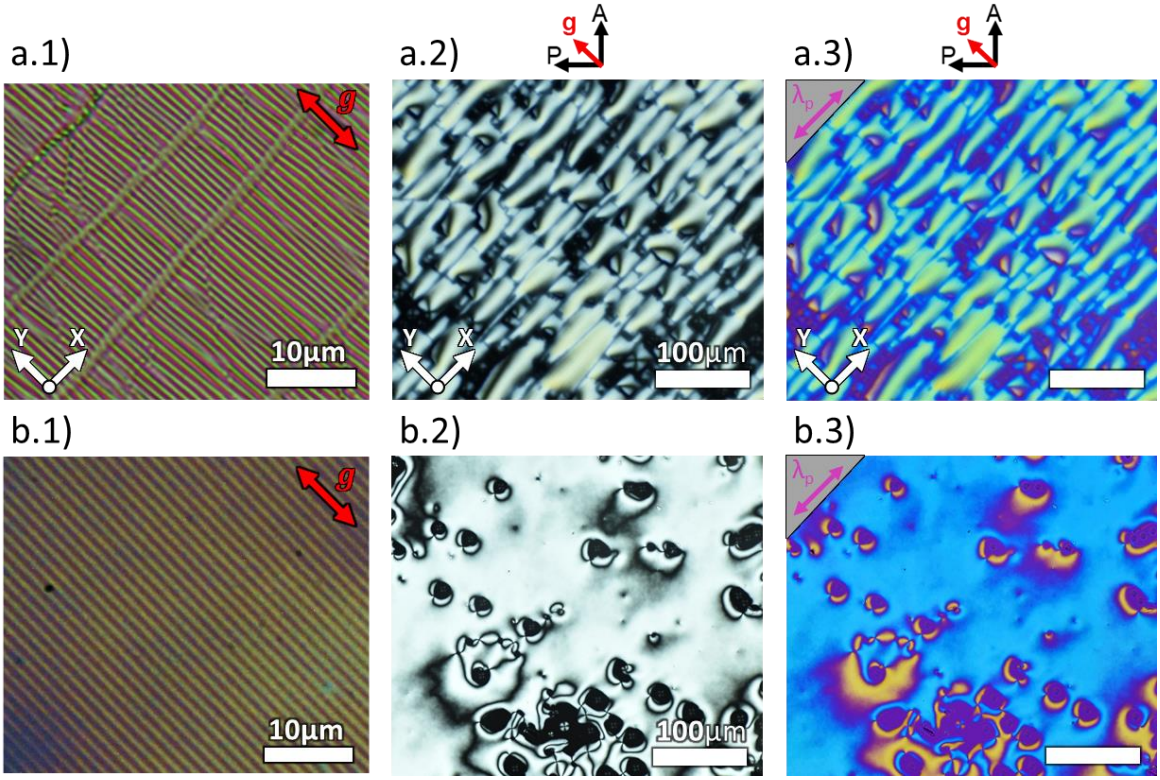

Figure 5-10: Comparison of alignment characteristics between VAN devices with (a) a homeotropic WIP surface and (b) a homeotropic PI surface imprinted with a linear surface relief grating (SRG), following a surface anchoring transition. Confirms the origin of the alignment domains observed in the homeotropic WIP device. (a.1) Optical microscopy image of a WIP surface. (a.2,a.3) POM observations of the homeotropic WIP device, exhibiting alignment domain formation. (b.1) Optical microscopy image of an imprinted SRG. (b.2,b.3) POM observations of the SRG device used as a control, exhibiting a near-uniform optical texture, without domains. Groove direction ($\boldsymbol{g}$), full-wave plate slow axis (λ_p).

5.4.3.c.i Origin of Confinement

To confirm that the domain structure is indeed caused by the walls, a control device is fabricated featuring a homeotropic polyimide imprinted with a linear surface relief grating (SRG); replacing the wrinkled texture in the homeotropic WIP device (Figure 5-7c). The imprinted SRG has a pitch within 15% (1040 $\pm$ 5nm), and a height within 5% (130 $\pm$ 5nm) of the dimensions of the periodic wrinkles. AFM analysis of this imprinted linear SRG surface is shown in appendix B.5. The resulting VAN device geometry, featuring a homeotropic SRG, has the same anchoring conditions and a comparable periodic surface topography to the hometropic WIP device, without the protruding wall structures found on the WIP surface. Optical microscopy images of the WIP and SRG surfaces are shown in Figure 5-10a.1 and Figure 5-10b.1 respectively, highlighting the comparable periodic grooves ($\boldsymbol{g}$) and the lack of features perpendicular to $\boldsymbol{g}$ in the case of the SRG.

POM observations of the control device show a similar anchoring transition at T/T_{NI} = 0.99, exhibiting a first-order white birefringence colour (Figure 5-10b.2). The addition of a full-wave plate, with λ_p perpendicular to $\boldsymbol{g}$, shows a similar blue-cyan birefringence colour (Figure 5-10b.3), indicating director tilt perpendicular to $\boldsymbol{g}$, as seen in the WIP device. The distinguishing feature of the resulting LC

alignment in the control device, is the lack of elongated domains, following the anchoring transition. This observation provides strong evidence that the domain formation in the homeotropic WIP device is due to the protruding wall features and their ability to spatially confine the frustrated alignment state.

5.4.3.c.ii Temperature Dependence

The domains formed by the spatial confinement, vary in size as a function of temperature. Within 0.3°C of the onset of the anchoring transition, the domains are approximately 10−20μm wide (parallel to Y in Figure 5-11a), which is of the order of the mean wall spacing, 13 ± 1μm. As the temperature of the system is increased to 0.9°C above the anchoring transition onset temperature, the domains broaden substantially to widths of ≈100μm (Figure 5-11b). Within these broader domains, large 4-brush defects are observed, around which the director orientation rotates azimuthally. This is indicated by the alternating yellow and blue birefringence colours in the λ-plate POM image shown in Figure 5-11b.2. The demonstrated temperature dependency of the domain size in this tilted alignment state, offers a potential facet of thermal tunability for future devices, which could utilize a spatially confined, frustrated alignment configuration.

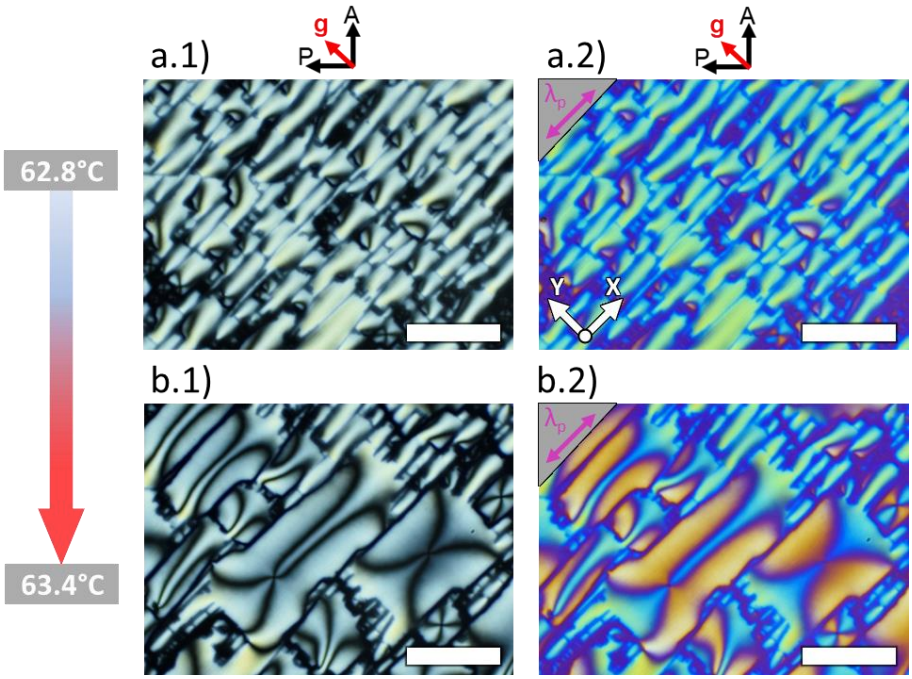

*Figure 5-11: POM images showing the broadening of spatially-confined alignment domains on heating. (a) Homeotropic WIP device at 62.8°C (0.3°C above anchoring transition onset temperature). (b) Homeotropic WIP device at 63.4°C (0.9°C above anchoring transition onset temperature). Wrinkle groove direction (**g**), full-wave plate slow axis (λ_p) and scale bars = 100μm.*

5.4.3.d Modulated Director Profile

The final aspect of the hometropic WIP system that will be discussed, is the intriguing, modulated director profiles observed following the surface anchoring transition. These observations shed light on an alignment configuration, induced by the combined influence of a frustrated director profile and

topographic spatial confinement, which bears a resemblance to the modulated director profiles found in planar optical LC devices.[224–226] Optical characterisation of this alignment state is presented, providing a base understanding of the modulation's origin, which has potential applications in engineered versions of similar topography-based LC devices.

5.4.3.d.i Alignment Overview

POM observations of the modulated director profile, exhibited by the homeotropic WIP device, are shown in Figure 5-12. The POM images in Figure 5-12a−c are captured at 63.8°C, after cooling through the isotropic-nematic phase transition. This is in contrast to the previous POM images in section 5.4.3b,c, which are all captured on heating in the nematic phase. At this temperature on cooling, the LC is in a biphasic state with island-domains of the nematic phase, surrounded by remaining isotropic regions (extinct areas around the perimeter of Figure 5-12a,b). Observing the anchoring transition of the LC, whilst additionally confined in these biphasic regions, showed that the length (parallel to X) was maximized while minimizing splitting of the tilted alignment domains. This ultimately leads to clearer images of the modulated director profile with more pronounced features (Figure 5-12c), compared to images captured on heating without the biphasic regions (Figure 5-12d).

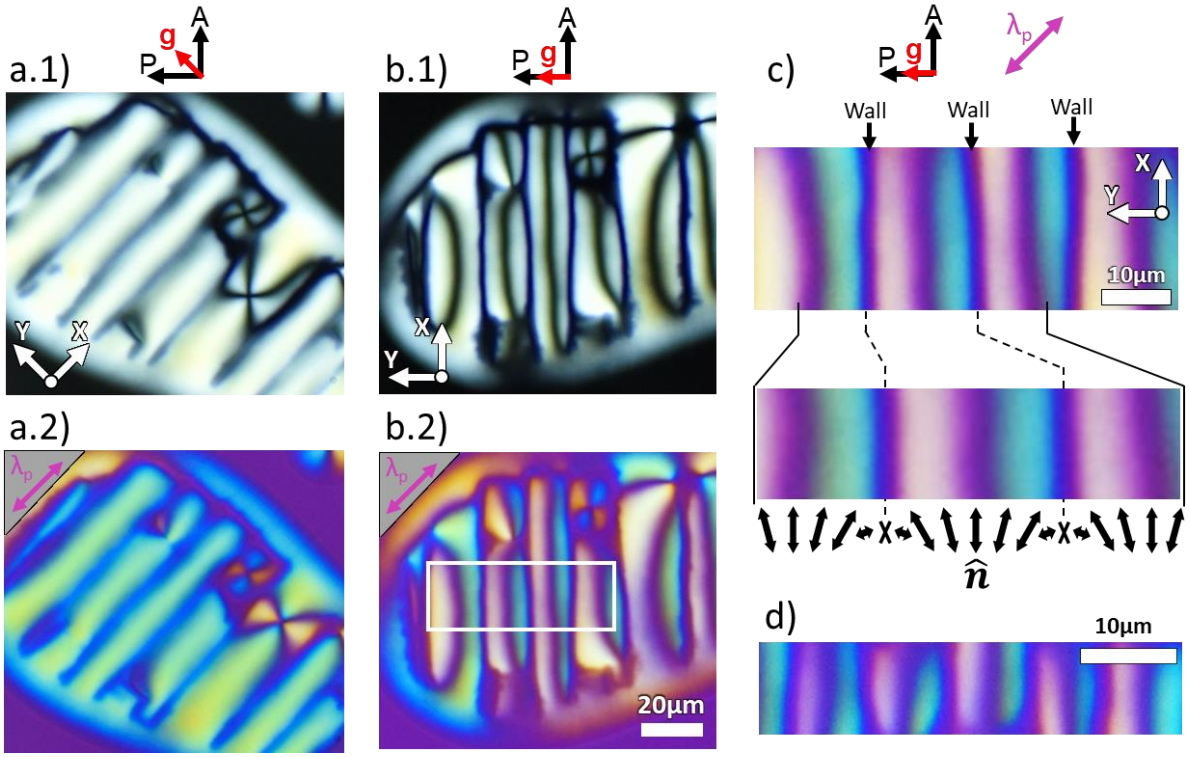

*Figure 5-12: POM observations of the modulated director profile in the homeotropic WIP device, (a−c) at 63.8°C after cooling through the isotropic-nematic phase transition and (d) at 62.7°C on heating through the nematic phase. (a) Wrinkle grooves (**g**) at 45° to the polarisers (P,A). (b) **g** aligned parallel to a polariser. (c) Enlarged image of the region indicated by the white box in b.2, with proposed director ($\hat{\boldsymbol{n}}$) profile denoted by black arrows. Full-wave plate slow axis (λ_p).*

Rotating the device between crossed polarisers, highlights the key features of the alignment state. With $\boldsymbol{g}$ at 45° to the polarisers (P, A), the elongated domains have a uniform pale-yellow birefringence colour throughout, separated by dark lines parallel to X (Figure 5-12a.1). These dark lines coincide with the wall orientation on the WIP surface, suggesting near-vertical director orientation on the walls, with some slight tilt causing them to appear grey rather than completely extinct.

Upon rotating the device by 45°, such that $\boldsymbol{g} \parallel$ P, the elongated domains remain mostly pale-yellow in appearance, but now exhibit a central dark band (Figure 5-12b.1). Given the known tilt direction is parallel to X, confirmed by the blue-cyan appearance of the λ-plate image in Figure 5-12a.2, it is safe to assume that these central dark bands correspond to the azimuthal director orientation also being parallel X, rather than parallel to Y. In this orientation, the dark lines separating the elongated domains appear completely extinct, further supporting the director being aligned vertically on the wall features.

5.4.3.d.ii Identifying Modulation

With the general properties of the alignment state covered, the following discussion focuses on the director modulation, revealed through λ-plate observations of the device with $\boldsymbol{g}$ parallel to one of the polarisers (Figure 5-12b.2). The addition of a λ-plate shows that the director orientation is splaying in the XY plane across the width of the domains, indicated by the contrasting cyan and pale-yellow colours separated by a central, diffuse magenta band. This behaviour is emphasized in Figure 5-12c, which shows enlarged views of the region indicated by the white box in Figure 5-12b.2.

These enlarged views show that there are two distinct length scales over which the director orientation varies; one is a gradual change over a distance of ≈15μm, of the order of the mean wall spacing (13 ± 1μm), and the second is a sharp change over a distance of ≈2μm, which is of the order of the width of the wall features, as shown in the AFM profile in Figure 5-4d. The proposed director ($\hat{\boldsymbol{n}}$) profile associated with these colour changes is denoted by the black arrows in Figure 5-12c, showing the periodic nature of this modulated alignment state, with a periodicity of ≈15μm. This proposed profile is supported by observations made by Yao *et al*., showing optical textures comparable to those in Figure 5-12c, and associated director profiles surrounding field-driven defect arrays in vertically-aligned LC devices.[221] Figure 5-12d shows the same director modulation observed on heating, demonstrating the potential for periodicities ≤10μm.

5.4.3.d.iii Origin of the Modulation

To aid in understanding the origin of this director modulation, schematics of the key contributing alignment behaviours are presented in Figure 5-13. Broadly speaking, the observed modulation is thought to be caused by director field distortions, simultaneously occurring in two orthogonal planes of reference.

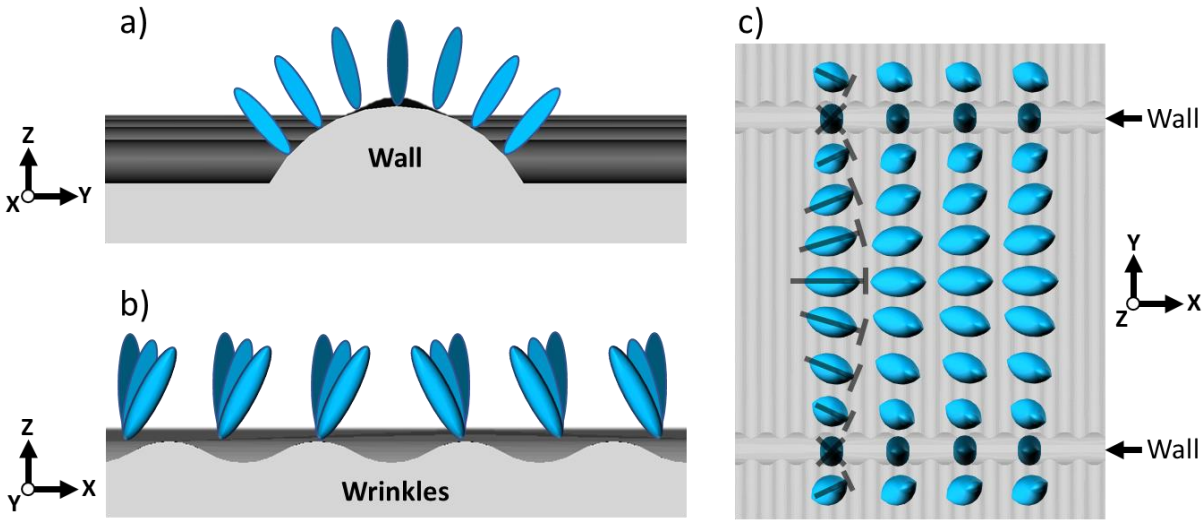

Figure 5-13: Schematic representations of, (a) director ($\hat{\boldsymbol{n}}$) splay in the YZ plane associated with the wall features, (b) director tilt in the XZ plane associated with the periodic wrinkles and (c) the proposed modulated director profile between two adjacent wall features. The 'nail representation' is used in (c) to signify tilt, where the 'T' *or nail symbols indicate the projection of* $\hat{\boldsymbol{n}}$ *onto the plane of the page. The head of the nail symbols protrude out of the plane of the page.*

The most notable contribution to the director modulation comes from the near-vertical director alignment on the protruding wall features. Given the dark/extinct appearance of the wall features shown in Figure 5-12, the director is likely to be near-vertical on the peaks of the walls and is then expected to splay in the YZ plane over the remaining width due to the homeotropic anchoring of the polyimide, as shown in Figure 5-13a. Similar director profiles have been reported around micro-pillar structures coated in homeotropically aligning polymers.[22,23]

As previously established in section 5.4.3.b.i, the periodic wrinkle texture induces director tilt in the XZ plane *via* a surface anchoring transition (Figure 5-13b). As the surface topography transitions from a wall to the wrinkled texture, the wall-induced director splay in the YZ plane, combines with the wrinkle-induced director tilt in the orthogonal XZ plane, resulting in a net azimuthal director reorientation in the XY plane that manifests as director splay between adjacent wall features or across the width of the alignment domains (parallel to Y). A two-dimensional overview of this three-dimensional modulated director profile is depicted in Figure 5-13c, showing the proposed tilt and XY orientation of the director between two adjacent wall features, using the 'nail representation' of the director (T symbols).

5.5 Summary

In this chapter, a spontaneously formed linear wrinkle texture, with sub-micron scale features, has been simply manufactured and transferred in to planar and homeotropic PI alignment layers, to study how LC surface alignment is affected by the resulting topography under different anchoring conditions.

A planar wrinkle-imprinted polyimide (WIP) surface is shown to uniformly align the nematic director, emphasized through the use of a hybrid-aligned nematic (HAN) device geometry, to minimize the opposing surface's influence on azimuthal director orientation. Full-wave plate observations of the planar WIP device, provide optical confirmation of the director ($\hat{\boldsymbol{n}}$) aligning parallel to the grooves ($\boldsymbol{g}$) of the periodic wrinkle texture. This was facilitated by the imprinted polyimide (IPI) workflow, which inherently forms regions of unpatterned PI surrounding the applied working stamp. This unpatterned, planar PI region results in a Schlieren texture containing point defects, which were used as in-built reference points to confirm the orientation of $\hat{\boldsymbol{n}}$ in the wrinkled area.

Wrinkles with homeotropic anchoring have been explored for the first time, with conoscopy observations indicating topography-induced, degenerate director tilt. A surface anchoring transition is observed in the homeotropic WIP device as $T \rightarrow T_{NI}$, resulting in a frustrated alignment configuration with the director tilted in a plane perpendicular to $\boldsymbol{g}$. Microscale confinement and spatial modulation of the director is also observed, notably attributed to director distortions induced by PDMS surface-cracking artefacts; a by-product of the wrinkling process that is typically ignored. These findings showcase PDMS wrinkling as a versatile, exploratory tool for studying LC-surface interactions and demonstrate a facile method of inducing microscale director modulation, which may aid in the design of engineered surfaces with similar functionality. The insight gained into the origin of these modulated surface alignments, has potential implications in the design of LC-based waveguides, flat optics and AR-VR devices.

Chapter 6 Liquid Crystal Surface Alignment and Pretilt on Sub-micron Homeotropic Gratings

6.1 Overview

In the previous chapter, a spontaneous patterning approach was used to create wrinkled LC alignment layers with a periodic grating-like morphology. In this chapter a high-precision micropatterning technique is used, in the form of electron-beam (e-beam) lithography, to fabricate bespoke surface relief gratings for transfer in to polyimide alignment layers. These tailored structures provide a precision testbed for characterising and elucidating the complex LC alignment behaviour induced by surface relief gratings with homeotropic anchoring.

A selection of gratings with square-wave profiles are fabricated with periodicities ranging from 300nm to 1.2μm. Initially patterned into a grown oxide layer on a silicon wafer, the grating structures are copied using replica moulding to allow transfer into LC alignment layers *via* soft lithography; the length-scale limitations of which will be discussed. The gratings are transferred into a homeotropic polyimide and the resulting LC alignment is analysed *via* orthoscopic and conoscopic polarized microscopy. Observations indicate the presence of a uniformly aligned, frustrated director profile that is stable at room temperature, induced by surface anchoring transitions on the homeotropic grating structures. Similar alignment behaviour was exclusively observed at high temperatures and therefore significantly reduced elastic constants, in the homeotropic wrinkle device discussed previously in section 5.4.3.b. Conoscopic examination shows that this frustrated alignment state possesses a controllable and spatially uniform surface pretilt at the grating interface, with a magnitude that scales inversely with the grating period/pitch. This highlights the potential for controlling LC surface pretilt by altering the lateral dimensions of surface relief gratings with homeotropic anchoring.

6.2 Introduction

As the focus of this chapter is on the LC alignment properties of homeotropic grating structures, a brief introduction is first given to the areas of LC alignment on homeotropic surface topographies and surface anchoring transitions, with the aim of highlighting how the work in this chapter relates to and builds upon prior knowledge in these areas.

Early studies of LC alignment on obliquely evaporated silicon oxide, demonstrated that adding homeotropically aligning surfactants to the column-like relief structures, provided a means controlling pretilt direction *via* distortion of the near-surface director field.[73] Aside from pretilt control, surface protrusions with homeotropic anchoring have also been used to guide the formation LC alignment domains in Multi-Domain Vertical Alignment (MVA) displays, leading to wider viewing angles and

higher contrast ratios than typical VAN displays.[227] The most notable and commercially successful use of homeotropic surface relief structures for LC alignment, is the Zenithal Bistable Display (ZBD).[16,228,229] This low-power display technology relies upon homeotropic blazed grating structures to distort the near-surface director field, giving rise to two unique surface pretilts at the grating interface. This forms the basis of the ZBD's optical modulation, by reversibly switching between two energetically stable and topologically distinct director configurations.[17,230]

The most recent exploration of the ZBD platform was carried out by Jones,[77] wherein device performance was studied as a function of polar anchoring strength on the grating surface [71] and, of particular relevance to the work in this chapter, initial investigations were carried out on the LC alignment properties of sub-micron scale homeotropic gratings. These e-beam fabricated gratings were transferred in to LC devices with the standard embossing methodology used in ZBD manufacturing,[128,231] utilizing specialized apparatus not readily available to all researchers. Conventional PDMS replica moulding of the gratings was attempted, but was found to only partially fill the grating masters and leave behind residue upon demoulding, resulting in poor fidelity replicas and spoiled master structures. Given the wider accessibility of replica moulding and the ability to imprint polyimides with PDMS, the work in this chapter revisits the replication of e-beam grating structures with PDMS. This aims to determine the limits of the technique and demonstrate the potential for creating sub-micron scale features with homeotropic anchoring, using a simple imprinting process and conventional polyimide alignment layers.

Although the work in this chapter is inspired by the bistable grating alignment exhibited by ZBD devices, bistability is not the focus of this investigation. Instead, the tilted alignment state with frustrated surface anchoring, known as the 'defect state' in ZBD terms, is exclusively studied to gain an insight into the relationship between grating dimensions and pretilt on the grating surface. Sub-micron scale homeotropic grating systems and associated surface anchoring transitions have been studied extensively by Cattaneo *et al*., where the impact of grating depth on the overall alignment and surface pretilt of frustrated director configurations was reported.[113] Similar anchoring transitions and frustrated surface alignments have also been demonstrated on topographies without homeotropic anchoring, such as self-assembled nanoparticle arrays [112] and microgroove grids with alternating groove directions.[232] The work by Cattaneo et al. and subsequent theoretical modelling of anchoring transitions on homeotropic gratings,[233] serve as critical references for the work in this chapter, which specifically focuses on how surface alignment properties, such as pretilt angle, are affected by the lateral grating dimensions for a fixed grating depth.

6.3 Methods

This section covers the experimental approach used to fabricate the surface relief gratings and transfer them into LC devices. Grating design will be discussed, to give an overview of the range of structures selected for the study, followed by their fabrication *via* electron-beam lithography (EBL) and dry-etching. Emphasis is placed on how the gratings are copied from the original silicon wafer *via* replica moulding, and the considerations made to account for their fine features. This includes pre-treating the wafer to aid demoulding and using a modified replica moulding process to create a more robust working-stamp for pattern transfer.

6.3.1 Grating Design

A 100mm diameter silicon wafer is used as the supporting substrate for the grating master structures in this work. The grating dimensions and arrangement of the wafer are specified by considering the following factors:

- Resolution limit of the EBL resist (UV60);
- Minimizing the time required for the EBL system to write the pattern;
- Dimensions and layout of the final LC device for effective characterisation;
- Ease-of-handling during pattern transfer.

The linear gratings are fabricated by first writing a line-space pattern in to an EBL resist layer (UV60, Microresist Technology). The lower bound of the grating pitch parameter space is therefore dictated by the minimum achievable linewidth (l) that can be reliably written into the UV60 resist, which is 150nm. This corresponds to a minimum grating pitch of 300nm, when using the highest density line-space ratio of 1:1. The upper bound of the pitch parameter space is specified by incrementally varying the linewidth between 150nm and 350nm, with line-space ratios of 1:1 – 1:2.5. The grating profiles associated with these line-space ratios are represented schematically in Figure 6-1. In relation to the final relief structures, a ‘line’ corresponds to a trench in the pattern and a ‘space’ corresponds to a ridge in the pattern. (Figure 6-1d).

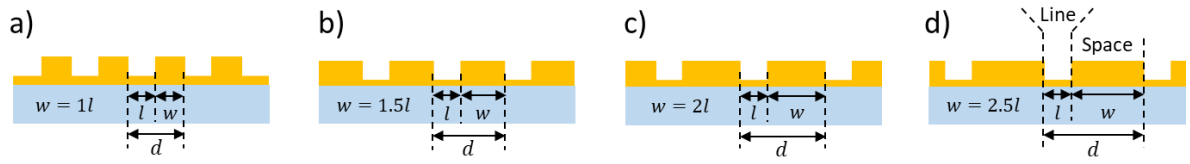

Figure 6-1: Schematic surface relief grating profiles with line/trench width (l), space/ridge width (w), pitch (d) and line-space ratios of a) 1:1, b) 1:1.5, c) 1:2 and d) 1:2.5. The terms ‘line’ and ‘space’ are defined in d).

A summary of the grating dimensions selected for fabrication is presented in Table 6-1, where gratings with the same linewidth (l) are grouped into 'arrays' numbered 1 through 5, for ease of reference.

Table 6-1: Summary of grating dimensions selected for study, showing the grating pitch (d) for a given line-space ratio and linewidth (l). Gratings with the same linewidth are grouped into 'arrays' numbered 1 through 5. Highlighted columns denote the structures used in the final LC devices, chosen based on the observed structural stability of the PDMS working stamps discussed in section 6.4.1.

Line-Space Ratio	Grating Pitch (d), nm				
	Array (1) l = 150nm	Array (2) l = 200nm	Array (3) l = 250nm	Array (4) l = 300nm	Array (5) l = 350nm
1 : 1	300	400	500	600	700
1 : 1.5	375	500	625	750	875
1 : 2	450	600	750	900	1050
1 : 2.5	525	700	875	1050	1225

With the grating dimensions selected, the arrangement of the supporting wafer is now considered. Given that each grating is comprised of sub-wavelength scale lines (<400nm), which are sequentially written by the EBL system, the write time for each grating area can be substantial. The area occupied by each grating is therefore specified to best suit the length scale on which the final device will be observed. The final LC devices are characterised with POM, using a 20x microscope objective with a 1mm^2 field of view. Each grating area is therefore sized at 5 x 5mm, providing adequate area to avoid any non-uniformities that may occur during replication and pattern transfer.

As covered in Table 6-1, gratings with the same linewidth are grouped into arrays, where each array contains four grating areas with a different line-space ratio. The wafer, array and final LC device layouts are summarized schematically in Figure 6-2. Since the aim of the study is to characterise the relationship between grating dimensions and LC alignment properties, each array of four gratings is arranged to fit within a typical 30 x 30mm active area of a LC device. For a given array, this enables the optical properties associated with each grating area to be compared at a fixed LC layer thickness, as all four grating areas are contained within the same parallel-plate device. This simplifies analysis because any variation in optical properties can be confidently attributed to changes in grating dimensions, rather than a difference in LC layer thickness, which would be difficult to avoid if separate devices were being compared. Additionally, spacing the gratings in this way means that when the full wafer replica is cleaved into individual working stamps for each array, the physical size of each stamp is of the order of 25 x 25mm (represented approximately in Figure 6-2b). This is a practical size for easy handling and provides a sufficiently large stamp contact area that maximizes the stability of the hotplate press apparatus used during imprinting, ultimately leading to more controlled and uniform pattern transfer.

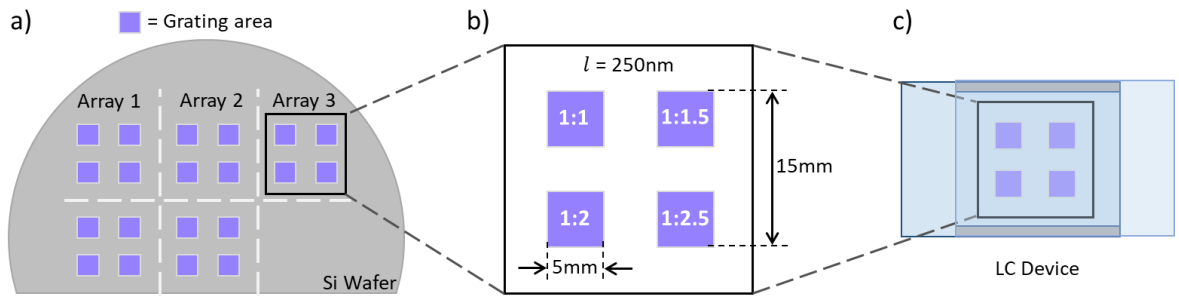

Figure 6-2: (a) Wafer, (b) array and (c) LC device arrangements, with grating areas denoted by purple boxes.

6.3.2 Master Fabrication

The grating master structures used in this work were fabricated in collaboration with the Leeds Nanotechnology Cleanroom, in the Electronic and Electrical Engineering department at the University of Leeds. Process development and fabrication of the grating masters was performed by Dr. Mark Rosamond. The adopted process flow is summarized in Figure 6-3.

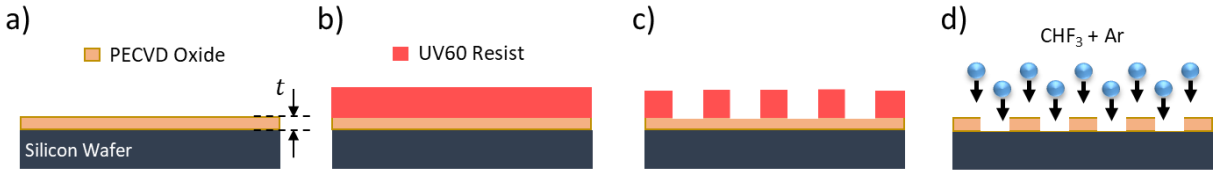

Figure 6-3: Process flow for patterning grating master structures into a silicon-oxide layer, on a silicon wafer. (a) Oxide layer is grown on the wafer using plasma-enhanced chemical vapour deposition (PECVD), with a layer thickness (t) of 372 ± 3nm. (b) A layer of UV60 (deep-UV photoresist) is spin coated on the oxide layer. (c) Line-space pattern is written into the photoresist using electron-beam lithography and developed to create an etch mask. (d) Anisotropic dry etching, with trifluoromethane (CHF_3) and Argon (Ar) process gases, transfers the mask pattern into the underlying oxide layer. The oxide is cleared in the etched regions (entirely removed to expose the underlying silicon surface).

The grating fabrication process revolves around the use of nanoscale patterning *via* EBL. An oxide layer is first grown on the surface of a 100mm diameter silicon wafer, using a plasma-enhanced chemical vapour deposition (PECVD) process. The thickness of the grown oxide layer is measured with a reflectometer (Thetametrisis FR-Pro D VIS/NIR), with a measured thickness of 372 ± 3nm. The oxide layer is spin coated with a high resolution, positive-tone photoresist (UV60 – 0.58, Microresist Technology), which serves as a mask for the subsequent etch process. The grating arrays and global alignment markers are written into the UV60 resist layer with a JEOL JBX-6300FS e-beam lithography system.

After exposure, the pattern is developed and transferred into the underlying oxide layer *via* reactive-ion etching (RIE) with trifluoromethane (CHF_3) and Argon (Ar) process gases. The RIE process was performed at a chamber pressure of 58mtorr, with gas flows of 25sccm (standard cubic centimetres per minute) for both CHF_3 and Ar, with an RF power of 90W. As illustrated in Figure 6-3d, the etch is

carried out until the oxide layer is cleared i.e. the underlying silicon surface is exposed. This allows the resulting feature heights to be confidently inferred from the previously measured thickness of the PECVD oxide layer. Any remaining UV60 is stripped from the wafer using a remover and the patterned wafer is re-coated with a conventional positive-tone photoresist (Microposit S1813). This is used to add larger labels to each grating area for identification, patterned with conventional optical lithography using the EBL-patterned global markers for alignment. Once developed, the labels are transferred into the oxide layer using the same RIE process as detailed above.

6.3.3 Pattern Transfer

As in the previous chapters, the aim of fabricating surface relief structures is to transfer them in to polyimide LC alignment layers *via* imprinting with a soft working stamp. In cases where the original relief structures have sub-micron scale dimensions, this soft lithographic approach benefits from modification to combat deformation and collapse of the copied structures. This structural instability is associated with the inherent flexibility of polydimethysiloxane (PDMS) and the tendency of adjacent features to adhere to one another.[234,235] The following section details the methodology used to create a soft replica of the sub-micron silicon-oxide grating structures, highlighting the additional steps taken to maximize the fidelity and robustness of the final working stamp. The overall process flow from grating master structures to LC device integration, is illustrated schematically in Figure 6-4.

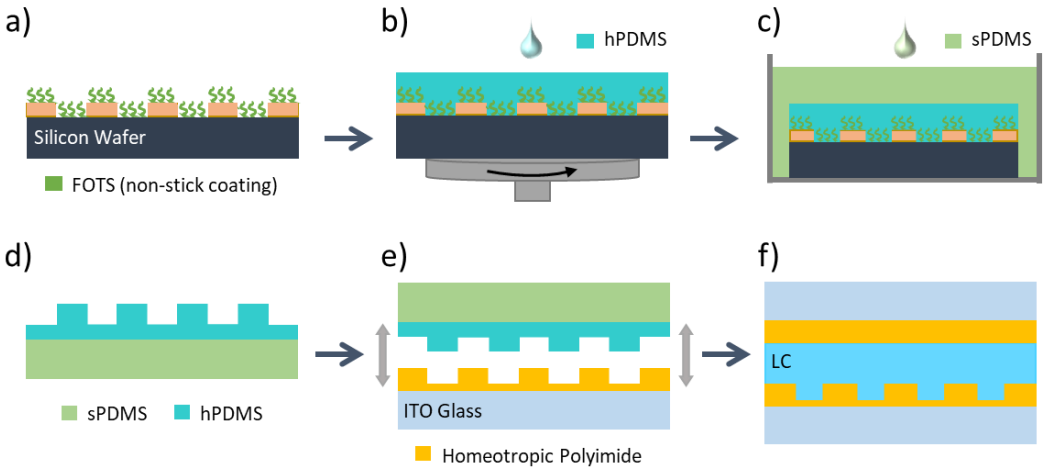

Figure 6-4: Process of transferring silicon-oxide grating structures in to a polyimide LC alignment layer via a soft replica. (a) Anti-stick coating of perfluorooctyltrichlorosilane (FOTS) is vapour deposited on the grating master structures, to assist in demoulding. (b) A high-modulus PDMS (hPDMS) prepolymer is spin coated on the FOTS-treated wafer and partially cured. (c) The wafer is then cast in a conventional 'soft' PDMS (sPDMS) prepolymer, followed by thermal curing. (d) The PDMS is demoulded from the wafer, forming a composite-PDMS working stamp with a stiff hPDMS surface layer supported by a compliant sPDMS backing. (e) A spin coated layer of homeotropic polyimide (SE-4811) is imprinted with the composite stamp and (f) assembled in to a parallel-plate LC device, opposite a flat layer of SE-4811.

6.3.3.a Anti-stick Coating

To aid demoulding of the PDMS replica from the grating structures, an anti-stick coating of 1H,1H,2H,2H-Perfluorooctyltrichlorosilane (FOTS) (Alfa Aesar), is vapour-deposited on the wafer prior to replication (Figure 6-4a). Anti-stick coatings are well-established in nanoimprint lithography processes, where they help prolong the lifespan of working stamps.[236] This is particularly important when handling sub-micron or nanoscale relief structures, where the adhesion between the master and the replica, or imprint layer, is more prominent.[237] Application of a FOTS coating reduces the surface energy of the grating structures, due to the fluorinated tail groups of the FOTS molecules. This minimizes adhesion between the gratings and the PDMS, leading to a smoother demoulding process and an increased likelihood of a faithful replica.[238]

The FOTS coating is applied to the wafer using a room temperature vapour-deposition process, as reported in other works.[239] A glass desiccator is used as the deposition chamber, which is cleaned with acetone and purged with nitrogen gas prior to deposition, to minimize humidity and the unwanted polymerization of chlorosilanes due to the presence of water.[237] The wafer and a glass coverslip are cleaned in isopropanol and dried in an oven at 130°C for 1 hour. The wafer is exposed to an ultraviolet-ozone treatment for 5 minutes before transfer in to the desiccator, to increase the number of –OH groups on the surface for the silanes to bond to.[240]. After a 15 minute nitrogen purge, 15µL of FOTS solution is dispensed on the coverslip adjacent to the wafer and the chamber is evacuated, sealed and left under vacuum for 2 hours for the deposition to take place. The chamber is then vented and the wafer is rinsed in acetone, dried and placed in an oven at 90°C for 1 hour to complete the reaction.[241] The reduced surface energy of the FOTS-treated silicon-oxide surface, is confirmed by the increased contact angle of a 10µL droplet of de-ionized water, relative to that of an untreated surface (Figure 6-5).

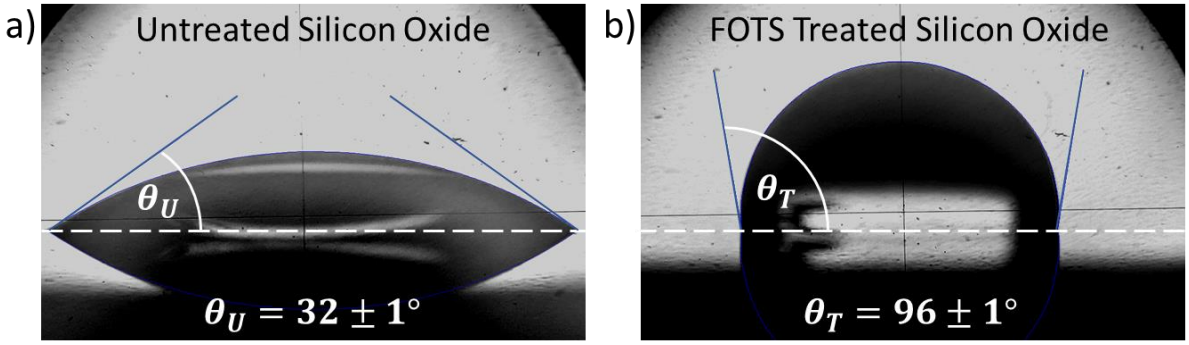

Figure 6-5: Imaged contact angles of 10µL droplets of de-ionized water on (a) untreated (θ_U) and (b) FOTS-treated (θ_T) sections of PECVD silicon-oxide. This shows the increased hydrophobicity/reduced surface energy of the master wafer, as a result of the FOTS anti-stick coating.

6.3.3.b Composite-PDMS Replication

The grating structures in this work are comprised of densely packed line features, with widths of the order of 150−350nm. The conventional approach to replica moulding (section 3.2.2.a), relying solely on Sylgard-184 PDMS (sPDMS), can lead to the deformation and collapse of structures on this length scale, due to the material's low Young's modulus. To address this limitation, a two-layer replica moulding technique was employed, initially developed by Odom *et al*.[242] This approach uses a composite-PDMS working stamp, formed from a high-modulus PDMS (hPDMS) surface layer and an sPDMS supporting slab, with respective Young's moduli of 8−12MPa and 2−3MPa.[243] The use of a compliant sPDMS support slab, ensures conformal contact with the substrate during imprinting and helps mitigate cracking of the relatively brittle hPDMS surface layer.[244]

This composite-PDMS methodology is used to create a soft replica of the grating wafer, using the original work and subsequent detailed reports of the method as guidance.[242,245] The sPDMS (Sylgard 184, Dow Corning, Inc.) and hPDMS (PP2-RG07 Gelest® hPDMS, Gelest, Inc.) precursor mixtures are prepared with prepolymer:crosslinker ratios of 10:1 and 1:1, in quantities of 50ml and 2ml respectively. Once thoroughly mixed, the precursors are degassed in a vacuum desiccator for 45 minutes. The hPDMS mixture is poured on to the FOTS-treated wafer and spin coated at 1000rpm for 40s (Figure 6-4b), followed by partial curing in an oven at 80°C for 4 minutes. A partial cure is identified by the spun hPDMS layer being tacky to the touch, tested in sacrificial areas of the wafer. The hPDMS-coated wafer is then placed in a FOTS-treated petri dish, on a shallow bed of the sPDMS mixture, to prevent air being trapped under the wafer. The remaining sPDMS is cast on top of the wafer and cured in an oven at 80°C overnight (16 hours), resulting in an overall slab thickness of ≈3mm (Figure 6-4c). The composite-PDMS replica is then slowly demoulded from the wafer (Figure 6-6b), and cleaved into 25 x 25mm sections to form the individual working stamps for each grating array.

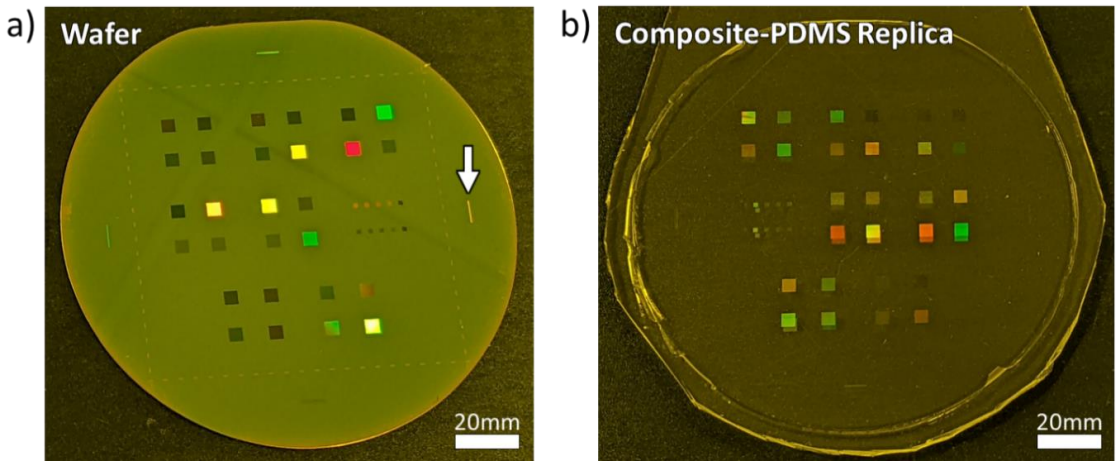

Figure 6-6: (a) Photograph of the original wafer, with square regions of linear surface relief gratings patterned via electron-beam lithography. Arrow denotes one of four sacrificial grating areas on the wafer perimeter, used for cross-sectional imaging via SEM. (b) Photograph of the composite-PDMS replica of the wafer.

6.3.4 LC Device Geometry

The grating structures are transferred in to LC devices by imprinting a spin-coated layer of homeotropic polyimide (SE-4811) on ITO glass (Figure 6-4e), using the composite-PDMS replicas as working stamps (imprinting process detailed in section 3.2.2.b). The imprinted grating surfaces are assembled in a parallel-plate configuration opposite an unpatterned layer of SE-4811, forming a vertically-aligned nematic (VAN) device geometry. The device is capillary filled with MLC-6204 in the isotropic phase at 70°C, with an LC layer thickness (d_{LC}) of the order of 7µm. Images of the working stamps and LC devices, along with a schematic cross-section of the device geometry, are shown in Figure 6-7.

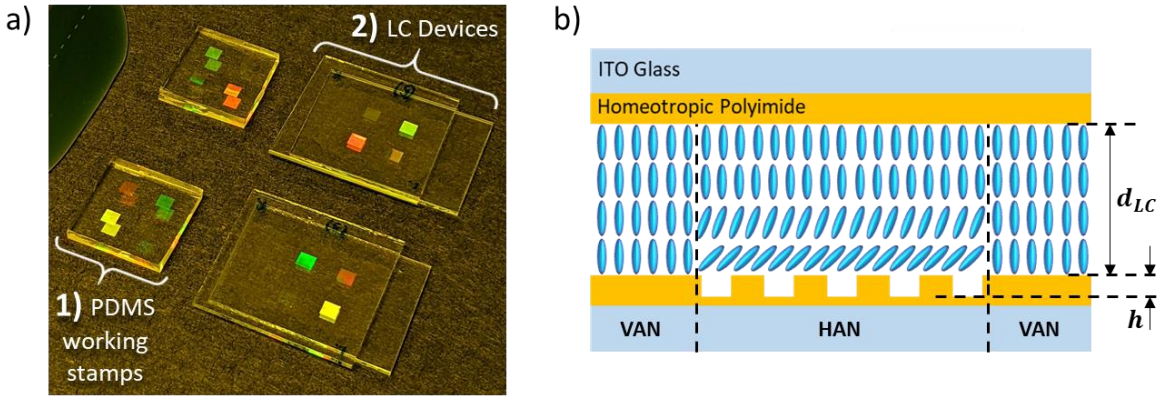

Figure 6-7: (a) Photograph of (1) composite-PDMS working stamps and (2) assembled LC devices. (b) Schematic cross-section of LC devices featuring homeotropic grating structures with a height (h), and an LC layer thickness (d_{LC}) of the order of 7µm. Vertical black dashed lines indicate the boundaries of grating and non-grating regions in the devices, highlighting the expected hybrid-aligned nematic (HAN) and vertically-aligned nematic (VAN) director profiles in each area.

6.4 Results and Discussion

The results of this study are now presented. Initial focus is placed on the observed limit of structural stability in the composite-PDMS working stamps, to ensure the most stable grating replicas are selected for pattern transfer in to the final LC devices. The impact of these homeotropic grating structures on LC surface alignment is then reported, where orthoscopic polarized microscopy provides an overview of the resulting alignment state and conoscopy is used to quantify the topography-induced changes in optical properties. Theoretical modelling of the bulk director profile is then discussed, as a means of extracting approximate values of surface pretilt at the LC-grating interface.

6.4.1 Stability of Composite-PDMS Replica

The fidelity of the composite-PDMS replicas is assessed using cross-sectional scanning-electron microscopy (SEM). Sacrificial areas of the original wafer and the corresponding PDMS replica (Figure 6-6), are cleaved perpendicular to the grating groove direction, providing a cross-sectional view of the grating structures. Prior to imaging, a layer of gold is sputter-coated on the samples to improve image contrast.

6.4.1.a Feature Collapse – Grating Array (1)

To better understand the limits of composite-PDMS replication, the structures with the finest features are used as an initial reference point (grating array 1, linewidth = 150nm). Figure 6-8 summarizes the cross-sectional SEM images captured of the original etched grating structures (Figure 6-8a) and the subsequent PDMS replicas (Figure 6-8b) of grating array 1. At a line-space ratio of 1:2.5, the PDMS replica shows good structural stability with no collapse of the 150nm wide ridges on the PDMS surface (Figure 6-8b.1). The peaks of the PDMS ridges are more rounded than the base of the silicon-oxide trenches from which the replica was taken. This is likely due to the hPDMS precursor struggling to entirely fill the trenches, given their 150nm width and ≈370nm height, along with the fluorinated anti-stick coating used, which can inhibit resins from filling microstructures.[246] Aside from a loss of fidelity in the profile of the structures, the height of the PDMS ridges remains within 1-2% of the oxide trench depth, indicating that the hPDMS filled the majority of the trenches and shrunk minimally after curing and demoulding. For the remaining line-space ratios of 1:2, 1:1.5 and 1:1, the replica became unstable, exhibiting lateral collapse of the PDMS ridges after demoulding. This can be seen in Figure 6-8b.2−b.4, where two or more adjacent ridges coalesce to form one wider ridge, due to the inherent flexibility of PDMS and the surface adhesion experienced between neighbouring features upon demoulding.[234,247]

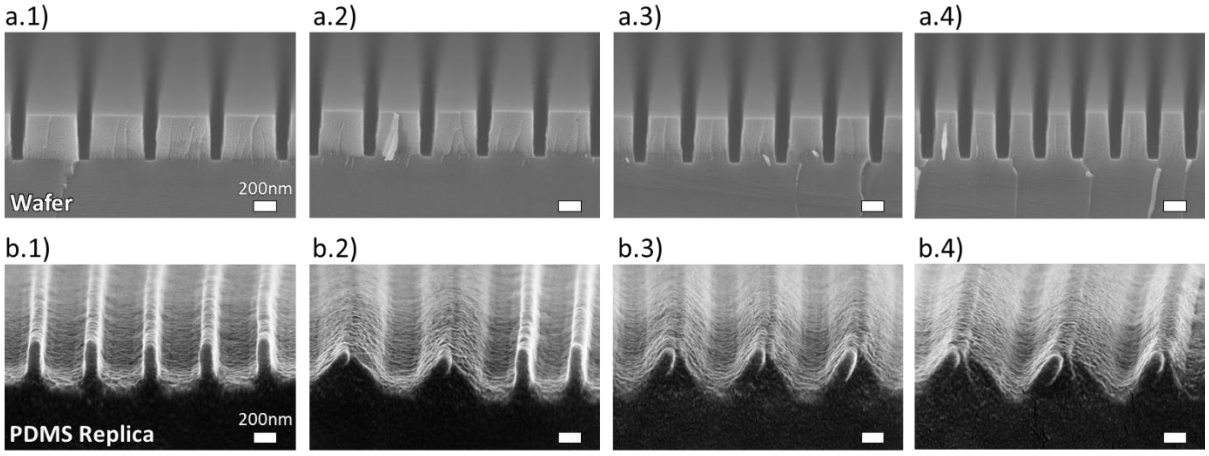

Figure 6-8: SEM cross sections of grating array 1 (linewidth = 150nm), with line-space ratios of (1) 1:2.5, (2) 1:2, (3) 1:1.5 and (4) 1:1. (a) Original, etched silicon-oxide grating structures and (b) composite-PDMS replicas. (b.2, b.3) Examples of paired ridges (two ridges coalescing in to one) due to lateral collapse. (b.4) Left and middle coalesced ridges show a three-ridge collapse. Scale bars = 200nm.

6.4.1.b Stable Features – Grating Array (3)

Given that only one out of the four grating regions in array 1 resulted in a stable PDMS replica, this array cannot be used for pattern transfer. Grating array 3, with linewidths of 250nm (100nm wider than array 1) was instead selected for SEM analysis, anticipating a reduction/removal of lateral collapse during demoulding, owing to the wider and therefore more robust ridges on the resulting PDMS replica. Figure 6-9 shows cross-sectional SEM images of the original etched oxide structures (Figure 6-9a) and subsequent composite-PDMS replica (Figure 6-9b) of grating array 3. At this linewidth of 250nm, the PDMS replica remains structurally stable at all line-space ratios, even at a ratio of 1:1 where the ridges are most densely packed and likely to adhere to one another (Figure 6-9b.4). The peaks of the PDMS ridges appear rounded relative to the sharp corners of the etched trenches, again suggesting that the hPDMS precursor did not fill into the corners of the trenches, as discussed in section 6.4.1.a.

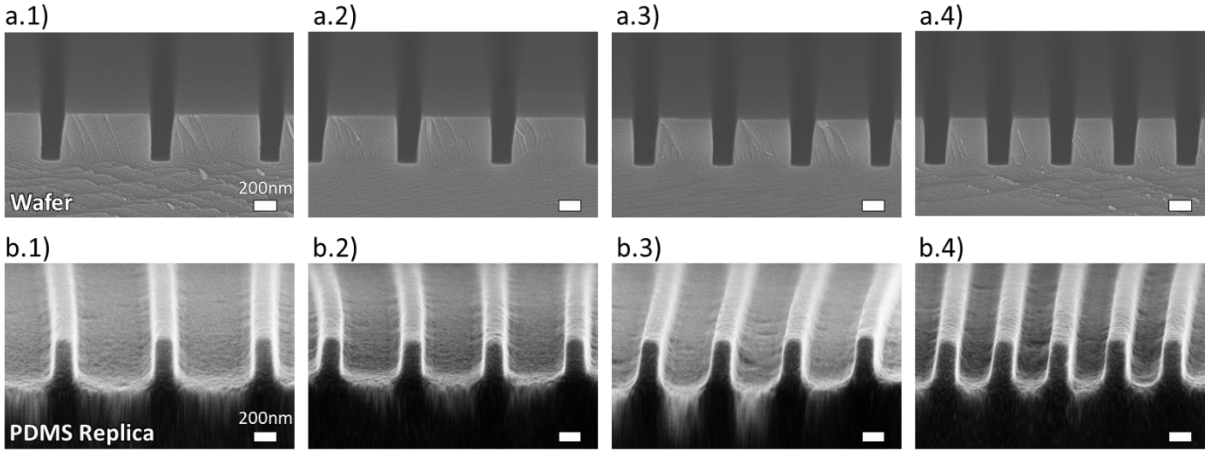

Figure 6-9: SEM cross sections of grating array 3 (linewidth = 250nm), with line-space ratios of (1) 1:2.5, (2) 1:2, (3) 1:1.5 and (4) 1:1. (a) Original, etched silicon-oxide grating structures and (b) composite-PDMS replicas. At this linewidth, the PDMS structures remain stable at all line-space ratios.

6.4.1.c Device Considerations

Using the information gathered from SEM analysis of the PDMS replicas, the choice of grating structures that will feature in the final LC devices is now considered. As covered in section 6.4.1.a, the PDMS replica of grating array 1 is unsuitable for pattern transfer, as three out of four of the associated grating regions suffered from lateral collapse and therefore no longer match the dimensions specified in the initial design. In contrast, the PDMS replica of grating array 3 was found to be structurally stable in all four grating regions after demoulding, with no indication of lateral collapse. With this in mind, the structures in array 3 were selected as the minimum linewidth gratings to be studied in the final LC devices; chosen over the lower-linewidth grating array 2 to err on the side of caution with respect to stamp deformation during imprinting.[235] Within array 3, the grating pitch varies between 500nm and 875nm, so in order to maximize the range of grating pitches in the study, array 5 is also selected for investigation, with grating pitches between 700nm and 1225nm (dimensions summarized in Table 6-1).

This enables the grating-mediated LC surface alignment and associated optical properties to be characterised over a broad pitch range of 725nm, with grating arrays 3 and 5 contained within their own individual LC devices (see Figure 6-7a.2).

6.4.1.d Imprinted Pitch Confirmation via Diffraction

After imprinting the polyimide alignment layers with the composite-PDMS stamps, the pitch of the resulting polyimide gratings is confirmed *via* optical diffraction patterns. This is done to ensure that the PDMS structures didn't deform or collapse during the imprinting process and that faithful pattern transfer was achieved, prior to final device assembly. Optical diffraction was chosen over SEM for pitch measurements, because it is non-contact and therefore won't impact surface alignment properties, non-destructive since no sample cleaving is required and feasible given that the gratings are on transparent ITO-glass substrates (as opposed to the opaque silicon wafer that supported the master structures). The diffraction experiment was performed with 404nm wavelength laser light as previously detailed in sections 3.3.2 and 4.3.3.a, and the results are summarised below in Figure 6-10.

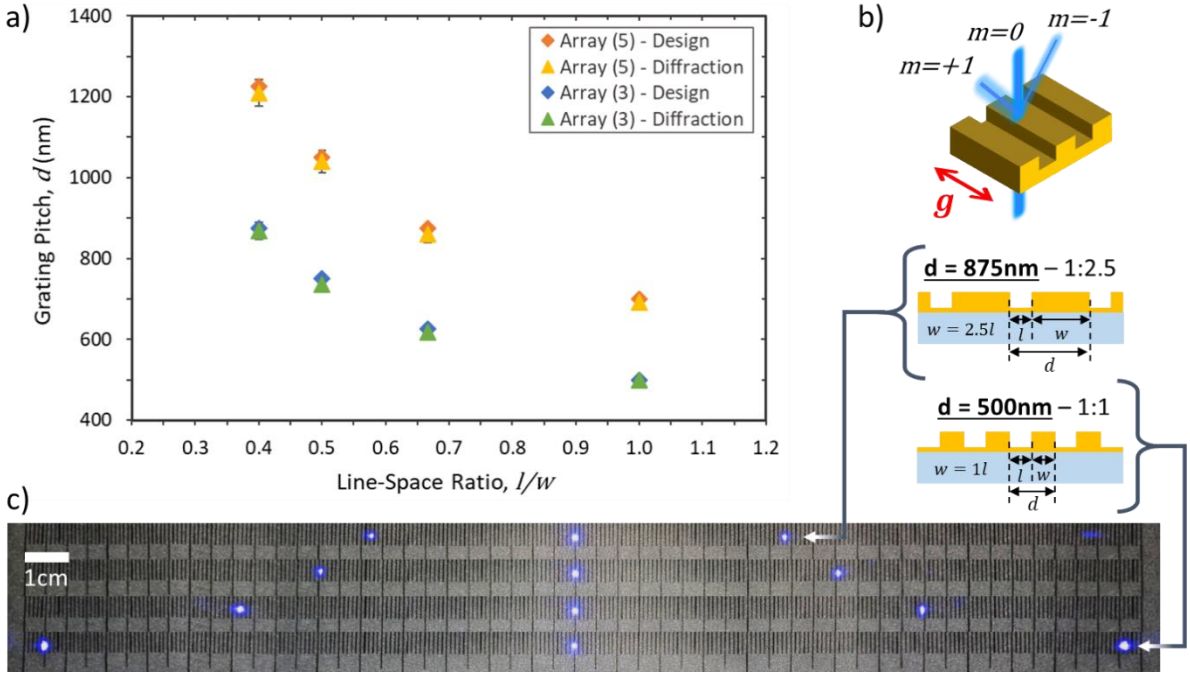

*Figure 6-10: Pitch measurements of imprinted polyimide gratings via optical diffraction. (a) Plot of grating pitch for a given line-space ratio in grating arrays 3 and 5, as specified in the initial design (diamonds) and as measured via optical diffraction (triangles). (b) Transmission diffraction grating schematic showing the grating groove direction (**g**) and zeroth (m=0) and first order (m=±1) diffraction modes. (c) Combined image of the diffraction patterns produced by 404nm laser light incident on each of the four imprinted gratings within array 3. Line-space ratios from top to bottom of the image are: 1:2.5, 1:2, 1:1.5 and 1:1. The patterns are projected on a screen at 91±1mm from the sample.*

Excellent agreement in observed between the grating pitch specified in the original design and the imprinted polyimide grating pitch measured *via* optical diffraction, for all imprinted gratings in arrays 3 and 5 (Figure 6-10a). The pitch is calculated by first measuring the lateral separation of the zeroth and first order diffraction modes (Figure 6-10b), from the diffraction patterns on the scaled projection screen (Figure 6-10c). The corresponding diffraction angle (θ_d) is then calculated from $\theta_d = \tan^{-1}(x/L)$, using this lateral separation (x) and the distance between the screen and the sample (L). The diffraction angle is then used in $m\lambda = d\sin(\theta_d)$, along with laser wavelength (λ) and the diffraction order (m=1) to extract the grating pitch (d). All measured pitch values are within ≤2% of the design specifications, confirming that the imprinted polyimide gratings are a faithful replication of the original silicon-oxide master structures, and that the PDMS stamps remained structurally stable during imprinting. Additionally, the agreement between designed and measured pitch values indicates reliability in the diffraction apparatus, given that the master structures are fabricated with a high precision electron-beam lithography system.

6.4.2 Liquid Crystal Device Characterization

Two liquid crystal devices are fabricated as detailed in section 6.3.4, one featuring grating array 3 with an LC layer thickness of 6 ± 1μm, and the other featuring grating array 5 with an LC layer thickness of 8 ± 1μm. After filling the devices with MLC-6204 in the isotropic phase at 70°C (Table 3-1), the devices are characterised at 20 °C using polarised microscopy with orthoscopic and conoscopic illumination.

6.4.2.a Birefringence Colour Observations

The resulting alignment in both devices was examined under white light illumination between crossed polarisers, using a 20x microscope objective. The images presented in Figure 6-11 are captured on the boundary of grating and non-grating regions within the device containing grating array 3. Only images of the array 3 device are shown here, as the general alignment characteristics and trends between grating regions are comparable between array 3 and array 5 devices.

Given that opposing homeotropic polyimide surfaces impose a vertically-aligned nematic (VAN) director profile (Figure 6-7b), which remains extinct under rotation between crossed polarisers, the most striking aspect of these devices is the marked transmission observed in the grating areas. Simultaneously imaging the grating and non-grating areas within the device, highlights their contrasting optical properties (Figure 6-11). As shown in the 0° (Figure 6-11.1) and 45° (Figure 6-11.2) images, the brighter/transmissive regions occupying the majority of the images correspond to areas where the homeotropic polyimide has been imprinted with a grating structure (Figure 6-11.4), whilst the dark/extinct regions correspond to areas of flat, unpatterned polyimide that give rise to a typical VAN director profile.

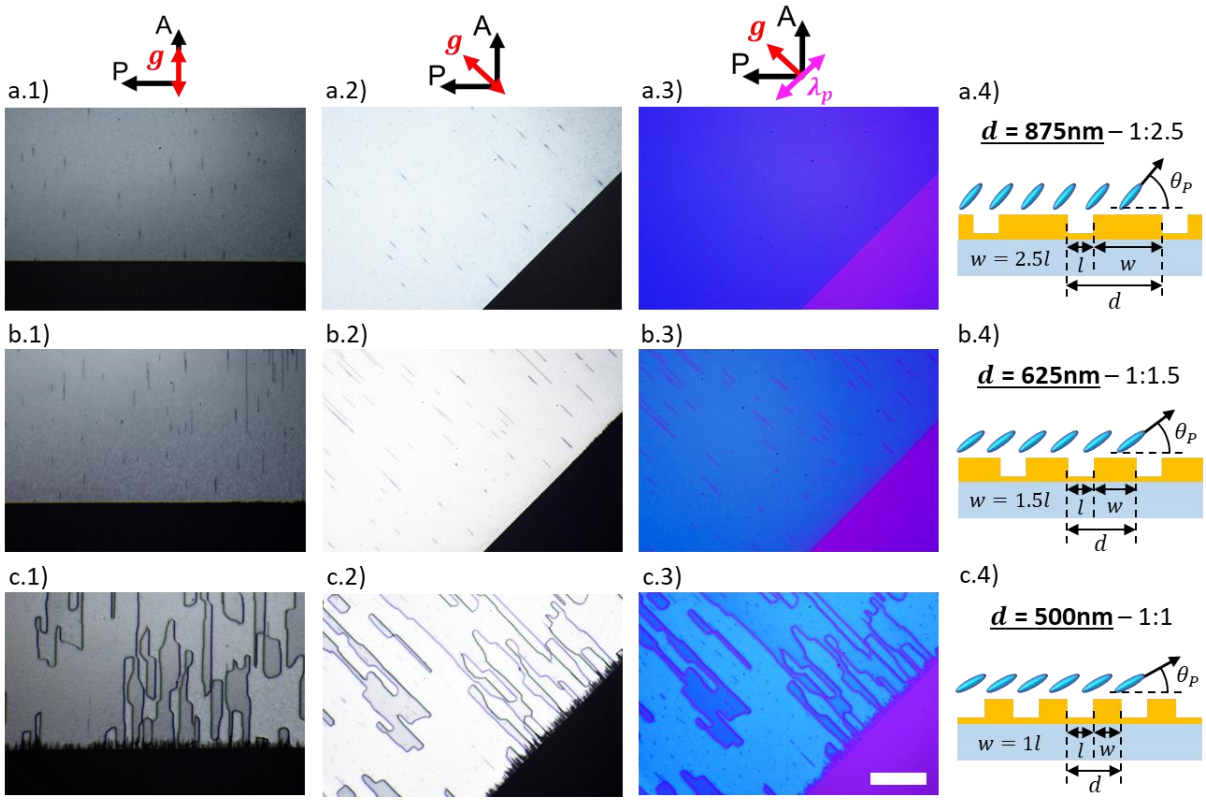

*Figure 6-11: Polarised microscopy images of an LC device featuring a homeotropic polyimide surface imprinted with grating array 3 (filled with MLC-6204, LC layer thickness = 6 ± 1μm, imaged at 20°C). The images show different grating areas within the device, with line-space ratios of (a) 1:2.5, (b) 1:1.5 and (c) 1:1. The grating groove direction (**g**) is varied between (1) 0° and (2, 3) 45° to the crossed polarisers (P, A), with full-wave plate slow axis orientation (λ_p) indicated in (3). Schematic cross sections of the grating profiles are shown in (4), indicating linewidth (l), spacewidth (w) and pitch (d). Surface pretilt on the grating surface (θ_P) is also shown, as a reference point and approximate guide as to how the gratings are influencing surface director orientation. Scale bar = 100μm.*

The observed transmission in the grating areas is attributed to the presence and increased birefringence of a hybrid-aligned nematic (HAN) director profile (Figure 6-7b), established *via* a surface anchoring transition on the grating surface.[113] As covered in section 5.4.3.b on wrinkled surface textures with homeotropic anchoring, this transition in surface anchoring occurs due to a combination of the grating structure's topographic distortion of the near-surface director field and the homeotropic anchoring associated with the polyimide. The balance of these competing alignment contributions results in a net tilt of the director away from the surface normal near the grating interface, resulting in a HAN director profile that is a free energy minimum of the system. Interestingly, the grating devices in this work exhibit a stable, tilted alignment configuration at room temperature, in contrast to the homeotropic wrinkle devices in section 5.4.3.b, which only displayed surface anchoring transitions at temperatures close to the nematic-isotropic transition, with reduced elastic constants. This is most likely due to the greater anchoring energy (W_ψ, Equation (2-10)) or elastic distortion associated with these imprinted grating structures, with a height of ≈300nm and pitches between 1200 – 500nm giving rise to $W_\psi \approx 9 \times 10^{-6} - 122 \times 10^{-6}$ Jm^{-2}, compared to the wrinkled surfaces with $W_\psi \approx 4 \times 10^{-6}$ Jm^{-2}. This

larger W_ψ enables the gratings to induce sufficient director field distortion and cause an anchoring transition, despite being opposed by the higher elastic constants of MLC-6204 at room temperature (Table 3-1).[113]

With the grating grooves ($\boldsymbol{g}$) at 45° to the crossed polarisers (Figure 6-11.2), the transmissive grating areas display first-order white birefringence colours with a retardance (Γ) of 150−200nm. The observed colour varies between a grey-white in the longer-pitch areas (Figure 6-11.a2), to a brilliant white in the shorter-pitch areas (Figure 6-11.c2). Although difficult to distinguish optically, this change in shade from grey-white (lower Γ) to brilliant white (higher Γ) with decreasing grating pitch, is the first indication that the grating dimensions provide a means of tuning the optical properties of this frustrated alignment state. For the array 3 device shown in Figure 6-11, with an LC layer thickness of 6 ± 1μm, the Michel-Lévy chart (Figure 2-4) indicates that this subtle variation in retardance corresponds an approximate change in effective-birefringence (Δn_{eff}) from 0.024 ± 0.003 to 0.034 ± 0.005, between the 875nm and 500nm pitch grating areas respectively. As the LC layer thickness is the same in each grating area, this change in Δn_{eff} can be attributed to the grating geometry altering the component of n_e contributing to the overall birefringence of the slab, in the form of varying the pretilt (θ_P) at the LC-grating interface. Given that Δn_{eff} increases as the grating pitch decreases, this suggests that shorter pitch gratings result in a more significant tilt of the director away from the surface normal and therefore a lower θ_P. The array 5 device, with an LC layer thickness of 8 ± 1μm, also shows a similar inverse relationship between Δn_{eff} and grating pitch, with approximate Δn_{eff} values of 0.018 ± 0.003 and 0.025 ± 0.003 in the 1225nm and 700nm pitch grating areas respectively. The apparently lower Δn_{eff} in the array 5 device indicates that these longer-pitch, wider-linewidth grating structures result in less director tilt away from the surface normal (higher θ_P), relative to grating array 3.

The addition of a full-wave plate with its slow axis (λ_p) at 45° to the polarisers, allows the direction of tilt to be inferred from the observed change in colour relative to the inherent colour of the compensation plate. The images in Figure 6-11.3 show the appearance the array 3 device with $\boldsymbol{g}$ at 45° to the polarisers and λ_p perpendicular to $\boldsymbol{g}$. In the extinct non-grating areas, a first-order magenta is observed as the incident linearly polarised light only experiences the LC's fast axis (n_o) and therefore shows the full-wave plate's inherent retardation of $\Gamma \approx 500nm$. However, the grating areas show a blue-cyan birefringence colour with $\Gamma > 500nm$, corresponding to an additive condition indicating that a component of the LC's slow axis (n_e) is aligned parallel to λ_p. As $\boldsymbol{g}$ and λ_p are perpendicular, and the increased n_e contribution is attributed to director tilt, this confirms that the tilt is occurring in a plane perpendicular to $\boldsymbol{g}$.

With the tilt direction confirmed, the suspected source of the non-zero transmission observed in the grating areas at the 0° orientation (Figure 6-11.1) is now discussed. A typical HAN state appears extinct when the azimuthal director orientation is aligned parallel to a polariser, as demonstrated by the HAN device with planar wrinkles shown in Figure 5-5b. The fact that the devices in this work appear a dull-grey birefringence colour in the grating areas, suggests that although the polar director tilt is predominantly perpendicular to $\boldsymbol{g}$, there is an azimuthal component to the tilt that induces a slight twist in the HAN director profile, resulting in non-zero transmission between crossed polarisers. The POM images in Figure 6-12 confirm the tilt's azimuthal deviation, where the first-order magenta of the full-wave plate (bottom of images) is shifted in the grating areas to blue (additive) or orange (subtractive), indicating that the azimuthal director orientation is tending towards parallel or perpendicular to λ_p respectively, and not at 45° to λ_p (i.e. not tilted exactly perpendicular to $\boldsymbol{g}$). This twisting is thought to be caused by the strong azimuthal anchoring (W_ψ) associated with the underlying grating grooves, which despite their homeotropic anchoring, still want to preferentially align the director parallel to $\boldsymbol{g}$, effectively 'pulling' the tilted director towards $\boldsymbol{g}$. Similar alignment behaviour has been reported by Shiina *et al.*, where gratings with planar anchoring are rubbed perpendicular to the grooves and the director is found to deviate from the rubbing direction due to the grating's azimuthal anchoring.[103]

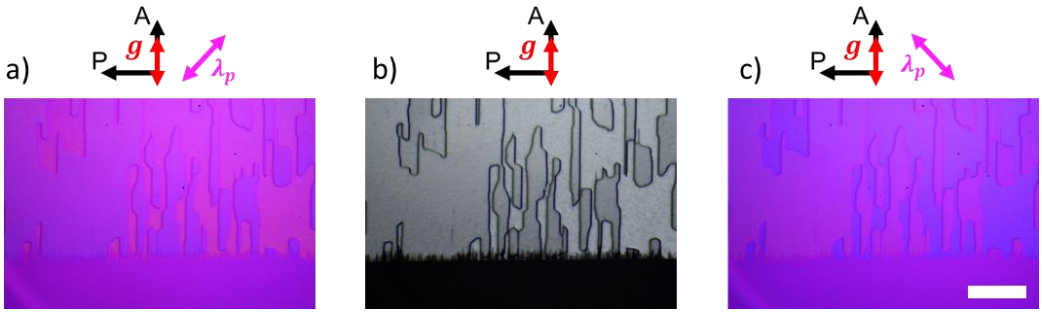

Figure 6-12: Polarised microscopy images of the 1:1 line-space ratio grating area of the array 3 device, with the grating grooves ($\boldsymbol{g}$) aligned parallel to one of the polarisers, highlighting the azimuthal deviation of the tilted HAN director profile. Images captured (a, c) with and (b) without a full-wave plate with slow axis orientation (λ_p). (b) Extinct and (a, c) first-order magenta regions at the bottom of the images correspond to areas without a grating, with a VAN director profile. Scale bar = 100μm.

The domain structures shown in Figure 6-11c and Figure 6-12b are regions of opposing tilt direction, related to tilt degeneracy in the absence of an applied rubbing direction or a blazed grating profile.[230,248] Although these tilt domains are prevalent in the grating area with a 1:1 line-space ratio, no such domains are observed in grating areas with line-space ratios >1:1 (Figure 6-11a, b). It is suggested that this may be due to the more varied spacing of edges/corners on the grating structures with higher line-space ratios, compared to the consistent spacing of edges in a grating with a 1:1 line-space ratio. The edges of the grating structures are points of high curvature, which act as pinning sites for the defects that are likely stabilizing this tilted alignment state,[17] and hence a more varied spacing of these tilt-inducing defects may be disrupting the formation of the tilt domains.

6.4.2.b Conoscopy

Analysis of the birefringence colours *via* polarised microscopy, allows a semi-quantitative relationship between grating dimensions and optical properties to be inferred, using the Michel-Lévy chart. As shown in Figure 6-11.2, the observed colours are varying shades of first-order white, which are difficult to accurately distinguish but do indicate a variation in director tilt with grating dimensions, warranting a more detailed evaluation. Hence, to gain a more quantitative understanding of the alignment properties, the devices are examined *via* conoscopy and the resulting conoscopic figures are used to differentiate and analyse the optical properties associated with each grating area. Conoscopy is performed with broadband green light ($\lambda = 533$nm, bandwidth $= 52$nm, see appendix A.1), an 80x microscope objective (Olympus ULWD MS Plan 80x, NA=0.75) and a Bertrand lens, as described in section 3.1.3.c.i. Figure 6-13 shows a summary of the imaged conoscopic figures produced by the array 3 and array 5 devices.

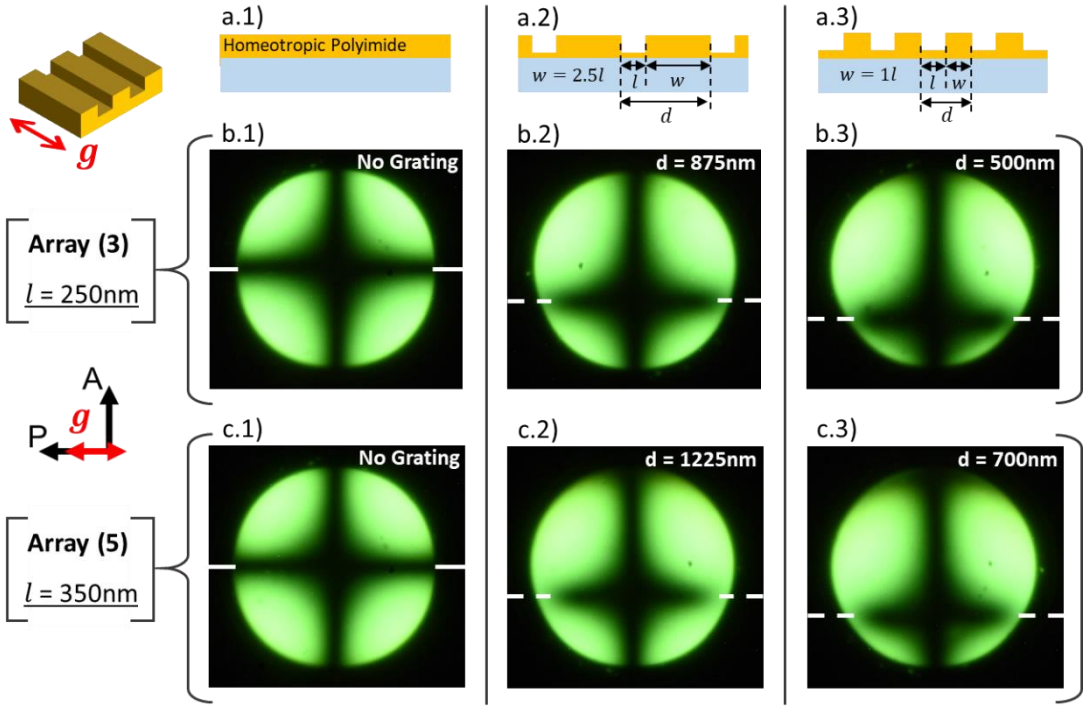

*Figure 6-13: Conoscopic examination of LC devices featuring homeotropic grating structures. (a) Schematic cross-sections of the homeotropic polyimide surface topographies where the conoscopic figures in (b) and (c) were captured, indicating grating linewidth (l), spacewidth (w) and pitch (d). Numbering denotes (1) an area of flat unpatterned polyimide, (2) a grating area with a 1:2.5 line-space ratio and (3) a grating area with a 1:1 line-space ratio. (b, c) Conoscopic figures produced by the devices containing grating array 3 and array 5 respectively, with grating groove (**g**) and polariser orientations (P, A). The grating pitch associated with each figure is indicated in the top-right of the images. Horizontal white lines denote the vertical position of the melatope in each figure, highlighting the change in position and thus optic axis orientation between different device areas.*

Conoscopic examination of the devices shows a clear distinction between grating and non-grating areas, but importantly between areas with different grating dimensions, which was difficult to ascertain conclusively *via* birefringence colour observations. In the device regions without a grating structure,

the conoscopic figures show a central dark cross (Figure 6-13.1), also known as the melatope or the point where the isogyres (dark bands) intersect. This central melatope indicates a vertically aligned optic axis, as expected from the opposing homeotropic alignment layers imposing a VAN director profile.[124,219] In contrast, the conoscopic figures obtained from the grating areas show an off-centre melatope position (Figure 6-13.2, 3), relative to the central position in the VAN areas. This shift in position indicates that the average optic axis of the device is uniformly tilted in the grating areas,[124,249,250] with comparable conoscopy figures to those observed in magnetically aligned photo-curable LC films [251] and chemically nanopatterned LC devices [252] with tilted optic axes. Since the opposing unpatterned polyimide substrate imposes vertical director alignment, this tilt of the optic axis must be due to varying amounts of surface pretilt on the grating substrate leading to a HAN director profile.

The extent by which the melatope shifts relative to the centre, varies as a function of grating dimensions, where a larger shift and thus a greater tilt of the optic axis is observed as the grating pitch decreases, in agreement with the birefringence colour observations in 6.4.2.a. This shift variation is highlighted in Figure 6-13, where the horizontal white lines on the conoscopy figures serve as a visual aid, indicating the vertical position of the melatope in each image. Since each of the grating areas is opposed by the same unpatterned homeotropic polyimide surface, this change in tilt of the optic axis must be due to a difference in surface pretilt on the gratings in each area, demonstrating the controllability offered by altering the grating geometry.

6.4.2.b.i Analysing Conoscopy Figures

Although the conoscopy figures show the presence of a tilted optic axis and that the tilt varies between different grating areas, further analysis is required to quantify the amount of tilt induced by each grating geometry. The following section will cover how data was extracted from the conoscopy figures and the calibration process used to convert distances on the images from pixel values, to angular deviation.

To measure the tilt of the optic axis, the shift in melatope position from the centre of each figure needs to be measured. A summary of how this measurement was carried out is presented in Figure 6-14. Using ImageJ software (National Institutes of Health, USA), the conoscopy figures shown in Figure 6-13 are converted to grayscale (Figure 6-14a) and intensity profiles are taken across the images (Figure 6-14b). The melatope position is identified as the minima of each intensity profile, denoted by the vertical dashed lines on the plot in Figure 6-14b. The shift in melatope position in the grating areas, with a tilted optic axis (Figure 6-14a.2, 3), is measured relative to the melatope position in a non-grating area, with a vertically aligned optic axis (Figure 6-14a.1). This corresponds to measuring the distance, in pixels, between the tilted minima position (orange or green dashed lines) and the vertical minima position (blue dashed line) using the intensity profile data shown in Figure 6-14b.

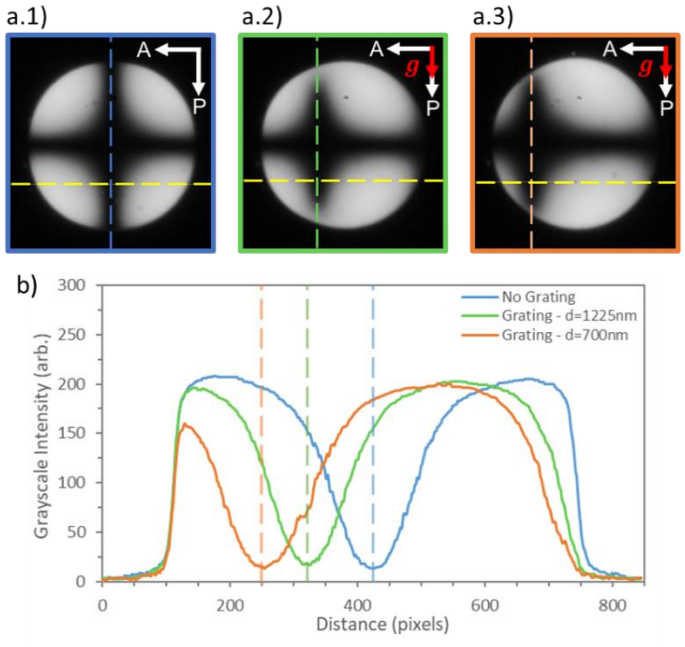

Figure 6-14: Method of measuring the shift in melatope position from conoscopy figures with varying degrees of optic axis tilt. (a) Grayscale versions of the conoscopy figures shown in Figure 6-13.c, from device regions with (1) unpatterned polyimide, (2) a 1225nm pitch grating and (3) a 700nm pitch grating. (b) Plot of grayscale intensity profiles taken along the horizontal, yellow dashed lines on each figure in (a). The blue, green and orange vertical dashed lines indicate the positions of the intensity minima/melatopes in the images of device areas (1), (2) and (3) respectively. The same colour-coding and vertical dashed lines are shown in the corresponding images in (a) for reference.

To extract the tilt angle of the optic axis from the measured shifts in melatope position, diffraction patterns are imaged under the same conoscopic illumination conditions as the devices, but with the condenser aperture narrowed to reduce the effective spot size. The same imprinted polyimide grating substrates, as were used in section 6.4.1.d, are applied here as transmission diffraction gratings to produce the diffraction patterns. As the diffraction angle for a given grating pitch is well defined by $m\lambda = d\sin(\theta_d)$, the positions of the first-order diffraction maxima in these images (Figure 6-15c), provides an angular point of reference for converting distances in pixels to angular deviation. This approach is summarized in Figure 6-15 and has previously been used by Miller and Gleeson to calibrate the back focal plane of an objective lens for analysing Kossel diagrams.[122]

The diffraction patterns produced by three of the gratings in grating array 5 are shown in Figure 6-15c, where the orange dashed lines show how the first-order maxima positions correlate to different radial positions (R) from the centre of the conoscopy figure in Figure 6-15a. The plot in Figure 6-15d shows these maxima positions, in pixels, plotted against $m\lambda/d$, where a good linear fit is found for $|R| < 300px$. The error in the gradient of this linear fit indicates the accuracy of using the melatope position on a conoscopic figure to measure the angle of a sample's optic axis, which is 1.0%. For values of $|R| > 300px$, the maxima positions begin to deviate from this linear relationship with $m\lambda/d$, indicated by the higher residuals of the linear fit for $|m\lambda/d| > 0.7$. This indicates some distortion in

the back focal plane at these distances from the centre of the figures, and hence measurements are not taken at these distances. Therefore for $|R| < 300px$, the linear fit in Figure 6-15d serves as a conversion tool, allowing a given pixel position in the conoscopy figures to be converted to a value of $m\lambda/d$ and subsequently angular orientation (θ_d), since $m\lambda/d = \sin(\theta_d)$. At this point it is worth noting that all of the measured shifts in melatope position from the tilted conoscopy figures, are within 100−187px from the centre of the figures. This range falls well within the linear regime established from the diffraction angle measurements (linear fit in Figure 6-15d), ensuring that the back focal plane is well calibrated and free of optical distortions for converting to tilt angles at these positions.

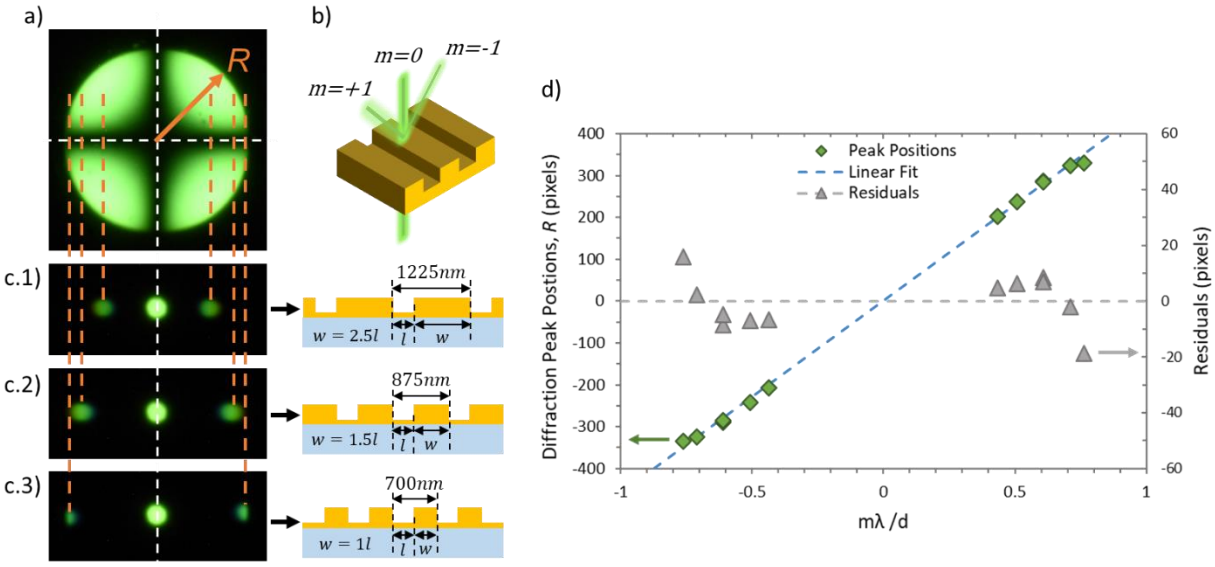

Figure 6-15: Calibration of the back focal plane of the objective via diffraction patterns, to convert distances on conoscopy figures to angular deviation. (a) Conoscopic figure with central melatope, defining the radial distance (R) from the centre of the figure. (b) Schematic of the transmission diffraction grating arrangement used to image the diffraction patterns. (c) Diffraction patterns of (1) 1225nm pitch, (2) 875nm pitch and (3) 700nm pitch gratings imaged on the back focal plane, using the same optical setup as used in (a). The vertical orange dashed lines show how the positions of the first-order ($m = 1$) diffraction maxima, with well-defined diffraction angles (θ_d), relate to different values of R in the conoscopy figures. (d) Plot of $m = 1$ diffraction peak positions on the imaged diffraction patterns (green diamonds), against $m\lambda/d = \sin\theta_d$. The good linear fit to the diffraction peaks (blue dashed line) indicates minimal optical distortions in back focal plane for values of $|R| < 300px$.

6.4.2.b.ii Induced Tilt of Optic Axis

Using the image analysis and conversion approach detailed in the previous section, the grating-induced tilt of the optic axis is extracted from the conoscopy figures of the array 3 and array 5 devices. The results are presented below in Figure 6-16, where the tilt of the optic axis away from the surface normal (ϕ) and the associated shift in melatope position, are plotted against grating pitch (Figure 6-16a) and mark-space ratio (Figure 6-16b) for each device. For a given device, wherever two data points are plotted for the same x-axis value, this corresponds to measurements of conoscopy figures that were captured in the same grating area, on either side of a tilt domain wall (domain structures shown in Figure 6-11c). It is also worth noting that the initial tilt angle obtained from the shift in melatope position

represents the apparent angle of the optic axis in air (E), which is converted to the true interior angle within the LC medium (V) by accounting the for average refractive index of the LC (n_{avg}) using the relation $\sin(E) = n_{avg}\sin(V)$, as detailed by Dana *et al.*[121] Herein, the tilt angle of the optic axis (ϕ) represents the true interior angle of the optic axis within the LC.

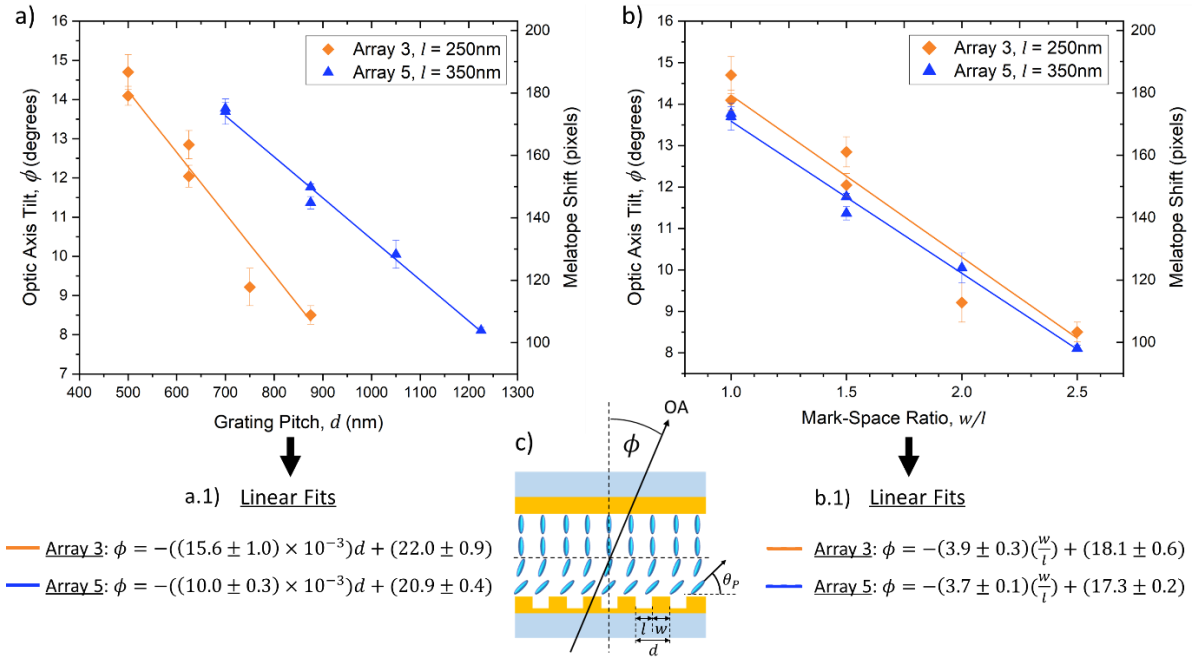

Figure 6-16: Analysis of conoscopy figures produced by devices containing grating arrays 3 and 5, with respective grating linewidths (l) of 250nm and 350nm. The calculated tilt of the optic axis away from the surface normal (ϕ) and measured shift in melatope position are plotted against (a) grating pitch and (b) mark-space ratio (w/l), where (a.1) and (b.1) show the equations of the linear fits in each the plot. (c) Schematic of the HAN director profile in the devices, approximating how the director orientation (blue rods) varies throughout the layer. An average optic axis (OA) is indicated to approximate the tilt represented by the conoscopy figures, which is some average of the different director orientations in the device. Pretilt at the grating interface (θ_P) and the dimensions of ridges/marks (w), lines/spaces (l) and pitch (d) are also included for reference.

The data in Figure 6-16a show that both devices exhibit an inverse relationship between grating pitch (d) and optic axis tilt (ϕ). The solid lines show linear fits to the two data sets, indicating that for a given grating linewidth (l), ϕ increases linearly as the pitch is decreased. An increase in ϕ corresponds to a decrease in pretilt (θ_P) on the grating surface, since the optic axis measured *via* conoscopy represents an average of the director orientations over the HAN director profile (Figure 6-16c). The pretilt on the grating surface therefore scales proportionally with grating pitch. The mark-space ratio (w/l) is introduced in Figure 6-16b, which is the ratio of the ridge/mark width (w) to the line/trench width (l) (see Figure 6-16c for reference). This is introduced here to allow for a more direct comparison to the work by Jones,[229] where the pretilt on a homeotropic grating surface is shown to increase linearly with increasing mark-space ratio, in a comparable defect-driven alignment state. The data in Figure 6-16b show that ϕ is inversely proportional to the mark-space ratio, but as discussed earlier, ϕ and θ_P

are inversely proportional, which means that this data also shows that θ_P scales proportionally with mark-space ratio, in agreement with the previous report of Jones.

Figure 6-16a.1,b.1 detail the equations of the linear fits for each plot, highlighting the difference in gradient between the grating arrays, where the smaller-linewidth grating array 3 possesses the steeper gradient of the two. These observations provide insight for future device applications, in terms of selecting an appropriate grating linewidth to best suit the tuning requirements i.e. if a specific tilt angle is required for a given device, it may be beneficial to use gratings with a larger linewidth to hone in on this tilt value, such that incremental changes in pitch/mark-space ratio result in smaller changes in tilt, as per the shallower gradient exhibited by the array 5 device. However, opting for larger-linewidth gratings does limit the range of accessible tilt angles, since the measured range of ϕ in the array 5 device is 5.6°, compared to the broader range of 6.2° in the array 3 device. For applications where a spatially modulated tilt angle is required and the length-scale over which the modulation occurs needs to be as small as possible, spatially varying the pitch of a smaller-linewidth grating would best suit this scenario, given the steeper gradient exhibited by the array 3 device.

6.4.2.b.iii Distinguishing Tilt Direction

As discussed in section 6.4.2.a, these tilted alignment states have a tendency to form domains with opposing tilt directions separated by reverse-tilt disclination lines. These regions of opposing polar director orientation, or reverse-tilt domains, are often formed in twisted-nematic and planar devices upon electric field application or transitioning from the isotropic to nematic phase, in the absence of an applied rubbing direction.[98,253] Without a rubbing direction the near-surface director does not have a preferential tilt direction, as is the case in the homeotropic grating devices in this work. Also, the symmetric nature of the square-wave grating profile used, similarly leads to a lack of tilt preference, as opposed to asymmetric grating profiles which are known to have an inherent pretilt and tilt direction.[230,248]

The polarised microscopy image in Figure 6-17a shows an example of these tilt domains, as observed in the 500nm pitch grating area of the array 3 device. Visually, the domains on either side of the disclination lines are indistinguishable, as shown in Figure 6-17b.1, which is an enlarged view of the device region marked by the orange box in Figure 6-17a, spanning a disclination line. However, conoscopy observations enable the tilt direction of adjacent domains to be readily distinguished, by simply observing the direction in which the melatope shifts on either side of the disclination lines. Figure 6-17c shows the conoscopy figures captured on the left (Figure 6-17c.1) and right (Figure 6-17c.2) of the disclination line shown in Figure 6-17b.1, where the melatopes have shifted in opposite directions in the two domains. This signifies that the optic axis in each domain is tilted in an opposing direction relative to one another. Schematic director profiles associated with these observations are shown in Figure 6-17b.2, indicating the two resulting HAN configurations with opposing surface

pretilts on either side of the disclination line (orange dashed line). Conoscopy has previously been used to differentiate between reverse-tilt domains in HAN devices, but likely due to a higher effective birefringence or greater optic axis tilt, melatopes are not visible in the conoscopic figures and therefore only slight shifts in isogyre position indicate the presence of opposing tilt directions.[98] Here, the visibility of the melatopes results in a more striking contrast in the conoscopy figures on either side of the tilt disclinations (Figure 6-17c), supporting the previous findings with improved clarity.

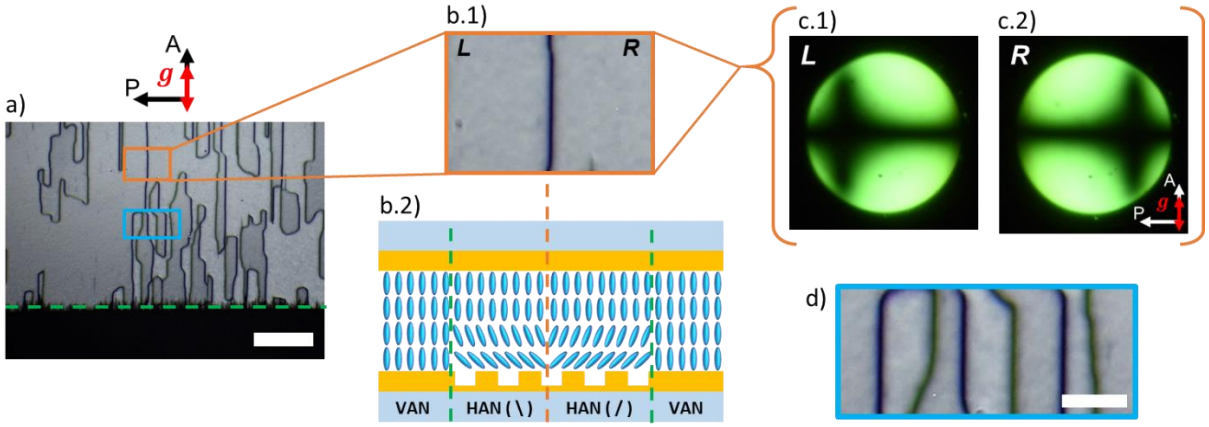

Figure 6-17: Differentiating between adjacent HAN domains with opposing tilt directions. (a) Polarised microscopy image of the 500nm pitch grating area in the array 3 device, showing an overview of the tilt domain structure. Green dashed line denotes the boundary between grating (HAN) and non-grating areas (VAN). Scale bar = 100μm. (b.1) Enlarged view of the area marked with the orange box in (a), spanning a reverse-tilt disclination line. (b.2) Schematic highlighting the HAN director profile on either side of the disclination line (marked by the orange dashed line). (c) Conoscopy figures imaged in the left (L, c.1) and right (R, c.2) regions shown in (b.1). (d) Enlarged view of the area marked by the blue box in (a), showing the alternating appearance of consecutive tilt disclination lines. Scale bar = 20μm.

Upon closer observation of the polarised microscopy image in Figure 6-17a, the domain walls can be seen to alternate in appearance between black and grey-green, as shown in the Figure 6-17d. This alternation suggests the presence of two distinct domain wall structures within the HAN areas, similar to those reported in work on field-driven defects in hybrid-aligned nematic layers.[254] As such, when transitioning between domains of opposing tilt direction, these domain wall structures are expected to be alternating between tilt-in (/ \) and tilt-out (\ /) configurations, where the slashes indicate the local tilt direction at the grating interface on either side of a domain wall. These observations are reminiscent of the distinct optical properties of 'thick' and 'thin' defect lines in the vertical chevron structures found in ferroelectric-smectic LCs, which are also attributed to a variation in tilt direction on either side of the defects.[255]. Seeing as conoscopic examination allows the reverse-tilt domains to be differentiated with relative ease, it should be possible to combine these observations with fine-adjustment sample translation to map out the arrangement of tilt-domains and identify specific domain wall structures within LC devices, which may be of use in focused studies on nematic disclination dynamics and morphology.[254]

6.4.3 Modelling Bulk Director Profile

The conoscopic analysis of the devices provides an insight in to the average optic axis orientation in the grating areas, allowing general relationships between grating dimensions and pretilt on the grating surfaces to be inferred. In order to relate the conoscopy measurements to a specific pretilt value for each grating area, the non-uniform director tilt profile of the HAN configuration needs to be estimated to understand how the director orientation varies throughout the device. The following section will cover the preliminary steps taken to extract pretilt from the conoscopy figures using theoretically predicted HAN profiles as a reference point.

6.4.3.a Extracting Pretilt from Conoscopy Figures

Pretilt measurements of HAN devices have previously been reported, whereby the angular dependent phase retardation was measured and pretilt values were derived from theoretical fitting to the data.[113,223]. This proven robust method of measuring the pretilt angle is beyond the scope of this work, however the conoscopic approach used here is better-suited for small sample areas and allows high resolution observation of tilt variation across domain walls, as shown in section 6.4.2.b.iii. From these previous works, the bulk director orientation ($\theta(z/d_{LC})$) within a HAN cell can be assumed to vary linearly between the pretilt on the grating surface (θ_P) and the pretilt on the unpatterned surface (θ_1). This assumption is based on the single-elastic constant approximation which is valid for sufficiently large LC layer thicknesses.[223] This linear variation in θ is represented by Equation (6-1) and plotted as a function of z/d_{LC} for three different grating pretilt values in Figure 6-18a, where z is the distance in to the LC layer and d_{LC} is the overall thickness of the LC layer.

$$\theta(z/d_{LC}) = (\theta_1 - \theta_P)(z/d_{LC}) + \theta_P \tag{6-1}$$

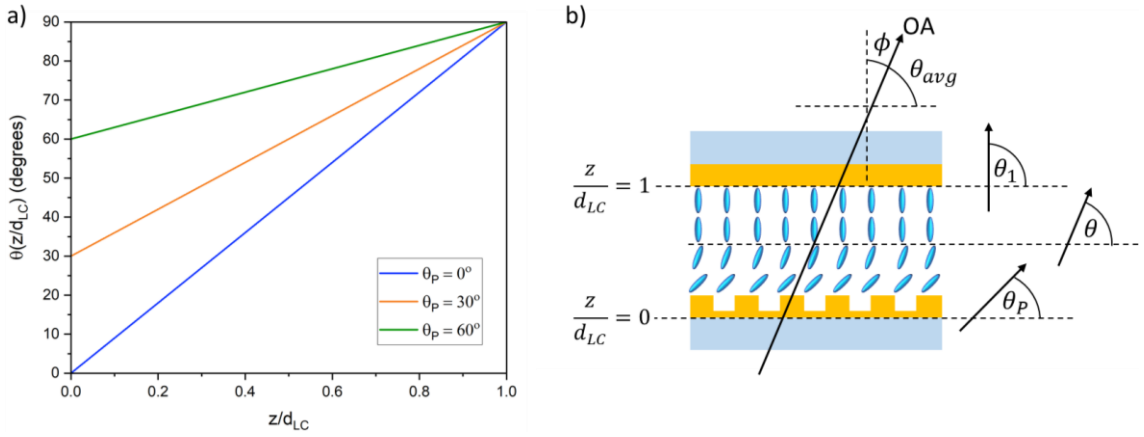

Figure 6-18: (a) HAN director profiles with a linearly varying director orientation (θ) with distance (z) in to the thickness (d_{LC}) of an LC slab, for various surface pretilts (θ_P). (b) Schematic of HAN director profile defining key device parameters such as, the pretilt on the grating surface (θ_P) and the unpatterned polyimide surface (θ_1), the average director orientation (θ_{avg}) for the HAN profile with a given θ_P and the average tilt of the optic axis from the surface normal (ϕ) obtained via conoscopy.

The value of θ_1 on the unpatterned polyimide substrate is taken to be 90°, validated by the conoscopy figures captured in the non-grating device areas that exhibit a central melatope position and therefore a vertically-aligned optic axis (Figure 6-13.1). Equation (6-1) is then used with values of θ_P between 0 - 90°, to generate a range of potential HAN director tilt profiles ($\theta(z/d_{LC})$). As indicated in the schematic in Figure 6-18b, an average director tilt (θ_{avg}) is calculated by taking the average over $\theta(z/d_{LC})$. This average director orientation is then approximated to be equivalent to the average optic axis orientation (ϕ) obtained via conoscopy, as previously employed in the conoscopic examination of hybrid-aligned LC devices by Park *et al.*,[252] where $\theta_{avg} = 90 - \phi$. The pretilt angle is then determined for a given conoscopy figure by finding the value of θ_P that results in a θ_{avg} that satisfies this relation. The results of this analysis are presented below in Figure 6-19a where ϕ and the corresponding values of θ_P are both plotted against mark-space ratio for each device studied. This indicates that over all of the grating areas measured across the two devices, the inferred pretilts on the grating surfaces range from 61 - 74°. Although broader pretilt ranges have been demonstrated by varying the depth [113] and the mark-space ratio of homeotropic grating structures,[229] the results presented here highlight the potential of adjusting lateral grating dimensions over a large range as a means of fine-tuning surface pretilt over a narrow range of ≈13°.

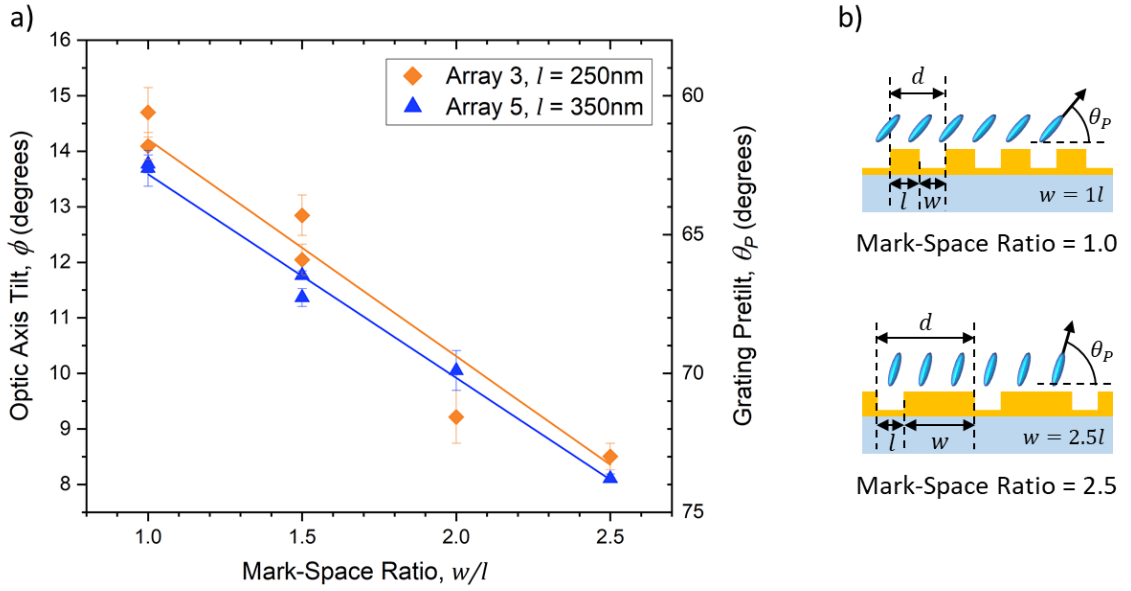

Figure 6-19: (a) Plot of the optic axis tilt (ϕ) obtained from conoscopy, and the inferred grating pretilt (θ_P) for each value, as a function of grating mark-space ratio (w/l). (b) Schematic grating profiles with mark-space ratios of 1.0 and 2.5 and their associated surface pretilts.

6.5 Summary

In this chapter, precision grating structures have been transferred into homeotropic polyimide alignment layers, to explore the relationship between lateral grating dimensions and LC surface alignment properties under frustrated surface anchoring conditions.

A composite-PDMS replication approach was used to create soft working stamps from rigid grating master structures. Scanning-electron microscopy revealed pattern instability and lateral collapse of the PDMS features at a linewidth of 150nm, whilst at a linewidth of 250nm, structural stability was observed for all tested line-space ratios. These findings provide a case study for the widely adopted composite-PDMS replication methodology, highlighting its limits for structures of the order of 300nm in height. Faithful pattern transfer into polyimides was achieved using the imprinted polyimide methodology, as confirmed by optical diffraction measurements, allowing homeotropic gratings with as low as 500nm pitch to be fabricated and incorporated into LC devices.

Birefringence colour observations showed that the homeotropic grating structures resulted in areas of increased effective birefringence of 0.018 – 0.034, within the predominantly extinct VAN devices. This is attributed to surface anchoring transitions and resulting director pretilt on the grating surfaces inducing stable HAN director profiles at room temperature, caused by the competing influence of the polyimide's homeotropic anchoring and the gratings' topographic distortion of the director field. Lower pretilt was inferred from the increased retardation exhibited by areas with lower grating pitch/mark-space ratio and full-wave plate observations confirmed that the induced tilt was occurring in a plane perpendicular to the grating grooves.

Conoscopic examination of the devices enabled grating areas with comparable optical appearance to be easily distinguished and provided quantitative analysis of the tilted alignment states. Conoscopy figures showed that the grating areas possessed a uniformly tilted average optic axis with tilt angles of 8.1 – 14.7° from vertical, scaling inversely with grating pitch/mark-space ratio. The resolution capability of conoscopic tilt measurements was demonstrated over distances of ≤100μm, through the identification of opposing tilt directions on either side of tilt domain walls. Theoretical modelling of HAN director profiles was used to infer pretilt values on the grating surfaces from the optic axis tilts measured *via* conoscopy, yielding pretilts of 61 - 74° for the 500 – 1200nm pitch gratings studied.

Chapter 7 Conclusions and Future Work

7.1 Conclusions

The work presented in this thesis has focused on the interactions between liquid crystals and micropatterned polyimide surface topographies. At the interface between a solid surface and a liquid crystal medium there exists a combination of chemical and physical interactions, which influence the near-surface molecular orientation and thus the bulk properties due to the elasticity of the LC phase. Surface alignment is a broad area of LC research centred on controlling and exploring these surface interactions, and is a critical parameter in the development of functional LC devices. The overall aim of this thesis was to demonstrate an accessible means of incorporating micron and sub-micron scale surface relief structures in to LC devices, using conventional polyimide alignment layers and their inherent chemical alignment properties, to augment the physical influence of the relief structures.

Chapter 2 introduced the relevant background physics of nematic liquid crystals and also the fundamental aspects of surface alignment such as, anchoring strengths, types of surface anchoring, alignment layer materials and treatments, and the alignment properties of surface relief structures. With topographically patterned alignment layers being the focal point of this work, notable literature utilizing surface relief structures for LC alignment was reviewed in section 2.3, providing context for the three chapters of experimental work and highlighting the novelty and potential applications of the results. The methods used throughout the experimental work are summarized in Chapter 3, covering the preparation and analysis of LC devices, general microfabrication techniques used to fabricate the polyimide relief structures and the surface metrology used to measure the critical dimensions of the surface features.

7.1.1 Micropatterned Liquid Crystal Elastomers

In the first results chapter (Chapter 4), planar polyimides imprinted with commercially-sourced linear grating structures were investigated as both alignment layers and moulds for fabricating micropatterned liquid crystal elastomers (μLCEs). As the grating structures were comprised of planar polyimide, conventional rubbed alignment could be used to override the topographic anchoring of the gratings, allowing a global easy axis to be defined with an arbitrary azimuthal director orientation relative to the underlying grating grooves. Although rubbed topographies have previously been applied in low molecular mass LC systems,[83,103] this is the first application of this approach in LCE fabrication, facilitating the fabrication of monodomain LCE films and also a means of controllably miniaturizing structures on the surface of the μLCEs *via* anisotropic deswelling. The extent by which the original grating pitch of the mould (1040nm) reduced upon deswelling, was dependent on whether the grating grooves were parallel ($\hat{\boldsymbol{n}}_{\parallel}$) or perpendicular ($\hat{\boldsymbol{n}}_{\perp}$) to the nematic director. The $\hat{\boldsymbol{n}}_{\perp}$ pitch reduced by only 3% (1010nm) whereas the $\hat{\boldsymbol{n}}_{\parallel}$ pitch reduced by 32% (707nm), demonstrating the sub-micron capability

of the μLCE platform. These pitch reduction factors were found to be consistent across three individually fabricated, chemically identical samples made using the same methodology, highlighting the repeatability of the deswelling mechanism and the suitability of all-acrylate LCEs as general substrates for feature size reduction.

Further dimensional tunability was demonstrated by varying the concentration of the non-reactive liquid crystalline component in the LCE precursor, which is responsible for swelling the polymer network during polymerisation and therefore dictates the amount of deswelling that occurs upon its subsequent removal. This additional control over the deswelling, *via* changes in chemical composition, provides a simple means of fine-tuning feature sizes, given that compositional adjustments can be readily made with standard laboratory practices, demonstrating the multi-faceted dimensional tunability offered by μLCE films.

The use of linear grating structures provided a clear reference point for quantifying the anisotropic deswelling behaviour, but also enabled the μLCE films to be applied as diffractive optical elements. The stimuli-responsiveness of the all-acrylate LCEs allowed for tunable grating dimensions and thus diffractive properties, which was explored by changing the temperature of the system and applying uniaxial tensile strain. Optical diffraction patterns were used to observe and quantify the opposing thermal responses of the $\hat{\boldsymbol{n}}_{\parallel}$ and $\hat{\boldsymbol{n}}_{\perp}$ μLCEs, where the grating pitch was found to expand and contract respectively upon heating, by as much as 33% over a 215°C temperature range. The associated changes in diffraction angle, with linear regimes spanning ≈55% of the operational temperature range, demonstrates the potential for μLCEs to be applied as diffraction-based thermal sensors, whose response can be tailored by simply changing the grating orientation with respect to the nematic director. The first-order diffraction efficiency was also investigated as a function temperature and upon heating was found to increase in $\hat{\boldsymbol{n}}_{\parallel}$ samples and decrease in $\hat{\boldsymbol{n}}_{\perp}$ samples; attributed to the changes in pitch shifting the peak efficiency wavelengths of the grating structures closer to ($\hat{n}_{\parallel}$), and further away from ($\hat{n}_{\perp}$) the 404nm wavelength laser light used in the diffraction experiments.

The strain response of the $\hat{n}_{\parallel}$ μLCEs was studied *via* diffraction experiments and atomic force microscopy (AFM). A linear variation in grating pitch was inferred from diffraction angle measurements of the μLCEs, as they were subjected to tensile strains of up to 156%. To gain a deeper insight into how the grating dimensions changed under strain, AFM was used to profile the structures whilst the films were under different static strains, varied in coarse increments of $20-40\%$. The variation in grating pitch from AFM showed good agreement with the linear response obtained from diffraction measurements and interestingly, given the depth measurement capability of AFM, the grating height was found to initially decrease at moderate strains (≤40%) and then begin increasing at higher strains (≥80%), attributed to the auxetic strain response of this class of LCEs. This is the first known demonstration of auxetic behaviour in microscale surface relief structures. A significant

nanoscale growth in feature height was observed, with the grating height increasing beyond the original height of the grating at rest, by as much as 26%. The impact of this auxetic growth in feature height on the μLCEs diffractive properties was investigated by measuring the first-order diffraction efficiency (η_1) as a function of strain. With the strain being applied perpendicular to the grating grooves, the pitch continuously increased along with the diffraction efficiency, as a result of the pitch increasing towards the required pitch for maximum η_1 at the 404nm wavelength used in the experiment. This same increasing η_1 behaviour was also observed during the pitch-expanding thermal response of the $\hat{n}_{\parallel}$ μLCE. However, a clear transition in the linear behaviour of η_1 was observed at ≈100% strain, after which point the increase in η_1 per unit strain was found to increase by a factor of 2.7, resulting in an overall higher sensitivity of η_1 to mechanical strain. This behaviour may be associated with the auxetic response increasing the height and thus the phase modulation of the grating structures.

Thermal and mechanical durability testing was also performed on the μLCEs, to gauge the dimensional stability of the grating structures under thermal and mechanical extremes and repeat actuation. Exposing the μLCEs to temperatures as high as 240°C showed some reduction in diffraction efficiency, suggesting potential damage at these temperatures, in agreement with previous thermal studies of this LCE composition.[57] Samples that were taken to a maximum strain of 156% and then allowed to relax for ≈2 hours, showed little change in grating dimensions, with pitch and height agreeing with pre-strained values within error. Preliminary cycle tests of the samples between temperatures of 20−100°C and strains of 0−30% for 50 cycles, also showed minimal change in grating pitch and height, both falling within <1% of the dimensions prior to testing.

7.1.2 Spontaneously Wrinkled Polyimide Alignment Layers

In the second results chapter (Chapter 5), a non-lithographic microfabrication technique was used to create periodic surface relief structures, which were then used to pattern planar and homeotropic polyimide alignment layers. The structures were formed *via* spontaneous wrinkling, an accessible means of pattern generation that relies on the formation of a stiff surface layer on a compliant substrate, which then buckles in a periodic fashion as the substrate is perturbed. In this work, a 60% tensile strain was applied to a compliant slab of polydimethylsiloxane (PDMS), which was then exposed to an oxygen plasma treatment to form a stiff silicon-oxide layer on the surface. Upon strain release, a wrinkled surface topography was formed due to the oxide layer buckling in response to the internal stresses associated with its formation under strain. The wrinkled PDMS slabs were used directly as stamps to transfer the wrinkled textures in to planar and homeotropic polyimides. The resulting wrinkle-imprinted polyimide (WIP) surfaces were measured with AFM, and the periodic wrinkles were found to have a pitch of 900 ± 20nm and height of 125 ± 10nm. The WIP surfaces also featured aperiodic features protruding above and aligned perpendicular to the wrinkles, formed as an artefact of the imprinting

process where cracks (valleys) in the PDMS oxide layer were inverted into walls (peaks) in the imprinted polyimide layer.

Both planar and homeotropic WIP surfaces were assembled in to LC devices opposite flat layers of homeotropic polyimide, forming hybrid-aligned nematic (HAN) and vertically-aligned nematic (VAN) device configurations respectively. The grating alignment capability of the periodic wrinkles, with an azimuthal anchoring strength (W_ψ) of approximately 4×10^{-6} Jm^{-2}, was demonstrated in the HAN device, where a uniform azimuthal director orientation was observed in device areas with a wrinkled texture, on an otherwise planar-degenerate polyimide surface. The director orientation was confirmed to be aligned parallel to the wrinkle grooves, using full-wave plate observations and $S = \pm 1$ point defects in an adjacent region of Schlieren texture as a reference point. The VAN device was used to study how LC alignment was affected by homeotropic anchoring combining with the wrinkled surface topography. At room temperature, the device appeared predominantly extinct with a slight increase in transmission when the wrinkle grooves were aligned at 45° to the crossed polarisers. Conoscopic examination of the device at 45°, showed centrosymmetric splitting of the isogyres in the conoscopy figure, indicating the presence of degenerate tilt of the director away from vertical, attributed to the director splaying over the peaks and troughs of the wrinkles.

Upon heating the device with homeotropic wrinkles to $T/T_{NI} \approx 0.95$, more complex alignment behaviour emerged in the form of a surface anchoring transition that caused the optical appearance to change from extinct to highly transmissive. This transition was attributed to the reduced elastic constants close to T_{NI}, which allowed the initially supressed physical alignment contribution of the wrinkled topography to now distort the near-surface director field, resulting in a frustrated alignment state with an induced surface pretilt that increased transmission. Birefringence colour observations were used to approximate the pretilt (θ_P) induced by the surface anchoring transition, with $\theta_P = 35 \pm 9°$. Full-wave plate observations of this alignment state confirmed that the azimuthal orientation of the induced tilt was perpendicular to the wrinkle grooves. The resulting optical texture also contained an elongated domain structure, where the domains had comparable widths to the average separation of the aperiodic wall structures formed during imprinting. These domains were attributed to the protruding wall structures imposing spatial confinement on the tilted alignment state, which was confirmed by a lack of domain formation in an identically made VAN device with the wrinkled texture replaced with a regular linear grating structure (without walls). The presence of the walls also produced an interesting director modulation effect, where between adjacent walls, the azimuthal director orientation was found to splay continuously, resulting in an overall spatially modulated director profile across multiple wall structures. This is thought to be caused by the director remaining near-vertically aligned on the protruding walls, which then combines with the tilted director orientation in the adjacent wrinkled areas to pull the tilt direction away from perpendicular to the grooves.

7.1.3 Liquid Crystal Alignment on Sub-Micron Homeotropic Gratings

The final results chapter (Chapter 6) focused on exploring the relationship between LC alignment characteristics and the dimensions of sub-micron pitch gratings with homeotropic anchoring. A variety of precision grating structures were fabricated on silicon *via* electron-beam lithography, with different pitches and mark-space ratios. Once treated with an anti-stick monolayer coating, the silicon gratings were copied using a modified replica moulding process, forming a composite-PDMS replica of the structures to be used as a working stamp for imprinting polyimide. Given the fine features of the master gratings, with linewidths between 150nm and 350nm, and the inherent flexibility of PDMS, scanning electron microscopy was used to image cross-sections of the PDMS replicas to assess their structural stability and how faithfully the original structures were copied. At a linewidth of 150nm, the PDMS replicas exhibited significant lateral collapse at all mark-space ratios other than 1:2.5, where adjacent peaks coalesced and the original grating dimensions were lost. However, at a linewidth of 250nm, no lateral collapse was observed and all the grating structures on the PDMS replica were found to be stable, for mark-space ratios ranging from 1:1 to 1:2.5. These findings provide a case study on taking composite-PDMS replicas of sub-micron relief structures, helping guide future efforts to create soft replicas of structures on this length scale, which is an integral part of making the polyimide imprinting workflow an accessible means of patterning industry-standard LC alignment materials.

The stable PDMS replicas were then used to imprint layers of homeotropic polyimide, resulting in a range of 8 unique grating structures with pitches between 500nm and 1200nm. Optical diffraction patterns were used to check the pitch of the imprinted gratings prior to device assembly, which confirmed that the PDMS stamps didn't deform during the imprinting process and that even the shortest pitch of 500nm (250nm line, 250nm space) was faithfully transferred. With the imprinted gratings assembled opposite flat layers of homeotropic polyimide in a VAN geometry, the grating areas of the devices were found to be markedly transmissive at room temperature, whilst the adjacent non-grating areas remained extinct as per the homeotropic anchoring on both surfaces. This increased transmission was attributed to surface anchoring transitions on the grating substrate, similar to those seen in the homeotropic wrinkle device close to T_{NI}, where the competing influences of the surface topography and the homeotropic anchoring result in a distorted director field and a net pretilt of the director away from vertical, leading to an overall HAN state in the grating areas. Full-wave plate observations confirmed that the induced tilt was occurring in a plane perpendicular to the grating grooves.

Optically, the grating areas were hard to distinguish given their birefringence colours were various shades of first-order white. These different shades indicated that the induced pretilt varied as a function of grating dimensions, so in order to quantify this relationship, conoscopy was used to measure the average optic axis tilt of the LC slab in each of the grating areas. The resulting conoscopy figures exhibited off-center melatope positions that were shifted further from the center as the grating pitch decreased, corresponding to an increasingly tilted optic axis. To extract the tilt angle of the optic axis,

angular calibration of the conoscopy figures was carried out by imaging the diffraction pattern of a linear grating with known pitch and diffraction angle, allowing the different melatope positions on the figures to be converted to tilt angles. The optic axis tilt angles were converted to approximate director pretilt on the grating surface by assuming a linear variation in director tilt over the thickness of the induced HAN director profile. The resulting pretilt angles were found to vary between 61 - 74° for grating pitches of 500 – 1200nm, demonstrating the ability to fine-tune surface pretilt angles by making broad changes to the lateral dimensions of homeotropic surface relief gratings. Conoscopy observations also enabled simple and precise identification of the tilt direction on either side of reverse-tilt domain walls, formed due to tilt degeneracy in the absence of a predefined tilt direction e.g. by rubbing or a blazed grating profile. This demonstrated the ≤100μm capability of conoscopy for mapping the tilt distribution in LC devices, with the potential for higher resolutions *via* precision translation and higher magnification optics.

7.2 Future Work

7.2.1 Imprinting Apparatus

The imprinting apparatus that was relied upon for patterning polyimides throughout this thesis, is a simple but effective attachment that mounts to a laboratory hotplate and enables imprinting to be carried out at elevated temperatures. Whilst it has proven to be an indispensable tool in this work, there are certain features that could be added to improve its versatility, usability and repeatability.

During imprinting, air can often get trapped between the target resist layer and the stamp as they are brought together, resulting in pattern defects. One approach that is used to mitigate this in dedicated imprint lithography systems is ‘centre-to-edge’ imprinting, where the centre of a stamp is the first point of contact with the resist layer and then the remainder of the stamp is brought into contact from this central point, minimizing the chance of air being trapped.[238] Smaller scale imprint systems with similar functionality have also been demonstrated by Haslinger *et al*.,[256] where stamps are mounted to a deformable membrane over a pressurized chamber, which would allow for a similar central contact point during imprinting. Incorporating a simplified version of this functionality in to the hotplate press would be a beneficial upgrade to reduce air inclusions, and could be achieved by adding a spring-loaded pin in the centre of the foot of the hotplate press, which bulges the stamp upon initial contact and then retracts as sustained pressure is applied. The addition of an imprint pressure sensor would also help improve repeatability, particularly when optimizing a given resist for a particular feature height. This would most easily be implemented using a thin-film pressure sensor.

7.2.2 Micropatterned Liquid Crystal Elastomers

7.2.2.a Intermediate Rubbing Directions

The work on micropatterned liquid crystal elastomers (μLCEs) was a feasibility study and initial demonstration of incorporating micro-scale relief structures in to all-acrylate LCEs. As such, there are various lines of investigation that could be pursued to build upon the results presented in this thesis, the first of which keeps the vast majority of the experiment the same and simply varies the rubbing direction. The results in section 4.4.2 showed that, due to the inherent anisotropic deswelling of the μLCEs, the resulting pitch of the embedded grating structures was dependent on the orientation of the grating grooves with respect to the rubbing-defined director orientation. This was demonstrated at the two extremes where the grooves were either parallel or perpendicular to the director, with respective pitch reduction factors of 32% and 3%. Given the potential for μLCEs to be applied as general substrates for miniaturizing feature sizes, it would worthwhile to explore the reduction factors at intermediate angles between parallel and perpendicular to the director, as a means of calibrating the deswelling and allowing specific reduction factors to be targeted. Varying the rubbing direction relative to the grooves in 15° increments between 0 and 90° would be sufficient to establish whether the reduction factor varies linearly or otherwise between the two extremes.

7.2.2.b Homeotropic μLCEs

Planar anchoring was the only alignment configuration studied in this work, however fabricating μLCEs with homeotropic anchoring, as previously demonstrated on unpatterned LCEs by Wang *et al*.,[55] has the potential to minimize feature-height reduction and provide alternative μLCE device functionality. Using the same polyimide imprinting approach, homeotropic surface relief structures could be fabricated and used to form a μLCE film with the director oriented perpendicular to the plane of the film. The impact on deswelling should be two-fold in this scenario; firstly, the in-plane deswelling should now be isotropic with a reduction factor of the order of 32% (as observed in the $\hat{n}_{\parallel}$ planar sample), which would be beneficial for retaining the arrangement of structures with two-dimensional periodicity upon deswelling, and secondly, the reduction in feature height should now be of the order of 3% (as observed in the $\hat{n}_{\perp}$ planar sample) rather than the ≈50% height reduction in the planar configuration, which would help maximize the phase modulation of a diffractive optical element.[186] In a homeotropic configuration, the auxetic response of the μLCE would be observed in the plane of the film, in the form an expansion in lateral feature dimensions perpendicular to the direction of applied strain. This contrasting mechanical response, relative to the planar μLCE's increase in thickness/feature height under strain, has the potential to demonstrate new functionalities such as an oscillation in structural pitch about the auxetic threshold. This offers a unique diffractive response for strain-tunable optical elements, which could also be used as a characterisation technique for optically tracking the dimensional changes induced by the auxetic response in all-acrylate LCEs.

7.2.2.c Reflective μLCEs and Surface Wettability

The final suggestions for future research on μLCEs, require more significant changes to the experimental approach used in this work, but have the potential to expand μLCE device capabilities and enable a broader range of physical phenomena to be investigated. The transmission μLCE diffraction gratings explored in this work, allow for simple measurement of the diffractive properties and demonstrates the inherent transparency of LCE medium. However, transmission diffraction gratings are rarely applied in optical systems due to the benefits offered by reflection gratings, such as, greater spectral flexibility since light doesn't pass through a substrate, more compact optical systems due to mirror-like operation (beam folding) and higher diffraction angles.[186] Guerrero *et al.* converted an elastomeric transmission grating in to a reflection grating *via* thermal evaporation of a reflective gold layer on to the surface, however upon strain application a reduction in reflectivity and diffraction efficiency was found due to buckling of the stiff gold layer on the compliant elastomeric substrate.[257] An alternative method for creating reflective elastomeric gratings, which avoids the limitations of metal thin-film deposition, is supersonic cluster beam implantation (SCBI).[258,259] This room temperature process involves directing a supersonic beam of neutral metallic clusters towards a polymer target, which penetrate the polymer surface and form a reflective nanocomposite surface layer. Deformable reflection gratings have been realized using this technique to metallize PDMS surface relief gratings,[260,261] and should therefore be transferrable for converting μLCEs in to reflective components.

Aside from optical functionality, the patterned surface topography and stimuli-responsiveness of the μLCEs offers a potential means of actively controlling surface wettability, with implications for anti-fouling, droplet manipulation and varifocal liquid lenses.[262] Both mechanical and thermal actuation of μLCEs, featuring topographic patterns such as pillar arrays, are capable of changing the dimensions of the surface structures and potentially the wetting state of liquids in contact with the surface.[263] The height and spacing of periodic microstructures influence the resulting water contact angle of a surface, where taller structures tend to be more hydrophobic (larger contact angle) [244] and those with wider spacings tend to be more hydrophilic (smaller contact angle).[192] With this in mind, a particularly interesting experiment would be to apply uniaxial strain parallel to the grooves of a planar, $\hat{n}_{\perp}$ μLCE grating sample, and monitor the changes in wetting characteristics using a contact angle goniometer (e.g. Droplet Lab [264] or L2004A1 by Ossila Ltd.). This would reduce the pitch of the grating as a function of strain due to necking, likely increasing the contact angle, followed by a unique increase in feature height once the auxetic threshold is surpassed, further increasing the contact angle and potentially causing wetting state transitions.

7.2.3 Spontaneously Wrinkled Alignment Layers

7.2.3.a Alternative Wrinkle Geometries

The wrinkle structures studied in thesis are a simple linear groove structure, formed by applying a uniaxial tensile strain to a compliant PDMS slab. There exists a wide range of potential wrinkle geometries that can be accessed by changing how the PDMS slab is prepared and perturbed, which will each have a unique and potentially favourable impact on LC surface alignment. Bowden *et al.* demonstrated how pre-patterning a PDMS slab with relief structures, enabled the wrinkling process to be guided and controlled to create intricate wrinkle textures that are dictated by the shape and arrangement of the relief structures.[196] Combining such patterns with the polyimide imprinting process described in this thesis, could allow for interesting patterned LC alignment configurations that combine the confinement of the wrinkled and pre-patterned structures with the surface anchoring of either planar of homeotropic polyimides.

An interesting wrinkle geometry to explore in LC systems would be one with a radially concentric or ripple-like texture, so as to impose circular grating alignment where the azimuthal director orientation varies continuously around the center of the pattern. The fabrication of concentric wrinkle textures has previously been demonstrated using a radial-strain approach, where a circular PDMS slab is stretched over a central pillar,[265] or by solvent swelling a pre-indented oxide layer.[266] Alone, concentric wrinkle textures on PDMS have been used for macroscopic optical focusing,[265] so incorporating these textures in to LC devices may enable this same focusing capability to be electrically tunable. Circular alignment of the nematic director has been used to study the polar nature of the ferroelectric nematic phase [267] and to create polarisation converters.[268] The ability for concentric wrinkles to impose circular director alignment, as confirmed during the preliminary investigations presented in section 7.2.3.a.i, means that they could be applied in similar applications as mentioned above, with the added benefit of being able to easily scale up to large areas and cater for large-aperture optical systems.

7.2.3.a.i Preliminary Work on LC Alignment with Concentric Wrinkles

The preliminary work carried out on the fabrication of concentric wrinkle textures and their LC alignment properties is now summarised. Using a similar radial-strain approach to the one reported by Li *et al.*,[265] a range of concentric wrinkle textures were formed on 1mm thick, 32mm diameter circular PDMS slabs, using a strain rig with an adjustable-height central pillar to apply strains (ε) of $52-112\%$ (Figure 7-1a,b). Under strain, the PDMS was exposed to an oxygen plasma treatment, where two different doses (D = Applied RF power (W) × Exposure time (s)) were selected to target sub-micron pitch (d) wrinkles, by staying within the stiff oxide layer's 'skin formation regime' where the layer thickness (h_f) remains small and therefore minimizes d (Equation (5-1)).[203]

Upon strain release, concentric wrinkle textures were formed on the PDMS slabs (Figure 7-1c), confirmed visually by the diffractive optical appearance closely resembling that of a CD (Figure 7-1d), which feature concentric microscale grating structures. The dimensions of the wrinkles were measured with AFM, where at $D = 3.6$kJ (lower h_f) wrinkles formed with $d = 390 - 560$nm and an average height (h) of $\approx$ 20nm, and at $D = 7.2$kJ (higher h_f) wrinkles formed with $d = 410 - 780$nm and $h \approx 45$nm.

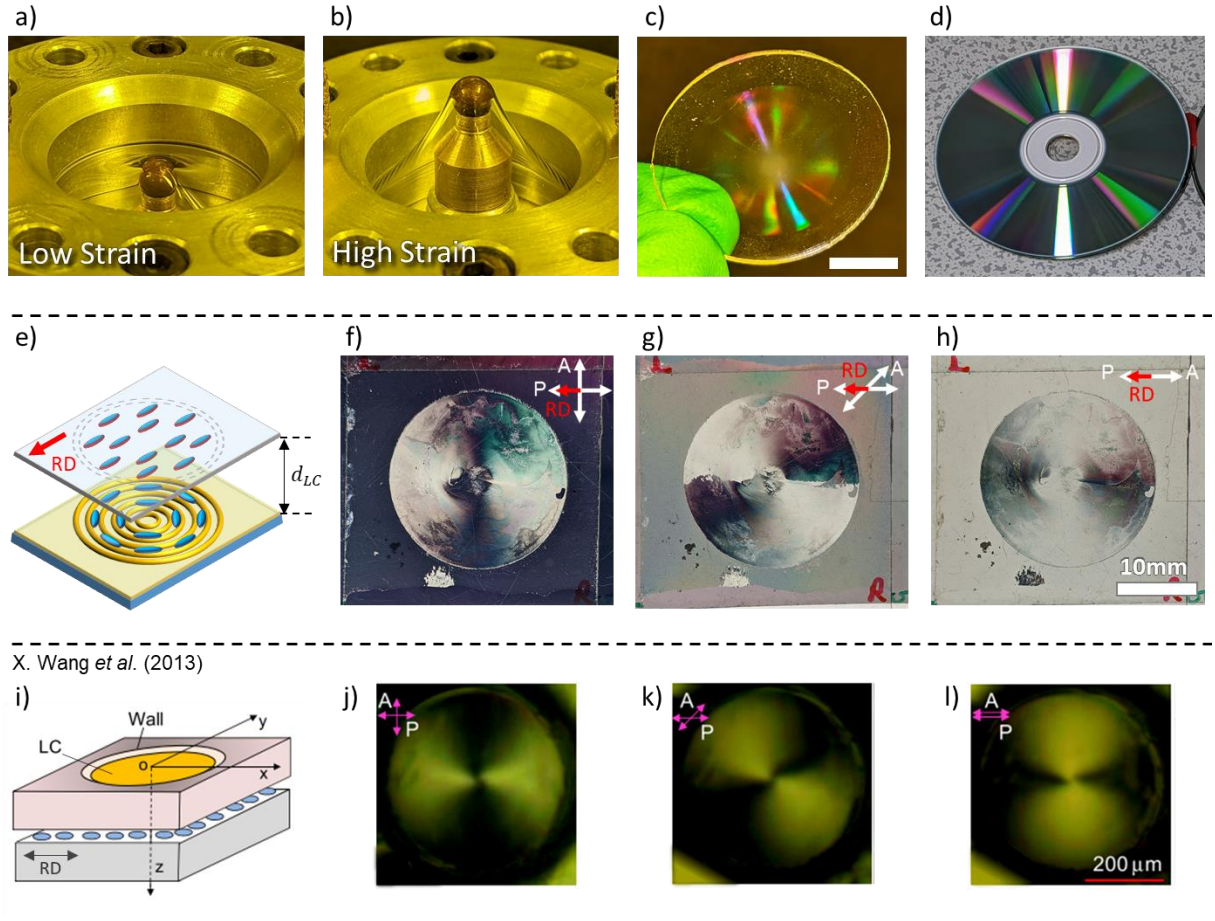

Figure 7-1: Fabrication and alignment properties of concentric wrinkle textures. (a,b) Circular PDMS slab mounted in the radial-strain apparatus at low and high tensile strains. (c) Visual appearance of wrinkled PDMS slab after oxygen plasma etching and strain release. Scale bar = 10mm. (d) Image of a CD as a reference point, with similar diffractive optical appearance to the wrinkled slab. (e) Schematic geometry of the LC device containing the concentric wrinkle texture. Upper, unpatterned planar polyimide surface is rubbed with a rubbing direction (RD) and the lower, wrinkle-imprinted polyimide surface is left unrubbed. Filled with 5CB, with an LC layer thickness (d_{LC}) of $10 \pm 1\mu$m. (f–h) Polarised microscopy images of the filled wrinkle device at different analyser (A) orientations. (i–l) Device geometry and polarised microscopy images of the reference device made by Wang et al., with the same bulk director configurations and comparable optical appearance to the wrinkle device.

The texture with the highest azimuthal anchoring strength (W_{Φ}) was selected using Equation (2-10) ($d = 410 \pm 20$nm, h = 42 $\pm$ 5nm, $W_{\psi} \approx (2.4 \pm 0.7) \times 10^{-6}$ Jm^{-2}), and then imprinted in to a layer of planar polyimide (SE-130) using the imprinting methodology detailed in section 3.2.2.b. This planar wrinkle texture was left unrubbed and assembled in to a device opposite a flat, rubbed layer of SE-130 (Figure 7-1e). This device geometry was chosen to match the resulting alignment found in the devices constructed by Wang *et al.*,[27] which utilize a cylindrical cavity to impose circular or azimuthal director alignment *via* confinement (Figure 7-1i), rather than the concentric groove structures used in this work. Polarised microscopy images of the wrinkle device, with different analyser orientations, are shown in Figure 7-1f−h. Below in Figure 7-1j−l, are the corresponding polarised microscopy images from the devices of Wang *et al*., with the same polariser orientations for a direct comparison to the wrinkle device. Both devices display a comparable 2-brush optical texture, due to the bulk director profile continuously varying between uniformly aligned (extinct in Figure 7-1f,j) and twisted nematic with a ≈90° twist (bright in Figure 7-1f,j). This optical appearance and agreement with the observations of Wang *et al*., confirms that the wrinkles are continuously varying the azimuthal director orientation with the director aligned parallel to the grooves. This is the first known demonstration of using a spontaneously formed concentric wrinkle texture, to promote circular or azimuthal surface alignment of the nematic director in a liquid crystal device.

7.2.3.b Exploring Director Modulation with Precision 'Wrinkle-Wall' Structures

One of the most intriguing observations made whilst studying the LC-wrinkle systems, was the spatially modulated azimuthal director orientation induced by the wrinkled textures with homeotropic anchoring (section 5.4.3.d). This alignment behaviour was attributed to the spatial confinement imposed by the 'wall' structures formed during imprinting, combined with the surface anchoring transitions and resulting director tilt caused by the periodic wrinkles. The periodicity of this modulation was found to be of the order of 10−20μm, which is comparable to the spacing between adjacent walls and suggests that controlling this spacing may offer a means of controlling the modulation periodicity. As such, it is suggested that fabricating precision microstructures to mimic these 'wrinkle-wall' textures would be a valuable future investigation, where the resulting surfaces would ideally be comprised of a periodic linear grating with protruding wall structures running perpendicular to the grating grooves, with different spacings, heights and shape profiles. The aim of this would be to establish whether these structures could serve as a topography-driven alternative for creating complex modulated director profiles, such as those defined by photoalignment [225,226,269] or grating alignment [21] in flat optical components. As demonstrated in section 5.4.3.b, the surface anchoring transition that causes the tilted and modulated alignment state is temperature dependant, and can therefore be switched on or off by heating or cooling the system respectively. This approach may therefore offer an alternative means of reversibly adding or removing director modulation from LC devices.

7.2.4 Sub-Micron Homeotropic Gratings

7.2.4.a Electrooptic Response of Current Devices and Inverted Master Structures

The alignment properties of the homeotropic grating structures was the focus of Chapter 6, where it was shown that a HAN director profile was formed as a result of a surface anchoring transition inducing director tilt on the grating surface. The electrooptic response of these HAN states was not investigated in this work, but would be worthwhile revisiting to determine properties such as the response time and whether the alignment state is bistable (using driving schemes similar to those used in Zenithal Bistable Displays [270]). During the pattern transfer process, it was found that at a linewidth of 150nm, the soft PDMS replicas suffered from lateral collapse where the 150nm wide PDMS peaks coalesced (section 6.4.1.a). A possible way to improve the stability of the PDMS replicas, to allow shorter pitch grating structures to be imprinted using this approach, would be to invert the original silicon-oxide master structures so that the narrower lines are peaks rather than valleys in the more rigid oxide layer. When the PDMS replicas are then taken of these structures, the narrow oxide peaks would become 150nm wide valleys in the PDMS which would be less likely to collapse given the now wider peaks (spaces) supporting them on either side (inverse of patterns shown in Figure 6-9b).

7.2.4.b Impact of Rubbing on Tilt Degeneracy and Potential Device Applications

The homeotropic grating devices investigated in this work showed varying levels of tilt degeneracy, in the form of reverse-tilt domain walls, as shown in Figure 6-11c. These domain walls form due to a lack preferential tilt direction on the grating surface, stemming from the imprinted polyimide layer being untreated and assembled in to a device directly after imprinting. A benefit of using polyimides is that a robust and uniform tilt direction can be readily defined *via* mechanical rubbing, and therefore an interesting future study would be to use the same fabrication method described in this work, but with mechanical rubbing applied perpendicular to the grooves of the grating substrate. It is likely that the rubbing will only interact with the peaks of the imprinted grating structures, but this may be enough to introduce a tilt preference. Establishing whether a similar tilted alignment state can be obtained in these devices and if the applied rubbing is sufficient to remove the tilt degeneracy, would broaden the applicability of these alignment layers for LC systems requiring tilted surface alignments. If the rubbing treatment is found to be capable of producing uniform tilt in these systems, an interesting device geometry to explore would be one with rubbed homeotropic gratings on both cell surfaces and parallel rubbing directions. Given that the grating dimensions can be used to adjust the pretilt angle on the grating surface (Figure 6-19a) and intermediate tilt angles have been demonstrated in comparable homeotropic grating systems,[113] this parallel rubbed configuration may have the ability to create and stabilize an optically-compensated bend (OCB) mode or Pi-cell geometry for high-speed electrooptic responses.[271–273]

7.2.4.c Detailed Director Profile Analysis

During this work, conoscopy was used to measure the average tilt angle of the optic axis for a given device, from which the pretilt angle on the grating surface was estimated by assuming that the director tilt varied linearly as a function of cell thickness. The homeotropic gratings studied in this work, with tilt induced by the grating's topographic distortion of the near-surface director field, bear a close resemblance to the homeotropic gratings found in Zenithal Bistable Displays and are therefore likely to behave in a similar way. In related work by Jones,[230] a comment is made on the ZBD's grating-induced deformation of the director field being limited to the vicinity of the grating surface, and that a uniform director profile exists at distances beyond half of the grating pitch away from the surface ($z > 500nm$). If this is also the case for the grating systems in this work, the quoted pretilt values are potentially overestimates of the actual value i.e. if the deformation decays in a 'ZBD-like' fashion, the pretilt on the grating must be lower (more significantly titled from vertical) to produce the same first-order white birefringence colour. Confirming the actual director profile in these devices is non-trivial, but one potential route that could provide some insight is confocal Raman microscopy.[274] This technique is capable of distinguishing between planar, intermediate and homeotropic director orientations and by capturing images at different depths, a 3D representation of the director profile can be obtained. Limited by the microscope's Z resolution (ideally need 1μm step size), this may not be able to provide a precise map of the director profile, but should be sufficient to determine whether the tilt/director deformation has decayed within 1-2μm of the grating surface.

References

1. Schadt, M.; Helfrich, W. Voltage-Dependent Optical Activity of a Twisted Nematic Liquid Crystal. *Appl. Phys. Lett.* **1971**, *18*, 127–128.

2. Hilsum, C. Flat-Panel Electronic Displays: A Triumph of Physics, Chemistry and Engineering. *Philos. Trans. R. Soc. A* **2010**, *368*, 1027–1082, doi:10.1098/rsta.2009.0247.

3. Schadt, M.; Seiberle, H.; Schuster, A. Optical Patterning of Multi-Domain Liquid-Crystal. *Nature* **1996**, *381*, 212–215, doi:381212a0.

4. Seiberle, H.; Schadt, M. Photoalignment and Photo-Patterning of Planar and Homeotropic Liquid-Crystal-Display Configurations. *J. Soc. Inf. Disp.* **2000**, *8*, 67, doi:10.1889/1.1828704.

5. Wang, M.; Li, Y.; Yokoyama, H. Artificial Web of Disclination Lines in Nematic Liquid Crystals. *Nat. Commun.* **2017**, *8*, doi:10.1038/s41467-017-00548-x.

6. Guo, Y.; Jiang, M.; Afghah, S.; Peng, C.; Selinger, R.L.B.; Lavrentovich, O.D.; Wei, Q.H. Photopatterned Designer Disclination Networks in Nematic Liquid Crystals. *Adv. Opt. Mater.* **2021**, *2100181*, 1–8, doi:10.1002/adom.202100181.

7. Pawale, T.; Yi, S.; Wang, X.; Zhang, R.; Li, X. The Fate of Liquid Crystal Topological Defects on Chemically Patterned Surfaces during Phase Transitions. *Soft Matter* **2022**, *18*, 5939–5948, doi:10.1039/d2sm00566b.

8. Provenzano, C.; Pagliusi, P.; Cipparrone, G. Highly Efficient Liquid Crystal Based Diffraction Grating Induced by Polarization Holograms at the Aligning Surfaces. *Appl. Phys. Lett.* **2006**, *89*, 1–4, doi:10.1063/1.2355456.

9. Oh, C.; Escuti, M.J. Achromatic Diffraction from Polarization Gratings with High Efficiency. *Opt. Lett.* **2009**, *34*, 3637, doi:10.1364/ol.34.003637.

10. Fan, F.; Srivastava, A.K.; Du, T.; Tseng, M.C.; Chigrinov, V.; Kwok, H.S. Low Voltage Tunable Liquid Crystal Lens. *Opt. Lett.* **2013**, *38*, 4116–4119, doi:10.1080/02678292.2019.1706109.

11. Nys, I.; Beeckman, J.; Neyts, K. Switchable 3D Liquid Crystal Grating Generated by Periodic Photo-Alignment on Both Substrates. *Soft Matter* **2015**, *11*, 7802–7808, doi:10.1039/c5sm01294e.

12. Wang, X.-Q.; Yang, W.-Q.; Liu, Z.; Duan, W.; Hu, W.; Zheng, Z.-G.; Shen, D.; Chigrinov, V.G.; Kwok, H.-S. Switchable Fresnel Lens Based on Hybrid Photo-Aligned Dual Frequency Nematic Liquid Crystal. *Opt. Mater. Express* **2017**, *7*, 8, doi:10.1364/ome.7.000008.

13. Gorkunov, M. V.; Kasyanova, I. V.; Artemov, V. V.; Ezhov, A.A.; Mamonova, A. V.; Simdyankin, I. V.; Palto, S.P. Liquid-Crystal Metasurfaces Self-Assembled on Focused Ion Beam Patterned Polymer Layers: Electro-Optical Control of Light Diffraction and Transmission. *ACS Appl. Mater. Interfaces* **2020**, *12*, 30815–30823, doi:10.1021/acsami.0c07320.

14. Simdyankin, I.V.; Geivandov, A.R. Synchronised Flexoelectric Instability in an LC Cell with Periodic Planar-Homeotropic Alignment. *Liq. Cryst.* **2022**, *00*, 1–11, doi:10.1080/02678292.2022.2154865.

15. Sami Franssila *Introduction to Microfabrication, Second Edition*; 2010; ISBN 9781119990413.

16. Bryan-Bown, G.P.; Brown, C. V.; Jones, J.C.; Wood, E.L.; Sage, I.C.; Brett, P.; Rudin, J. Grating Aligned Bistable Nematic Device. *SID Symp. Dig. Tech. Pap.* **1997**, 37–40.

17. Jones, J.C. The Zenithal Bistable Display: From Concept to Consumer. *J. Soc. Inf. Disp.* **2008**, *16*, 143, doi:10.1889/1.2835021.

18. Akselrod, G.M.; Yang, Y.; Bowen, P. Tunable Liquid Crystal Metasurfaces, US Patent No.: 10,665,953 B1., **2020**.

19. Akselrod, G.M.; Iyer, P.P.; Uthoff, R.D. Lidar Systems Based on Tunable Optical Metasurfaces, US Patent No.: 11,092,675 B2., **2021**.

20. Lininger, A.; Zhu, A.Y.; Park, J.S.; Palermo, G.; Chatterjee, S.; Boyd, J.; Capasso, F.; Strangi, G. Optical Properties of Metasurfaces Infiltrated with Liquid Crystals. *Proc. Natl. Acad. Sci. U. S. A.* **2020**, *117*, 20390–20396, doi:10.1073/pnas.2006336117.

21. He, Z.; Lee, Y.-H.; Chen, R.; Chanda, D.; Wu, S.-T. Switchable Pancharatnam–Berry Microlens Array with Nano-Imprinted Liquid Crystal Alignment. *Opt. Lett.* **2018**, *43*, 5062, doi:10.1364/ol.43.005062.

22. Kim, M.S.; Serra, F. Tunable Dynamic Topological Defect Pattern Formation in Nematic Liquid Crystals. *Adv. Opt. Mater.* **2020**, *8*, 1–8, doi:10.1002/adom.201900991.

23. Kim, M.; Serra, F. Topological Defect Arrays in Nematic Liquid Crystals Assisted by Polymeric Pillar Arrays: Effect of the Geometry of Pillars. *Crystals* **2020**, *10*, doi:10.3390/cryst10040314.

24. Kim, M.S.; Serra, F. Quasicrystalline Arrays and Moiré Patterns in Nematic Liquid Crystals for Soft Photonics. *Adv. Opt. Mater.* **2022**, *10*, doi:10.1002/adom.202200916.

25. Chang, A.S.P.; Morton, K.J.; Tan, H.; Murphy, P.F.; Wu, W.; Chou, S.Y. Tunable Liquid Crystal-Resonant Grating Filter Fabricated by Nanoimprint Lithography. *IEEE Photonics Technol. Lett.* **2007**, *19*, 1457–1459, doi:10.1109/LPT.2007.903719.

26. Sadani, B.; Boisnard, B.; Lafosse, X.; Camps, T.; Doucet, J.B.; Daran, E.; Paranthoen, C.; Levallois, C.; Dupont, L.; Bouchoule, S.; et al. Liquid-Crystal Alignment by a Nanoimprinted Grating for Wafer-Scale Fabrication of Tunable Devices. *IEEE Photonics Technol. Lett.* **2018**, *30*, 1388–1391, doi:10.1109/LPT.2018.2849641.

27. Wang, X.; Xu, M.; Ren, H.; Wang, Q. A Polarization Converter Array Using a Twisted-Azimuthal Liquid Crystal in Cylindrical Polymer Cavities. *Opt. Express* **2013**, *21*, 16222, doi:10.1364/oe.21.016222.

28. Hahm, S.G.; Ko, Y.G.; Rho, Y.; Ahn, B.; Ree, M. Liquid Crystal Alignment in Advanced Flat-Panel Liquid Crystal Displays. *Curr. Opin. Chem. Eng.* **2013**, *2*, 71–78, doi:10.1016/j.coche.2012.09.010.

29. Nishikawa, M. Design of Polyimides for Liquid Crystal Alignment Films. *Polym. Adv. Technol.* **2000**, *11*, 404–412, doi:10.1002/1099-1581(200008/12)11:8/12<404::AID-PAT41>3.0.CO;2-T.

30. Moorhouse, T.; Raistrick, T. Sub-Micron Diffractive Optical Elements Facilitated by Intrinsic Deswelling of Auxetic Liquid Crystal Elastomers. *Adv. Opt. Mater.* **2024**, *12*, 2400866, doi:10.1002/adom.202400866.

31. Jones, R.A.L. *Soft Condensed Matter*; Oxford University Press, **2002**; pp. 105-115, ISBN 0-19-850589-2

32. Collings, P.J.; Hird, M. *Introduction to Liquid Crystals Chemistry and Physics*; G.W. Gray, J. W. Goodby, A.F., Ed.; Taylor & Francis, **1997**; pp. 1-19, ISBN 0-203-21119-7.

33. de Gennes, Pierre Gilles; Prost, J. *The Physics of Liquid Crystals*; 2nd ed.; Oxford University Press, **1993**; pp. 10-13, 98-107, ISBN 0198520247.

34. Goodby, J.W. Chirality in Liquid Crystals. *J. Mater. Chem.* **1991**, *1*, 307–318, doi:10.1039/jm9910100307.

35. Dierking, I. Chiral Liquid Crystals: Structures, Phases, Effects. *Symmetry (Basel).* **2014**, *6*, 444–472, doi:10.3390/sym6020444.

36. Cestari, M.; Diez-Berart, S.; Dunmur, D.A.; Ferrarini, A.; De La Fuente, M.R.; Jackson, D.J.B.; Lopez, D.O.; Luckhurst, G.R.; Perez-Jubindo, M.A.; Richardson, R.M.; et al. Phase Behavior and Properties of the Liquid-Crystal Dimer 1″,7″-Bis(4-Cyanobiphenyl-4′-Yl) Heptane: A Twist-Bend Nematic Liquid Crystal. *Phys. Rev. E - Stat. Nonlinear, Soft Matter Phys.* **2011**, *84*, 1–20, doi:10.1103/PhysRevE.84.031704.

37. Mandle, R.J.; Cowling, S.J.; Goodby, J.W. A Nematic to Nematic Transformation Exhibited by a Rod-like Liquid Crystal. *Phys. Chem. Chem. Phys.* **2017**, *19*, 11429–11435, doi:10.1039/c7cp00456g.

38. Nishikawa, H.; Shiroshita, K.; Higuchi, H.; Okumura, Y.; Haseba, Y.; Yamamoto, S.; Sago, K.; Kikuchi, H. A Fluid Liquid-Crystal Material with Highly Polar Order. *Adv. Mater.* **2017**, *29*, 1–8, doi:10.1002/adma.201702354.

39. Gibb, C.J.; Hobbs, J.; Nikolova, D.I.; Raistrick, T.; Berrow, S.R.; Mertelj, A.; Osterman, N.; Sebastián, N.; Gleeson, H.F.; Mandle, R.J. Spontaneous Symmetry Breaking in Polar Fluids. *Nat. Commun.* **2024**, *15*, 1–9, doi:10.1038/s41467-024-50230-2.

40. Oseen, C.W. The Theory of Liquid Crystals. *Trans. Faraday Soc.* **1933**, *29*, 883–899, doi:10.1039/tf9332900883.

41. Frank, F.C. On the Theory of Liquid Crystals. *Liq. Cryst.* **1958**, *25*, 19–28.

42. Maier, W.; Saupe, A. Eine Einfache Molekular-Statistische Theorie Der Nematischen Kristallinflüssigen Phase. Teil II. *Zeitschrift für Naturforsch. A* **1960**, *15*, 287–292.

43. Berreman, D.W.; Meiboom, S. Tensor Representation of Oseen-Frank Strain Energy in Uniaxial Cholesterics. *Phys. Rev. A* **1984**, *30*, 1955–1959, doi:10.1103/PhysRevA.30.1955.

44. Cui, M.; Kelly, J.R. Temperature Dependence of Visco-Elastic Properties of 5CB. *Mol. Cryst. Liq. Cryst. Sci. Technol. Sect. A Mol. Cryst. Liq. Cryst.* **1999**, *331*, 49–57, doi:10.1080/10587259908047499.

45. Kaur, S.; Liu, H.; Addis, J.; Greco, C.; Ferrarini, A.; Görtz, V.; Goodby, J.W.; Gleeson, H.F. The Influence of Structure on the Elastic, Optical and Dielectric Properties of Nematic Phases Formed from Bent-Core Molecules. *J. Mater. Chem. C* **2013**, *1*, 6667–6676, doi:10.1039/c3tc31545b.

46. *Handbook of Visual Display Technology*; Chen, J., Cranton, W., Fihn, M., Eds.; **2016**; pp. 77-80, 1979-2002, 2003-2019, ISBN 9783319143460.

47. Hecht, E. *Optics*; 5th ed.; Pearson Education Inc., **2017**; p. 377 ISBN 0133977226.

48. Bloss, F.D. *An Introduction to the Methods of Optical Crystallography*; 1961; p. 100, ISBN 9781626239777.

49. Sørensen, B.E. A Revised Michel-Lévy Interference Colour Chart Based on First-Principles Calculations. *Eur. J. Mineral.* **2013**, *25*, 5–10, doi:10.1127/0935-1221/2013/0025-2252.

50. Finkelmann, H.; Kock, H.J.; Rehage, G. Investigations on Liquid Crystalline Polysiloxanes 3, Liquid Crystal Elsatomers - A New Type of Liquid Crystalline Material. *Die Makromol. Chemie, Rapid Commun.* **1981**, *2*, 317–322.

51. Ford, J.R.; Bassett, D.C.; Mitchell, G.R.; Ryan, T.G. Morphology of a Main Chain Liquid Crystal Polymer Containing Semi-Flexible Coupling Chain. *Mol. Cryst. Liq. Cryst. Inc. Nonlinear Opt.* **1990**, *180*, 233–243, doi:10.1080/00268949008042205.

52. Bladon, P.; Terentjev, E.M.; Warner, M. Transitions and Instabilities in Liquid Crystal Elastomers. *Phys. Rev. E* **1993**, *47*, 3838–3840, doi:10.1103/PhysRevE.47.R3838.

53. Küpfer, J.; Finkelmann, H. Nematic Liquid Single Crystal Elastomers. *Die Makromol. Chemie, Rapid Commun.* **1991**, *12*, 717–726.

54. Mitchell, G.R.; Davis, F.J.; Guo, W. Strain-Induced Transitions in Liquid-Crystal Elastomers. *Phys. Rev. Lett.* **1993**, *71*, 2947–2950, doi:10.1103/PhysRevLett.71.2947.

55. Wang, Z.; Raistrick, T.; Street, A.; Reynolds, M.; Liu, Y.; Gleeson, H.F. Direct Observation of Biaxial Nematic Order in Auxetic Liquid Crystal Elastomers. *Materials (Basel).* **2023**, *16*, 1–15.

56. Urayama, K.; Arai, Y.O.; Takigawa, T. Volume Phase Transition of Monodomain Nematic Polymer Networks in Isotropic Solvents Accompanied by Anisotropic Shape Variation. *Macromolecules* **2005**, *38*, 3469–3474, doi:10.1021/ma047391c.

57. Mistry, D.; Morgan, P.B.; Clamp, J.H.; Gleeson, H.F. New Insights into the Nature of Semi-Soft Elasticity and "Mechanical-Fréedericksz Transitions" in Liquid Crystal Elastomers. *Soft Matter* **2018**, *14*, doi:10.1039/c7sm02107k.

58. Kundler, I.; Finkelmann, H. Strain-Induced Director Reorientation in Nematic Liquid Single Crystal Elastomers. *Macromol. Rapid Commun.* **1995**, *16*, 679–686.

59. Bladon, P.; Terentjev, E.M.; Warner, M. Deformation–Induced Orientational Transitions in Liquid Crystals Elastomer. *J. Phys. II* **1994**, *4*, 75–91.

60. Mistry, D.; Gleeson, H.F. Mechanical Deformations of a Liquid Crystal Elastomer at Director Angles Between 0 and 90 : Deducing an Empirical Model Encompassing Anisotropic Nonlinearity. *J. Polym. Sci. Part B Polym. Phys.* **2019**, *57*, 1367–1377, doi:10.1002/polb.24879.

61. Mistry, D.; Connell, S.D.; Mickthwaite, S.L.; Morgan, P.B.; Clamp, J.H.; Gleeson, H.F. Coincident Molecular Auxeticity and Negative Order Parameter in a Liquid Crystal Elastomer. *Nat. Commun.* **2018**, *9*, 5095, doi:10.1038/s41467-018-07587-y.

62. M. Warner and E. M. Terentjev *Liquid Crystal Elastomers*; Clarendon Press: Oxford, **2003**; pp. 106-107, ISBN 978-0-19-852767-1

63. Goodman, L.A. Liquid-Crystal Displays - Packaging and Surface Treatments. *RCA Rev.* **1974**, *35*, 331–479.

64. Ishihara, S.; Wakemoto, H.; Nakazima, K.; Matsuo, Y. The Effect of Rubbed Polymer Films on the Liquid Crystal Alignment. *Liq. Cryst.* **1989**, *4*, 669–675, doi:10.1080/02678298908033202.

65. Toney, M.F.; Russell, T.P.; Logan, J.A.; Kikuchi, H.; Sands, J.M.; Kumar, S.K. Near-Surface Alignment of Polymers in Rubbed Films. *Nature* **1995**, *374*, 709–711, doi:10.1038/374709a0.

66. Schadt, M.; Schmitt, K.; Kozinkov, V.; Chigrinov, V. Surface-Induced Parallel Alignment of Liquid Crystals by Linearly Polymerized Photopolymers. *Jpn. J. Appl. Phys.* **1992**, *31*, 2155–2164, doi:10.1143/JJAP.31.2155.

67. Chigrinov, V.G.; Kwok, H.-S.; Hasebe, H.; Takatsu, H.; Takada, H. Liquid-Crystal Photoaligning by Azo Dyes. *J. Soc. Inf. Disp.* **2008**, *16*, 897, doi:10.1889/1.2976648.

68. Nys, I.; Nersesyan, V.; Beeckman, J.; Neyts, K. Complex Liquid Crystal Superstructures Induced by Periodic Photo-Alignment at Top and Bottom Substrates. *Soft Matter* **2018**, *14*, 6892–6902, doi:10.1039/c8sm01145a.

69. Kahn, F.J. Orientation of Liquid Crystals by Surface Coupling Agents. *Appl. Phys. Lett.* **1973**, *22*, 386–388, doi:10.1063/1.1654684.

70. Malone, S.M.; Schwartz, D.K. Polar and Azimuthal Alignment of a Nematic Liquid Crystal by Alkylsilane Self-Assembled Monolayers: Effects of Chain-Length and Mechanical Rubbing. *Langmuir* **2008**, *24*, 9790–9794, doi:10.1021/la801322x.

71. Jones, S.A.; Bailey, J.; Walker, D.R.E.; Bryan-Brown, G.P.; Jones, J.C. Method for Tuneable Homeotropic Anchoring at Microstructures in Liquid Crystal Devices. *Langmuir* **2018**, *34*, 10865–10873, doi:10.1021/acs.langmuir.8b01951.

72. Goodman, L.; McGinn, J.T.; Anderson, C.H.; Digeronimo, F. Topography of Obliquely Evaporated Silicon Oxide Films and Its Effect on Liquid-Crystal Orientation. *Proc Soc Inf Disp* **1977**, *24*, 795–804.

73. Heffner, W.R.; Berreman, D.W.; Sammon, M.; Meiboom, S. Liquid Crystal Alignment on Surfactant Treated Obliquely Evaporated Surfaces. *Appl. Phys. Lett.* **1980**, *36*, 144–146.

74. Berreman, D.W. Solid Surface Shape and the Alignment of an Adjacent Nematic Liquid Crystal. *Phys. Rev. Lett.* **1972**, *28*, 1683–1686, doi:10.1103/PhysRevLett.28.1683.

75. Kim, M.H.; Kim, J.D.; Fukuda, T.; Matsuda, H. Alignment Control of Liquid Crystals on Surface Relief Gratings. *Liq. Cryst.* **2000**, *27*, 1633–1640, doi:10.1080/026782900750037194.

76. Ishihara, S. How Far Has the Molecular Alignment of Liquid Crystals Been Elucidated? *IEEE/OSA J. Disp. Technol.* **2005**, *1*, doi:10.1109/JDT.2005.852493.

77. Jones, S.A. Zenithal Bistable Display: Avenues for Improved Performance., PhD Thesis, University of Leeds, **2019**.

78. Jägemalm, P. On the Optics and Surface Physics of Liquid Crystals, Phd Thesis, Chalmers University of Technology, Göteborg University, **1999**.

79. Nastishin, Y.A.; Polak, R.D.; Shiyanovskii, S. V.; Bodnar, V.H.; Lavrentovich, O.D. Nematic Polar Anchoring Strength Measured by Electric Field Techniques. *J. Appl. Phys.* **1999**, *86*, 4199–4213, doi:10.1063/1.371347.

80. Nie, X.; Lin, Y.-H.; Wu, T.X.; Wang, H.; Ge, Z.; Wu, S.-T. Polar Anchoring Energy Effect and Measurement of Vertically Aligned Liquid-Crystal Cells. *J. Appl. Phys.* **2005**, *98*, 013516, doi:10.1109/AUTEST.2005.1609178.

81. Fonesca, J.G.; Galerne, Y. Simple Method for Measuring the Azimuthal Anchoring Strength of Nematic Liquid Crystals. *Appl. Phys. Lett.* **2001**, *2910*, 1999–2002, doi:10.1063/1.1415344.

82. Wood, E.L.; Bradberry, G.W.; Cann, P.S.; Sambles, J.R. Determination of Azimuthal Anchoring Energy in Grating-Aligned Twisted Nematic Liquid-Crystal Layers. *J. Appl. Phys.* **1997**, *82*, doi:10.1063/1.366060.

83. Choi, Y.; Yokoyama, H.; Gwag, J.S. Determination of Surface Nematic Liquid Crystal Anchoring Strength Using Nano-Scale Surface Grooves. *Opt. Express* **2013**, *21*, 12135, doi:10.1364/oe.21.012135.

84. Mauguin, C. Sur Les Cristaux Liquides de M. Lehmann. *Bull. la Société française Minéralogie* **1911**, *34*, 71–117, doi:10.3406/bulmi.1911.3472.

85. Lee, S.W.; Chae, B.; Kim, H.C.; Lee, B.; Choi, W.; Kim, S. Bin; Chang, T.; Ree, M. New Clues to the Factors Governing the Perpendicular Alignment of Liquid Crystals on Rubbed Polystyrene Film Surfaces. *Langmuir* **2003**, doi:10.1021/la034883u.

86. Seo, D.S.; Muroi, K.I.; Isogami, T.R.; Matsuda, H.; Kobayashi, S. Polar Anchoring Strength and the Temperature Dependence of Nematic Liquid Crystal (5CB) Aligned on Rubbed Polystyrene Films. *Jpn. J. Appl. Phys.* **1992**, *31*, 2165–2169, doi:10.1143/JJAP.31.2165.

87. Stöhr, J.; Samant, M.G. Liquid Crystal Alignment by Rubbed Polymer Surfaces: A Microscopic Bond Orientation Model. *J. Electron Spectros. Relat. Phenomena* **1999**, *98–99*, 189–207, doi:10.1016/s0368-2048(98)00286-2.

88. Lu, M.; Yang, K.H.; Nakasogi, T.; Chey, S.J. 29.4: Homeotropic Alignment by Single Oblique Evaporation of SiO 2 and Its Application to High Resolution Microdisplays. *SID Symp. Dig. Tech. Pap.* **2000**, *31*, 446–449, doi:10.1889/1.1832977.

89. Zhao, D.; Huang, W.; Cao, H.; Zheng, Y.; Wang, G.; Yang, Z.; Yang, H. Homeotropic Alignment of Nematic Liquid Crystals by a Photocross-Linkable Organic Monomer Containing Dual Photofunctional Groups. **2009**, 2961–2965.

90. Li, X.; Armas-Perez, J.C.; Martinez-Gonzalez, J.A.; Liu, X.; Xie, H.; Bishop, C.; Hernandez-Ortiz, J.P.; Zhang, R.; De Pablo, J.J.; Nealey, P.F. Directed Self-Assembly of Nematic Liquid Crystals on Chemically Patterned Surfaces: Morphological States and Transitions. *Soft Matter* **2016**, *12*, 8595–8605, doi:10.1039/c6sm01733a.

91. Jayathilake, H.D.; Zhu, M.H.; Rosenblatt, C.; Bordenyuk, A.N.; Weeraman, C.; Benderskii, A. V. Rubbing-Induced Anisotropy of Long Alkyl Side Chains at Polyimide Surfaces. *J. Chem. Phys.* **2006**, *125*, doi:10.1063/1.2238865.

92. Liu, Z.; Yu, F.; Zhang, Q.; Zeng, Y.; Wang, Y. Preparation and Characterization of a Novel Polyimide Liquid Crystal Vertical Alignment Layer. *Eur. Polym. J.* **2008**, *44*, 2718–2727, doi:10.1016/j.eurpolymj.2008.05.009.

93. Lee, Y.J.; Choi, J.G.; Song, I.K.; Oh, J.M.; Yi, M.H. Effect of Side Chain Structure of Polyimides on a Pretilt Angle of Liquid Crystal Cells. *Polymer (Guildf).* **2006**, *47*, 1555–1562, doi:10.1016/j.polymer.2006.01.001.

94. Hatoh, H.; Shohara, K.; Kinoshita, Y.; Ookoshi, N. Molecular Tilt Direction in a Slightly Tilted Homeotropic Aligned Liquid Crystal Cell. *Appl. Phys. Lett.* **1993**, *63*, 3577–3579, doi:10.1063/1.110102.

95. Berreman, D.W. Alignment of Liquid Crystals By Grooved Surfaces. *Mol. Cryst. Liq. Cryst.* **1973**, *23*, 215–231, doi:10.1080/15421407308083374.

96. Faetti, S. Azimuthal Anchoring Energy of a Nematic Liquid Crystal at a Grooved Interface. *Phys. Rev. A* **1987**, *36*.

97. Fukuda, J.I.; Yoneya, M.; Yokoyama, H. Surface-Groove-Induced Azimuthal Anchoring of a Nematic Liquid Crystal: Berreman's Model Reexamined. *Phys. Rev. Lett.* **2007**, *98*, 1–4, doi:10.1103/PhysRevLett.98.187803.

98. Kawata, Y.; Takatoh, K.; Hasegawa, M.; Sakamoto, M. The Alignment of Nematic Liquid Crystals on Photolithographic Micro-Groove Patterns. *Liq. Cryst.* **1994**, *16*, 1027–1036, doi:10.1080/02678299408027872.

99. Gear, C.; Diest, K.; Liberman, V. Engineered Liquid Crystal Anchoring Energies with Nanopatterned Surfaces. *Opt. Express* **2015**, *23*, 894–898, doi:10.1364/OE.23.000807.

100. Cheng, J.; Boyd, G.D. The Liquid - Crystal Alignment Properties of Photolithographic Gratings. *Appl. Phys. Lett.* **1979**, *35*, 444–446.

101. Ozaki, R.; Shinpo, T.; Yoshino, K.; Ozaki, M.; Moritake, H. Tunable Liquid Crystal Laser Using Distributed Feedback Cavity Fabricated by Nanoimprint Lithography. *Appl. Phys. Express* **2008**, *1*, doi:10.1143/APEX.1.012003.

102. Park, M.J.; Park, O.O. Alignment of Liquid Crystals on a Topographically Nano-Patterned Polymer Surface Prepared by a Soft-Imprint Technique. *Microelectron. Eng.* **2008**, *85*, 2261–2265, doi:10.1016/j.mee.2008.07.007.

103. Shiina, T.; Saito, S.; Takahashi, T. Alignment Characteristics of Nematic Liquid Crystal on UV Curable Resin Film with Periodical Groove Structure. *Mol. Cryst. Liq. Cryst.* **2009**, *507*, 101–107, doi:10.1080/15421400903050277.

104. Flanders, D.C.; Shaver, D.C.; Smith, H.I. Alignment of Liquid Crystals Using Submicrometer Periodicity Gratings. *Appl. Phys. Lett.* **1978**, *32*, 597–598, doi:10.1063/1.89864.

105. Jeong, H.S.; Jeon, H.J.; Kim, Y.H.; Oh, M.B.; Kumar, P.; Kang, S.W.; Jung, H.T. Bifunctional ITO Layer with a High Resolution, Surface Nano-Pattern for Alignment and Switching of LCs in Device Applications. *NPG Asia Mater.* **2012**, *4*, 1–7, doi:10.1038/am.2012.12.

106. Li, X.T.; Natansohn, A.; Rochon, P. Photoinduced Liquid Crystal Alignment Based on a Surface Relief Grating in an Assembled Cell. *Appl. Phys. Lett.* **1999**, *74*, 3791–3793.

107. Ohzono, T.; Monobe, H.; Shimizu, Y. Liquid Crystal Alignment on Self-Organized Microwrinkles. *Appl. Phys. Express* **2008**, *1*, 0650011–0650013, doi:10.1143/APEX.1.065001.

108. Jiang, M.; Wang, Z.; Sun, R.; Ma, K.; Ma, R.; Huang, X. Method of Studying Surface Torsional Anchoring of Nematic Liquid Crystal. *Jpn. J. Appl. Phys.* **1994**, *33*, L1242–L1244, doi:10.1143/JJAP.33.L1242.

109. Wang, J.; Li, K.; He, H.; Cai, W.; Liu, J.; Yin, Z.; Mu, Q.; Hisao, V.K.S.; Gérard, D.; Luo, D.; et al. Metasurface-Enabled High-Resolution Liquid-Crystal Alignment for Display and Modulator Applications. *Laser Photonics Rev.* **2022**, *16*, 1–10, doi:10.1002/lpor.202100396.

110. Zhichao, J.; Zhang, X.; Shi, B.; Li, W.; Luo, W.; Drevensek-Olenik, I.; Wu, Q.; Xu, J. Compartmentalized Liquid Crystal Alignment Induced by Sparse Polymer Ribbons with Surface Relief Gratings. *Opt. Lett.* **2016**, *41*, 336–339.

111. Wang, X.; Xu, M.; Ren, H. Polarization Converting Textures of Nematic Liquid Crystal in Glass Cavities. *J. Appl. Phys.* **2014**, *115*, doi:10.1063/1.4862185.

112. Kumar, P.; Oh, S.Y.; Baliyan, V.K.; Kundu, S.; Lee, S.H.; Kang, S.-W. Topographically Induced Homeotropic Alignment of Liquid Crystals on Self-Assembled Opal Crystals. *Opt. Express* **2018**, *26*, 8385, doi:10.1364/oe.26.008385.

113. Cattaneo, L.; Zhang, J.; Zuiddam, M.; Savoini, M.; Rasing, T. Gaining Control through Frustration: Two-Fold Approach for Liquid Crystal Three-Dimensional Command Layers. *Nano Lett.* **2014**, *14*, 3903–3907, doi:10.1021/nl501155h.

114. Di, H.; Jiang, W.; Sun, H.; Zhao, C.; Liao, F.; Zhao, Y. Effects of ITO Substrate Hydrophobicity on Crystallization and Properties of MAPbBr3 Single-Crystal Thin Films. *ACS Omega* **2020**, *5*, 23111–23117, doi:10.1021/acsomega.0c02889.

115. Norrman, K.; Larsen, N.B. 6 Studies of Spin-Coated Polymer Films. *Annu. Reports Prog. Chemsity, Sect. C* **2005**, *101*, 174–201, doi:10.1039/b408857n.

116. Mayer, A.; Scheer, H. Guiding Chart for Initial Layer Choice with Nanoimprint Lithography. *Nanomaterials* **2021**, 11, 710, doi:10.3390/nano11030710

117. Wu, S.-T.; Efron, U.; Hess, L.D. Birefringence Measurements of Liquid Crystals. *Appl. Opt.* **1984**, *23*, 3911, doi:10.1364/ao.23.003911.

118. Bruyneel, F.; De Smet, H.; Vanfleteren, J.; Van Calster, A. Method for Measuring the Cell Gap in Liquid-Crystal Displays. *Opt. Eng.* **2001**, *40*, 259, doi:10.1117/1.1337036.

119. Litt, H.J. Surface Functionalisation Effects in Liquid Crystal Nanocomposites, PhD Thesis, University of Leeds, **2023**.

120. Jones, J.C.; Beldon, S.; Brett, P.; Francis, M.; Goulding, M. 26.3: Low Voltage Zenithal Bistable Devices with Wide Operating Windows. *SID Symp. Dig. Tech. Pap.* **2003**, *34*, 954, doi:10.1889/1.1832442.

121. Dana, E.S.; Ford, W.E. *A Text-Book of Mineralogy with an Extended Treatise on Crystallography and Physical Mineralogy*; John Wiley & Sons, Inc., **1922**; pp. 285-313

122. Miller, R.J.; Gleeson, H.F. Lattice Parameter Measurements from the Kossel Diagrams of the Cubic Liquid Crystal Blue Phases. *J. Phys. II* **1996**, *6*, 909–922, doi:10.1051/jp2:1996219.

123. Van Horn, B.L.; Winter, H.H. Conoscopic Measurement of Birefringence and Orientation in Biaxially Stretched Polymer Films and Sheets. *Macromolecules* **2003**, *36*, 8513–8521.

124. Van Horn, B.L.; Winter, H.H. Analysis of the Conoscopic Measurement for Uniaxial Liquid-Crystal Tilt Angles. *Appl. Opt.* **2001**, *40*, 2089–2094.

125. Pečar, M.; Čepič, M. Conoscopic Figure: A Complex Consequence of a Not so Simple Phenomenon. *Eur. J. Phys.* **2014**, *36*, 015014, doi:10.1088/0143-0807/36/1/015014.

126. Ahn, S.H.; Guo, L.J. High-Speed Roll-to-Roll Nanoimprint Lithography on Flexible Plastic Substrates. *Adv. Mater.* **2008**, *20*, 2044–2049, doi:10.1002/adma.200702650.

127. Ahn, S.H.; Guo, L.J. Large-Area Roll-to-Roll and Roll-to-Plate Nanoimprint Lithography : A Step toward High-Throughput Application of Continuous Nanoimprinting. *ACS Nano* **2009**, *3*, 2304–2310.

128. Amos, R.M.; Bryan-Brown, G.P.; Wood, E.L.; Jones, J.C.; Worthing, P.T. Embossing Method and Apparatus, US Patent No.: 7,824,516 B2, **2005**, *2*, 1–50.

129. Wyatt, P.J.M. Grating Aligned Ferroelectric Liquid Crystal Devices., PhD Thesis, University of Leeds, **2019**.

130. Wahle, M.; Snow, B.; Sargent, J.; Jones, J.C. Embossing Reactive Mesogens: A Facile Approach to Polarization-Independent Liquid Crystal Devices. *Adv. Opt. Mater.* **2019**, doi:10.1002/adom.201801261.

131. Xia, Y.; Whitesides, G.M. Soft Lithography. *Angew. Chemie Int. Ed.* **1998**, *37*, 550–575.

132. Qin, D.; Xia, Y.; Whitesides, G.M. Soft Lithography for Micro- and Nanoscale Patterning. *Nat. Protoc.* **2010**, *5*, 491–502, doi:10.1038/nprot.2009.234.

133. Kane, R.S.; Takayama, S.; Ostuni, E.; Ingber, D.E.; Whitesides, G.M. Patterning Proteins and Cells Using Soft Lithography. *Biomaterials* **1999**, *20*, 2363–2376, doi:10.1016/S0142-9612(99)00165-9.

134. Hansen, T.S.; West, K.; Hassager, O.; Larsen, N.B. Direct Fast Patterning of Conductive Polymers Using Agarose Stamping. *Adv. Mater.* **2007**, *19*, 3261–3265, doi:10.1002/adma.200602671.

135. Park, J.; Park, J.H.; Kim, E.; Ahn, C.W.; Jang, H.I.; Rogers, J.A.; Jeon, S. Conformable Solid-Index Phase Masks Composed of High-Aspect-Ratio Micropillar Arrays and Their Application to 3D Nanopatterning. *Adv. Mater.* **2011**, *23*, 860–864, doi:10.1002/adma.201003885.

136. Jeong, O.C.; Konishi, S. Controlling the Size of Replicable Polydimethylsiloxane (PDMS) Molds/Stamps Using a Stepwise Thermal Shrinkage Process. *Microelectron. Eng.* **2011**, *88*, 2286–2289, doi:10.1016/j.mee.2010.12.005.

137. Lohse, M.; Heinrich, M.; Grützner, S.; Haase, A.; Ramos, I.; Salado, C.; Thesen, M.W.; Grützner, G. Versatile Fabrication Method for Multiscale Hierarchical Structured Polymer Masters Using a Combination of Photo- and Nanoimprint Lithography. *Micro Nano Eng.* **2021**, *10*, 100079, doi:10.1016/j.mne.2020.100079.

138. Zhu, X.; Cui, T. Polymer Shrinkage of Hot Embossed Microstructures for Higher Aspect Ratio and Smaller Size. *Sensors Actuators, A Phys.* **2013**, *195*, 21–26, doi:10.1016/j.sna.2013.02.015.

139. Dore, C.; Osmond, J.; Mihi, A. A Water-Processable Cellulose-Based Resist for Advanced Nanofabrication. *Nanoscale* **2018**, *10*, 17884–17892, doi:10.1039/c8nr04851g.

140. Fang, C.; Dai, B.; Li, Z.; Zahid, A.; Wang, Q.; Sheng, B.; Zhang, D. Tunable Guided-Mode Resonance Filter with a Gradient Grating Period Fabricated by Casting a Stretched PDMS Grating Wedge. *Opt. Lett.* **2016**, *41*, 5302, doi:10.1364/ol.41.005302.

141. Moharana, A.R.; Außerhuber, H.M.; Mitteramskogler, T.; Haslinger, M.J.; Mühlberger, M.M. Multilayer Nanoimprinting to Create Hierarchical Stamp Masters for Nanoimprinting of Optical Micro-and Nanostructures. *Coatings* **2020**, *10*, doi:10.3390/coatings10030301.

142. Rogers, J.A.; Paul, K.E.; Jackman, R.J.; Whitesides, G.M. Generating 90 Nanometer Features Using Near-Field Contact-Mode Photolithography with an Elastomeric Phase Mask. *J. Vac. Sci. Technol. B* **1998**, *59*, doi:10.1116/1.589836.

143. Hsieh, Y.T.; Hsieh, H.; Lee, Y.C. A Soft Photo-Mask with Embedded Carbon Black and Its Application in Contact Photolithography. *J. Micromechanics Microengineering* **2014**, *24*, doi:10.1088/0960-1317/24/8/085006.

144. Kim, B.E.; Xia, Y.; Zhao, X.; Whitesides, G.M. Solvent-Assisted Microcontact Molding A Convenient Method for Fabricating Three-Dimensional Structures on Surfaces of Polymers. *Adv. Mater.* **1997**, *9*, 651–654.

145. Paul, K.E.; Breen, T.L.; Aizenberg, J.; Whitesides, G.M. Maskless Photolithography : Embossed Photoresist as Its Own Optical Element. *Appl. Phys. Lett.* **1998**, *73*, 2–5.

146. Lee, M.H.; Huntington, M.D.; Zhou, W.; Yang, J.C.; Odom, T.W. Programmable Soft Lithography: Solvent-Assisted Nanoscale Embossing. *Nano Lett.* **2011**, *11*, 311–315, doi:10.1021/nl102206x.

147. Sayed, S.; Selvaganapathy, P.R. Multi-Step Proportional Miniaturization to Sub-Micron Dimensions Using Pre-Stressed Polymer Films. *Nanoscale Adv.* **2020**, *2*, 5461–5467, doi:10.1039/d0na00785d.

148. Hwang, J.H.; Hong, J.S.; Oh, C.W.; Joe, M.J.; Jeong, H.C.; Park, H.G. Soft Imprint Lithography for Liquid Crystal Alignment Using a Wrinkled UVO-Treated PDMS Transferring Method. *J. Mol. Liq.* **2021**, *323*, 115150, doi:10.1016/j.molliq.2020.115150.

149. Gwag, J.S.; Oh-E, M.; Yoneya, M.; Yokoyama, H.; Satou, H.; Itami, S. Advanced Nanoimprint Lithography Using a Graded Functional Imprinting Material Tailored for Liquid Crystal Alignment. *J. Appl. Phys.* **2007**, *102*, doi:10.1063/1.2778742.

150. Park, H.G.; Lee, J.J.; Dong, K.Y.; Oh, B.Y.; Kim, Y.H.; Jeong, H.Y.; Ju, B.K.; Seo, D.S. Homeotropic Alignment of Liquid Crystals on a Nano-Patterned Polyimide Surface Using Nanoimprint Lithography. *Soft Matter* **2011**, *7*, 5610–5614, doi:10.1039/c1sm05083d.

151. He, Y.; Liu, B.; Ren, H.; Wang, X. Polyimide Liquid Crystal Alignment Layers Prepared by Soft-Lithography. *Front. Chem. China* **2007**, *2*, 318–321, doi:10.1007/s11458-007-0059-8.

152. Glasgow, I.K.; Beebe, D.J.; White, V.E. Design Rules for Polyimide Solvent Bonding. *Sensors Mater.* **1999**, *11*, 269–278.

153. He, J.; Kovach, A.; Wang, Y.; Wang, W.; Wu, W.; Armani, A.M. Stretchable Optical Diffraction Grating from Poly(Acrylic Acid)/Polyethylene Oxide Stereocomplex. *Opt. Lett.* **2021**, *46*, 5493–5496.

154. Jin, J.; Wang, X.; Di, S.; Lin, W.; Bi, H.; Zhang, J. A Method to Increase Line-Density of Grating Based on PDMS Stretching and PUA Replication Process. *Microelectron. Eng.* **2021**, *247*, 111586, doi:10.1016/j.mee.2021.111586.

155. Binning, G.; Quate, C.F.; Gerber, C. Atomic Force Microscope. *Phys. Rev. Lett.* **1986**, *56*, 930–933.

156. Smith, J.R.; Breakspear, S.; Campbell, S.A.; Smith, J.R.; Breakspear, S.; Afm, S.A.C.; Smith, J.R. AFM in Surface Finishing : Part I . An Introduction. *Int. J. Surf. Eng. Coatings* **2003**, *81*, B26–B29, doi:10.1080/00202967.2003.11871484.

157. Gołek, F.; Mazur, P.; Ryszka, Z.; Zuber, S. AFM Image Artifacts. *Appl. Surf. Sci.* **2014**, *304*, 11–19, doi:10.1016/j.apsusc.2014.01.149.

158. Shen, J.; Zhang, D.; Zhang, F.H.; Gan, Y. AFM Tip-Sample Convolution Effects for Cylinder Protrusions. *Appl. Surf. Sci.* **2017**, *422*, 482–491, doi:10.1016/j.apsusc.2017.06.053.

159. Wei, J.; Zhu, M.; Du, T.; Li, J.; Dai, P.; Liu, C.; Duan, J.; Liu, S.; Zhou, X.; Zhang, S.; et al. Full-Color Persistent Room Temperature Phosphorescent Elastomers with Robust Optical Properties. *Nat. Commun.* **2023**, *14*, doi:10.1038/s41467-023-40193-1.

160. Feng, J.; Zheng, Y.; Jiang, Q.; Włodarczyk-Biegun, M.K.; Pearson, S.; del Campo, A. Elastomeric Optical Waveguides by Extrusion Printing. *Adv. Mater. Technol.* **2022**, *7*, doi:10.1002/admt.202101539.

161. Zhong, H.; Xue, Q.; Li, J.; He, Y.; Xie, Y.; Yang, C. Stretchable Transparent Polyelectrolyte Elastomers for All-Solid Tunable Lenses of Excellent Stability Based on Electro–Mechano–Optical Coupling. *Adv. Mater. Technol.* **2023**, *8*, 1–9, doi:10.1002/admt.202200947.

162. Ryabchun, A.; Wegener, M.; Gritsai, Y.; Sakhno, O. Novel Effective Approach for the Fabrication of PDMS-Based Elastic Volume Gratings. *Adv. Opt. Mater.* **2016**, *4*, 169–176, doi:10.1002/adom.201500351.

163. Zubritskaya, I.; Cichelero, R.; Faniayeu, I.; Martella, D.; Nocentini, S.; Rudquist, P.; Wiersma, D.S.; Brongersma, M.L. Dynamically Tunable Optical Cavities with Embedded Nematic Liquid Crystalline Networks. *Adv. Mater.* **2023**, *35*, 2209152, doi:10.1002/adma.202209152.

164. Kocabas, A.; Ay, F.; Dâna, A.; Kiyat, I.; Aydinli, A. High-Refractive-Index Measurement with an Elastomeric Grating Coupler. *Opt. Lett.* **2005**, *30*, 3150–3152.

165. Kocabas, A.; Ay, F.; Dâna, A.; Aydinli, A. An Elastomeric Grating Coupler. *J. Opt. A Pure Appl. Opt.* **2006**, *8*, 85–87, doi:10.1088/1464-4258/8/1/013.

166. de Oliveira Hansen, R.M.; Liu, Y.; Madsen, M. Flexible Organic Solar Cells Including Efficiency Enhancing Grating Structures. *Nanotechnology* **2013**, *24*, 145301, doi:10.1088/0957-4484/24/14/145301.

167. Song, M.; Feng, L.; Huo, P.; Liu, M.; Huang, C.; Yan, F.; Lu, Y. qing; Xu, T. Versatile Full-Colour Nanopainting Enabled by a Pixelated Plasmonic Metasurface. *Nat. Nanotechnol.* **2023**, *18*, 71–78, doi:10.1038/s41565-022-01256-4.

168. Khudiyev, T.; Hou, C.; Stolyarov, A.M.; Fink, Y. Sub-Micrometer Surface-Patterned Ribbon Fibers and Textiles. *Adv. Mater.* **2017**, *29*, doi:10.1002/adma.201605868.

169. Wang, Y.; Shang, L.; Chen, G.; Sun, L.; Zhang, X.; Zhao, Y. Bioinspired Structural Color Patch with Anisotropic Surface Adhesion. *Sci. Adv.* **2020**, *6*, doi:10.1126/sciadv.aax8258.

170. Ryba, B.; Förster, E.; Brunner, R. Flexible Diffractive Gratings: Theoretical Investigation of the Dependency of Diffraction Efficiency on Mechanical Deformation. *Appl. Opt.* **2014**, *53*, 1381, doi:10.1364/ao.53.001381.

171. Guglielmelli, A.; Nemati, S.; Vasdekis, A.E. Stimuli Responsive Diffraction Gratings in Soft-Composite Materials. *J. Phys. D. Appl. Phys.* **2019**, *52*, 053001.

172. Kim, S.T.; Finkelmann, H. Cholesteric Liquid Single-Crystal Elastomers (LSCE) Obtained by the Anisotropic Deswelling Method. *Macromol. Rapid Commun.* **2001**, *22*, 429–433, doi:10.1002/1521-3927(20010301)22:6<429::aid-marc429>3.0.co;2-%23.

173. Kizhakidathazhath, R.; Geng, Y.; Jampani, V.S.R.; Charni, C.; Sharma, A.; Lagerwall, J.P.F. Facile Anisotropic Deswelling Method for Realizing Large-Area Cholesteric Liquid Crystal Elastomers with Uniform Structural Color and Broad-Range Mechanochromic Response. *Adv. Funct. Mater.* **2020**, *30*, doi:10.1002/adfm.201909537.

174. Huang, Y.; Xu, Y.; Bisoyi, H.K.; Liu, Z.; Wang, J.; Tao, Y. Photocontrollable Elongation Actuation of Liquid Crystal Elastomer Films with Well-Defined Crease Structures. *Adv. Mater.* **2023**, *2304378*, 1–9, doi:10.1002/adma.202304378.

175. Mistry, D.; Nikkhou, M.; Raistrick, T.; Hussain, M.; Jull, E.I.L.; Baker, D.L.; Gleeson, H.F. Isotropic Liquid Crystal Elastomers as Exceptional Photoelastic Strain Sensors. *Macromolecules* **2020**, *53*, doi:10.1021/acs.macromol.9b02456.

176. Brannum, M.T.; Steele, A.M.; Venetos, M.C.; Korley, L.T.J.; Wnek, G.E.; White, T.J. Light Control with Liquid Crystalline Elastomers. *Adv. Opt. Mater.* **2019**, *7*, 1801683, doi:10.1002/adom.201801683.

177. Zhuang, X.; Zhang, W.; Wang, K.; Gu, Y.; An, Y.; Zhang, X.; Gu, J.; Luo, D.; Han, J.; Zhang, W. Active Terahertz Beam Steering Based on Mechanical Deformation of Liquid Crystal Elastomer Metasurface. *Light Sci. Appl.* **2023**, *12*, doi:10.1038/s41377-022-01046-6.

178. Devetak, M.; Zupančič, B.; Lebar, A.; Umek, P.; Zalar, B.; Domenici, V.; Ambrošič, G.; Žigon, M.; Čopič, M.; Drevenšek-Olenik, I. Micropatterning of Light-Sensitive Liquid-Crystal Elastomers. *Phys. Rev. E - Stat. Nonlinear, Soft Matter Phys.* **2009**, *80*, 5–8, doi:10.1103/PhysRevE.80.050701.

179. Tašič, B.; Li, W.; Sánchez-Ferrer, A.; Čopič, M.; Drevenšek-Olenik, I. Light-Induced Refractive Index Modulation in Photoactive Liquid-Crystalline Elastomers. *Macromol. Chem. Phys.* **2013**, *214*, 2744–2751, doi:10.1002/macp.201300493.

180. Zhang, P.; Debije, M.G.; de Haan, L.T.; Schenning, A.P.H.J. Switching between 3D Surface Topographies in Liquid Crystal Elastomer Coatings Using Two-Step Imprint Lithography. *Small* **2023**, *19*, 2302051, doi:10.1002/SMLL.202302051.

181. Raistrick, T.; Zhang, Z.; Mistry, D.; Mattsson, J.; Gleeson, H.F. Understanding the Physics of the Auxetic Response in a Liquid Crystal Elastomer. *Phys. Rev. Res.* **2021**, *3*, doi:10.1103/PhysRevResearch.3.023191.

182. Quan, Y.; Kim, Y.; Kim, M.; Min, S.; Ahn, S. Stretchable Biaxial and Shear Strain Sensors Using Diffractive Structural Colors. *ACS Nano* **2020**, *14*, 5392–5399, doi:10.1021/acsnano.9b08953.

183. Finkelmann, H.; Kundler, I.; Terentjev, E.M.; Warner, M. Critical Stripe-Domain Instability of Nematic Elastomers. *J. Phys. II* **1997**, *7*, 1059–1069.

184. Kundler, I.; Finkelmann, H. Director Reorientation via Stripe-Domains in Nematic Elastomers Influence of Cross-Link Density, Anisotropy of the Network and Smectic Clusters. *Macromol. Chem. Phys.* **1998**, *199*, 677–686.

185. Raistrick, T.; Reynolds, M.; Gleeson, H.F.; Mattsson, J. Influence of Liquid Crystallinity and Mechanical Deformation on the Molecular Relaxations of an Auxetic Liquid Crystal Elastomer. *Molecules* **2021**, *26*, doi:10.3390/molecules26237313.

186. Palmer, C. *Diffraction Grating Handbook*; MKS Instruments, I., Ed.; 8th ed.; MKS Instruments, Inc.: New York, **2020**; pp. 123-126, 173-176

187. Srinivasarao, M. Nano-Optics in the Biological World: Beetles, Butterflies, Birds, and Moths. *Chem. Rev.* **1999**, *99*, 1935–1961, doi:10.1021/cr970080y.

188. Nishikawa, E.; Yamamoto, J.; Yokoyama, H.; Finkelmann, H. Smectic A Elastomers with Uniform Homeotropic Orientation Obtained by Applying a Biaxial Mechanical Field. *Macromol. Rapid Commun.* **2004**, *25*, 611–617, doi:10.1002/marc.200300183.

189. Meshalkin, A.Y.; Podlipnov, V. V.; Ustinov, A. V.; Achimova, E.A. Analysis of Diffraction Efficiency of Phase Gratings in Dependence of Duty Cycle and Depth. *J. Phys. Conf. Ser.* **2019**, *1368*, doi:10.1088/1742-6596/1368/2/022047.

190. Cooper, E.J.; Reynolds, M.; Raistrick, T.; Berrow, S.R.; Jull, E.I.L.; Reshetnyak, V.; Mistry, D.; Gleeson, H.F. Controlling the Optical Properties of Transparent Auxetic Liquid Crystal Elastomers. *Macromolecules* **2024**, *57*, 2030–2038, doi:10.1021/acs.macromol.3c02226.

191. Belyaev, V. V.; Solomatin, A.S.; Margaryan, H.; Hakobyan, N.; Kumar, S.; Chausov, D.N.; Belyaev, A.A.; Smirnov, A.G.; Gorbunov, A.A. Diffraction on Periodic Surface Microrelief Grating with Positive or Negative Optical Anisotropy. *Appl. Opt.* **2020**, *59*, 8443, doi:10.1364/ao.397133.

192. Coux, M.; Clanet, C.; Quéré, D. Soft, Elastic, Water-Repellent Materials. *Appl. Phys. Lett.* **2017**, *110*, 251605, doi:10.1063/1.4985011.

193. Bowden, N.; Brittain, S.; Evans, A.G.; Hutchinson, J.W.; Whitesides, G.M. Spontaneous Formation of Ordered Structures in Thin Films of Metals Supported on an Elastomeric Polymer. *Nature* **1998**, *393*, 146–149, doi:10.1038/30193.

194. Loh, J.Y.Y.; Zeineddine, A.; Shayegannia, M.; Mcneil, R.; Mcrae, L.; Kherani, N.P. A One-Step , Tunable Method of Selective Reactive Sputter Deposition as a Wrinkling Approach for Silver / Polydimethylsiloxane for Electrically Conductive Pliable Surfaces. **2022**, doi:10.1038/s41378-022-00420-z.

195. Khang, D.-Y.; Jiang, H.; Huang, Y.; Rogers, J.A. A Stretchable Form of Single-Crystal Silicon for High-Performance Electronics on Rubber Substrates. *Science (80-.).* **2006**, *311*, 208–212.

196. Bowden, N.; Huck, W.T.S.; Kateri, P.E.; Whitesides, G.M. The Controlled Formation of Ordered, Sinusoidal Structures by Plasma Oxidation of an Elastomeric Polymer. *Appl. Phys. Lett.* **1999**, *75*, 2557.

197. Efimenko, K.; Rackaitis, M.; Manias, E.; Vaziri, A.; Mahadevan, L.; Genzer, J.A.N. Nested Self-Similar Wrinkling Patterns in Skins. **2005**, *4*, 0–4, doi:10.1038/nmat1342.

198. Chiche, A.; Stafford, C.M.; Cabral, J.T. Complex Micropatterning of Periodic Structures on Elastomeric Surfaces. *Soft Matter* **2008**, *4*, doi:10.1039/b811817e.

199. Park, J.Y.; Chae, H.Y.; Chung, C.H.; Sim, S.J.; Park, J.; Lee, H.H.; Yoo, P.J. Controlled Wavelength Reduction in Surface Wrinkling of Poly(Dimethylsiloxane). *Soft Matter* **2010**, *6*, 677–684, doi:10.1039/b916603c.

200. Béfahy, S.; Lipnik, P.; Pardoen, T.; Nascimento, C.; Patris, B.; Bertrand, P.; Yunus, S. Thickness and Elastic Modulus of Plasma Treated PDMS Silica-like Surface Layer. *Langmuir* **2010**, *26*, 3372–3375, doi:10.1021/la903154y.

201. Mills, K.L.; Zhu, X.; Takayama, S.; Thouless, M.D. The Mechanical Properties of a Surface-Modified Layer on Polydimethylsiloxane. *J. Mater. Res.* **2008**, *23*, 37–48, doi:10.1557/jmr.2008.0029.

202. Bayley, F.A.; Liao, J.L.; Stavrinou, P.N.; Chiche, A.; Cabral, J.T. Wavefront Kinetics of Plasma Oxidation of Polydimethylsiloxane : Limits for Sub- m m Wrinkling. **2014**, 1155–1166, doi:10.1039/c3sm52766b.

203. Nania, M.; Matar, O.K.; Cabral, J.T. Frontal Vitrification of PDMS Using Air Plasma and Consequences for Surface Wrinkling. *Soft Matter* **2015**, *11*, 3067–3075, doi:10.1039/c4sm02840f.

204. Huck, W.T.S.; Bowden, N.; Onck, P.; Pardoen, T.; Hutchinson, J.W.; Whitesides, G.M. Ordering of Spontaneously Formed Buckles on Planar Surfaces. *Langmuir* **2000**, *16*, 3497–3501, doi:10.1021/la991302l.

205. Chan, E.P.; Crosby, A.J. Spontaneous Formation of Stable Aligned Wrinkling Patterns. *Soft Matter* **2006**, *2*, 324–328, doi:10.1039/b515628a.

206. Rand, C.J.; Sweeney, R.; Morrissey, M.; Hazel, L.; Crosby, A.J. Fracture-Induced Alignment of Surface Wrinkles. *Soft Matter* **2008**, *4*, 1805–1807, doi:10.1039/b802271b.

207. Song, J.; Jiang, H.; Liu, Z.J.; Khang, D.Y.; Huang, Y.; Rogers, J.A.; Lu, C.; Koh, C.G. Buckling of a Stiff Thin Film on a Compliant Substrate in Large Deformation. *Int. J. Solids Struct.* **2008**, *45*, 3107–3121, doi:10.1016/j.ijsolstr.2008.01.023.

208. Jiang, X.; Takayama, S.; Qian, X.; Ostuni, E.; Wu, H.; Bowden, N.; LeDuc, P.; Ingber, D.E.; Whitesides, G.M. Controlling Mammalian Cell Spreading and Cytoskeletal Arrangement with Conveniently Fabricated Continuous Wavy Features on Poly(Dimethylsiloxane). *Langmuir* **2002**, *18*, 3273–3280, doi:10.1021/la011668+.

209. Ma, T.; Zhou, L.; Hua, J.; Li, J.; Ma, X.; Qiao, W.; Yin, J.; Jiang, X. Dynamic Surface Wrinkles for in Situ Light-Driven Dynamic Gratings. *ACS Appl. Mater. Interfaces* **2022**, *14*, 16949–16957, doi:10.1021/acsami.2c03235.

210. Wilder, E.A.; Guo, S.; Lin-gibson, S.; Fasolka, M.J.; Stafford, C.M. Measuring the Modulus of Soft Polymer Networks via a Buckling-Based Metrology. **2006**, 4138–4143.

211. Choi, I.S.; Park, S.; Jeon, S.; Kwon, Y.W.; Park, R.; Taylor, R.A. Strain-Tunable Optical Microlens Arrays with Deformable Wrinkles for Spatially Coordinated Image Projection on a Security Substrate. *Microsystems Nanoeng.* **2022**, doi:10.1038/s41378-022-00399-7.

212. Wang, Y.; Xiao, J. Programmable, Reversible and Repeatable Wrinkling of Shape Memory Polymer Thin Films on Elastomeric Substrates for Smart Adhesion. *Soft Matter* **2017**, *13*, 5317–5323, doi:10.1039/c7sm01071k.

213. Li, Z.; Zhai, Y.; Wang, Y.; Wendland, G.M.; Yin, X.; Xiao, J. Harnessing Surface Wrinkling–Cracking Patterns for Tunable Optical Transmittance. *Adv. Opt. Mater.* **2017**, *5*, 1–7, doi:10.1002/adom.201700425.

214. Ohzono, T.; Fukuda, J.I. Zigzag Line Defects and Manipulation of Colloids in a Nematic Liquid Crystal in Microwrinkle Grooves. *Nat. Commun.* **2012**, *3*, doi:10.1038/ncomms1709.

215. Lim, S.I.; Jang, E.; Yu, D.; Koo, J.; Kang, D.G.; Lee, K.M.; Godman, N.P.; McConney, M.E.; Kim, D.Y.; Jeong, K.U. When Chirophotonic Film Meets Wrinkles: Viewing Angle Independent Corrugated Photonic Crystal Paper. *Adv. Mater.* **2023**, *35*, 1–11, doi:10.1002/adma.202206764.

216. Ohzono, T.; Monobe, H.; Yamaguchi, R.; Shimizu, Y.; Yokoyama, H. Dynamics of Surface Memory Effect in Liquid Crystal Alignment on Reconfigurable Microwrinkles. *Appl. Phys. Lett.* **2009**, *95*, 2–4, doi:10.1063/1.3167547.

217. Jeong, H.-C.; Lee, J.H.; Won, J.; Oh, B.Y.; Kim, D.H.; Lee, D.W.; Song, I.H.; Liu, Y.; Seo, D.-S. One-Dimensional Surface Wrinkling for Twisted Nematic Liquid Crystal Display Based on Ultraviolet Nanoimprint Lithography. *Opt. Express* **2019**, *27*, 18094, doi:10.1364/oe.27.018094.

218. Lydon, J.E.; Gleeson, H.; Jull, E.I.L. The Identification of the Sign and Strength of Disclinations in the Schlieren (Nucleated Domain) Texture of the Nematic Phase, by Optical Microscopy. *Liq. Cryst.* **2017**, *44*, 1775–1786, doi:10.1080/02678292.2017.1336580.

219. Holmes, C.J. Surface Alignment Control of Nematodynamics, PhD Thesis, University of Exeter, **2012**.

220. Senyuk, B.; Kim, Y.K.; Tortora, L.; Shin, S.T.; Shiyanovskii, S. V.; Lavrentovich, O.D. Surface Alignment, Anchoring Transitions, Optical Properties and Topological Defects in Nematic Bent-Core Materials C7 and C12. *Mol. Cryst. Liq. Cryst.* **2011**, *540*, 20–41, doi:10.1080/15421406.2011.568324.

221. Yao, S.-K.; Wang, C.-C.; Chou, J.-K.; Wang, Y.-Z.; Tsung, J.-W. Dense Packing of Topological Defects in Nematic Liquid Crystal Cells with Pads, Crossed-Strips, and Porous Electrodes. *Opt. Mater. Express* **2023**, *13*, 1883, doi:10.1364/ome.494440.

222. Gim, M.J.; Beller, D.A.; Yoon, D.K. Morphogenesis of Liquid Crystal Topological Defects during the Nematic-Smectic A Phase Transition. *Nat. Commun.* **2017**, *8*, 1–9, doi:10.1038/ncomms15453.

223. Wang, S.Y.; Wu, H.M.; Yang, K.H. Simple and Direct Measurements of Pretilt Angles in Hybrid-Aligned Nematic Liquid-Crystal Cells. *Appl. Opt.* **2013**, *52*, 5106–5111, doi:10.1364/AO.52.005106.

224. Nys, I.; Chen, K.; Beeckman, J.; Neyts, K. Periodic Planar-Homeotropic Anchoring Realized by Photoalignment for Stabilization of Chiral Superstructures. *Adv. Opt. Mater.* **2018**, *6*, 1701163, doi:10.1002/adom.201701163.

225. Nys, I. Patterned Surface Alignment to Create Complex Three-Dimensional Nematic and Chiral Nematic Liquid Crystal Structures. *Liq. Cryst. Today* **2020**, *29*, 65–83, doi:10.1080/1358314X.2020.1886780.

226. Liu, Y.; Wang, G.P. Beam Manipulations With Compact Planar Dielectric Pancharatnam–Berry Phase Devices. *Front. Phys.* **2022**, *10*, 1–8, doi:10.3389/fphy.2022.894703.

227. Takeda, A.; Kataoka, S.; Sasaki, T.; Chida, H.; Tsuda, H.; Ohmuro, K.; Sasabayashi, T.; Koike, Y.; Okamoto, K. 41.1: A Super-High Image Quality Multi-Domain Vertical Alignment LCD by New Rubbing-Less Technology. *SID Symp. Dig. Tech. Pap.* **1998**, *29*, 1077–1080, doi:10.1889/1.1833672.

228. Bryan-Brown, G.P.; Brown, C. V.; Sage, I.C.; Hui, V.C. Voltage-Dependent Anchoring of a Nematic Liquid Crystal on a Grating Surface. *Nature* **1998**, *392*, 365–367, doi:10.1038/32849.

229. Jones, J.C. 51.2: Novel Geometries of the Zenithal Bistable Device. *SID Symp. Dig. Tech. Pap.* **2006**, *37*, 1626, doi:10.1889/1.2433313.

230. Jones, J.C. Defects, Flexoelectricity and RF Communications: The ZBD Story. *Liq. Cryst.* **2017**, *44*, 2133–2160, doi:10.1080/02678292.2017.1365383.

231. Bryan-Brown, G.P.; Walker, D.R.E.; Jones, C. Controlled Grating Replication for the ZBD Technology. *SID Symp. Dig. Tech. Pap.* **2009**, *40*, 1334, doi:10.1889/1.3256546.

232. Zhang, B.; Lee, F.K.; Tsui, O.K.C.; Sheng, P. Liquid Crystal Orientation Transition on Microtextured Substrates. *Phys. Rev. Lett.* **2003**, *91*, 2–5, doi:10.1103/PhysRevLett.91.215501.

233. Rojas-Gomez, O.A.; Romero-Enrique, J.M.; Silvestre, N.M.; Telo Da Gama, M.M. Pattern-Induced Anchoring Transitions in Nematic Liquid Crystals. *J. Phys. Condens. Matter* **2017**, *29*, doi:10.1088/1361-648X/29/6/064002.

234. Delamarche, E.; Schmid, H.; Michel, B. Stability of Molded Polydimethylsiloxane Microstructures. *Adv. Mater.* **1997**, *9*, 741–746.

235. Sharp, K.G.; Blackman, G.S.; Glassmaker, N.J.; Jagota, A.; Hui, C.Y. Effect of Stamp Deformation on the Quality of Microcontact Printing: Theory and Experiment. *Langmuir* **2004**, *20*, 6430–6438, doi:10.1021/la036332+.

236. Schift, H.; Saxer, S.; Park, S.; Padeste, C.; Pieles, U.; Gobrecht, J. Controlled Co-Evaporation of Silanes for Nanoimprint Stamps. *Nanotechnology* **2005**, *16*, doi:10.1088/0957-4484/16/5/007.

237. Beck, M.; Graczyk, M.; Maximov, I.; Sarwe, E.L.; Ling, T.G.I.; Keil, M.; Montelius, L. Improving Stamps for 10 Nm Level Wafer Scale Nanoimprint Lithography. *Microelectron. Eng.* **2002**, *61–62*, 441–448, doi:10.1016/S0167-9317(02)00464-1.

238. Handte, T.; Scheller, N.; Dittrich, L.; Thesen, M.W.; Messerschmidt, M.; Sinzinger, S. Manufacturing of Nanostructures with High Aspect Ratios Using Soft UV-Nanoimprint Lithography with Bi- and Trilayer Resist Systems. *Micro Nano Eng.* **2022**, *14*, 100106, doi:10.1016/j.mne.2022.100106.

239. Amalathas, A.P.; Alkaisi, M.M. Fabrication and Replication of Periodic Nanopyramid Structures by Laser Interference Lithography and UV Nanoimprint Lithography for Solar Cells Applications. In *Micro/Nanolithography - A Heuristic Aspect on the Enduring Technology*; IntechOpen, **2018**; pp. 30–32.

240. Munief, W.M.; Heib, F.; Hempel, F.; Lu, X.; Schwartz, M.; Pachauri, V.; Hempelmann, R.; Schmitt, M.; Ingebrandt, S. Silane Deposition via Gas-Phase Evaporation and High-Resolution Surface Characterization of the Ultrathin Siloxane Coatings. *Langmuir* **2018**, *34*, 10217–10229, doi:10.1021/acs.langmuir.8b01044.

241. Badv, M.; Jaffer, I.H.; Weitz, J.I.; Didar, T.F. An Omniphobic Lubricant-Infused Coating Produced by Chemical Vapor Deposition of Hydrophobic Organosilanes Attenuates Clotting on Catheter Surfaces. *Sci. Rep.* **2017**, *7*, 1–10, doi:10.1038/s41598-017-12149-1.

242. Odom, T.W.; Love, J.C.; Wolfe, D.B.; Paul, K.E.; Whitesides, G.M. Improved Pattern Transfer in Soft Lithography Using Composite Stamps. *Langmuir* **2002**, 5314–5320.

243. Verschuuren, M.A. Substrate Conformal Imprint Lithography for Nanophotonics, PhD Thesis, Utrecht University, **2010**.

244. Scharin-Mehlmann, M.; Häring, A.; Rommel, M.; Dirnecker, T.; Friedrich, O.; Frey, L.; Gilbert, D.F. Nano- and Micro-Patterned S-, H-, and X-PDMS for Cell-Based Applications: Comparison of Wettability, Roughness, and Cell-Derived Parameters. *Front. Bioeng. Biotechnol.* **2018**, *6*, 1–13, doi:10.3389/fbioe.2018.00051.

245. Lo, J.C.; Horsley, D.A.; Skinner, J.L. Fabrication of Large Arrays of Plasmonic Nanostructures via Double Casting. *Adv. Fabr. Technol. Micro/Nano Opt. Photonics V* **2012**, *8249*, 824915, doi:10.1117/12.909943.

246. Yan, Y.H.; Chan-Park, M.B.; Yue, C.Y. CF4 Plasma Treatment of Poly(Dimethylsiloxane): Effect of Fillers and Its Application to High-Aspect-Ratio UV Embossing. *Langmuir* **2005**, *21*, 8905–8912, doi:10.1021/la051580m.

247. Hui, C.Y.; Jagota, A.; Lin, Y.Y.; Kramer, E.J. Constraints on Microcontact Printing Imposed by Stamp Deformation. *Langmuir* **2002**, *18*, 1394–1407, doi:10.1021/la0113567.

248. Sheu, C.R.; Wang, T.J.; Lin, C.H. Homeotropic Liquid Crystal Alignments through Periodically Unidirectional Nano-Wedges Patterned by Nanoimprint Lithography. *Micro Nano Eng.* **2021**, *12*, 100090, doi:10.1016/j.mne.2021.100090.

249. Crossland, W.A.; Morrissy, J.H.; Needham, B. Tilt Angle Measurements of Nematic Phases of Cyano-Biphenyls Aligned by Obliquely Evaporated Films. *J. Phys. D. Appl. Phys.* **1976**, *9*, 2001–2014.

250. Baylis, L.J.; Gleeson, H.F.; Seed, A.J.; Styring, P.J.; Hird, M.; Goodby, J.W. Conoscopic Observations of Multiple Ferrielectricity in a Chiral Liquid Crystal. *Mol. Cryst. Liq. Cryst. Sci. Technol. Sect. A Mol. Cryst. Liq. Cryst.* **1999**, *328*, 13–20, doi:10.1080/10587259908026040.

251. Yonetake, K.; Takahashi, T. New Material Design for Liquid Crystals and Composites by Magneto-Processing. *Sci. Technol. Adv. Mater.* **2006**, *7*, 332–336, doi:10.1016/j.stam.2006.02.008.

252. Park, S.; Padeste, C.; Schift, H.; Gobrecht, J.; Scharf, T. Chemical Nanopatterns via Nanoimprint Lithography for Simultaneous Control over Azimuthal and Polar Alignment of Liquid Crystals. *Adv. Mater.* **2005**, *17*, 1398–1401, doi:10.1002/adma.200400989.

253. Wang, R.; Atherton, T.J.; Zhu, M.; Petschek, R.G.; Rosenblatt, C. Naturally Occurring Reverse Tilt Domains in a High-Pretilt Alignment Nematic Liquid Crystal. *Phys. Rev. E - Stat. Nonlinear, Soft Matter Phys.* **2007**, *76*, 1–5, doi:10.1103/PhysRevE.76.021702.

254. Bhadwal, A.S.; Mottram, N.J.; Saxena, A.; Sage, I.C.; Brown, C. V. Electrically Controlled Topological Micro Cargo Transportation. *Soft Matter* **2020**, *16*, 2961–2970, doi:10.1039/c9sm01956a.

255. Dierking, I. *Textures of Liquid Crystals*; Wiley-VCH: Weinheim, **2003**; pp. 110 - 114, ISBN 3-527-30725-7

256. Haslinger, M.J.; Mitteramskogler, T.; Kopp, S.; Leichtfried, H.; Messerschmidt, M.; Thesen, M.W.; Mühlberger, M. Development of a Soft UV-NIL Step&repeat and Lift-off Process Chain for High Speed Metal Nanomesh Fabrication. *Nanotechnology* **2020**, *31*, doi:10.1088/1361-6528/ab9130.

257. Guerrero, R.A.; Barretto, J.T.; Uy, J.L. V; Culaba, I.B.; Chan, B.O. Effects of Spontaneous Surface Buckling on the Diffraction Performance of an Au-Coated Elastomeric Grating. *Opt. Commun.* **2007**, *270*, 1–7, doi:10.1016/j.optcom.2006.08.024.

258. Ravagnan, L.; Divitini, G.; Rebasti, S.; Marelli, M.; Piseri, P.; Milani, P. Poly(Methyl Methacrylate)-Palladium Clusters Nanocomposite Formation by Supersonic Cluster Beam Deposition: A Method for Microstructured Metallization of Polymer Surfaces. *J. Phys. D. Appl. Phys.* **2009**, *42*, doi:10.1088/0022-3727/42/8/082002.

259. Corbelli, G.; Ghisleri, C.; Marelli, M.; Milani, P.; Ravagnan, L. Highly Deformable Nanostructured Elastomeric Electrodes with Improving Conductivity upon Cyclical Stretching. *Adv. Mater.* **2011**, *23*, 4504–4508, doi:10.1002/adma.201102463.

260. Ghisleri, C.; Siano, M.; Ravagnan, L.; Potenza, M.A.C.; Milani, P. Nanocomposite-Based Stretchable Optics. *Laser Photonics Rev.* **2013**, *7*, 1020–1026, doi:10.1002/lpor.201300078.

261. Ghisleri, C.; Potenza, M.A.C.; Ravagnan, L.; Bellacicca, A.; Milani, P. A Simple Scanning Spectrometer Based on a Stretchable Elastomeric Reflective Grating. *Appl. Phys. Lett.* **2014**, *104*, 061910, doi:10.1063/1.4865427.

262. Li, C.; Li, M.; Ni, Z.; Guan, Q.; Blackman, B.R.K.; Saiz, E. Stimuli-Responsive Surfaces for Switchable Wettability and Adhesion. *J. R. Soc. Interface* **2021**, *18*, 202110162.

263. Chu, C.; Zhao, Y.; Hao, P.; Lv, C. Wetting State Transitions of Individual Condensed Droplets on Pillared Textured Surfaces. *Soft Matter* **2022**, *19*, 670–678, doi:10.1039/d2sm01271e.

264. Chen, H.; Muros-Cobos, J.L.; Amirfazli, A. Contact Angle Measurement with a Smartphone. *Rev. Sci. Instrum.* **2018**, *89*, 035117, doi:10.1063/1.5022370.

265. Li, R.; Yi, H.; Hu, X.; Chen, L.; Shi, G.; Wang, W.; Yang, T. Generation of Diffraction-Free Optical Beams Using Wrinkled Membranes. *Sci. Rep.* **2013**, *3*, 2775, doi:10.1038/srep02775.

266. Chung, J.Y.; Nolte, A.J.; Stafford, C.M. Diffusion-Controlled , Self-Organized Growth of Symmetric Wrinkling Patterns. *Adv. Mater.* **2009**, *21*, 1358–1362, doi:10.1002/adma.200803209.

267. Rudquist, P. Revealing the Polar Nature of a Ferroelectric Nematic by Means of Circular Alignment. *Sci. Rep.* **2021**, *11*, 1–5, doi:10.1038/s41598-021-04028-7.

268. Xu, M.; Wang, Z.; Lu, H.; Qiu, L. Liquid Crystal Polarisation Converter Arrays Based on Microholes Patterned Hydrophobic Layers. *Liq. Cryst.* **2021**, *48*, 1–7, doi:10.1080/02678292.2021.1903107.

269. Lin, T.; Xie, J.; Zhou, Y.; Zhou, Y.; Yuan, Y.; Fan, F.; Wen, S. Recent Advances in Photoalignment Liquid Crystal Polarization Gratings and Their Applications. *Crystals* **2021**, *11*.

270. Wood, E.L.; Bryan-Brown, G.P.; Brett, P.; Graham, A.; Jones, J.C.; Hughes, J.R. 11.2: Zenithal Bistable Device (ZBD^{TM}) Suitable for Portable Applications. *SID Symp. Dig. Tech. Pap.* **2000**, *31*, 124–127, doi:10.1889/1.1832893.

271. Xu, M.; Yang, D.-K.; Bos, J.; Jin, X.; Harris, F.W.; Cheng, S.Z.D. 11.4L: Late-News Paper: Very High Pretilt Alignment and Its Application in Pi-Cell LCDS. *SID Symp. Dig. Tech. Pap.* **1998**, *29*, 139, doi:10.1889/1.1833713.

272. Acosta, E.J.; Towler, M.J.; Walton, H.G. The Role of Surface Tilt in the Operation of Pi-Cell Liquid Crystal Devices. *Liq. Cryst.* **2000**, *27*, 977–984, doi:10.1080/02678290050043932.

273. Acosta, E.; Henley, B.; Kean, D.; Tillin, M.; Tombling, C.; Towler, M.; Walton, E.; Walton, H.; Winlow, R. Nucleation of the Pi-Cell Operating State: A Comparison of Techniques. *Liq. Cryst.* **2004**, *31*, 1619–1625, doi:10.1080/02678290412331315968.

274. Büyüktanir, E.A.; Zhang, K.; Gericke, A.; West, J.L. Raman Imaging of Nematic and Smectic Liquid Crystals. *Mol. Cryst. Liq. Cryst.* **2008**, *487*, 39–51, doi:10.1080/15421400802198540.

Appendix A Experimental Methods

A.1 Broadband Green Light Spectrum – Conoscopy Experiments

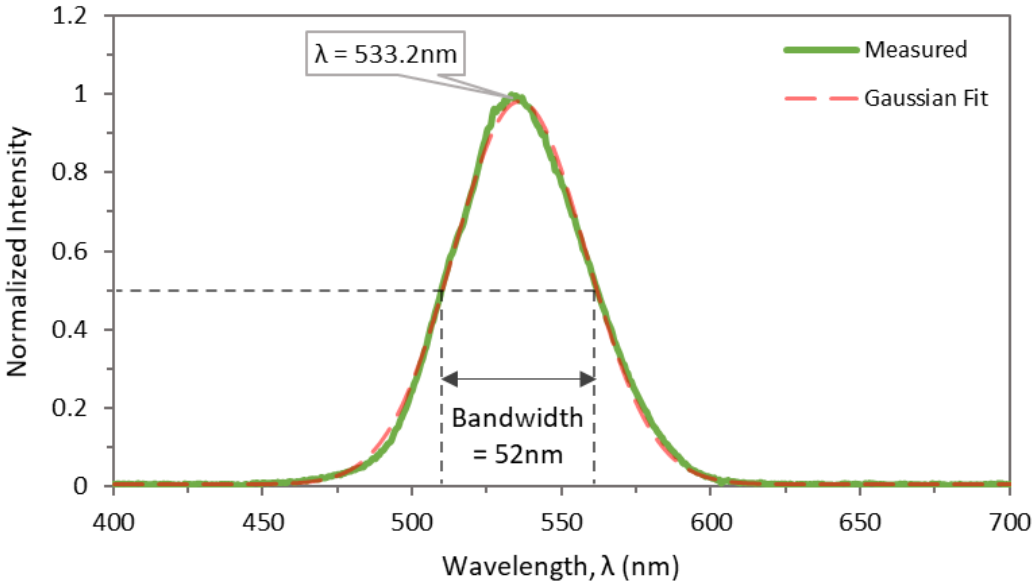

Figure A-1: Spectrum of broadband green light referred to in the conoscopy methods section (3.1.3.c.i) and used during conoscopy experiments on devices with homeotropic wrinkles (section 5.4.3) and homeotropic gratings (section 6.4.2.b). This light is produced by placing a green filter over the white light source of a Leica DM2700P optical microscope. The light's bandwidth of 52nm is taken from a Gaussian fit of the spectrum (red), as the full width at half of the maximum/peak intensity.

A.2 Blue Laser Spectrum (PL205, Thorlabs) – Diffraction Experiments

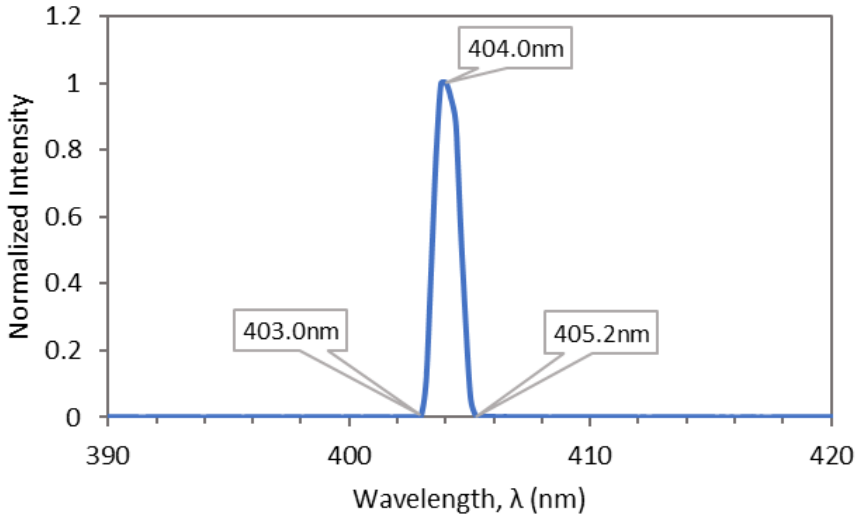

Figure A-2: Spectrum of Thorlabs PL205 blue laser diode, used during diffraction experiments on micropatterned liquid crystal elastomers (section 4.4) and imprinted polyimide grating structures (section 6.4.1.d).

Appendix B Micropatterned LCEs

B.1 Rubbed vs Unrubbed Polyimide Gratings in µLCE Cell Geometry

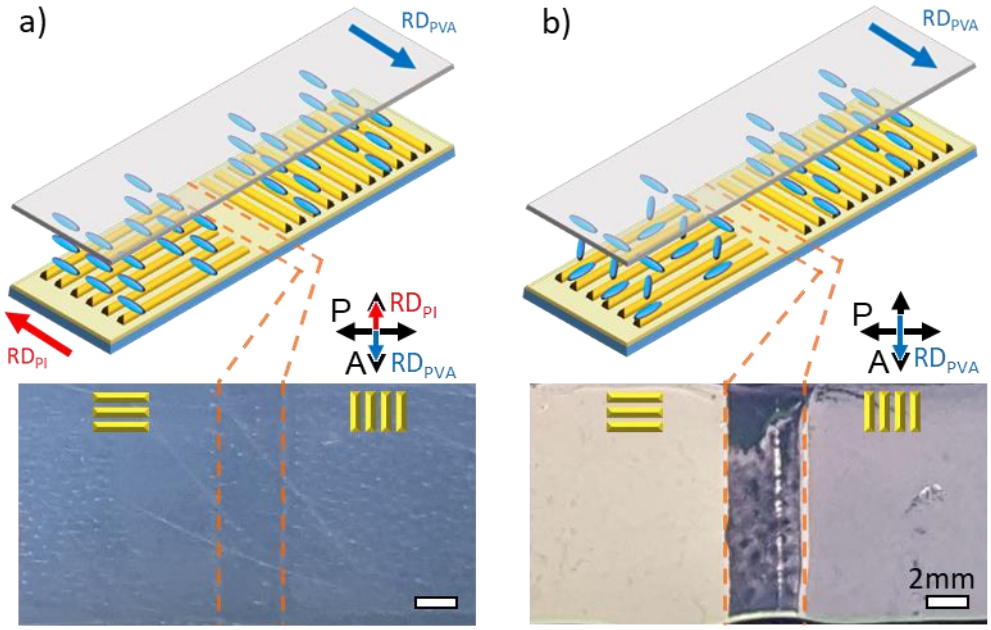

Figure B-1: Polarised microscopy observations of the same cell geometry used to fabricate nematic µLCE films in Chapter 4, comparing (a) rubbed and (b) unrubbed imprinted polyimide (IPI) grating surfaces. This comparison is referred to in the sections on µLCE fabrication (section 4.3.2.a) and resulting appearance and alignment (section 4.4.1). Devices are imaged at 20°C, filled with E7 and the confining surfaces are separated by 100µm thick spacer film. (a) Homogeneously rubbed IPI cell shows uniform extinction in both mutually-orthogonal grating regions, indicating that the surface alignment is dominated by the applied rubbing direction (RD_{PI}) and not the grating topography. If this wasn't the case it would be most visible in the left-hand region where the grating grooves and RD_{PI} are perpendicular, which would have increased transmittance if any induced twist was present. (b) Unrubbed IPI cell showing significant transmission in the left-hand region, where RD_{PVA} is perpendicular to the IPI grating grooves. This indicates that a twisted nematic (TN) director profile is present, due to the director aligning parallel to the grating grooves on the IPI surface, in the absence of an applied rubbing direction.

The cells used to fabricate the nematic µLCEs in Chapter 4 are somewhat atypical, as they feature an imprinted planar polyimide (PI) alignment layer with two competing surface anchoring contributions. One is from the linear surface relief grating imprinted in to the PI layer, acting to align the nematic director ($\hat{\boldsymbol{n}}$) parallel to the grooves to minimize the free energy.[74,75] The other is from the subsequent mechanical rubbing applied to the imprinted polyimide (IPI) surface, which acts to align $\hat{\boldsymbol{n}}$ parallel to the applied rubbing direction (RD_{PI}) by reorienting the near-surface polymer backbones of the PI layer.[64,65] The aim of these µLCE cells is to form a homogeneously aligned, monodomain µLCE films where $\hat{\boldsymbol{n}}$ is aligned parallel to the RD, ignoring the alignment influence of the underlying, mutually-orthogonal grating regions. This is targeted as a means of demonstrating the anisotropic deswelling and stimuli responses of the nematic µLCEs, using the common dimensions shared by each

IPI grating region as a reference point. Given this atypical geometry, it seems appropriate to confirm that the alignment on the rubbed IPI surfaces is in fact dominated by the mechanical rubbing. This is demonstrated in Figure A-1, using individual cells with the same geometry as those used for the μLCEs, with rubbed (Figure A-1a) and unrubbed (Figure A-1b) IPI substrates opposed by a rubbed PVA surface.

B.2 Differential Scanning Calorimetry

Differential scanning calorimetry (DSC) was performed using a TA Instruments Q20 DSC to determine phase transitions in the precursor mixture. 10mg of LCE precursor mixture was pipetted into a TZero Aluminum pan and an empty pan was used as a reference. DSC cycles were performed from 100°C to -20°C at a rate of 10°C/min. These data are referred to in the sections on LCE synthesis (section 4.3.2.b) and the deswelling tunability offered by changing the composition of the LCEs (section 4.4.2.c).

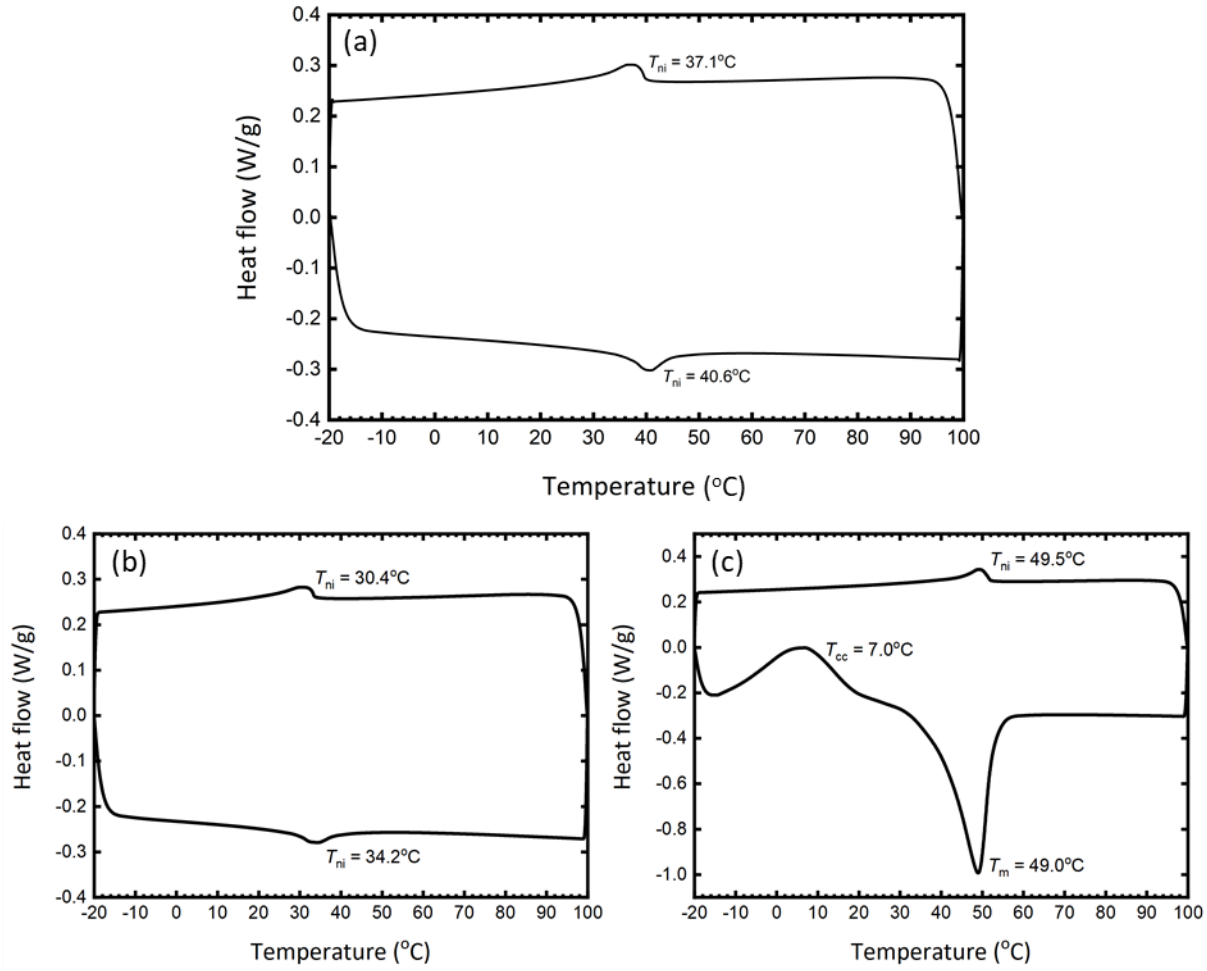

Figure B-2: DSC traces of the (a) 54.6 mol% 6OCB precursor mixture. (b) 45.7 mol% 6OCB precursor mixture and (c) 70.7% 6OCB precursor mixture. The nematic-to-isotropic transition temperature, T_{ni}, for each sample is shown. The 70.7 mol% 6OCB precursor mixture displays a cold crystallization (T_{cc}) and melting (T_m) peak on heating.

B.3 Visual Appearance of µLCE Film

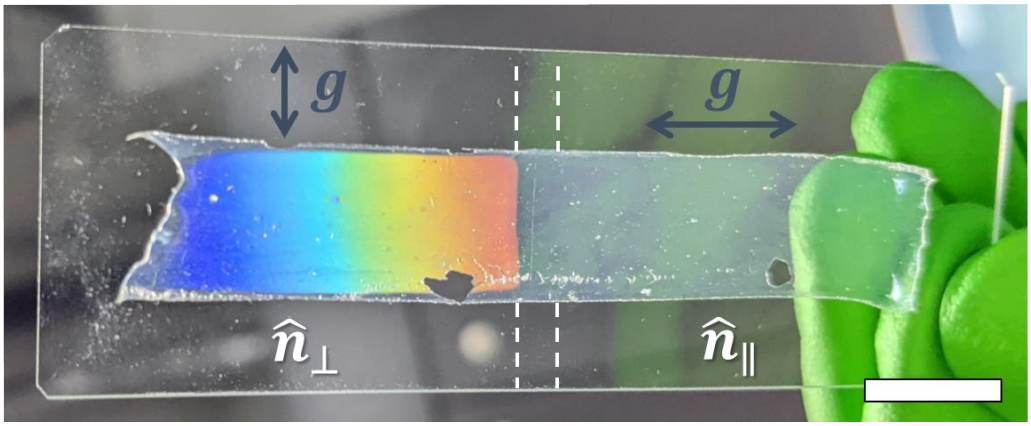

Figure B-3: Photograph of a fabricated µLCE film in ambient white light, highlighting the structural colour in the $\hat{n}_{\perp}$ region of the film, caused by the diffractive nature of the periodic grating structure. The variation in colour is due to the sample being at an angle relative to direction of observation, which shows the wavelength dispersion of white light associated with the 1st order diffraction mode. This is referred to in section 4.4.1 on the appearance and alignment of the µLCE films.

B.4 Polarised Light Appearance of µLCE Film – No Colour Bands

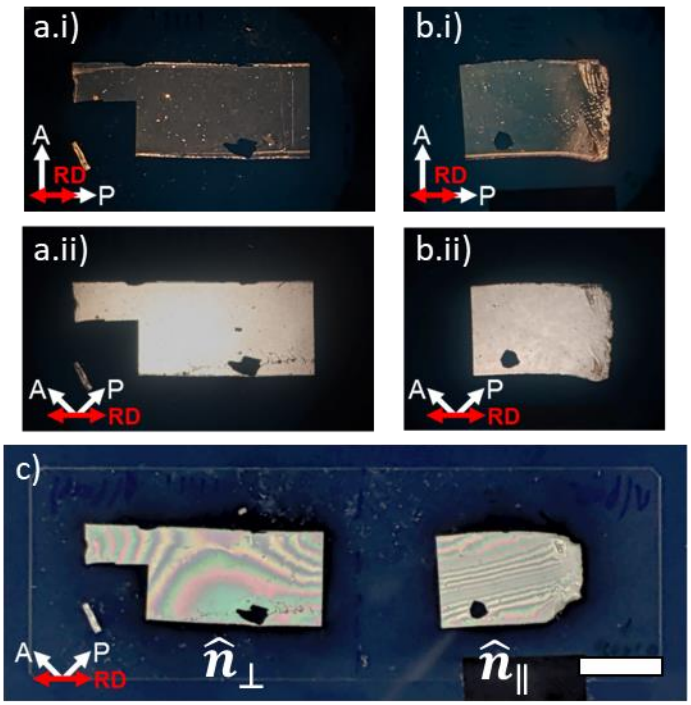

Figure B-4: Confirmation that the birefringence colour bands shown in Figure 4-7b.ii in section 4.4.1 are an artefact of the screen backlight used to illuminate the sample. (a, b) Monodomain µLCE film illuminated with an alternative white light source, imaged between crossed polarisers (P, A), with the rubbing direction (RD)/director orientation at (i) 0° and (ii) 45° to the polarisers. The images in (a.ii) and (b.ii) show the expected saturated white appearance of the µLCE film, compared to the banded appearance when imaged in the same orientation using the screen backlight shown in (c). Scale bar = 10mm.

B.5 Atomic Force Microscopy Data

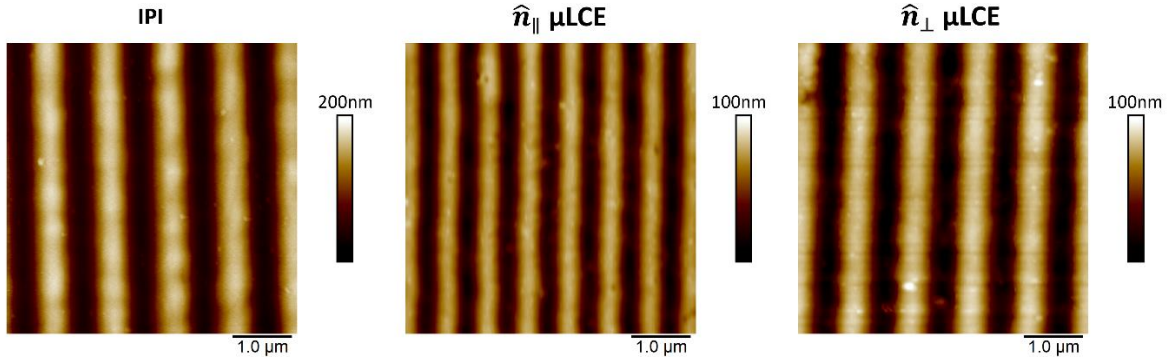

Figure B-5: (Left) AFM scan of an imprinted polyimide (IPI) grating, with a pitch of 1040 ± 5nm and a height of 130 ± 5nm, used as a mould in Chapter 4 for fabricating µLCEs and as a reference surface for the homeotropic wrinkle device in section 5.4.3.c.i. (Middle, Right) AFM scans of µLCEs fabricated with the nematic director parallel ($\hat{\boldsymbol{n}}_{\parallel}$) and perpendicular ($\hat{\boldsymbol{n}}_{\perp}$) to the grating orientation.

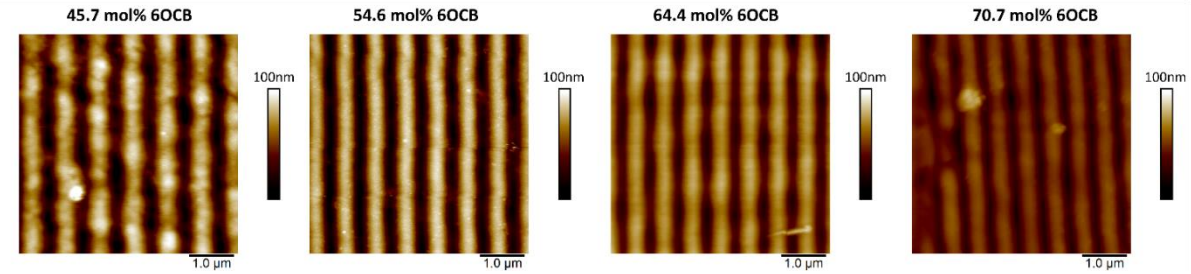

Figure B-6: AFM scans of $\hat{\boldsymbol{n}}_{\parallel}$ µLCEs with varying concentrations of 4'-hexyloxy-4-cyanobiphenyl (6OCB).

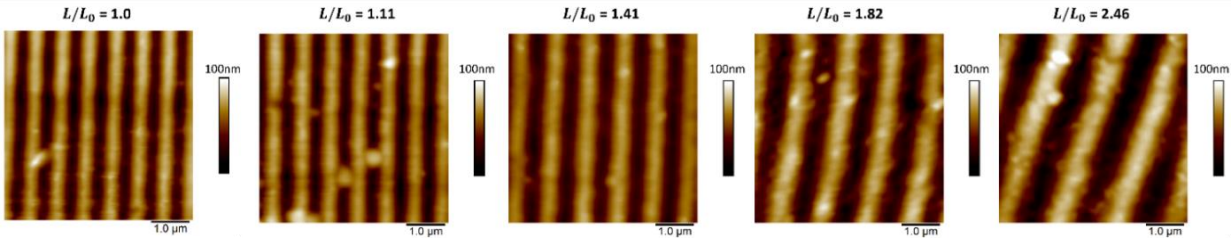

Figure B-7: AFM scans of $\hat{\boldsymbol{n}}_{\parallel}$ µLCEs under strain, at various fractional lengths (L/L_0), where applied strain (ε) = (L/L_0)− 1 .

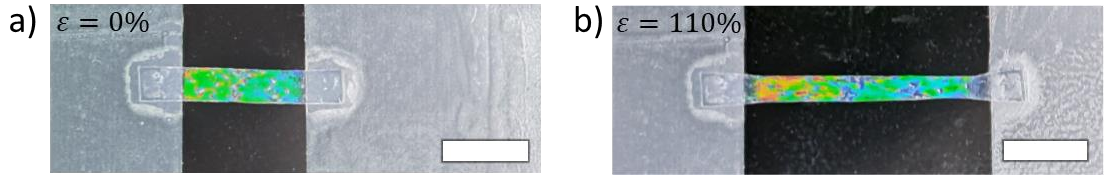

Figure B-8: Photographs showing the manual strain approach used to perform AFM measurements on µLCE films under strain, referred to in section 4.4.4 on the strain response of the µLCEs. The images show a µLCE film with both ends secured to a glass slide using adhesive tape, at (a) 0% and (b) 110% tensile strain. The strain is adjusted by moving one end of the film and re-adhering it in a different location. Strain is calculated from measurements of the sample length/tape separation at each strain increment. Scale bars = 5mm.

B.6 Thermogravimetric Analysis

Thermogravimetric analysis (TGA) was performed using a TA Instruments Q50 TGA to determine the decomposition temperature of the µLCE, as referred to in section 4.4.6 on durability testing the µLCE films. 2mg of the µLCE film was loaded into the TGA and a temperature ramp from 20°C to 500°C at a rate 10°C/min was performed. The degradation temperature, T_{deg}, was defined as the temperature in which 5% mass loss has occurred.

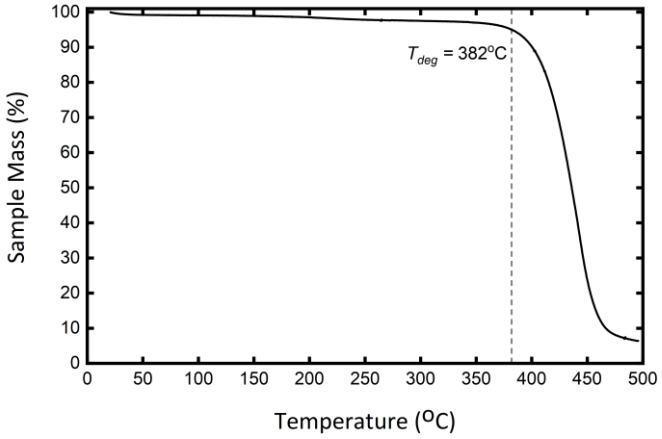

Figure B-9: TGA results on the 54.6 mol% 6OCB µLCE with thermal degradation (defined as the temperature at 5% mass loss) occurring at $T_{deg} = 382°C$.

Appendix C Wrinkled LC Alignment Layers

C.1 Birefringence Colours of HAN Device with Planar Wrinkles

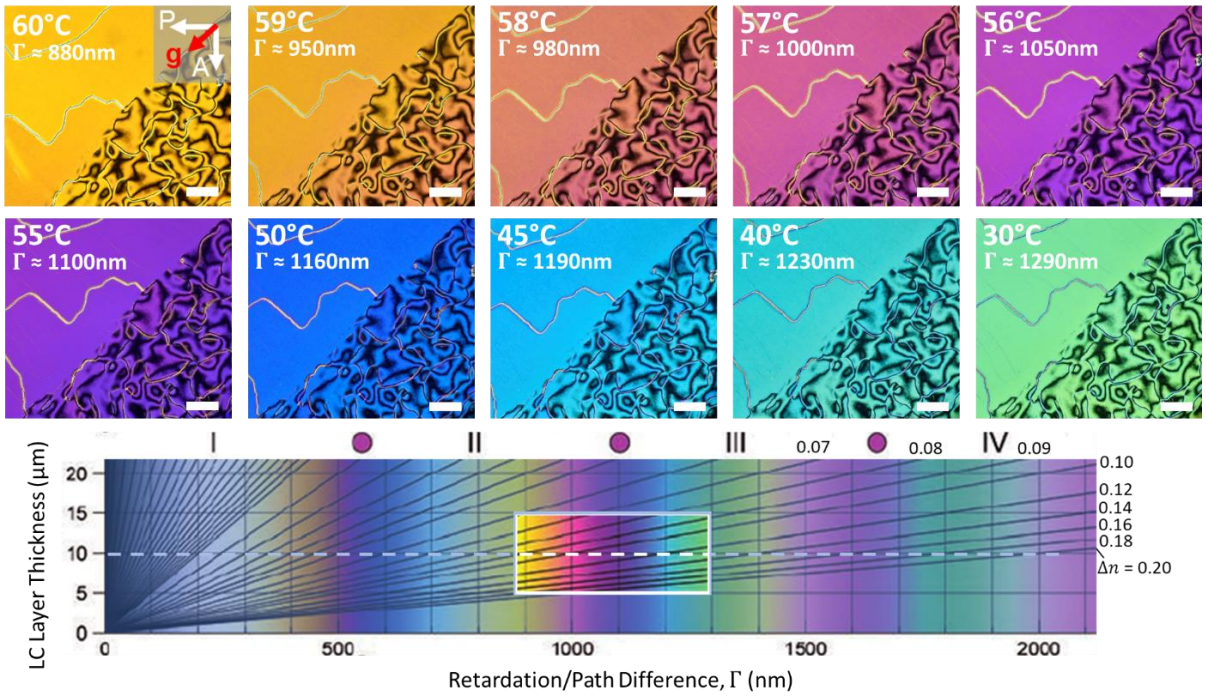

Figure C-1: Polarised optical microscopy (POM) observations of the hybrid aligned nematic (HAN) device discussed in section 5.4.2.a, featuring a planar wrinkle-imprinted polyimide surface. The device has an LC layer thickness of 10 ± 1μm and is imaged upon cooling from 60 to 30°C, on the boundary between wrinkled (uniform) and flat (Schlieren) polyimide regions. Temperatures and approximate retardations (Γ) associated with the observed colours are indicated on the POM images. A section of the Michel-Lévy colour chart, adapted from reference [49]*, is shown at the bottom of the figure, with a rectangular highlighted region indicating a range of 2nd (II) order birefringence colours that correspond closely to those shown in the POM images above. The sequence of colours observed in the POM images upon cooling therefore confirms that the observed orange colour at 59°C is 2nd order orange (Γ ≈ 950nm), rather than 1st order orange (Γ ≈ 450nm).*

C.2 Identifying Sign of $|s| = 1$ Point Defect

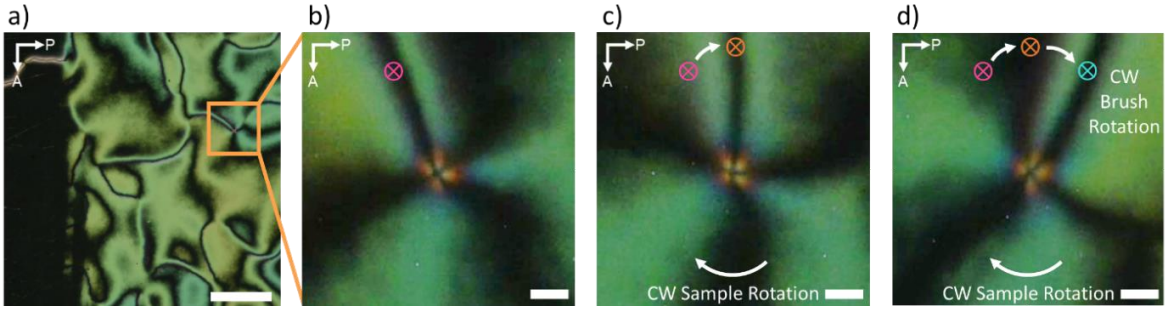

Figure C-2: POM observations of the HAN device with planar wrinkles, discussed in section 5.4.2. These images confirm the sign (±) of the $|s| = 1$ point defect, which is used as a reference point in section 5.4.2.b to confirm the azimuthal director orientation. (a) Broad view of the device with the reference defect highlighted by the orange box. Scale bar = 200μm. (b – d) Enlarged views of the 4-brush $|s| = 1$ point defect at successive stages during clockwise (CW) sample rotation, with scale bars = 5μm. The dark brush marked with the pink ⊗ symbol in (b) is used as a reference point. This brush can be seen to rotate CW as the sample is rotated CW, indicated by the orange and turquoise ⊗ symbols in (c) and (d) respectively. This matching sense of rotation between the sample and the brushes confirms that this is a $s = -1$ defect, as the brushes of a $s = +1$ defect would rotate in the opposite sense relative to the sample rotation.[218]

C.3 Conoscopy: Calibrating Back Focal Plane *via* Diffraction

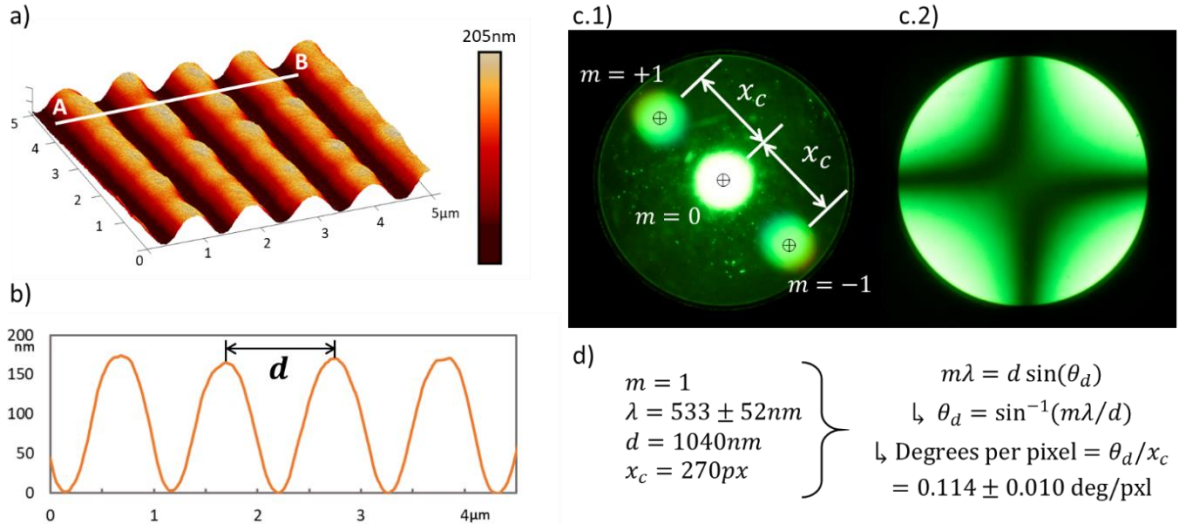

Figure C-3: Conoscopy figure calibration using the diffraction pattern of a linear surface relief grating, as referred to in section 3.1.3.c.i on the conoscopy methodology and section 5.4.3.a on the tilt of homeotropic wrinkles. (a) 3D topographic data from a 5x5μm atomic force microscopy scan of the calibration grating. (b) Cross-sectional height profile of the grating, with pitch (d=1040nm), taken along line A-B in (a). (c) Conoscopic figures with identical fields of view, produced by (c.1) the calibration grating, imaged without an analyser, and (c.2) a vertically aligned nematic LC device with homeotropic wrinkles, imaged between crossed polarisers. The diffraction pattern in (c.1) shows the grating's zeroth ($m = 0$) and first ($m = \pm 1$) order diffraction modes, with x_c denoting the separation of $m = 0$ and $m = \pm 1$ in pixels. This is measured from the centre of each maxima (⊕), located using the 'Analyze Particles' tool in ImageJ analysis software (NIH, USA). (d) The 'degrees per pixel' calibration factor for the conoscopy figures is calculated by relating the diffraction angle (θ_d) of light with a given wavelength (λ), from a grating with pitch (d), to the zeroth and first order maxima separation (x_c) shown in (c.1).

C.4 Director Tilt and Effective Birefringence Profiles

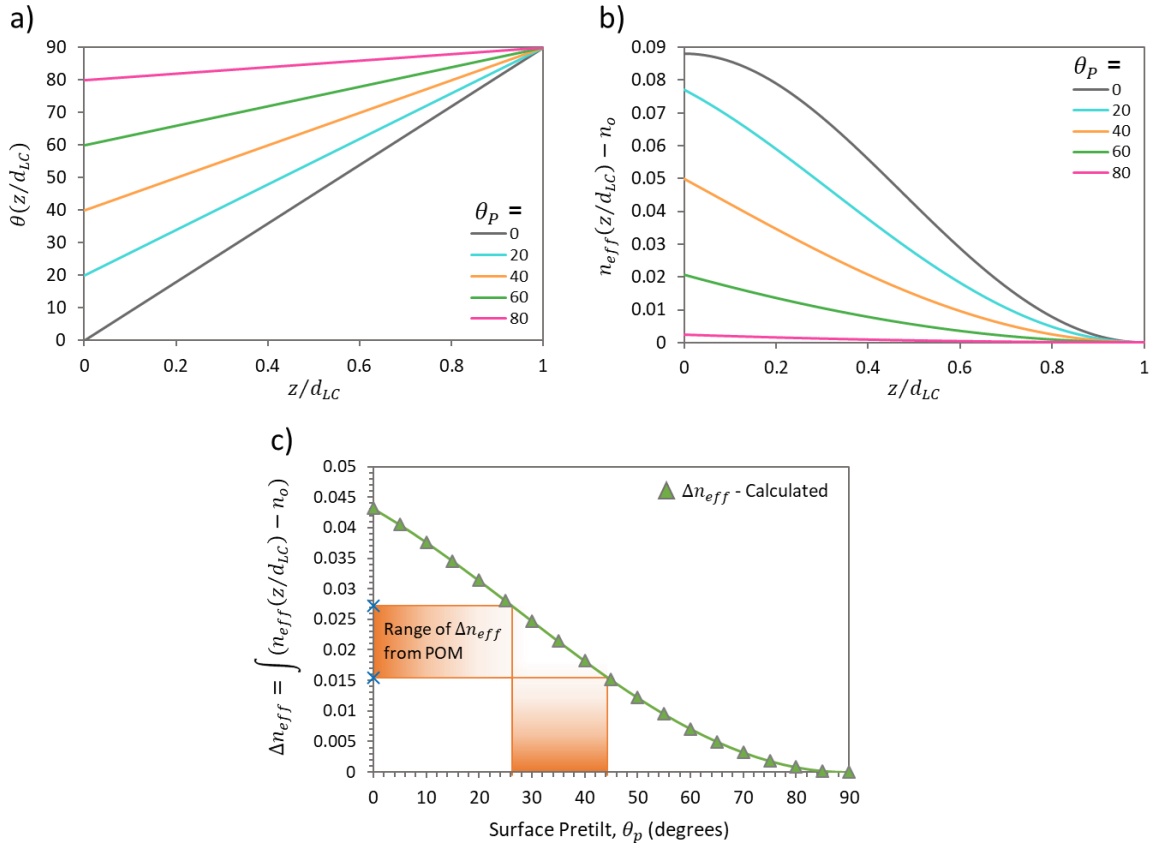

Figure C-4: Supporting data used to approximate wrinkled surface pretilt (θ_p) in the homeotropic wrinkle device discussed in section 5.4.3.b.ii, following the surface anchoring transition. (a) Theoretical linear director tilt profiles ($\theta(z/d_{LC})$) as a function of normalized slab thickness (z/d_{LC}), for a hybrid-aligned nematic (HAN) device geometry with different θ_p on one surface, generated from equation (5-3). (b) Corresponding variation in ($n_{eff}(z/d_{LC})) - n_o$) for each tilt profile, calculated using equation (5-4) for the effective refractive index (n_{eff}), and the refractive indices of MLC-6204 at T/T_{NI} = 0.99 (n_e=1.595 and n_o=1.507). (c) Resulting birefringence of the LC slab (Δn_{eff}) as a function of θ_p, calculated by integrating the functions in (b) from z/d_{LC} = 0 to z/d_{LC} = 1. The two blue cross (×) symbols on the y-axis denote the top and bottom of the range of Δn_{eff} values obtained from comparing the observed birefringence colours of the device with the Michel-Lévy chart (Figure 2-4). The orange shaded areas indicate how these measured values are cross-referenced with the calculated Δn_{eff} data to obtain a range of θ_p for the wrinkled surface.